Transition Metal Complexes as Solar Cell Dyes

A thesis submitted for the degree of Doctor of Philosophy by

Elaine A. M. Geary

School of Chemistry
Faculty of Science and Engineering
University of Edinburgh
August 2005

This thesis is dedicated
to my family and Chris.

Acknowledgements

Firstly I would like to thank my supervisors Dr. Neil Robertson and Prof. Lesley Yellowlees for their guidance and support during my three years at Edinburgh. Thanks also to Lesley for help with EPR simulations. I would also like to thank Prof. Peter Tasker for his sound advice and encouragement.

I would like to thank my collaborating groups at Imperial College London (Dr. James Durrant *et al.*) and the Università di Cagliari (Prof. Paola Deplano and Prof. Maria Laura Mercuri *et al.*) for teaching me new chemistry and valuable techniques.

Thanks to the technicians and researchers who helped with analytical/structural problem solving: Alan Taylor and Robert Smith (Mass Spec.), John Millar (NMR), Dr. Simon Parsons, Dr. Iain Oswald, Dr. Alice Dawson, Stephen Moggach (Crystallography) and Dr. Patricia Richardson (Fluorescence Spectroscopy).

I would like to thank the past and present members of my group (i.e. Sarah and more recently Lucy), my other group (Lorna, Paul, Salma and Ed) and my surrogate groups (Dr. Dave Henderson, Dr. Vesna Gasperov, Stuart, Jenny, Rachel, Dot, Robert, Iria and Ross, Dr. Euan Brechin, Dr. Costas Milios, Maria Manoli, Richard Scott) for including me in so many of your professional/social activities...!

Thanks to all my friends from around Europe who work along the corridor - too numerous to mention but especially Michele and Emiliano for persevering with my terrible efforts at learning Italian!

I would like to thank all my friends in Marchmont for making my time here the happiest three years I could have hoped for. Thanks to Iain (for being a great flatmate and taking me in, in the first place) and Jane, Dave & Mon, Andrew & Judith, Pete & Sally (for lots of really great nights out and dinners in...) and all my friends at "Sweet Melindas" where I've had lots of fun.

I would especially like to thank my family – To my Mam and Dad for constantly looking after me in every way, to my sisters Ciara, Una and Aine who I am so proud of for everything that they do, to my Nan for keeping me up to date with all the news from home and being a great friend and to all my numerous extended family members who will undoubtedly be glad I've finally got a job...! To my Dollar family, Tommy, Joey, Lou, Vern, Vicki, Bill and Lara – Thanks for being great fun to visit and for the general use of the 3rd floor when I needed it!

Finally thanks to Chris for being the best friend and adventure partner anyone could ask for. I'd have come here sooner if I'd known how much fun it would be...!

Abstract

Dye-Sensitised Solar Cells (DSSC) were first reported in the early 1990's and function by the sensitisation of a semiconductor using a dye molecule such as organic and transition metal organometallic dyes. This thesis reports the synthesis and characterisation of transition metal dyes with applications as sensitisers in DSSC. Complexes of Ni, Pd and Pt were investigated for use in standard liquid electrolyte cells and Donor-Acceptor type solid-state solar cells.

A family of [Pt(II)(diimine)(dithiolate)] complexes of general formula [Pt{X,X'$(CO_2R)_2$-bpy}(mnt)] (where X=3, 4 or 5; R= H or Et, bpy = 2,2'-bipyridyl and mnt = maleonitriledithiolate), have been synthesised, spectroscopically and electrochemically characterised and attached to a TiO_2 substrate to be tested as solar cell sensitisers. A single crystal X-ray structure showing a large torsion angle between the bipyridyl rings was determined for [Pt{3,3'$(CO_2Et)_2$-2,2'-bpy}(mnt)].MeCN. The effect of changing the position of the bpy substituents from 3,3' to 4,4' and 5,5' is discussed with reference to structural and electronic changes seen within the different members of the family of molecules. The UV/Vis/NIR and *in-situ* EPR spectroelectrochemical studies of the family and its related precursor molecules are discussed. All three complexes (where R=H) were tested as solar cell sensitisers with the 3,3'-disubstituted bpy complex giving an intermediate dye loading value but superior photovoltaic performance to those of the other two. The performance of this sensitiser is then compared with that of a well known Ru(polypyridyl) sensitiser.

A family of unsymmetrical [Ni(II)(dithione)(dithiolate)] complexes of general formula, [Ni(R_1R_2pipdt)(dmit)], where R = Me, Bz and Pr^i, pipdt = 1,4-disubstituted-piperazine-3,2-dithione and dmit = 1,3-dithiole-2-thione-4,5-dithiolate, have been synthesised and characterised and investigated for use in solid-state solar cells. Electrochemistry and UV/Visible spectroscopy results show that the reduction potential of a complex is related to the number of aromatic substituents on the pipdt ligand. The dibenzyl substituted complex shows the longest absorption wavelength in the NIR which is

attributed to it having the smallest HOMO-LUMO gap of the complexes studied. *In-situ* EPR results show the reduction electron to be located on the R_1R_2pipdt ligand which confirms previous proposals that the LUMO is in part located on this part of the complex. Raman spectroscopy confirms the dmit ligand to be formally dianionic with the R_1R_2pipdt having a formally neutral charge.

Complexes of the general formula [M(phendione)(mnt)], where M = Pd and Pt and phendione = 1,10-phenanthroline-5,6-dione have been synthesised, characterised and investigated as sensitisers for DSSC. Complexes of phendione were investigated following reports of natural dyes which attach to TiO_2 *via* a diketone functional group. The electrochemical and *in-situ* EPR studies of these molecules show that the complexes retain similar characteristics to their dichloride precursors and confirm the site of the LUMO to be mainly based on the diimine ligand.

In a move to develop longer wavelength dyes for DSSC, the [Pt(II)(diimine)(dithiolate)] complexes, [Pt(5,5′(CO_2H)$_2$-bpy)(tdt)] and [TBA]$_2$[Pt(5,5′(CO_2)$_2$-bpy)(tdt)] (tdt = 3,4-toluenedithiolate) have been prepared, characterised and attached to TiO_2. A single-crystal X-ray structure was obtained for [TBA]$_2$[Pt(5,5′(CO_2)$_2$-2,2′-bpy)(tdt)].EtOH.EtOAc. The effect of the position of the carboxylic acid substituents on the electrochemistry of the 5,5′-disubstituted complexes is discussed in comparison with the previously reported [Pt(4,4′(CO_2H)$_2$-2,2′-bpy)(tdt)]. Electrochemical studies show a change in reduction potential of the compound on moving the carboxylic acid substituents from the 4,4′ to the 5,5′ positions. The dyes were attached to a TiO_2 substrate and tested as solar cell sensitisers with the di-TBA salt giving lower dye loading but superior photovoltaic performance to the neutral dye.

Table of Contents

Chapter 2. Experimental Techniques

Table of abbreviations

λ	wavelength
ε	extinction coefficient
°	degree
° C	degree centigrade
Å	angstrom
Bpy	2,2′-bipyridine
Bz	benzyl
ca.	*circa*
CV	cyclic voltammogram
DMF	Dimethyl formamide
DMIT	1,3-dithiole-2-thione-4,5-dithiolate
DMSO	Dimethyl sulfoxide
DSSC	Dye-Sensitised Solar Cell
et al.	*et alli* (and others)
EtOH	Ethanol
EPR	Electron Paramagnetic Resonance
eV	electron volts
FABMS	fast atom bombardment mass spectroscopy
ff	fill factor
HOMO	Highest Occupied Molecular Orbital
h	hour
IR	infra-red
IPCE	Internal Photon to Current Efficiency
I_{sc}	short circuit current
K	kelvin
LMCT	Ligand to Metal Charge Transfer

m (IR)	medium
m/z	mass per unit charge
Me	methyl
MeCN	acetonitrile
MeOH	methanol
min	minute
mL	millilitre
MLCT	Metal to Ligand Charge Transfer
mmol	milli moles
mnt	maleonitriledithiolate
mol	moles
Ph	phenyl
phendione	1,10-phenanthroline-5,6-dione
pipdt	1,4-disubstitutedpiperazine-2,3-dithione
Pr^i	iso-propyl
s (IR)	strong
T	temperature
tdt	toluenedithiolate
TTF	Tetrathiafulvalene
UV/vis	ultra violet/visible
V	Volts
V_{oc}	open circuit voltage
w (IR)	weak

Table of structures

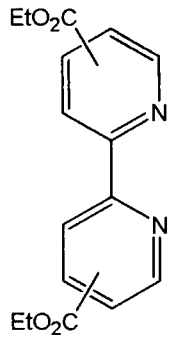

1a = 3,3'-$(CO_2Et)_2$-bpy
2a = 4,4'-$(CO_2Et)_2$-bpy
3a = 5,5'-$(CO_2Et)_2$-bpy

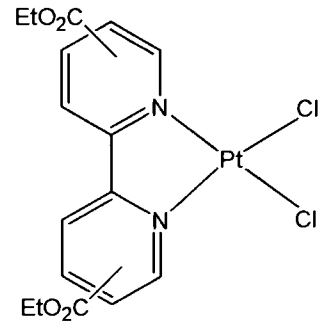

1b = [Pt{3,3'-$(CO_2Et)_2$-bpy}Cl_2]
2b = [Pt{4,4'-$(CO_2Et)_2$-bpy}Cl_2]
3b = [Pt{5,5'-$(CO_2Et)_2$-bpy}Cl_2]

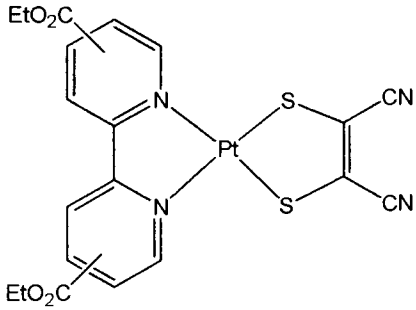

1c = [Pt{3,3'-$(CO_2Et)_2$-bpy}(mnt)]
2c = [Pt{4,4'-$(CO_2Et)_2$-bpy}(mnt)]
3c = [Pt{5,5'-$(CO_2Et)_2$-bpy}(mnt)]

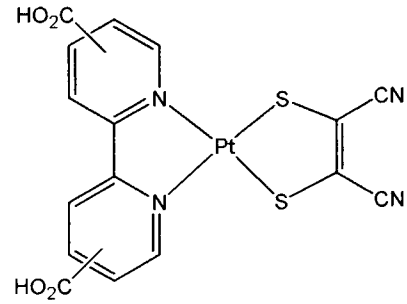

1d = [Pt{3,3'-$(CO_2H)_2$-bpy}(mnt)]
2d = [Pt{4,4'-$(CO_2H)_2$-bpy}(mnt)]
3d = [Pt{5,5'-$(CO_2H)_2$-bpy}(mnt)]

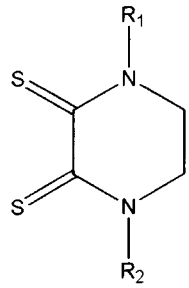

4a = $R_1 = R_2 = Bz$
5a = R_1 = Me, $R_2 = Bz$
6a = $R_1 = R_2 = Pr^i$

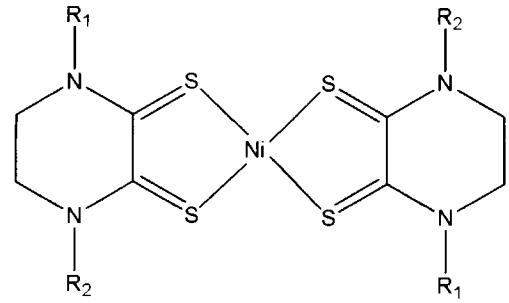

4b = $R_1 = R_2 = Bz$
5b = R_1 = Me, $R_2 = Bz$
6b = $R_1 = R_2 = Pr^i$

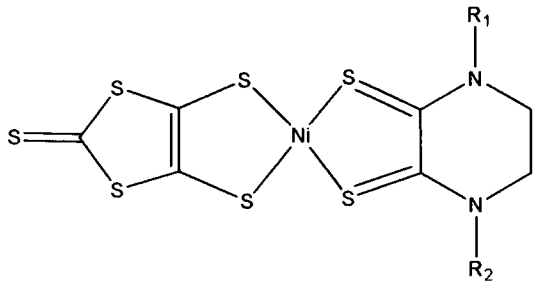

4c = $R_1 = R_2 = Bz$
5c = $R_1 = Me$, $R_2 = Bz$
6c = $R_1 = R_2 = Pr^i$

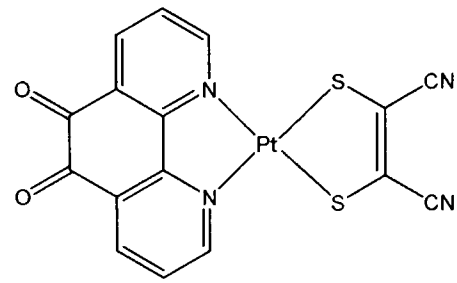

7 = [Pt(phendione)(mnt)]

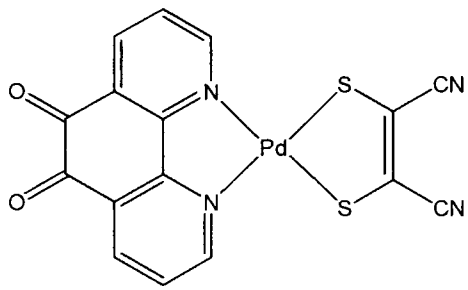

8 = [Pd(phendione)(mnt)]

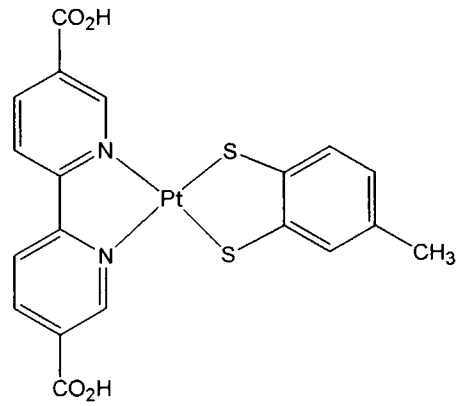

9 = [Pt{5,5'-$(CO_2H)_2$-bpy}(tdt)]

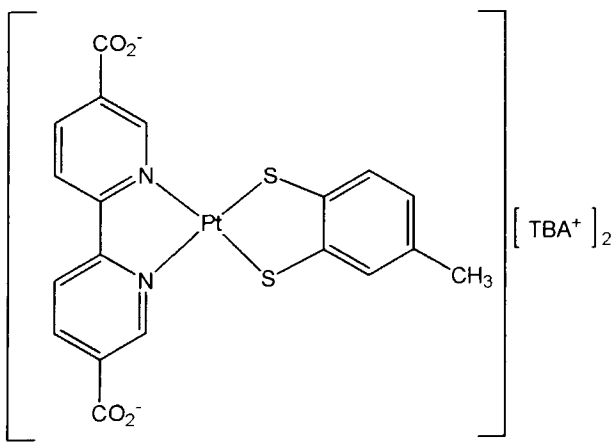

10 = $[TBA]_2$[Pt{5,5'-$(CO_2)_2$-bpy}(tdt)]

Chapter 1

Introduction

1. Introduction

1.1 History of the solar cell

The history of sensitisation of semiconductors with dye molecules dates back to initial experiments within the field of photography. The silver halide grains used in photographic films are composed of mixtures of AgI, AgBr and AgCl. AgX compounds have a band gap of 2.7 – 3.2 eV and are therefore insensitive to much of the visible spectrum. They are sensitised to light in the visible region by dyes which are adsorbed on to the AgX crystal in the photographic film. On exposure to light these dyes inject an electron into the AgX and this eventually produces a "latent image centre" on the surface of the grain of AgX. This centre can be chemically reduced by developing agents to create the picture.[1] In 1887 the concept of dye enhancement was carried over from the field of photography to that of photoelectrochemical cells by Moser (reference [2] and references therein).

1.1.1 Photoelectrochemical cells

Much work on the modern field of photoelectrochemical cells was performed in the 1950's and 1960's by Brattain, Garet and Gerischer (reference [2] and references therein). Many detailed electrochemical and photoelectrochemical studies on the semiconductor-electrolyte interface were performed and investigations focussed on regenerative and photosynthetic cells. However it was after the oil crisis of 1973 that research in this field went through an intensely productive period as a worldwide quest for alternative energy sources began.

1.1.2 Photochemical production of H_2

Development of an artificial photosynthetic system for conversion of light into chemical energy began in the 1970's with the first reports on photochemically driven water splitting.[3] This reaction is promoted by derivatives of $[Ru(bpy)_3]^{2+}$, where bpy is 2,2′-

bipyridyl. Each of these early reports were based on a multicomponent system which involved several electron transfer steps involving a d^6 Ru(II) chromophore, an electron acceptor and an electron donor. This resulted in H^+ reduction to yield H_2 and the irreversible reaction of a sacrificial electron donor.[4] These same Ru sensitisers were used in later years by Grätzel and others to convert sunlight to electrical energy using photovoltaic devices.[5, 6]

1.2 Photovoltaic Devices

Photovoltaic devices convert solar radiation directly into electrical power *via* charge separation at the interface of two materials. In the past the science of solar cells has focussed on devices which make use of inorganic materials such as doped forms of silicon. In more recent years III/V compounds e.g. GaAs have been studied. Throughout this time, the silicon cell has proven to be the most efficient; however the large capital cost associated with these devices makes them unsuitable for large scale everyday use. Over the last decade, the dominance of inorganic materials has faced new challenges with the advent of a cost effective solar cell, known as the Dye-Sensitised Solar Cell (DSSC), which is based on nanocrystalline metal oxides. In a move from classical solid state junction devices, present day photovoltaic devices can function with huge surface area junctions. This has been facilitated by recent progress in the fabrication and characterisation of nanocrystalline materials. These devices based on interpenetrating networks of mesoporous semiconductors have shown very high conversion efficiencies which compete with those of some conventional devices.

1.3 Dye-Sensitised Solar Cells

This family of devices using a high surface area semiconductor is based on a system that mimics photosynthesis in its conversion of solar energy. Here a dye molecule, analogous to the light absorbing chlorophyll molecule found in nature, is anchored to a wide band gap semiconductor (usually nanocrystalline TiO_2) which absorbs in the UV region of the solar spectrum. DSSC differ from traditional solid-state junction

photovoltaic devices in their basic mode of function. In a traditional device the semiconductor performs both the light absorption and charge generation functions whereas in a DSSC the dye is employed to absorb light and the TiO_2 semiconductor is involved in charge generation.

1.3.1 Cell Design

The solar cell consists of two conducting glass electrodes in a sandwich configuration with a redox electrolyte (typically I^-/I_3^-) separating the two (fig. 1.1). A layer of TiO_2 a few microns thick is deposited and annealed on to the surface of the FTO (fluorine doped tin oxide) coated glass and the dye is adsorbed on the surface of this. The redox electrolyte interpenetrates the pores of the TiO_2 creating a conducting network. A Pt counter electrode which is deposited on to the other glass surface functions not only as the counter electrode but also to catalyse the cathodic reduction of triiodide to iodide.

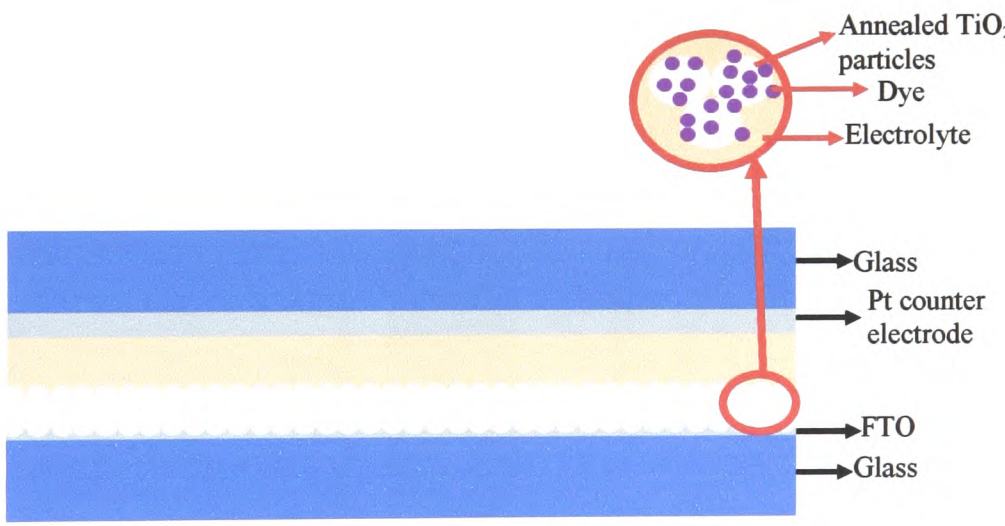

Fig. 1.1 A cross section of a simple DSSC

1.3.2 Mode of function of a DSSC

The potential energy diagram describing one cycle of a DSSC is shown in fig. 1.2. On exposure to visible light the ground state of the dye becomes excited and in its excited state, the dye molecule injects an electron into the conduction band of TiO_2 at a rate k_1, which can be as fast as 10^{13} s^{-1}.[7] The ground state of the now oxidised dye is restored by electron donation from the iodide/triiodide redox electrolyte at a rate of *ca.* 10^8 s^{-1}, k_2. The photoinjected electron migrates through the TiO_2 at a rate of 10^3-10^0 s^{-1}, k_3 and through the external circuit to the counter electrode where the redox electrolyte is regenerated by reduction of the triiodide to iodide at a rate k_4. A number of loss processes can be identified in the cell including recombination of the photo-injected electron with the triiodide at a rate k_5 which is known as the dark current, recombination of the injected electron with the oxidised form of the dye, k_6, and radiative and non radiative decay, k_7.[8]

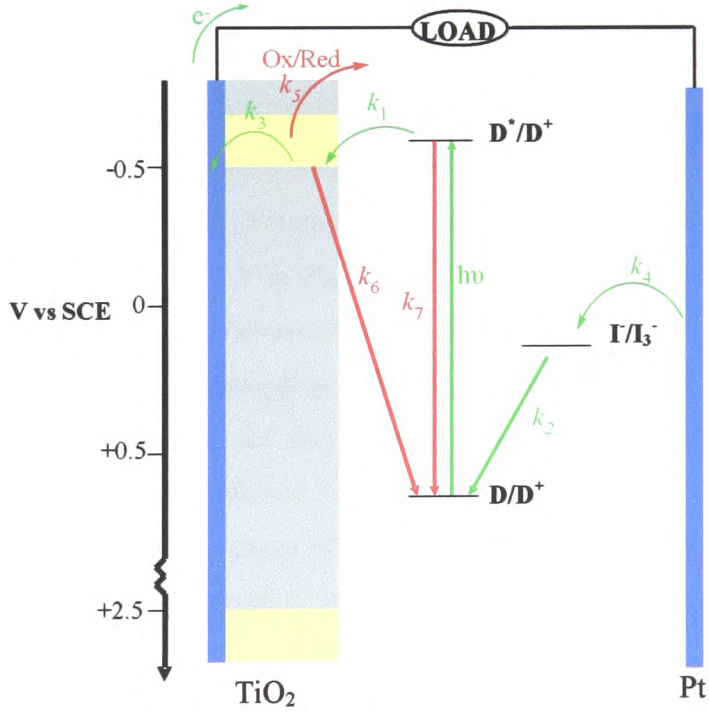

Fig. 1.2 Schematic diagram showing the kinetic steps involved in one cycle of a DSSC. Green arrows indicate favourable processes while red arrows indicate loss mechanisms.

The yellow bands shown on the TiO_2 indicate the conduction band (upper) and valence band (lower) of the semiconductor.

The processes which occur in one cycle of the cell can also be explained using a set of equations as follows:

$$D_{(ads)} + h\upsilon \rightarrow D^*_{(ads)}$$

$$D^*_{(ads)} \rightarrow D^+_{(ads)} + e^-_{(injected)} \ (k_1)$$

$$D^+_{(ads)} + 3/2\ I^- \rightarrow D_{(ads)} + \tfrac{1}{2}\ I_3^- \ (k_2)$$

$$I_3^-{}_{(cathode)} + 2e^- \rightarrow 3I^-_{(cathode)} \ (k_4)$$

$$I_3^- + 2e^-(TiO_2) \rightarrow 3I^-_{(anode)} \ (k_5)$$

$$D^+_{(ads)} + e^-(TiO_2) \rightarrow D_{(ads)} \ (k_6)$$

D = Dye, ads = adsorbed on TiO_2.

1.3.3 Parameters affecting DSSC performance

Each cell variable can individually effect the cell's overall performance.[9] To a large extent the nanocrystalline film properties and dye spectral response are responsible for the high efficiency of the cells. In the case of the nanocrystalline TiO_2 a high surface area film and predefined thickness are required to facilitate a high optical density for the dye resulting in a high light-harvesting efficiency. The dye for its part plays a crucial role. Efficient engineering of the dye structure can change its electrochemical and photophysical properties and enhance its trapping of visible and near infra-red (IR) solar radiation. The electrolyte also plays an important role in maximising the power output of the cell since the redox potential of the electrolyte directly influences the open circuit voltage (V_{oc}) capable of being produced by a particular cell. This is because the maximum V_{oc} value which can theoretically be obtained from the cell corresponds to the difference between the redox potential of the electrolyte couple and the Fermi level of the nanocrystalline film.

1.4 Dyes

1.4.1 Dye requirements

The key features a dye must possess to be an efficient sensitiser include:

1. The presence of an anchor group which firmly attaches it to the semiconductor substrate to prevent leaching and enable it to attain an injection efficiency of 100 %.
2. An excited state redox potential which must be more negative than that of the conduction band of TiO_2 in order to inject electrons quantitatively.
3. A ground state which should be at a sufficiently positive potential to be regenerated rapidly *via* electron donation from the electrolyte.
4. A molar extinction coefficient, (ε) which should be high over the whole absorption spectrum.
5. An excited state lifetime which is long in comparison with the rate of injection.
6. Solubility in an organic solvent to facilitate adsorption onto TiO_2.

Meeting each individual requirement is essential to the overall function and performance efficiency of the cell and many of the requirements are mutually dependant, thus making each individual parameter difficult to change without affecting another. Much research into dye chemistry is devoted to the synthesis and identification of dyes which meet and maximise the potential of each of these individual requirements, a process known as "dye tuning".[9]

1.4.2 Matching the solar emission spectrum

One requirement stated in section 1.4.1 is that ε should be high over the whole absorption spectrum as this ensures that the dye absorbs over as much of the solar emission spectrum as is possible. The solar emission spectrum has its maximum at 500 nm but extends into both the IR and UV regions of the electromagnetic spectrum. Fig. 1.3[9] shows a standard intensity spectrum for solar radiation on the earth's surface at sea level. A large proportion of UV and IR radiation is removed after absorption of the

energy in this region by O_3, H_2O and CO_2, however almost all of the visible region radiation is incident on the Earth's surface. It is desirable to harvest all wavelengths of 900 nm or shorter. This limit is imposed after thermodynamic calculations which show that the conversion efficiency of any single junction photovoltaic solar converter peaks at 33 % at the threshold energy of 1.4 eV.[10] For the purpose of dye tuning it is imperative that the LUMO and HOMO of a dye are maintained at levels where photoinduced electron injection into the TiO_2 and regeneration of the ground state of the dye by the electrolyte still proceed efficiently. Manipulation of both the HOMO[11, 12] and the LUMO[4] have led to changes in the absorption wavelength in solar cell sensitisers. Keeping the wavelength as long as possible is desirable in order to make maximum use of the solar emission spectrum, however difficulty in synthesising dyes which meet all of the requirements of the cell mean that the majority of dyes currently in use absorb at short wavelengths.

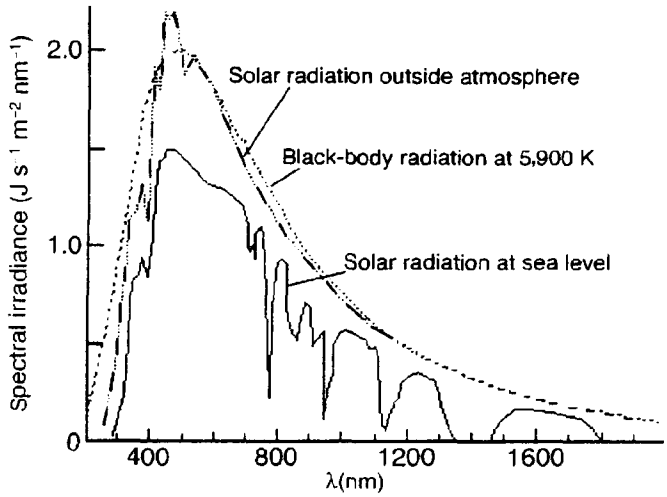

Fig. 1.3 Solar emission spectrum

1.4.3 Commonly used dyes

1.4.3.1 Ru(polypyridyl) dyes

$[Ru(bpy)_3]^{2+}$ and analogous complexes were used extensively in the 1980's as redox sensitisers (reference [5] and references therein). Complexes of $[Ru(bpy)_2(X)_2]$, where X

= halide, CN, SCN, were not initially used since it was originally thought that their excited states are too short lived to allow for electron injection. However, the short timescale required for electron injection to occur means that injection efficiencies from this type of complex are sufficient for the forward reaction to proceed. Complexes like these are desirable since they have a large degree of chemical stability, transfer interfacial charge efficiently and have a large visible light harvesting capacity which is superior to that of the $[Ru(bpy)_3]^{2+}$ complexes originally studied.[6]

In terms of conversion yield and long term stability, the best photovoltaic performance has been achieved by $[Ru\{4,4'\text{-}(CO_2H)_2\text{-}bpy\}_2(NCS)_2]$, known as N719 (fig. 1.4). N719 is almost universally used when comparing cell parameters and dye performances in the liquid-electrolyte DSSC and the neutral dye has λ_{max} at 380 nm and 518 nm, both of which have ε of *ca.* 13,000 M^{-1} cm^{-1}. It has been stated that the dye sustains 10^8 redox cycles without a noticeable loss of performance, corresponding to 20 years of continuous use[13] and this stability was attributed to the fact that the dye deactivates its excited state *via* rapid electron injection to the semiconductor.

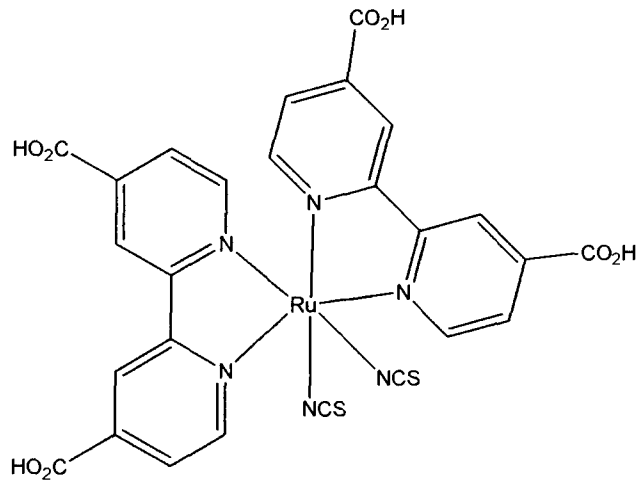

Fig. 1.4 $[Ru\{4,4'\text{-}(CO_2H)_2\text{-}bpy\}_2(NCS)_2]$, known as N719

There is no doubting the appeal of N719 as a solar cell sensitiser with efficiencies of up to 12 % and its use in DSSC, which was published first in 1993,[6] was unrivalled in its performance until a publication on the Ru, "black dye" in 1997.[14, 15] This "black dye", (fig. 1.5) $[NHEt_3][RuL(NCS)_3]$ where L = {4,4',4''-$(CO_2H)_3$-2,2':6',2''-terpyridine} exhibits efficient panchromatic sensitisation of nanocrystalline titania solar cells over the entire visible wavelength up to 920 nm. The "black dye" has subsequently been studied further by varying the degree of protonation and the counterion used.[15] A comparative study of the spectral response of N719 and the "black dye" shows that both chromophores exhibit very high Incident Photon to Current Efficiency, (IPCE) values in the visible range, however the "black dye" absorbs *ca.* 100 nm further into the IR than N719, with its photocurrent onset near to 920 nm (i.e. near the optimal threshold for single junction converters).

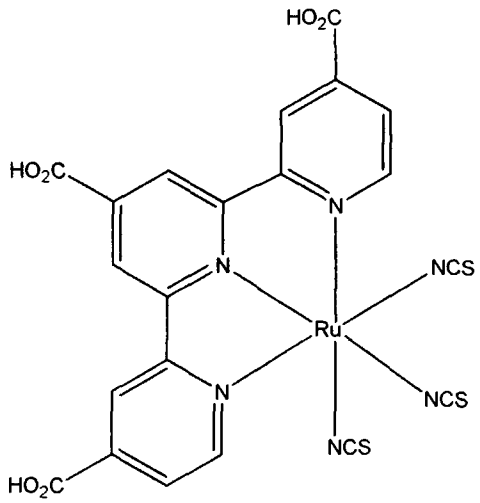

Fig. 1.5 The "black dye" [Ru{4,4',4''-$(CO_2H)_3$-2,2':6',2''-terpyridine}$(NCS)_3$]

A current goal within the field of DSSC is to obtain a cell with an overall efficiency of *ca.* 15 % using Ru sensitisers and in this respect, complexes of quaterpyridyl derivatives may show promise.[16] A near vertical rise of photocurrent near the 920 nm absorbance threshold would increase I_{sc} from 20.5 mA cm^{-2} to 28 mA cm^{-2}, thus resulting in the desired efficiency of 15 %.

1.4.3.2 Organic dyes

Organic dyes such as porphyrins, phthalocyanines,[17] coumarins and polyenes have been reported as solar cell sensitisers,[7, 10, 18] with a coumarin dye having recently been reported with an efficiency of 7.7 %.[19] Porphyrins are attractive as light harvesters given their involvement in photosynthesis and their relative ease of synthesis. Various porphyrins have been tested for a DSSC, the most common being the free base and Zn derivatives of mesobenzoic acid substituted TCPP (tetrakis(4-carboxyphenyl)porphyrin.[20] Electron injection and charge recombination studies of TCPP and Zn TCPP on TiO_2 have been studied by Durrant *et al.* which showed that TCPP, ZnTCPP and N719 have almost indistinguishable kinetic parameters for injection and recombination.[21] In general therefore, it is thought that lower efficiencies of porphyrins (an order of magnitude less than N719) in DSSC are due to the increased probability of exciton annihilation since the inherent tendency of porphyrins to aggregate is large; therefore at a high degree of coverage, rapid migration of the excited state between neighbouring dyes via dipole/dipole interactions occurs.[20] There are also a number of difficulties associated with phthalocyanines including their tendency to aggregate.

1.4.3.3 Other transition metal (TM) dyes

TM complexes have been said to be better suited to DSSC than purely organic dyes since they have a metal centred charge transfer (MLCT) transition which results in a stable system able to undergo many sensitisation cycles without degradation.[13] Other metal centres outside of Ru have been looked at in the context of solar cells and Fe,[22-24] Os[25] and Re[26, 27] have been studied, though none give as consistently efficient performances as Ru complexes. Argazzi *et al.*, have also reported the use of homo/heterometallic bi and polynuclear dyes.[28-30]

1.5 Studies on complexes of Pt(II)

1.5.1 Luminescent properties of complexes of Pt(II)

In the late 1980's the first reports of photoemission in fluid solution of Pt(II) four coordinate complexes were published. Prior to this, luminescence from square planar complexes was uncommon and restricted mainly to frozen glasses.[31, 32] The original studies showed binuclear systems like $[Pt_2(\mu\text{-}P_2O_5H_2)_4]^{4-}$ to be luminescent in fluid solution. It was known that for mononuclear complexes of square planar geometry the absence of luminescence in fluid solution arises because of efficient radiationless decay *via* collisions with solvent molecules in the open coordination sites of the square plane. The few mononuclear Pt(II) complexes which did emit in solution were assigned as π-π^* or intraligand transitions. Only one complex $Pt(thpy)_2$ (where thpy = 2,2'-thiophenylatopyridine), shown by Zelewsky and Balzani showed metal orbital involvement in the excited state.[33]

In the last decade studies on [Pt(II)(diimine)(dithiolate)] molecules (fig. 1.6) by Eisenberg *et al.* showed that these molecules exhibit luminescence in fluid solution at ambient temperatures and emission in rigid media with a moderately intense solvatochromic transition.[4, 34, 35] The initial investigations involved ligands such as bpy and *o*-phenanthroline as the diimine moiety and maleonitriledithiolate (mnt) or ethyl-2-cyano-3,3'-dithiolatoacrylate (ecda) as the dithiolate. The charge transfer in these [Pt(II)(diimine)(dithiolate)] molecules has been defined as MMLL'CT (Mixed Metal-Ligand to Ligand Charge Transfer). This is based on spectroscopic changes as a result of ligand modification and semi-empirical molecular orbital calculations on model systems. This means that the HOMO is a mixture of both metal and dithiolate character while the LUMO resides solely on the diimine. The emission spectroscopy of such compounds showed them to have multiple emitting states at low temperature and the excited state emission was assigned as $^3(Pt(d)/S(p)_{dithiolate}\text{-}\pi^*_{diimine})$.

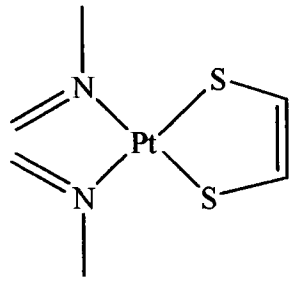

Fig. 1.6 General formula for a [Pt(II)(diimine)(dithiolate)] species. The diimine acts as a neutral donor and the dithiolate is a dianionic species giving an overall neutral product.

1.5.2 Use of Pt(II) dyes in solar cells

In order to understand how complexes of Pt(II) can be used as chromophores for energy conversion systems the electrochemistry, emission and excited state lifetimes of a series of compounds has been performed. Tuning of [Pt(II)(diimine)(dithiolate)] compounds by manipulation of both the HOMO and the LUMO has been shown by Eisenberg *et al.*[35] and Arakawa *et al.*[11, 12] Eisenberg *et al.* had previously studied the properties of [Pt(II)(diimine)(dithiolate)] systems and discussed them with reference to their use in molecular photochemical devices.[35] However, before the work presented in this thesis there were only two reports of Pt(II) complexes used in DSSC, both by Arakawa *et al.* [11, 12]

1.6 Anchor groups

As previously mentioned in section 1.4.1, in order to attach itself to the TiO_2 surface, a dye is required to contain a linker moiety.[36, 37] In recent years, this has usually been {4,4′$(CO_2H)_2$-bpy}, however this has not always been the case. In early experiments, dye molecules were adsorbed on the semiconductor films by physisorption. This was done by dipping the films which were cast on a substrate like a conductive glass slide, in a solution of the dye then drying them in air. As it became evident that it was important to develop better methods to control binding, dyes containing anchor groups which bound covalently to the semiconductor surface were synthesised. The inclusion of anchor groups led to some very positive results including substantially improved

sensitised films with higher surface coverage and more stable dyes which showed minimal desorption and a more even distribution in monolayers. The covalent interaction increased the strength of electronic coupling between the dye and the semiconductor thereby increasing the rate of electron injection.

1.6.1. Carboxylic acid substituted bpy linkers

Currently most dyes used in DSSC contain a ligand which is substituted with a carboxylic acid group which acts as an anchor ligand since these carboxylic acids form strong bonds with metal oxide nanoparticles. Other groups such as silanyl (-O-Si-), amide (-NH-(C=O)-) and phosphonato (-O-(HPO_2)-) have also been shown to form stable links with TiO_2. Several symmetric and asymmetric carboxylated bpy ligands have been prepared and examples are seen in fig. 1.7.[36, 37]

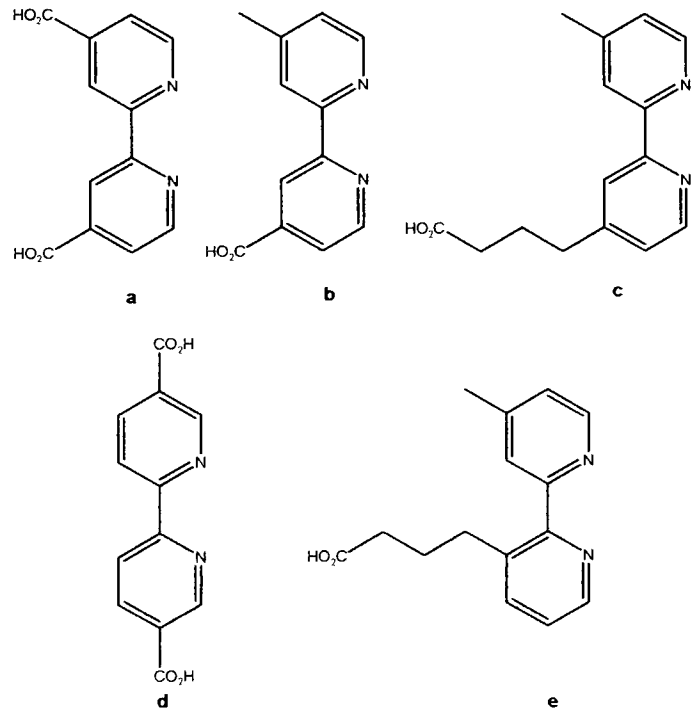

Fig. 1.7 Examples of some of the carboxylic acid substituted bpy ligands which have been studied as anchor groups to attach dyes to the surface of a metal oxide

semiconductor. **(a)** 4,4′$(CO_2H)_2$-bpy, **(b)** 4-Me,4′-(CO_2H)-bpy, **(c)** 4-Me,4′-$\{HO_2C(CH_2)_3\}$-bpy, **(d)** 5,5′-$(CO_2H)_2$-bpy, **(e)** 4-Me,3′-$\{HO_2C(CH_2)_3\}$-bpy.

1.6.1.1 Other carboxylic acid substituted linkers

Substituted bpy ligands are not the only ligands to have been tested as anchors for DSSC dyes as significant work has also been done using analogues of biquinoline[38] and terpyridine[14] (fig. 1.8).

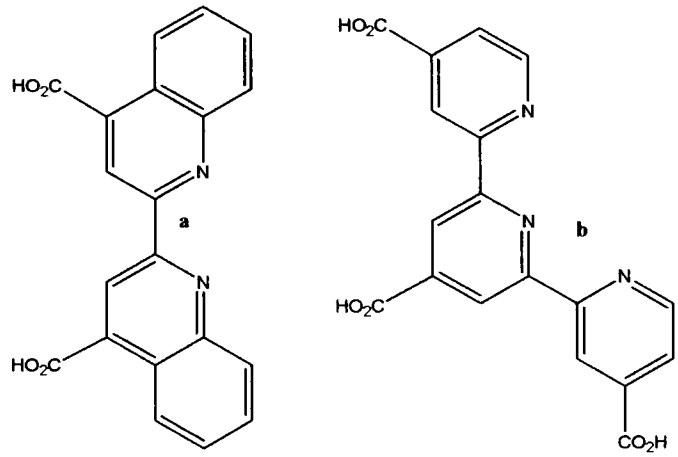

Fig. 1.8 (a) 4,4′-$(CO_2H)_2$-2,2′-biquinoline and **(b)** 4,4′,4″-$(CO_2H)_3$-2,2′:6′,2″-terpyridine

1.6.2 Binding of the carboxylic acid moiety

The CO_2H groups ensure efficient adsorption of the dye to the surface of the semiconductor, thus promoting electronic coupling between the donor levels of the excited dye (a molecular orbital which is largely composed of π^* character of the ligand) and the acceptor levels of the semiconductor (the 3d wavefunction of the conduction band of TiO_2). There are several possible modes of chelation available when a CO_2H containing ligand binds to TiO_2, including ionic bond formation, physisorption *via* H-bonding and covalent bond formation to the surface by monodentate, chelating or bridging modes of attachment. The dominant mode of binding can be analysed using IR and Raman spectroscopy with a number of key markers having been identified previously. IR and Raman alone cannot be used to tell whether one or both carboxylato

groups are bound to the surface, however a recent study using an interface sensitive molecular probe showed that 63% of surface binding was from mode B, 34% from C and D and 3% from a combination of A, E and F.[39] (fig. 1.9)

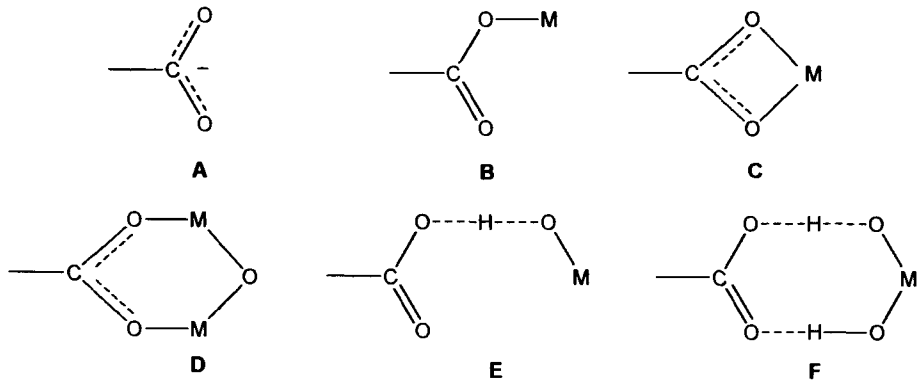

Fig. 1.9 Possible binding modes of the carboxylic acid moiety on the anchor of a solar cell dye

Bignozzi *et al.* published an interesting study on the mode of attachment of bimetallic dyes with carboxylic acid substituted linker ligands. The study aimed to determine the importance of the mode of binding of the sensitiser on the overall cell performance, since the Ru chromophore was not itself directly attached to the semiconductor substrate. The remarkably high monochromatic photocurrent efficiency obtained in these complexes raised the question as to whether or not a direct covalent linking of the chromophore involved in charge injection was necessary and it was concluded that efficient electron injection from a MLCT excited state to TiO_2 can occur in the absence of any semiconductor-to-sensitiser link.[30]

1.6.3 Recent developments to linkers

In recent years the study of linkers has progressed to look at linkers containing a bridge between the chromophore and the binding group. Carefully designed linkers can fix the distance of the dye from the semiconductor surface, tune the properties of the dye, prevent aggregation of the chromophores and prepare models for interfacial electron

transfer studies. A selection of chromophore linkers have been investigated including alkyl chains, rigid rods and tripod shaped molecules. "Designer linkers" are being developed by several groups to study ultrafast heterogeneous electron transfer to determine the distance dependence of electron transfer at the interface of semiconductors. Linkers with so-called "large footprints" can be used to prevent dye aggregation and bridges varying in structure and degree of unsaturation can tune the properties of the chromophore.[29, 37]

1.7 Measures of success

The cell performance can be measured on a macroscopic level using parameters such as the Incident Photon to Current Efficiency (IPCE), open circuit voltage (V_{oc}), short-circuit current (I_{sc}) and overall efficiency of the cell (η_{cell}).

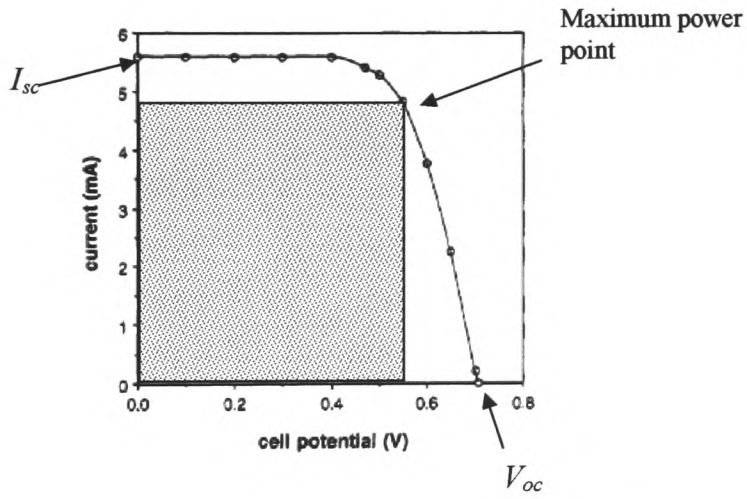

Fig. 1.10 Typical I-V curve for a DSSC showing the point of maximum power, V_{oc} and I_{sc} (from reference [40])

1.7.1 IPCE

IPCE is a parameter measuring how efficiently incident photons are converted to electrons and is measured as a function of wavelength. It is expressed as the product of

quantum yield for charge injection (Φ), the efficiency of collecting electrons in the external circuit (η) and the fraction of radiant power absorbed by the material, its Light Harvesting Efficiency (LHE). Φ and η are kinetic parameters but the LHE is a function of wavelength and depends on the active surface area of the semiconductor and on the cross section for light absorption of the molecular sensitiser. IPCE can be defined therefore by the following equation:

$$IPCE = LHE.\Phi.\eta$$

1.7.2 Open Circuit Voltage, V_{oc}

The maximum V_{oc} attainable is the difference of the Fermi level of the solid under illumination and the potential of the redox couple in the electrolyte. However it is found in practice to be kinetically limited, that is, dependant on the rate of all the electron transfer processes. One way of making V_{oc} larger has been to add Pyridine derivatives to the electrolyte. They are thought to adsorb to the TiO_2 surface and inhibit recombination of the injected electrons with triiodide and are also known to raise the energy of the semiconductor conduction band.

1.7.3 Short-circuit current, I_{sc}

The short-circuit current is the maximum photocurrent which can be obtained from the cell (fig. 1.10).

1.7.4 Fill Factor, *ff*

The maximum power produced by the cell can be recorded from a plot of current *versus* voltage (fig. 1.10). The ratio of the actual maximum power output to the maximum theoretical power output is known as the fill factor.

1.7.5 Overall cell efficiency, η_{cell}

The overall cell efficiency is the maximum power produced by the cell divided by the power of the light shining on the cell. η_{cell} for the DSSC is determined by the

photocurrent density (i_{ph}) measured at short circuit, V_{oc}, ff and the intensity of incident light (I_s) as shown in the following equation:

$$\eta_{cell} = \frac{i_{ph} V_{oc} ff}{I_s}$$

1.8 Limitations of the DSSC

The main limitations of the DSSC described in this thesis stem from its use of a liquid redox electrolyte. Replacing the volatile organic solvent normally used in DSSC is desirable in order to make more robust, long-lived systems. In addition to the problems associated with using a volatile solvent in the electrolyte, I^-/I_3^- also suffers from a mismatch between the redox level of the electrolyte (*ca.* +0.2 V vs SCE) and that of the ground state of the most efficient dyes used (*ca.* +0.85 V for N719). This implies that regeneration of the dye uses *ca.* 0.7 eV even though for reduction to occur efficiently a potential difference of only 0.3 eV would still ensure regeneration of the ground state at a fast enough rate to avoid recombination of the photoinduced electron with the oxidised form of the dye and would result in an overall gain in V_{oc}.

Advances in this area were made recently when the I^-/I_3^- redox couple was replaced by a new cobalt complex which has a more positive redox potential and this resulted in a gain of *ca.* 0.1-0.2 eV in V_{oc}.[41] In addition, this complex is less corrosive towards the silver contact fingers and sealing materials used in the DSSC. However it also has disadvantages since on using this electrolyte at high light intensities the efficiency of the cell decreased due to mass transport limitations. Further work in this area involves manipulation of this complex to increase its solubility and thereby help to overcome diffusion problems.

1.8.1 Requirements of a redox electrolyte

Just as in the case of the dye, the redox electrolyte has a number of requirements which must be met for it to function efficiently. It,

1. Must rapidly re-reduce the oxidised form of the dye to the ground state.
2. Must be a fully chemically reversible redox couple.
3. Should not significantly absorb in the same region as the dye sensitiser.
4. Should ideally be matched to the dye in order to maximise V_{oc}.

1.8.2 Using alternative electrolytes

In theory all materials which behave as p-type semiconductors, capable of accepting holes from dye cations could replace the liquid electrolyte in a DSSC. A number of studies have been undertaken which involve different electrolyte systems including solvent free ionic liquid electrolytes, e.g. 1-ethyl-3-methylimidazolium selenocyanate (EMISeCN) which has been reported to give an efficiency of 7-8.3 %.[42] Other systems such as p-type inorganic semiconductors[43] and solvent free polymer electrolytes, incorporating I^-/I_3^- [44] have yet to reach efficiencies of 5%. Hole transport materials (HTM), could also be organic molecular solids or polymers such as triarylamine derivatives e.g. Spiro-MeOTAD, [2,2',7,7'-tetrakis{(N,N)-di(p)-methoxy-phenylamine}-9,9'-spirobifluorene].[45, 46]

Intrinsically conducting polymers like polyaniline, polythiophene or polypyrrole are well known as good HTM and are commonly known as "synthetic metals" since they possess many metallic properties such as electrical, magnetic and optical properties. They can be used in the DSSC since they are wettable (i.e. can be cast from solutions thereby penetrating into the pores of the titania nanoparticles thus forming good contact with the adsorbed sensitiser). Gel electrolytes have also been studied where these electrolytes have both the cohesive properties of solids and the diffusive transport properties of liquids. Gel electrolytes are formed by incorporating a large amount of solvent containing the desired ionic salts into a polymer matrix which gives a stable gel.[47]

1.9 Bulk-Heterojunction Solar Cells

Studies into removing the liquid electrolyte have evolved simultaneously with a new generation of bulk-heterojunction solar cells which are more practical and robust than the liquid electrolyte cells; however these cells are still in their infancy and have yet to reach the same efficiencies as liquid electrolyte cells. These solar cells are based on a generic system involving two materials with complementary properties. Organic solid-state solar cells are based on a p/n junction system, containing both donor (n-type) and acceptor (p-type) molecules. A "polymer blend" solar cell is an example of a Donor-Acceptor (D-A) type solar cell where the p-type and n-type polymers used have complementary electrical and optical properties.[48] Photoinduced electron transfer between the D and A molecules results in charge generation at a junction, followed by charge separation. Poor performance of bilayer polymer devices has in the past been attributed to the limitation of exciton diffusion to the interface where charge separation occurs and also to the carrier transport to the collecting electrodes. A bulk heterojunction approach is attractive to counteract this, since in this case D and A exist as a bulk interpenetrating network. Much work on bulk-heterojunction solar cells has been done in the area of polymer fullerene blends where fullerenes and derivatised fullerenes are used as electron acceptors and polythiophene or p-phenylenevinylenes are used as donors.[49]

Bulk-heterojunction solar cells may be created either using blends of polymers or by mixing molecular substances whilst keeping a path for charge carriers.[50] In many cases conjugated polymers are used in these cells as they have a number of distinct advantages including:

1. The possibility of an all polymer device thus leading to a plastic solar cell.
2. The use of "doctor blade" or screen printing techniques for thin film application
3. Solution processing of bulk heterojunction devices is possible.

However these systems are not without limitations; most polymers used in these systems absorb at short wavelengths and therefore do not absorb in much of the visible region of the solar spectrum. In addition to this, the limited charge mobility in bulk-heterojunction cells leads to a greater amount of recombination of the excited state electron with the electron acceptor thus resulting in a poorer overall performance of these cells with respect to liquid electrolyte DSSC.

1.10 Conclusion

More study in the area of electrolytes and solid state solar cells will no doubt advance the field of photovoltaics significantly in the coming years. However, intrinsic to those studies will be matching new electrolytes and electron acceptors with dyes and electron donors which have complimentary properties. The following chapters in this thesis outline a number of systematic studies carried out on families of Pt and Ni dyes for their use in liquid electrolyte DSSC and solid state DA cells respectively. Much of the focus is on elucidating the electronic structure of these molecules which in turn affects their performances in solar cells.

1.11 References

1 M. T. Spitler, *J. Chem. Educ.*, 1983, **60**, 330.

2 M. Gratzel, *Nature*, 2001, **414**, 338.

3 K. Kalyanasundaram, J. Kiwi, and M. Graetzel, *Helv. Chim. Acta*, 1978, **61**, 2720.

4 W. Paw, S. D. Cummings, M. A. Mansour, W. B. Connick, D. K. Geiger, and R. Eisenberg, *Coord. Chem. Rev.*, 1998, **171**, 125.

5 P. Liska, N. Vlachopoulos, M. K. Nazeeruddin, P. Comte, and M. Graetzel, *J. Am. Chem. Soc.*, 1988, **110**, 3686.

6 M. K. Nazeeruddin, A. Kay, I. Rodicio, R. Humphry-Baker, E. Mueller, P. Liska, N. Vlachopoulos, and M. Graetzel, *J. Am. Chem. Soc.*, 1993, **115**, 6382.

7 M. Gratzel, *J. Photochem. Photobiol., A*, 2004, **164**, 3.

8 A. Hagfeldt and M. Graetzel, *Chem. Rev.*, 1995, **95**, 49.

9 M. K. Nazeeruddin and M. Graetzel, *Comp. Coord. Chem. II*, 2004, **9**, 719.

10 M. Gratzel, *J. Photochem. Photobiol., C*, 2003, **4**, 145.

11 A. Islam, H. Sugihara, K. Hara, L. Pratap Singh, R. Katoh, M. Yanagida, Y. Takahashi, S. Murata, and H. Arakawa, *New J. Chem.*, 2000, **24**, 343.

12 A. Islam, H. Sugihara, K. Hara, L. P. Singh, R. Katoh, M. Yanagida, Y. Takahashi, S. Murata, H. Arakawa, and G. Fujihashi, *Inorg. Chem.*, 2001, **40**, 5371.

13 H. Tributsch, *Coord. Chem. Rev.*, 2004, **248**, 1511.

14 M. K. Nazeeruddin, P. Pechy, and M. Graetzel, *Chem. Commun.*, 1997, 1705.

15 M. K. Nazeeruddin, P. Pechy, T. Renouard, S. M. Zakeeruddin, R. Humphry-Baker, P. Comte, P. Liska, L. Cevey, E. Costa, V. Shklover, L. Spiccia, G. B. Deacon, C. A. Bignozzi, and M. Graetzel, *J. Am. Chem. Soc.*, 2001, **123**, 1613.

16 T. Renouard, R. A. Fallahpour, M. K. Nazeeruddin, R. Humphry-Baker, S. I. Gorelsky, A. B. P. Lever, and M. Graetzel, *Inorg. Chem.*, 2002, **41**, 367.

[17] M. K. Nazeeruddin, R. Humphry-Baker, M. Gratzel, D. Wohrle, G. Schnurpfeil, G. Schneider, A. Hirth, and N. Trombach, *Journal of Porphyrins and Phthalocyanines*, 1999, **3**, 230.

[18] K. Hara, K. Sayama, H. Arakawa, Y. Ohga, A. Shinpo, and S. Suga, *Chem. Commun.*, 2001, 569.

[19] K. Hara, M. Kurashige, Y. Dan-oh, C. Kasada, A. Shinpo, S. Suga, K. Sayama, and H. Arakawa, *New J. Chem.*, 2003, **27**, 783.

[20] W. M. Campbell, A. K. Burrell, D. L. Officer, and K. W. Jolley, *Coord. Chem. Rev.*, 2004, **248**, 1363.

[21] Y. Tachibana, S. A. Haque, I. P. Mercer, J. R. Durrant, and D. R. Klug, *J. Phys. Chem. B*, 2000, **104**, 1198.

[22] S. Ferrere, *Chem. Mater.*, 2000, **12**, 1083.

[23] S. Ferrere, *Inorg. Chim. Acta*, 2002, **329**, 79.

[24] S. Ferrere and B. A. Gregg, *J. Am. Chem. Soc.*, 1998, **120**, 843.

[25] G. Sauve, M. E. Cass, S. J. Doig, I. Lauermann, K. Pomykal, and N. S. Lewis, *J. Phys. Chem. B*, 2000, **104**, 3488.

[26] Y. Wang, J. B. Asbury, and T. Lian, *J. Phys. Chem. A*, 2000, **104**, 4291.

[27] J. B. Asbury, E. Hao, Y. Wang, and T. Lian, *J. Phys. Chem. B*, 2000, **104**, 11957.

[28] R. Argazzi, N. Y. Murakami Iha, H. Zabri, F. Odobel, and C. A. Bignozzi, *Coord. Chem. Rev.*, 2004, **248**, 1299.

[29] C. A. Bignozzi, R. Argazzi, and C. J. Kleverlaan, *Chem. Soc. Rev.*, 2000, **29**, 87.

[30] R. Argazzi, C. A. Bignozzi, T. A. Heimer, and G. J. Meyer, *Inorg. Chem.*, 1997, **36**, 2.

[31] J. A. Zuleta, M. S. Burberry, and R. Eisenberg, *Coord. Chem. Rev.*, 1990, **97**, 47.

[32] J. A. Zuleta, J. M. Bevilacqua, and R. Eisenberg, *Coord. Chem. Rev.*, 1991, **111**, 237.

[33] D. Sandrini, M. Maestri, V. Balzani, L. Chassot, and A. Von Zelewsky, *J. Am. Chem. Soc.*, 1987, **109**, 7720.

[34] S. D. Cummings and R. Eisenberg, *J. Am. Chem. Soc.*, 1996, **118**, 1949.

[35] M. Hissler, J. E. McGarrah, W. B. Connick, D. K. Geiger, S. D. Cummings, and R. Eisenberg, *Coord. Chem. Rev.*, 2000, **208**, 115.

[36] K. Kalyanasundaram and M. Gratzel, *Coord. Chem. Rev.*, 1998, **177**, 347.

[37] E. Galoppini, *Coord. Chem. Rev.*, 2004, **248**, 1283.

[38] A. Islam, H. Sugihara, L. P. Singh, K. Hara, R. Katoh, Y. Nagawa, M. Yanagida, Y. Takahashi, S. Murata, and H. Arakawa, *Inorg. Chim. Acta*, 2001, **322**, 7.

[39] Y.-X. Weng, L. Li, Y. Liu, L. Wang, and G.-Z. Yang, *J. Phys. Chem. B*, 2003, **107**, 4356.

[40] J. Clifford, *PhD Thesis*, 2004.

[41] H. Nusbaumer, J.-E. Moser, S. M. Zakeeruddin, M. K. Nazeeruddin, and M. Graetzel, *J. Phys. Chem. B*, 2001, **105**, 10461.

[42] P. Wang, S. M. Zakeeruddin, J.-E. Moser, R. Humphry-Baker, and M. Graetzel, *J. Am. Chem. Soc.*, 2004, **126**, 7164.

[43] B. O'Regan, F. Lenzmann, R. Muis, and J. Wienke, *Chem. Mater.*, 2002, **14**, 5023.

[44] T. Stergiopoulos, I. M. Arabatzis, G. Katsaros, and P. Falaras, *Nano Lett.*, 2002, **2**, 1259.

[45] J. Kruger, R. Plass, L. Cevey, M. Piccirelli, M. Gratzel, and U. Bach, *Appl. Phys. Lett.*, 2001, **79**, 2085.

[46] U. Bach, D. Lupo, P. Comte, J. E. Moser, F. Weissortel, J. Salbeck, H. Spreitzer, and M. Gratzel, *Nature*, 1998, **395**, 583.

[47] A. F. Nogueira, C. Longo, and M. A. De Paoli, *Coord. Chem. Rev.*, 2004, **248**, 1455.

[48] S. A. Jenekhe and S. Yi, *Appl. Phys. Lett.*, 2000, **77**, 2635.

[49] J. L. Segura, N. Martin, and D. M. Guldi, *Chem. Soc. Rev.*, 2005, **34**, 31.

[50] C. Winder and N. S. Sariciftci, *J. Mater. Chem.*, 2004, **14**, 1077.

Chapter 2

Experimental Techniques

2. Introduction

Several experimental techniques were used on a regular basis in the course of the work described in this thesis. Specific details of the techniques involved and their experimental setups are described in this chapter. The figures for the apparatus used in electrochemistry and spectroelectrochemistry experiments were modified from those taken from the thesis of Dr. Lorna Jack.

2.1 Cyclic Voltammetry

Cyclic voltammetry is a technique which involves the measurement of electrode current as a function of voltage applied to the electrolysis cell. Cyclic voltammetry is usually conducted using a three electrode system in order to compensate for the iR drop across the cell. The three electrode system consists of a working electrode (where the reaction of interest takes place), a reference electrode (which provides a stable and fixed potential) and a counter electrode. The electrodes are controlled by a potentiostat which ensures current only flows between the working electrode and the counter electrode. The potential of the working electrode is held relative to the stable reference electrode.

In a cyclic voltammetry experiment the voltage applied to the working electrode is scanned linearly from an initial value E_1 to a predetermined limit E_2 (known as the switching potential), where the direction of the scan is reversed. This gives a triangular potential cycle. The current response is plotted as a function of the applied potential. A reversible reduction scan is shown in figure 2.1 and described as follows:

Initially no current flows, (a) since the applied potential is not large enough to induce electron transfer. As the potential is swept to more reducing potential values it reaches values that are capable of inducing the reduction of a species **X** at the electrode, thereby passing a current. Initially the current rises with an exponential dependence on potential, (b) however the electrolysis of the reactant depletes its concentration at the surface. Since the experiment is performed at a stationary electrode in an unstirred

solution, diffusion is the principle means of moving the reactant to the surface of the electrode. This relatively slow mode of mass transport cannot maintain a steady state concentration in the region close to the electrode. Therefore the maximum point in the current/voltage curve reflects a balance between an increasing rate constant and a decrease in surface concentration. The maximum current is known as the peak current, (c). Since the concentration gradient continues to decrease, the rate of mass transport continues to decrease causing a drop in current, (d). When the scan direction is reversed, the reduced form of **X**, i.e. $\mathbf{X}^{\cdot}$ is oxidised back to the original starting material and a current of the opposite sign is seen.

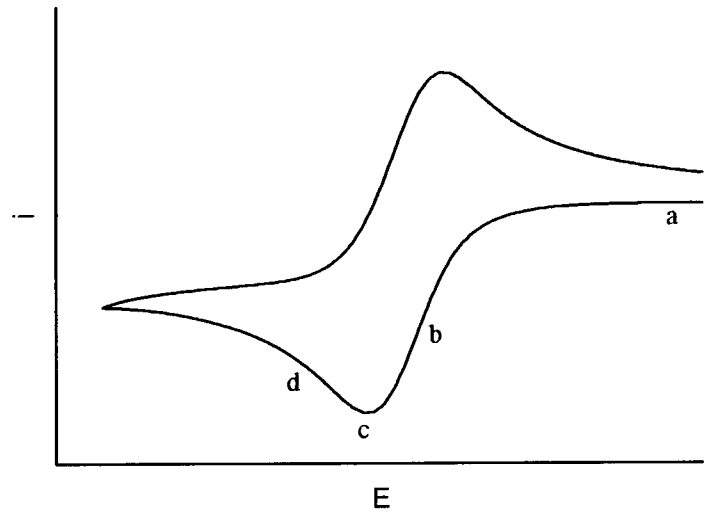

Fig. 2.1 Cyclic voltammogram showing the shape of a typical reversible reduction process

There are a number of criteria which must be met for an electrochemical process to be considered reversible. Each oxidation and reduction process reported in this thesis which is reported as reversible meets these criteria. They include:

1. The height of the forward and reverse current peaks must be the same.
2. For a one electron transfer step, peaks are separated by 59 mV (at RT) which is independent of scan rate.

3. There is no change in the potential of peak position with changes in sweep rate.
4. The peak current increases linearly as a function of (scan rate)$^{1/2}$.

If the electron transfer at the electrode is slow (electrochemically irreversible), the peak currents are separated by more than the reversible value of 59 mV. Therefore cyclic voltammetry also provides us with some information on the electron transfer kinetics of the reaction. In the event of a chemically irreversible reaction where the product of the electrode reaction undergoes a rapid chemical transformation before the potential is swept back in the reverse direction, the reverse peak will be absent in the cyclic voltammogram.[1-3]

2.1.1 Experimental Setup

The cyclic voltammetry setup used in this work involves a glass container to hold the solution under test. The Teflon cover has inlets for a number of items including the three electrodes, a nitrogen bubbler and a glass stopper. The solutions are fully degassed using nitrogen before any experiments are performed (fig. 2.2).

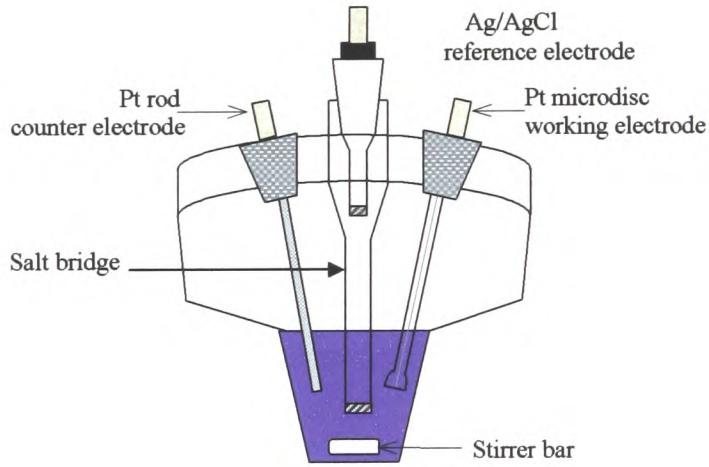

Fig. 2.2 Setup of a three electrode configuration for a standard cyclic voltammetry experiment.

Electrochemical studies were carried out using a DELL GX110 PC with General Purpose Electrochemical System (GPES), version 4.8, software connected to an autolab system containing a PGSTAT 20 potentiostat. The techniques used a three electrode configuration, with a 0.5 mm diameter Pt disc working electrode, a Pt rod counter electrode and an Ag/AgCl (saturated KCl) reference electrode against which the ferrocenium/ferrocene couple was measured to be $E_{1/2}$ = +0.55 V. A supporting electrolyte, (0.1M tetrabutylammonium tetrafluoroborate, $TBABF_4$) was used to increase the conductivity of the solutions studied and to eliminate migration as a mode of mass transport for the electroacive species. This allows us to consider only diffusion controlled processes.

For each redox process reported in this thesis, $E_{1/2}$, the half wave potential, is defined as $(E_{pa} + E_{pc})/2$ where E_{pa} is the anodic peak potential and E_{pc} is the cathodic peak potential.

2.2 Spectroelectrochemistry

Spectroelectrochemistry is the study of electrode processes by experiments that involve more than the usual electrochemical variables (i.e. current, potential and charge). It involves the use of electrochemistry combined with another analytical technique e.g. UV/Visible spectroscopy, IR spectroscopy or EPR.

2.2.1 OTTLE

One spectroelectrochemical technique frequently used in this study involved the combination of UV/Vis/NIR spectroscopy with electrochemistry. It was used to monitor how the formation of reduced or oxidised species can bring about changes in the UV/Vis absorption spectrum. This is known as Optically Transparent Thin Layer Electrode (OTTLE). Using OTTLE, electrochemically generated products can be monitored *in-situ* by UV/Vis absorption spectroscopy and information on the frontier orbitals of related molecules can be ascertained.

2.2.1.1 Experimental Setup

The setup of OTTLE is shown in fig. 2.3. A flat quartz cell of 0.5 mm thickness contains a Pt/Rh gauze working electrode. The wire connection at the top of the gauze is covered by a Teflon coat to prevent bulk electrolysis. The quartz reservoir at the top of the cell is covered by a Teflon cap which has special holes in it for fitting the Pt wire counter electrode and the reference electrode. Both the counter and reference electrodes are separated from the bulk solution by salt bridges which prevent contamination of the electroactive species during bulk electrolysis.

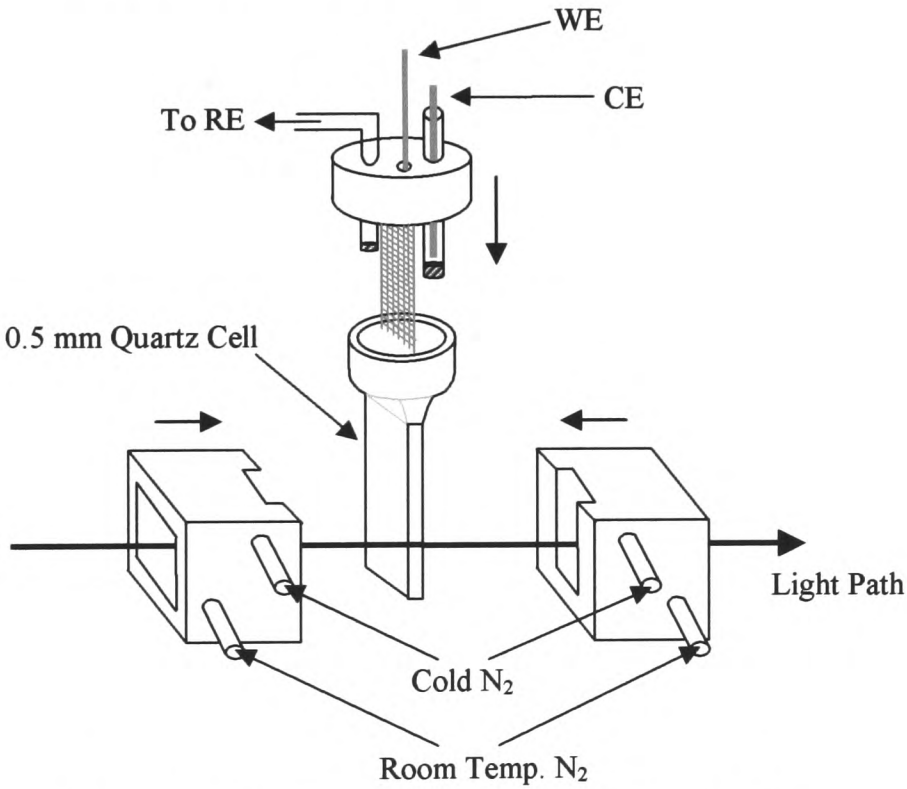

Fig. 2.3 Experimental setup for an OTTLE experiment

During the course of an OTTLE experiment, the cell is held in a Teflon block which contains a quartz window to allow transmission of radiation from the spectrometer. The temperature is controlled by a thermocouple and is reduced using a supply of nitrogen gas which has been cooled prior to use. Spectra are constantly scanned from the NIR to the UV and on application of a potential the spectrum is seen to change as the

electroactive species forms in solution. It continues to change until the redox process is complete. For a redox process to be fully chemically reversible, the scan must return back to its original position when the potential is set back to a value that should regenerate the starting species (usually 0 V).

OTTLE measurements were taken using a quartz cell of 0.5 mm thickness, a Pt/Rh gauze working electrode, an Ag/AgCl (saturated KCl) reference electrode and a Pt wire counter electrode. Spectra were recorded on a Perkin-Elmer Lambda 9 spectrophotometer, controlled by a Datalink PC, running UV/Winlab software. Measurements on all samples were carried out at 213K or 233K in DMF as specified in the text. 0.1M $TBABF_4$ was used as the supporting electrolyte in all cases.

2.2.2 *In-Situ* EPR Spectroelectrochemistry

Another spectroelectrochemical tool used in this study is *in-situ* EPR (Electron Paramagnetic Resonance, also known as Electron Spin Resonance, ESR) spectroelectrochemistry. Here an electroactive species with an odd number of electrons is generated *in-situ*. EPR spectroelectrochemistry is a very sensitive technique and can result in distinctive fingerprint-like spectra.

EPR is the electronic analogue of NMR and it is a powerful tool for studying complexes with unpaired electrons. It can be used to map the distribution of an unpaired electron in a molecule and help to elucidate to what extent electrons are delocalised over the ligands. EPR studies the interaction between the electronic magnetic moment and magnetic fields. It is based on the fact that an electron spin can adopt two orientations along the direction defined by an applied magnetic field B. The energy difference between these states $m_s = +1/2$ and $m_s = -1/2$ is given by

$$\Delta E = g\mu_B B$$

where μ_B = Bohr magneton, g = constant which is characteristic of the electron in a given environment, B = applied magnetic field. For a free electron g has the "free spin" value of g_e = 2.0023. On exposure to electromagnetic radiation of frequency ν, a resonance occurs when the magnetic field satisfies the condition

$$h\nu = g\mu_B B$$

Hyperfine structure

Magnetic nuclei (those with non-zero spin) give rise to an additional magnetic field in a complex and any free unpaired electrons respond to this. Magnetic nuclei with spin I adopt 2I + 1 orientations and give rise to hyperfine structure. In the presence of a simple nucleus of spin I the 2 I + 1 resonance conditions can be expressed as

$$h\nu = g\mu_B(B + Am_I)$$

where A is the hyperfine splitting constant. The size of A depends on the probability that the unpaired electron is found close to the magnetic nucleus responsible for the splitting. Therefore measuring A can provide a means of mapping the wavefunction of the molecular orbital occupied by the unpaired electron. The observation of hyperfine structure due to nuclei in the ligands shows that the unpaired electron is delocalised. The value of A for the interaction with either the ligand or metal nuclei can be used as a good indication of the extent to which electrons are located on the ligands.

2.2.2.1 Experimental Setup

The setup for *in-situ* EPR has a high grade quartz flat cell which contains two quartz side arms (fig. 2.4). The Pt gauze working electrode sits in the flat cell as in the OTTLE experiments and again the wire is covered in a Teflon sheet to prevent bulk electrolysis of the solution in the reservoir. A stopper at the end of the cell allows for the removal of the solution at the end of the experiment. A Pt wire counter electrode and an Ag/AgCl reference electrode complete the cell. The EPR cavity contains a specially designed

quartz holder. A special dewar containing liquid nitrogen and a heater is connected to the quartz sample holder by insulated tubing. A thermocouple inserted through the bottom of the quartz holder regulates the temperature.

All *in-situ* EPR spectra were recorded on an X-band Bruker ER200D-SCR spectrometer, connected to datalink 486DX PC running EPR Acquisition System, version 2.42 software. *In-situ* EPR experiments were electrogenerated using a BAS CV-27 Voltammograph. Variable temperature work was carried out using a Bruker ER111VT variable temperature unit.

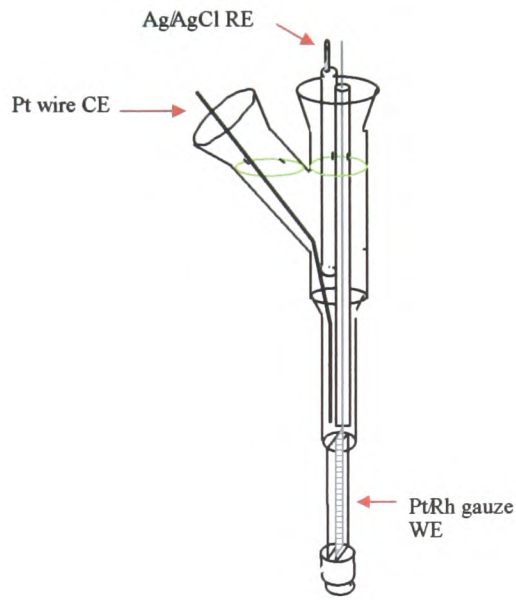

Fig. 2.4 Experimental setup of *in-situ* EPR cell

2.3 Solar Cell Assembly

All work on DSSC fabrication and testing was done in conjunction with Narukuni Hirata and Dr. John Clifford, under the supervision of Dr. James Durrant at Imperial College, London. Nanocrystalline colloidal films were prepared in a number of steps including, preparation and deposition of the colloid solution and sintering of the resultant film.

2.3.1 TiO_2 paste preparation

Preparation of the colloidal TiO_2 paste involved synthesis via a sol-gel method, previously reported by Willis *et al.*[4] A carbowax polymer was added to provide a support matrix for the film thus ensuring its homogeneity and also increasing the porosity of the film to allow for more dye adsorption.

2.3.2 Film preparation

The TiO_2 paste was deposited onto fluorine doped tin oxide (FTO) coated conducting glass slides. Prior to deposition the slide was cleaned by sonication in a beaker of Ethanol and heating to 400-500°C for 15 minutes. The slide was then placed on a flat surface with the conducting side exposed and was taped with a layer of Scotch Magic tape™ whilst keeping a separation of greater than 1 cm between the layers of tape as seen in the fig. 2.5. The tape has previously been measured as having a thickness of 4 microns. A small amount (*ca.* 0.2 ml) of TiO_2 paste was dropped at one end of the slide and was spread down the length of the slide using a glass rod in a technique known as "doctor blading". The tape was then removed and the slides were allowed to dry in air for 20 minutes before the sintering process began. The originally white paste becomes transparent on drying.

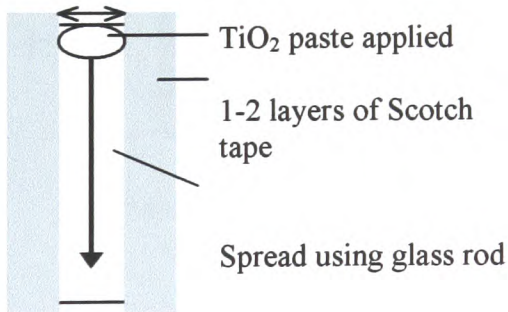

Fig. 2.5 "Doctor blading" technique for making TiO_2 on glass films

2.3.3 Film sintering

Sintering of the films generally involved heating the dry films at 450°C for *ca.* 20-30 minutes. Sintering removes any traces of organic and aqueous impurities and also the carbowax which was introduced during the paste formation. This leaves a porous structure to allow for dye adsorption. Sintering also ensures free movement of electrons within the TiO_2 matrix by creating good electrical contact throughout the film. Each TiO_2 piece measured 1 cm^2 in geometric area as this is the standard area under which all solar cell measurements are carried out. This area was created by shaving away excess TiO_2 using a scalpel.

2.3.4 Sensitisation procedure and cell assembly

A saturated solution of the dye in an organic solvent, specific to each dye used was prepared. Sensitisation of the TiO_2 coated glass slide involved dipping the slide in the saturated solution of dye overnight and leaving it in the dark (fig. 2.6). Excess dye was washed from the surface using the same organic solvent as was present in the solution of dye. At this stage the film was used for measuring transient absorption spectra before being assembled into the full cell.

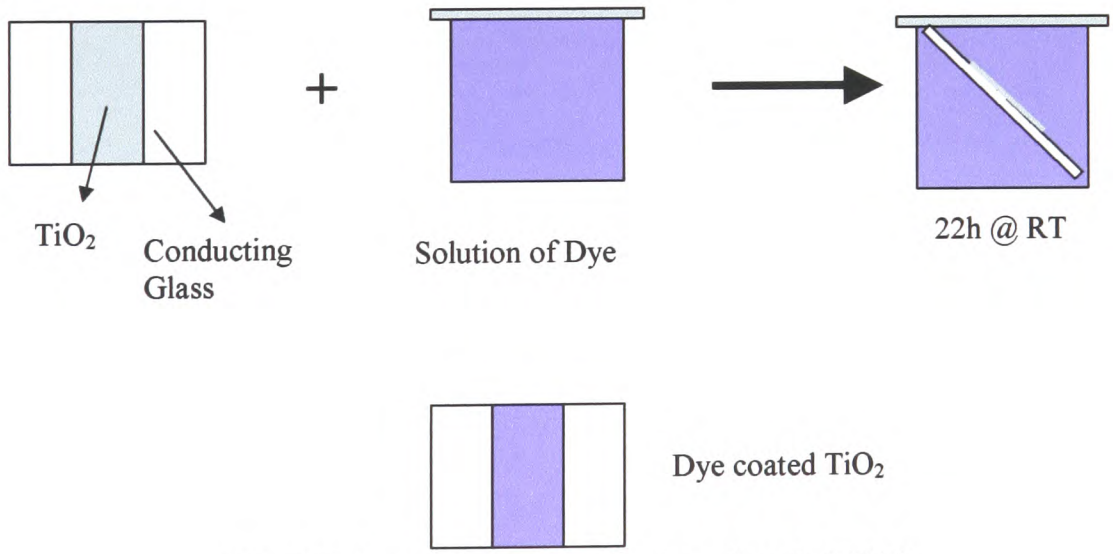

Fig. 2.6 Overnight sensitisation procedure for DSSC

Platinised counter electrodes were prepared by Narukuni Hirata of Imperial College London, using the "doctor blade" technique as a thin layer of 0.5 M hexachloroplatinic acid [H_2PtCl_4] in isopropanol was spread on a conducting glass slide. The slide was then heated to 400°C for 20 minutes and following cooling to room temperature, it was dissected into pieces of a similar size as those slides coated with TiO_2. Two small holes were drilled in the electrode slide to allow for injection of the electrolyte into the cell. The electrolyte used contained 0.1 M LiI, 0.8 M TBAI, 0.1 M I_2, 0.5 M ^{t}Bu-Pyridine in acetonitrile. The working (TiO_2 coated) and counter electrodes were assembled together using a special polymer called Surlyn (Du Pont). A strip of it was placed around the outside of the 1 cm^2 surface of the TiO_2 and the counter electrode was placed on top. The cell was sealed by placing the sandwich cell under pressure and at a temperature of 110°C for 10 seconds and the Surlyn permanently seals the two sides together as it melts. The electrolyte was injected into the cavity of the cell through one of the holes in the counter electrode as air escaped from the other and the two holes were sealed using araldite (fig 2.7).

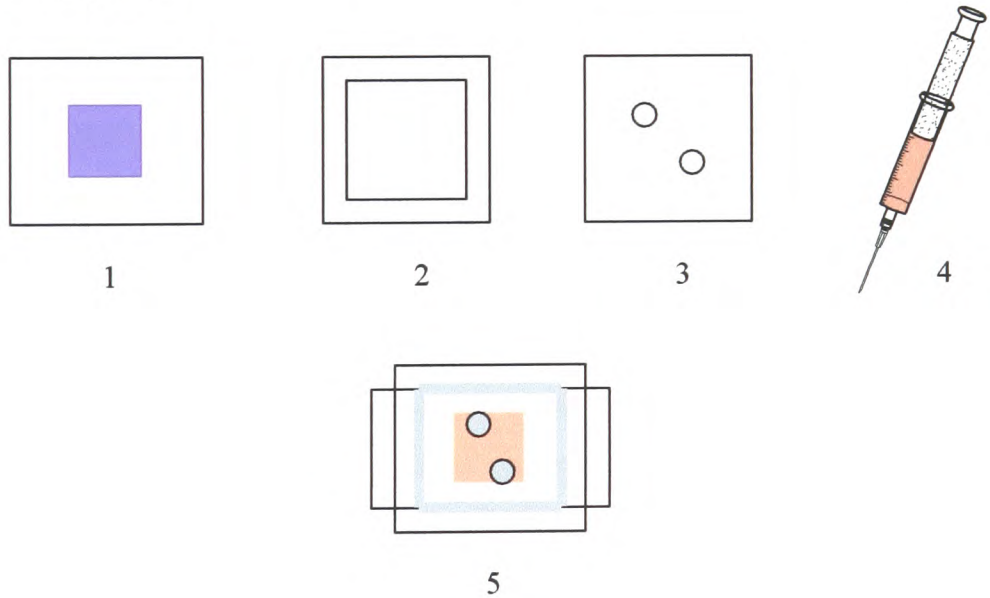

Fig. 2.7 Cell assembly procedure for DSSC. 1. 1 cm^2 of dye covered TiO_2 on conducting glass. 2. A Surlyn strip is placed on the glass slide around the perimeter of the dye coated TiO_2. 3. The platinised counter electrode containing two holes is placed

on top of these two and the outside of the cell sealed. 4. Liquid electrolyte is injected into one of the holes allowing air to escape from the other hole. 5. The cell is sealed using Araldite.

2.3.5 Transient Absorption Spectroscopy

The technique of transient absorption spectroscopy allows short lived transient species in a reaction to be observed. The apparatus uses a spectrophotometer capable of observing signature absorbance spectra and decay kinetics of transient species. The change in optical density (O.D.) of a sample is monitored after irradiation with a short intense pulse of light (known as the excitation pulse). The change in O.D. is determined by monitoring the transmission of a second less intense light beam (probe) passing through the sample. The technique gives information for a single excitation wavelength at a single probe wavelength over a broad range of timescales (micro to milliseconds) and the overall result is data on the decay of the transient species.

2.3.5.1 Experimental Setup

A PTI GL-3300 nitrogen laser was used as the excitation source. This laser produced 600 ps laser pulses at a wavelength of 337 nm with pulse energy of 1 mJ at a variable repetition rate using a frequency generator. A GL-301 PTI dye laser was used in conjunction with the nitrogen laser to provide a variable wavelength excitation source (730 – 400 nm). The dye was changed in the dye laser to vary the energy of the pulse at different wavelengths and a light guide transmitted the excitation pulse to the sample. A 150 W tungsten lamp was used as the probe light source and a probe wavelength selected using a monochromator. A second monochromator was used after the sample to reduce the intensity of emission and laser light scatter reaching the photodiode detector. The detection system comprised of a silicon photodiode and optical transient voltage amplifier coupled to an oscilloscope.

2.3.5.2 Experiment types

Transient absorption spectroscopy can be used to monitor a number of processes in the cell. These include

1. The recombination reaction
2. The regeneration and dark reactions

Using a dye sensitised TiO_2 film only, transient species such as the dye cation and the photoinduced electron were identified. This was done manually by keeping the excitation wavelength constant and changing the probe wavelength while observing changes in signal size (at a fixed time). A transient absorption maximum at *ca.* 1000 nm indicates the absorption to be dominated by the photoinjected electron in the TiO_2 and a visible absorption maximum indicates absorption dominated by the dye cation.

The kinetics of charge recombination between the photoinjected electron (injected into the TiO_2 by the dye following laser excitation) and the resultant dye cation on the surface of the film were monitored. In this case the excitation wavelength was pumped at λ_{max} for the dye (usually *ca.* 500 nm) and a probe wavelength of *ca.* 900 nm was selected. These spectra were recorded with respect to time. Half lives for the species were calculated from plots of ΔO.D. vs time. Using a complete cell setup with electrolyte included, the regeneration and dark reactions were measured by the same experimental procedure.

2.3.6 Photocurrent I/V measurement

This technique quantitatively examines the power output of solar cells under a load. This is measured by gradually increasing the applied potential and recording the current produced. The short circuit current (I_{sc}) is the maximum current produced in the cell and the open circuit voltage (V_{oc}) is the maximum voltage output.

2.3.6.1 Light sources

All of the measurements reported in this thesis were made with a Science Tech Solar simulator which used a Xenon light source and an A.M. (Air Mass) 1.5 solar filter placed in front of the cell which results in "1 Sun" illumination. Calibration of the light intensity was achieved using band-pass filters of known transmission combined with a silicon photodiode with an independently certified spectral response. The lamp intensity was adjusted to give close agreement (± 5 %) with theoretical A.M. 1.5 intensity over the spectral region of 450-700 nm.

2.3.7 IPCE measurements

Incident photon to current efficiency (IPCE) measurements were carried out using a tungsten lamp as a light source with a wavelength varied by a monochromator. The photocurrent was monitored using a potentiostat. The incident light falling on the sample was calibrated using a silicon photodiode. IPCE as a function of wavelength was calculated using the following equation.

$$IPCE\ (\lambda) = [I_1/I_2]R_2 \times 100\%$$

Where I_1 = observed photocurrent of the sample at wavelength λ, I_2 = photocurrent of calibrated photodiode at the same wavelength λ in the sample position, R_2 = efficiency of the photodiode at wavelength λ.

2.5 References

1 G. A. Mabbott, *J. Chem. Educ.*, 1983, **60**, 697.

2 A. C. Fisher, 'Electrode Dynamics', Oxford University Press, 1996.

3 D.F. Shriver and P. W. Atkins, 'Inorganic Chemistry', Oxford University Press, 1999.

4 R. L. Willis, C. Olson, B. O'Regan, T. Lutz, J. Nelson, and J. R. Durrant, *J. Phys. Chem. B*, 2002, **106**, 7605.

Chapter 3

Synthesis and Properties of [Pt{X,X′-$(CO_2R)_2$bpy}(mnt)], X,X′ = 3,3′; 4,4′; 5,5′

3. Introduction

The introduction to this thesis referred to recent work in the synthesis of transition metal dye molecules for use as solar cell sensitisers. As mentioned, Ru(polypyridyl) complexes have received much attention, due to their many desirable properties for this purpose, including a strong absorption in the visible region with a large molar extinction coefficient. Other metal centres have also been studied including complexes of Fe,[1-3] Os,[4] and Re.[5, 6] Recent preliminary studies on [Pt(II)(diimine)(dithiolate)] compounds by Eisenberg *et al.*[7-9] and Arakawa *et al.*[10, 11] have shown that these complexes possess a number of key features which make them of interest as sensitisers for DSSC. These include an absorption band in the visible region with a large molar extinction coefficient and in some cases, luminescent properties in fluid solution.

The charge transfer transition in [Pt(II)(diimine)(dithiolate)] dyes has been assigned as a "mixed metal-ligand to ligand" charge transfer (MMLL'CT) involving a HOMO which is a mixture of Pt(d) and dithiolate S(p) and a LUMO which involves a π^* bpy orbital.[7, 9] Substituents on the diimine ligand affect the photophysical and electrochemical properties of the complex by influencing the LUMO, while substituents on the dithiolate ligand affect the photophysical and electrochemical properties of the complex by influencing the HOMO. Tuning of these Pt dye compounds by manipulation of both the HOMO and the LUMO energy levels has been studied[8, 11] and this tuning is relevant to DSSC since the electrochemical and photophysical properties of the dye greatly affect the overall performance of the solar cell.

All dyes investigated for DSSC contain a functionality which anchors the dye to the TiO_2 surface. For the majority of dyes this anchor is {4,4'$(CO_2H)_2$-bpy}, where bpy is 2,2'-bipyridyl. The focus of this chapter lies on the effect of the position of the carboxylic acid functionality on the bpy on the photophysical and electrochemical properties of the dye and how this relates to its solar cell performance. Previous publications have shown that the LUMO energy of related [Pt(bpy)Cl_2] complexes can

be altered by changing the position of the carboxylic acid on the bpy ring. DFT calculations, electrochemistry, spectroelectrochemistry and EPR on a family of compounds of general formula [Pt{5,5'$(X)_2$-bpy}Cl_2] (X = H, Me, CO_2Me, CO_2Et, NH_2) have shown that the electron density at the 5,5' positions is significantly greater than at the 4,4' positions.[12] Therefore it is expected that substituents at the 5,5' position have more influence on the electronic characteristics of the bpy than substituents at the 4,4' or 3,3' positions. In a complimentary study, Arakawa *et al.* made systematic changes to a family of [Pt(II)(diimine)(dithiolate)] molecules by varying the dithiolate and thus influencing the properties of the HOMO. It was found that λ_{max} for the complexes could be tuned by 140 nm by changing the dithiolate used in the complex.[11]

Maleonitriledithiolate (mnt) was chosen in our study as the common dithiolate for several reasons. Pt(II) compounds containing mnt have been shown to be emissive in fluid solution as well as frozen glass. The oxidation potential of these complexes is much more positive than the minimum +0.2 V required for a liquid electrolyte solar cell. Finally previous [Pt(II)(diimine)(mnt)] complexes which have been studied have shown a strong absorption in the visible region.[13, 14]

Pt coordination complexes containing a 3,3'-disubstituted bpy ligand have previously been reported in other fields and [Pt{3,3'$(CO_2H)_2$-bpy}$(Cl)_2$] has been investigated as an anticancer agent.[15] However no study has been reported of a [Pt(II)(diimine)(dithiolate)] complex with a 3,3'-disubstituted bpy ligand and initial studies on solar cell dyes containing the {3,3'$(CO_2H)_2$-bpy} anchor has been limited to Ru dyes.[16] In this chapter the synthesis, characterisation and properties of a family of [Pt(II)(diimine)(dithiolate)] dyes where the variation lies in the position of the COOH group on the bpy ring are reported. The first report of a Pt dye containing the {3,3'$(CO_2H)_2$-bpy} anchor and the first crystal structure of a 3,3'-disubstituted bpy in a [Pt(bpy)(1,2-dithiolate)] complex are also reported. A comparison of the electrochemical, spectroelectrochemical and optical properties between dyes with

substituents at the 3,3′, 4,4′ and 5,5′ positions is made. Finally, the performances of the complexes in a DSSC are assessed.

3.1 Results and Discussion

3.1.1 Synthesis and structure

A numbering scheme for the ligands and complexes made in this study is given in table 3.1 and fig. 3.1. The syntheses of some of the ligands and precursor molecules (**1a**,[17] **2a**,[18] **2b**,[7] **3a**,[18] **3b**,[19] **3c**[19]) discussed in this chapter have been reported previously but adaptations were made to some literature preparations and these are detailed in the experimental section (3.3.1). The dicarboxylic acid substituted-bpy ligands were made by oxidation of 1,10-phenanthroline to give the 3,3′-dicarboxylic acid product[20] and by oxidation of the 4,4′ and 5,5′-dimethyl substituted-bpy to give the 4,4′ and 5,5′-dicarboxylic acid products respectively[18]. Reaction of {X,X′$(CO_2H)_2$-bpy} with potassium tetrachloroplatinate gave the dichloro-substituted platinum precursors [Pt{X,X′$(CO_2H)_2$-bpy}Cl_2]. Further reaction of these molecules with the disodium salt of mnt gave the desired products **1d**, **2d** and **3d** (fig. 3.1)

Compounds **1c**, **2c** and **3c** were synthesised to facilitate characterisation of the dye molecules since they are soluble in a greater number of organic solvents including acetonitrile and DMF and **1d**, **2d** and **3d** have limited solubility and only dissolve in DMSO and DMF. They were synthesised by a similar method to compounds **1d**, **2d** and **3d**. Esterification of {X,X′$(CO_2H)_2$-bpy} gave {X,X′$(CO_2Et)_2$-bpy} (**1a**,[20] **2a**[18] and **3a**[18]). The ease of synthesis of the ligands followed the order 5,5′ > 4,4′ > 3,3′ and modifications had to be made to some literature preparations as detailed in the experimental section. Refluxing these ligands with potassium tetrachloroplatinate gave the dichloro-substituted platinum precursors [Pt{X,X′$(CO_2Et)_2$-bpy}Cl_2] (**1b**, **2b** and **3b**). Further reation of these molecules with the disodium salt of mnt gave the desired products **1c**, **2c** and **3c**[19]. **3c** was the easiest to synthesise and purify due to it being more soluble than **1c** and **2c** hence recrystallisation of this complex proved reasonably facile.

In all cases the yield of the 5,5′ ligands and complexes were highest, reflecting it's lesser solubility, hence these products crashed more readily out of solution.

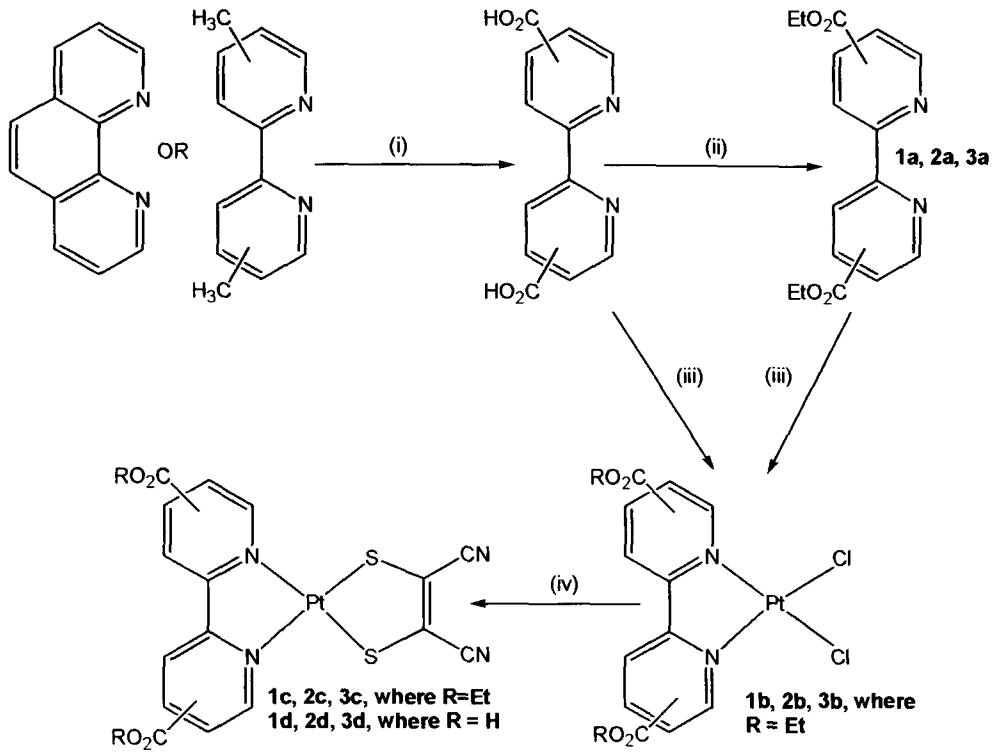

Fig 3.1 Synthesis of members of the family of [Pt{X,X'$(CO_2R)_2$-bpy}(mnt)]. (i) $KMnO_{4(aq.)}$, 120°C/HCl (ii) $EtOH/H_2SO_4$, 115°C (iii) K_2PtCl_4, 125°C (iv) Na_2(mnt), RT (140°C for **2c**).

Crystals of **1c** were grown from a hot saturated solution of the complex in acetonitrile. Only thirteen crystal structures of [Pt(bpy)(1,2-dithiolate)] systems have previously been reported.[21] Seven of the thirteen structures have a 4,4′-disubstituted bpy, one is a 5,5′-disubstituted bpy and the remaining five feature an unsubstituted bpy. Only seven structures are known of any complex where Pt is attached to a 3,3′-disubstituted bpy. There have however been no previous reports of a crystal structure with a 3,3′-disubstituted bpy in a [Pt(bpy)(dithiolate)] complex. The structure of **1c** shows bond

lengths and angles to be similar to those for [Pt(bpy)(dithiolate)] complexes previously reported (Fig. 3.2).[21] The [Pt-N(12)-N(1)-(dithiolate)] unit shows a 0.0768Å deviation from planarity. In general bpy ligands have been seen to retain a planar geometry at square planar Pt centres. Only two of the thirteen published [Pt(bpy)(1,2-dithiolate)] structures show a bpy torsion angle of greater than five degrees and the greater of these is only 12.7°, in a 4,4'-^{t}Bu$_2$ substituted bpy.[22] The other is an unsubstituted bpy ligand.[22, 23] Unsurprisingly, the steric interference between the ester substituents of **1b** causes a twist in the pyridine rings with respect to one another. This results in a significant torsion angle of 30.7 ° between the pyridine rings in the 3,3'-disubstituted bpy moiety, the largest known angle in any [Pt(bpy)(1,2-dithiolate)] complex. This is only slightly smaller than the largest reported torsion angle of 34.4°, where in a [Pt(bpy)$(Cl)_2$] complex the 3,3' positions of bpy were substituted with a crown ether.[24] The twisting of the two pyridine rings with respect to each other as seen in the crystal structure may in some part help in the explanation of the interesting electrochemistry of the complex (see fig. 3.3 (a)). The complex packs in layers with a short contact of 3.488 Å between the sulfur atom on the mnt and the carbonyl oxygen atom from the ester group on the bpy (fig. 3.3 (b)).

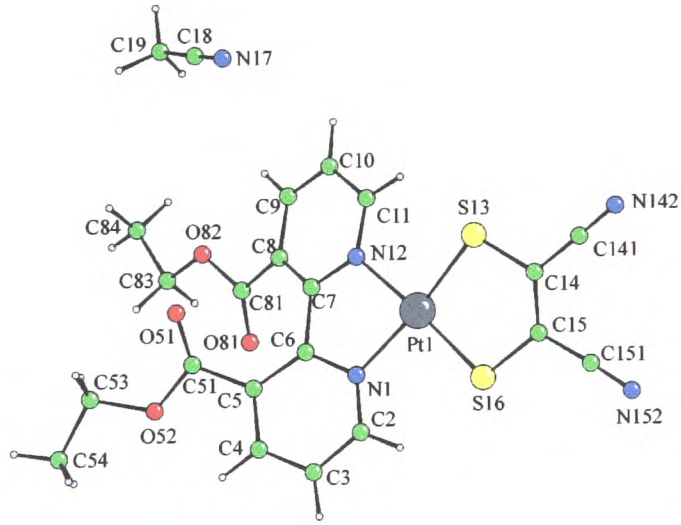

Fig. 3.2 X-Ray crystal structure of **1c**. Selected bond lengths (Å) and angles (°): Pt-S(13) 2.258(2), Pt-S(16) 2.245(3), Pt-N(1) 2.074(10), Pt-N(12) 2.058(8), N(1)-Pt-N(12) 79.4(3), N(12)-Pt-S(13) 96.2(2), S(13)-Pt-S(16) 89.54(9), S(16)-Pt-N(1) 95.3(1).

Fig. 3.3 (a) X-Ray crystal structure of **1c** with a view down the C=C bond of mnt, showing the large torsion angle induced between the pyridyl rings by the 3,3'CO_2Et substituents. Sulfur atoms are shown in yellow, platinum in pink, carbon in grey, nitrogen in pale blue, oxygen in red and hydrogen in white.

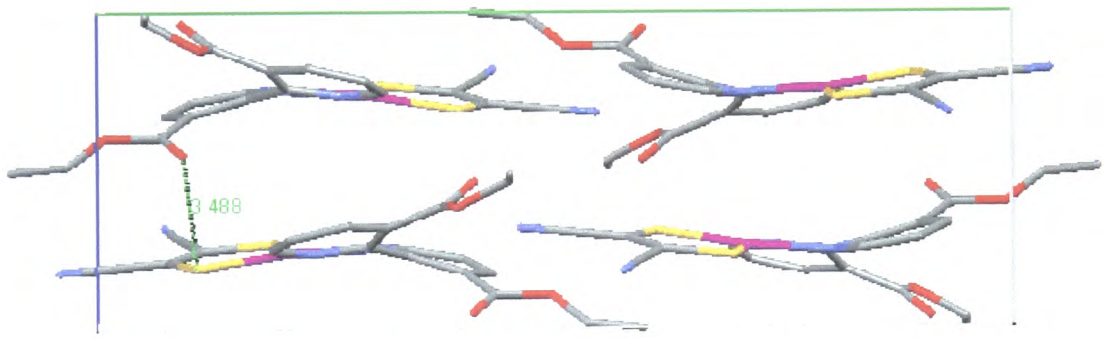

Fig. 3.3 (b) Packing diagram of **1c** with a view down the a-axis. The S-O short contact is highlighted. Hydrogen atoms and solvent molecules have been omitted for clarity.

3.1.2 Electrochemistry

The electrochemistry of the members of the [Pt{X,X'$(CO_2Et)_2$-bpy}(mnt)] family, related precursor molecules and uncoordinated ligands was studied by cyclic voltammetry of the complexes in solution of 0.1 M $TBABF_4$ in DMF at 293 K. Redox potentials for the processes are listed in table 3.1. In each figure shown in this and subsequent chapters, the cyclic voltammograms have been normalised to allow for small changes in concentration of the species involved.

No.	Compound	E_1/V	E_2/V	E_3/V	$E_1 - E_2$/V
1a	3,3'$(CO_2Et)_2$-bpy	-	-1.84[§]	-	-
1b	[Pt{3,3'$(CO_2Et)_2$-bpy}Cl_2]	-1.27	-0.61	-	0.66
1c	[Pt{3,3'$(CO_2Et)_2$-bpy}(mnt)]	-1.20	-0.59	1.35*	0.61
1d	[Pt{3,3'$(CO_2H)_2$-bpy}(mnt)]	-1.05*	-0.69*	1.27*	0.36
2a	4,4'$(CO_2Et)_2$-bpy	-	-1.53	-	-
2b	[Pt{4,4'$(CO_2Et)_2$-bpy}Cl_2]	-1.25	-0.67	-	0.58
2c	[Pt{4,4'$(CO_2Et)_2$-bpy}(mnt)]	-1.20	-0.65	1.39*	0.55
2d	[Pt{4,4'$(CO_2H)_2$-bpy}(mnt)]	-1.19[§]	-0.82*	1.27*	0.37
3a	5,5'$(CO_2Et)_2$-bpy	-1.61	-1.23	-	0.38
3b	[Pt{5,5'$(CO_2Et)_2$-bpy}Cl_2]	-1.03	-0.53	-	0.5
3c	[Pt{5,5'$(CO_2Et)_2$-bpy}(mnt)]	-0.99	-0.52	1.41*	0.47
3d	[Pt{5,5'$(CO_2H)_2$-bpy}(mnt)]	-1.16[§]	-0.69*	1.27*	0.47

Table 3.1 Redox potentials, $E_{1/2}$ of the members of the [Pt{X,X'$(CO_2Et)_2$-bpy}(mnt)] family and its related precursor molecules and ligands. *irreversible and [§]quasi reversible peak potential values, E_p.

The cyclic voltammetry of the members of the [Pt{X,X'$(CO_2Et)_2$-bpy}(mnt)] family and its related precursor molecules shows various trends which are common within each of the 3,3', 4,4' and 5,5' motifs. In each case the free ligand shows either one or two reductions within the solvent window. On binding to the Pt centre, the reduction potentials significantly shift to more positive values due to the stabilisation of the LUMO after complexation of the free ligand to the Pt metal. On substitution of the two chloride ligands with the mnt ligand, each [Pt{X,X'$(CO_2Et)_2$-bpy}(mnt)] complex (**1c**, **2c** and **3c**) shows two fully reversible reductions, the potentials of which stay almost identical to those of their respective [Pt{X,X'$(CO_2Et)_2$-bpy}Cl_2] precursors. This implies that there is a negligible effect on the LUMO of the complex after substitution of the chloride ligands for mnt and reaffirms that the LUMO may be assigned as bpy based, consistent with previous reports.[8]

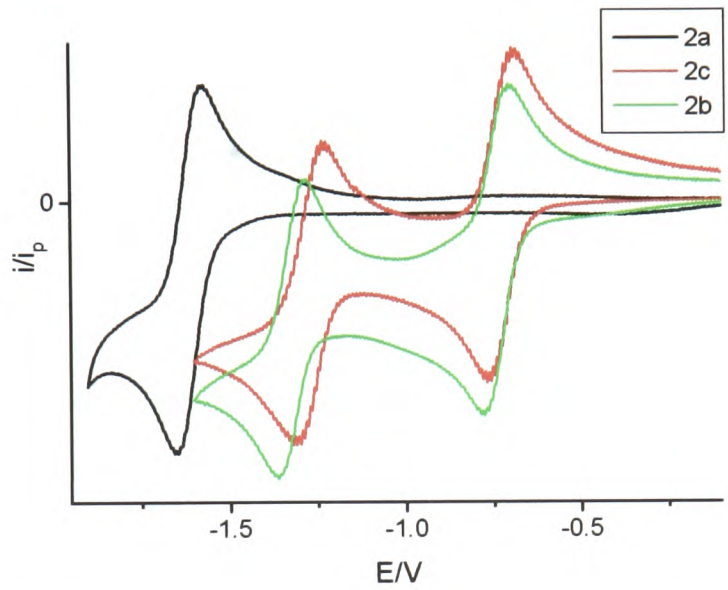

Fig. 3.4 Cyclic voltammogram showing reduction processes for **2a**, **2b** and **2c** in 0.1 M TBABF4/DMF at 293 K and scan rate 0.1 V/s.

In addition to the two reversible reductions, each of the [Pt{X,X'$(CO_2Et)_2$-bpy}(mnt)] complexes (**1c**, **2c** and **3c**) also shows one irreversible oxidation peak. The oxidation for all three ester dyes (**1c**, **2c** and **3c**) occurs at very similar potentials and is unaffected by the position of substitution on the bpy ring. Therefore this is assigned as the oxidation of the HOMO on the dithiolate moiety.[8] The dithiolate moiety is identical in all three of the complexes hence it is expected that these oxidations will occur at similar potentials.

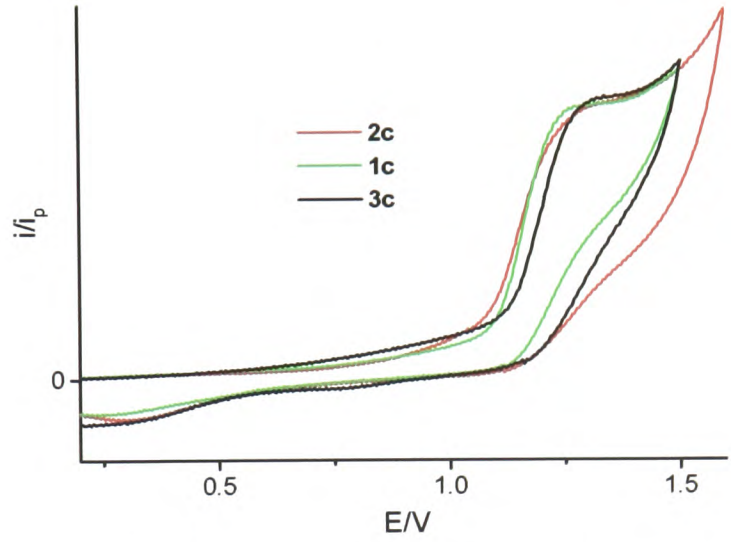

Fig. 3.5 Cyclic voltammogram of the mnt based oxidations of **1c**, **2c** and **3c** in solution of 0.1 M $TBABF_4$ in DMF at 293 K.

The reduction potentials, (E_2) of the free ligands follow the order {5,5′(CO$_2$Et)$_2$-bpy} > {4,4′(CO$_2$Et)$_2$-bpy} > {3,3′(CO$_2$Et)$_2$-bpy} consistent with previous findings, since substituents at the 5,5′ position have more influence on the electronic characteristics of the bpy than substituents at the 4,4′ or 3,3′ positions.[12, 19] The electrochemistry of [Pt{5,5′(CO$_2$Et)$_2$-bpy}(mnt)] (**3c**) has previously been studied. Both of the reductions on **3c** occur at the least negative potential of the three compounds, as expected,[19] however the first reduction potential of [Pt{3,3′(CO$_2$Et)$_2$-bpy}(mnt)] (**1c**) occurs at less negative potential than that of [Pt{4,4′(CO$_2$Et)$_2$-bpy}(mnt)] (**2c**) which is in contrast to the reduction potentials of the free ligands **1a** and **2a**. The crystal structure of [Pt{3,3′(CO$_2$Et)$_2$-bpy}(mnt)] shows a significant torsion angle (30.7°) between the two pyridine rings of the bpy moiety while [Pt(II)(bpy)(dithiolate)] complexes with substituents at the 4,4′ positions have much smaller torsion angles e.g. 0.68° for a di-Me substituted bpy,[25] and 12.69° for a di-tBu substituted bpy[22] (the biggest for any 4,4′-disubstituted bpy). The structural differences between the 3,3′ and 4,4′ disubstituted molecules must then influence their relative electrochemical responses and this results in the electrochemistry of **1c** being intermediate between that of **2c** and **3c**.

For each of the molecules studied, in all cases the second reduction occurs between 0.36 V and 0.66 V after the first reduction. This potential separation is associated with the spin pairing energy of the two added electrons in the redox active orbitals. This fact was investigated further in an EPR study of the compounds as detailed in section 3.1.5 of this chapter.

The cyclic voltammetry of the related carboxylic acid substituted family of compounds, [Pt{X,X'$(CO_2H)_2$-bpy}(mnt)] (**1d, 2d** and **3d**), in DMF show very similar oxidation and reduction potentials to those of the [Pt{X,X'$(CO_2Et)_2$-bpy}(mnt)] family (**1c, 2c** and **3c**). In addition to this, the similarity of the UV/visible spectra of **1c, 2c** and **3c** in DMF and those of **1d, 2d** and **3d** on TiO_2 enables the data for **1c, 2c** and **3c** in solution to be used as models for **1d, 2d** and **3d** on TiO_2. This can be rationalised by analysing the mode of binding which is employed by carboxylic acid anchors at the TiO_2 surface, where the major binding motif involves the acid reacting with a hydroxyl group on the TiO_2 to form a monodentate ester linkage.[26]

3.1.3 UV/visible Spectroscopy

The UV/visible spectra of compounds **1c, 2c** and **3c** in solution show an intense UV band at *ca.* 300 nm (35,000 cm^{-1}), assigned to the intra-ligand π-π^* transition of the diethylester-bpy ligand (fig. 3.6).[7] The charge transfer band of compounds **1c, 2c** and **3c** peaks at *ca.* 550 nm (*ca.* 18,000 cm^{-1}) with absorbance maxima listed in table 3.2. The charge transfer band in [Pt(II)(diimine)(dithiolate)] complexes has previously been assigned by Eisenberg and co-workers and is said to occur from a HOMO consisting of a mixture of Pt(d) and dithiolate(p) orbital character to a low energy π^* orbital LUMO located on the bpy.[7, 9]

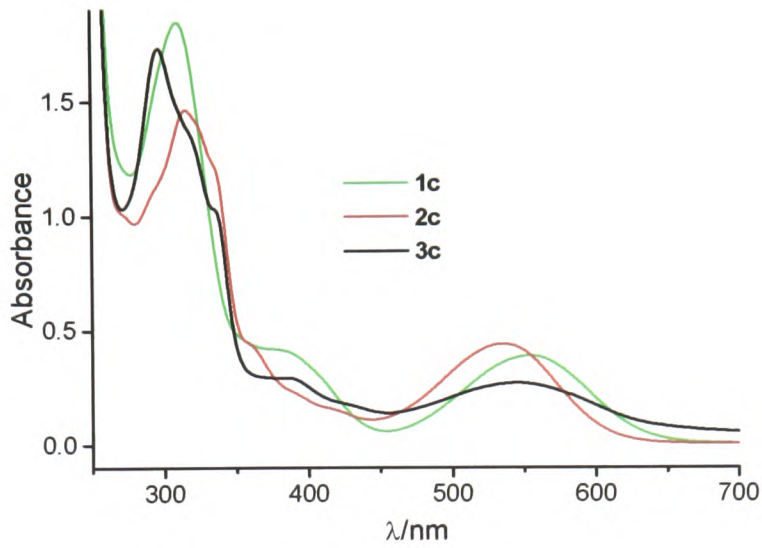

Fig. 3.6 UV/visible spectra of **1c**, **2c** and **3c** in DMF at 298K

Compound	λ_{max}/nm (υ/cm^{-1})	ε/M^{-1} cm^{-1}
1c	556 (18,000)	4204
2c	537 (18,640)	5615
3c	546 (18,330)	3054

Table 3.2 Visible absorption maxima and molar extinction coefficients for compounds **1c**, **2c** and **3c** (in solution of DMF)

3.1.4 UV/Vis/NIR Spectroelectrochemistry

UV/Vis/NIR spectroelectrochemistry was performed to electronically characterise the frontier orbitals of compounds **1c**, **2c** and **3c**. This involved electrochemical reduction of **1c**, **2c** and **3c** to $\mathbf{1c}^{1-}$, $\mathbf{2c}^{1-}$ and $\mathbf{3c}^{1-}$ and also to $\mathbf{1c}^{2-}$, $\mathbf{2c}^{2-}$ and $\mathbf{3c}^{2-}$ respectively. On comparison of each species to its related platinum dichloro precursor and uncoordinated free ligand in their related neutral, monoreduced and direduced states, attempts may be made to assign the location of the reduction electron in the monoreduced and direduced complexes. This section attempts to give a comprehensive explanation of the electronic

structure of the neutral, monoreduced and direduced members of this family and for this purpose a detailed analysis of **2a**, **2b** and **2c** is given, however this same analysis applies within **1a-1c** and **3a-3c**, as each series behaves in a similar fashion. Peaks observed and their relative ε values are shown in table 3.3. The UV/Vis/NIR spectroelectrochemistry of **1b**,[27] **3a**, **3b** and **3c** have been reported previously.[19]

Complex	**+1**, ν/cm^{-1} ($M^{-1}cm^{-1}$)	**0**, ν/cm^{-1} ($M^{-1}cm^{-1}$)	**-1**, ν/cm^{-1} ($M^{-1}cm^{-1}$)	**-2**, ν/cm^{-1} ($M^{-1}cm^{-1}$)
1a	----	37,200 (6,600)	37,200 (8,300) 25,300 (2,500)	---------
1c	31,600 (16,900) 23,000 (3,800) 18,300 (2,900)	32,000 (25,600) 25,700 (5,900) 18,300 (6,300)	30,000 (21,350) 25,300 (10,600) 22,900 (12,400) 19,400 (9,000)	33,500 (23,400) 27,400 (23,200) 23,600 (6,900) 20,600 (1,500) 19,300 (1,000)
2a	--------	33,200 (14,000) 32,000 (10,800)	33,100 (15,400) 26,700 (6,800) 25,000 (9,200) 18,000 (5,500) 16,400 (3,500) 11,150 (1,300)	----------
2b	---------	33,700 (22,350) 30,300 (9,000) 29,000 (8,800) 25,700 (2,600) 24,300 (4,400)	32,200 (19,900) 26,300 (11,800) 22,200 (4,500) 21,200 (4,300) 19,700 (4,900) 15,900 (600) 8,700 (2,600) 7,100 (6,500)	36,400 (15,800) 32,900 (19,800) 31,500 (19,600) 27,600 (20,500) 24,300 (10,300) 19,700 (3,500) 10,600 (11,600)

2c	29,800 (16,900)	34,200 (16,300)	33,100 (17,900)	33,300 (22,900)
	22,200 (5,000)	31,400 (21,000)	31,500 (18,100)	27,300 (28,600)
	18,300 (2,500)	27,500 (6,600)	29,200 (19,100)	24,200 (16,200)
		18,900 (6,300)	27,000 (15,400)	10,300 (7,400)
			21,200 (7,200)	
			19,600 (7,500)	
			18,200 (5,300)	
			15,900 (3,600)	
			8,300 (2,700)	
			7,000 (4,700)	

Table 3.3 Peaks observed in the UV/visible spectra for complexes **1a**, **1c**, **2a**, **2b** and **2c** in their monooxidised (**+1**), neutral (**0**), monoreduced (**-1**) and direduced (**-2**) states. ε ($M^{-1}cm^{-1}$) are given in brackets.

The spectrum of the neutral ligand **2a** (fig 3.7), shows one intense band at greater than 30,000 cm^{-1} which is assigned as a π-π^* intraligand bpy transition as previously reported.[8] Reduction of the neutral molecule to give $\mathbf{2a^{1-}}$ results in the formation of three new bands at *ca.* 12,000 cm^{-1}, *ca.* 18,000 cm^{-1} and *ca.* 25,000 cm^{-1}. These are assigned as intraligand transitions of the monoreduced disubstituted bpy ligand. The spectrum of bpy^{1-} has previously been studied and three sets of absorption bands that are diagnostic for the presence of co-ordinated bpy^{1-} have been assigned.[28] These are i) a nir band at *ca.* 10,000 cm^{-1}, ii) a visible band at *ca.* 20,000 cm^{-1} and iii) an intense near UV band at *ca.* 25,000 cm^{-1}. Therefore the spectrum of $\mathbf{2a^{1-}}$ is similar to that of bpy^{1-}. It is not possible to see the spectrum of the direduced species ($\mathbf{2a^{2-}}$) since the reduction potential occurs outside of the solvent window.

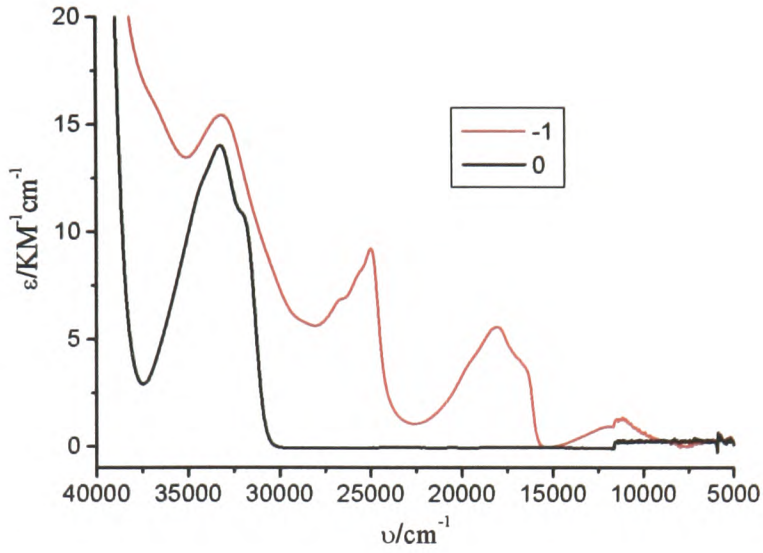

Fig. 3.7 UV/visible spectra of **2a**$^{0/1-}$ in 0.1 M solution of $TBABF_4$ in DMF at 213 K.
E_{gen} = 0.00 V(0), -1.86 V(-1)

The spectrum of the neutral dichloro complex **2b** (fig 3.8), shows a π-π^* transition at greater than 30,000 cm^{-1} as seen in the spectrum of **2a**. In addition to this, a peak at 25,000 cm^{-1} is assigned as the MLCT of the Pt-bpy transition. On reduction of this species to **2b**$^{1-}$ the peak representing the π-π^* transition of the neutral species decreases, there is a growth of a peak at *ca.* 27,000 cm^{-1} as well as a band at *ca.* 20,000 – 22,000 cm^{-1}, a band at at *ca.* 16,000 cm^{-1} and a peak in the NIR. This spectrum is similar to that of **2a**$^{1-}$ and this may therefore imply that the reduction electron in the monoreduced complex locates itself on the derivatised bpy ligand. The direduced species **2b**$^{2-}$ shows a broadening of the peak above 30,000 cm^{-1} with a shoulder at *ca.* 24,000 cm^{-1}, growth of the peak at *ca.* 28,000 cm^{-1} and an intense peak in the NIR.

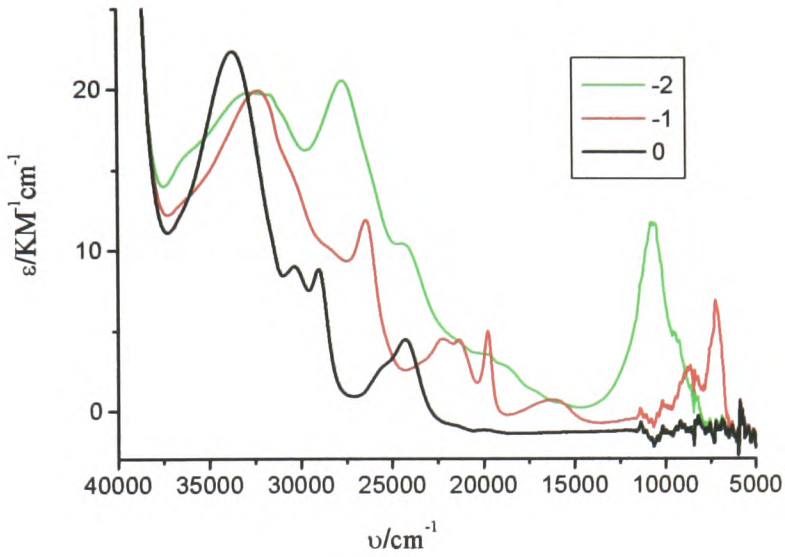

Fig. 3.8 UV/visible spectra of $\mathbf{2b}^{0/1-/2-}$ in 0.1 M solution of $TBABF_4$ in DMF at 213 K. E_{gen} = 0.00 V(0), -1.10 V(-1) and -1.81 V(-2)

The spectrum of the neutral mnt complex **2c** (fig 3.9), shows a peak at greater than 30,000 cm^{-1} assigned as the π-π^* intraligand transition of the derivatised bpy motif. The shoulder at *ca.* 30,000 – 25,000 cm^{-1} is assigned as the MLCT previously seen in **2b** however the intensity of this peak may be slightly masked by a new peak at *ca.* 20,000 cm^{-1} which is assigned as a MMLL'CT from the Pt/mnt to bpy. Reduction of this species to $\mathbf{2c}^{1-}$ results in a spectrum with a broad band at greater than 30,000 cm^{-1}, a shoulder at *ca.* 28,000 cm^{-1}, a broad band from *ca.* 17,500 – 22,000 cm^{-1}, a band at *ca.* 16,000 cm^{-1} and a peak in the NIR. This spectrum is very similar to that of $\mathbf{2b}^{1-}$, implying that in both cases the reduction electron locates itself in the same place i.e. the derivatised bpy ligand. The direduced species $\mathbf{2c}^{2-}$ shows a peak above 30,000 cm^{-1}, growth of the peak at *ca.* 27,000 cm^{-1} with a shoulder at 24,000 cm^{-1} and an intense peak in the NIR, which is again similar to that of $\mathbf{2b}^{2-}$ showing that the second reduction electron in $\mathbf{2c}^{2-}$ is located in the same place as it is in $\mathbf{2b}^{2-}$. The UV/Vis/NIR spectroelectrochemistry suggests that in each case, the reduction electron enters an orbital which is primarily located on the bpy. This is consistent with previous reports of

a bpy based LUMO and supplements the findings of the electrochemical study. Note that the band associated with the MMLL'CT no longer features in the UV/visible spectrum of $\mathbf{2c}^{2-}$ since the LUMO which is located on the bpy is now fully occupied.

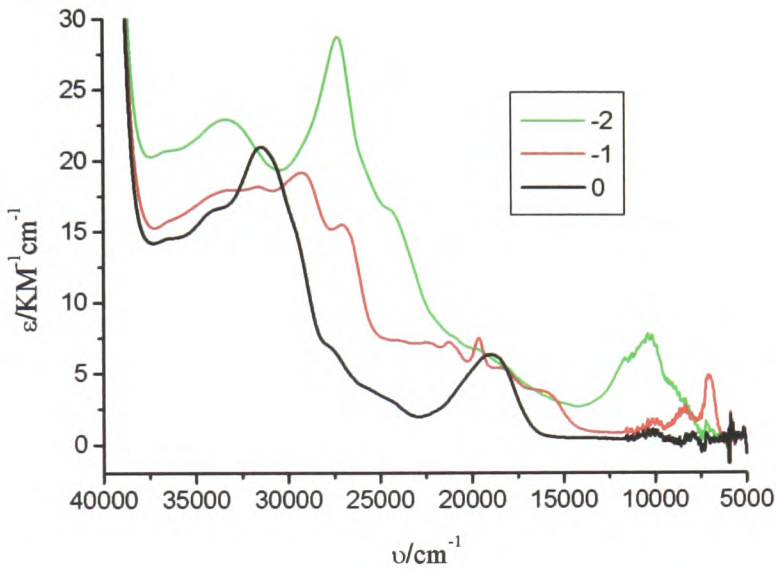

Fig. 3.9 UV/visible spectra of $\mathbf{2c}^{0/1-/2-}$ in 0.1 M $TBABF_4$/DMF at 213 K. E_{gen}= 0.00 V(0), -1.00 V(-1), -1.60 V(-2)

On oxidation of **1c**, **2c** and **3c**, each of the spectra show similar features (fig 3.10). On generation of the $\mathbf{1c}^{1+}$, $\mathbf{2c}^{1+}$ and $\mathbf{3c}^{1+}$ species, the peaks associated with the π-π^* transition of the coordinated bpy shift to lower energy. This has previously been shown in a study of $[Ru(bpy)_3]^{3+}$ and $[Ir(bpy)_3]^{3+}$ where the π-π^* transition of the coordinated bpy shifted to lower energy as the positive charge on the complex was increased.[29, 30] In the monooxidised species, the decrease in intensity of the peak at 19,000 cm^{-1}, which has already been assigned as a MMLL'CT peak from the mnt moiety, suggests that the site of oxidation on the molecule is based at least in part on the mnt motif.

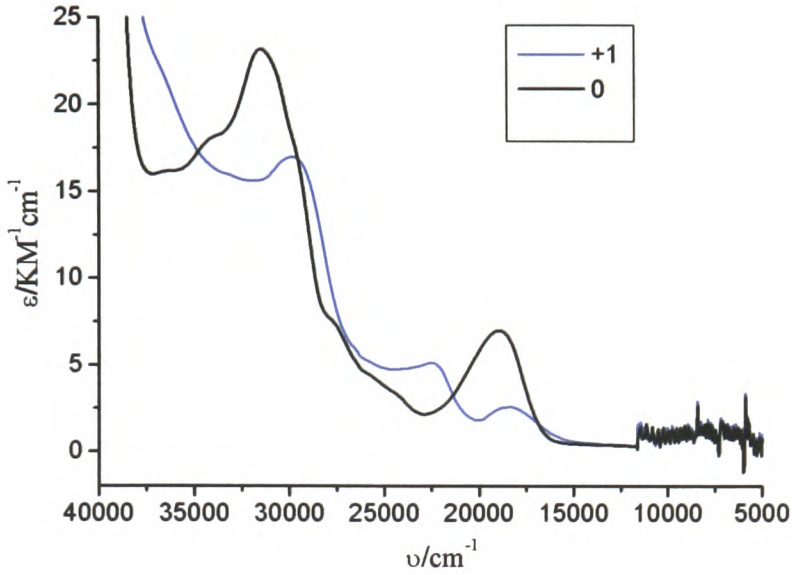

Fig. 3.10 UV/visible spectra of $\mathbf{2c^{0/1+}}$ in 0.1 M $TBABF_4$/DMF at 213 K. E_{gen}= 0.00 V(0), 1.5 V(+1)

For each ligand and complex, in every case after recording the final spectrum the potential was adjusted so that the neutral starting material was regenerated and each absorption spectrum was observed to return to exactly that of the starting species. Thus the monooxidised, monoreduced and direduced species of [Pt{X,X'$(CO_2Et)_2$-bpy}(mnt)] and its precursor molecules are all stable at 213 K.

Although UV/Vis/NIR spectroelectrochemistry can give a good indication as to the location of the redox electron in reduced species, a more comprehensive picture may be painted using *in-situ* EPR spectroelectrochemistry. Using this technique, an EPR active species is formed *in-situ* and its EPR spectrum measured. Thus the coupling of the reduction electron to EPR active nuclei within the complex may be ascertained.

3.1.5 *In-Situ* EPR Spectroelectrochemistry

In-situ EPR spectroelectrochemistry was performed on each member of the [Pt{X,X'$(CO_2Et)_2$-bpy}(mnt)] family. The location of the electron introduced *in-situ* was studied by analysing the couplings observed. The purpose of the EPR study was to compare the location of the first reduction electron in the compound to its location in the Pt-dichloro complex and the uncoordinated ligand.

Reduction of **1c** in solution of 0.1 M $TBABF_4$ in DMF at 233 K gives an EPR active solution. At a higher temperature (293 K) the superhyperfine coupling to the ligand nuclei can be resolved. The EPR coupling values of $\mathbf{1c^{1-}}$ are listed in table 3.4. Coupling is seen to the Pt centre, two ring N atoms and two ring H atoms. These are likely to be the hydrogens in the 5,5' positions as this has previously been shown to be the most electronically coupled position on this type of substituted bpy ring.[19] The *in-situ* EPR spectroelectrochemistry of the corresponding Pt-dichloro complex ($\mathbf{1b^{1-}}$) has previously been studied[27] and the resulting spectrum of $\mathbf{1b^{1-}}$ at 293 K (fig 3.12) is very similar to that of $\mathbf{1c^{1-}}$ (fig. 3.11(a)) studied in an identical manner. In both cases, on introduction of another electron to the complex and formation of $\mathbf{1b^{2-}}$ and $\mathbf{1c^{2-}}$ respectively, the signal collapses as the second electron enters the same orbital as the first and they spin pair thus the system becomes diamagnetic. The similarities between the spectra of $\mathbf{1c^{2-}}$ and $\mathbf{1b^{2-}}$ suggest that the reduction electron enters an orbital primarily located on the derivatised bpy motif analogous to the results found in the UV/Vis/NIR spectroelectrochemistry experiments.

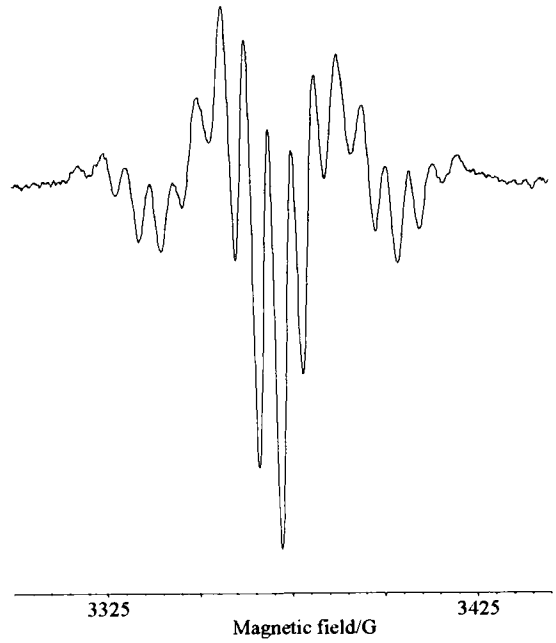

Fig. 3.11(a) 2nd derivative EPR spectrum of **1c**$^{1-}$ in 0.1 M TBABF$_4$/DMF at 293 K. E_{gen} = -2.00 V

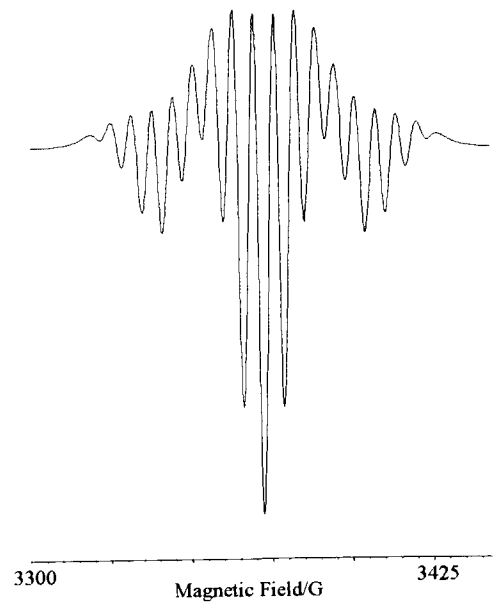

Fig. 3.11(b) 2nd derivative simulated EPR spectrum of **1c**$^{1-}$ using parameters given in table 3.4

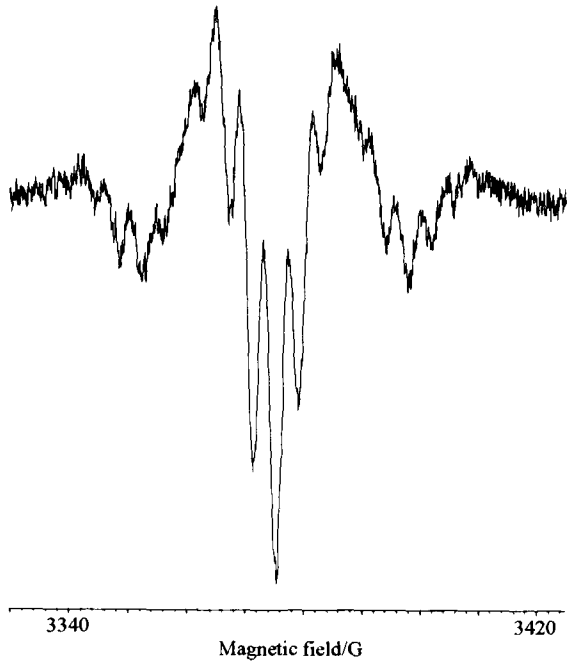

Fig. 3.12 2nd derivative EPR spectrum of $\mathbf{1b}^{1-}$ in 0.1 M $TBABF_4$/DMF at 293 K[27]

Unfortunately we were unable to resolve the spectrum of the free ligand (**1a**) and therefore further comparison between the ligand (**1a**) and the complexes (**1b** and **1c**) is not possible.

Parameter	$\mathbf{1b}^{1-}$	$\mathbf{1c}^{1-}$
a(H×2)	3.7	6.186
a(N×2)	3.7	6.186
a(Pt)	45.5	63.0
Δ	4.1	6.0
g	1.99745	2.00135

Table 3.4 EPR data for $\mathbf{1b}^{1-}$ (ref. 27) and $\mathbf{1c}^{-1}$ in 0.1 M $TBABF_4$ in DMF at 293 K. All hyperfine coupling constants given in G. Δ = linewidth

In-situ reduction of the {4,4'$(CO_2Et)_2$-bpy} ligand (**2a**) gives an EPR active solution (fig. 3.13(a)) with EPR coupling values listed in table 3.5. The reduction electron

couples strongly to the ring nitrogen and to one ring hydrogen on each pyridine ring; this is likely to be the hydrogens in the 5,5′ positions as discussed for $\mathbf{1c}^{1-}$. A significant but smaller coupling is also seen to 10 equivalent hydrogens which is assigned as the coupling to the 10 hydrogens on the ester substituents.

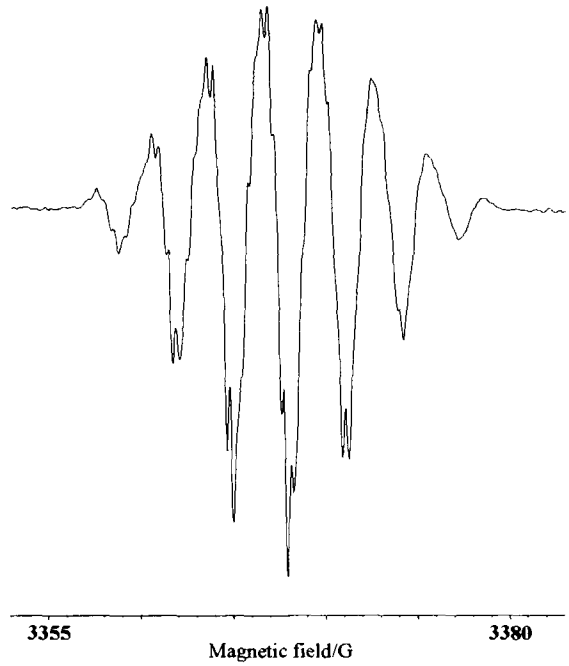

Fig. 3.13(a) 2nd derivative EPR spectrum of $\mathbf{2a}^{1-}$ in 0.1 M $TBABF_4$/DMF at 233 K. E_{gen} = -1.85 V

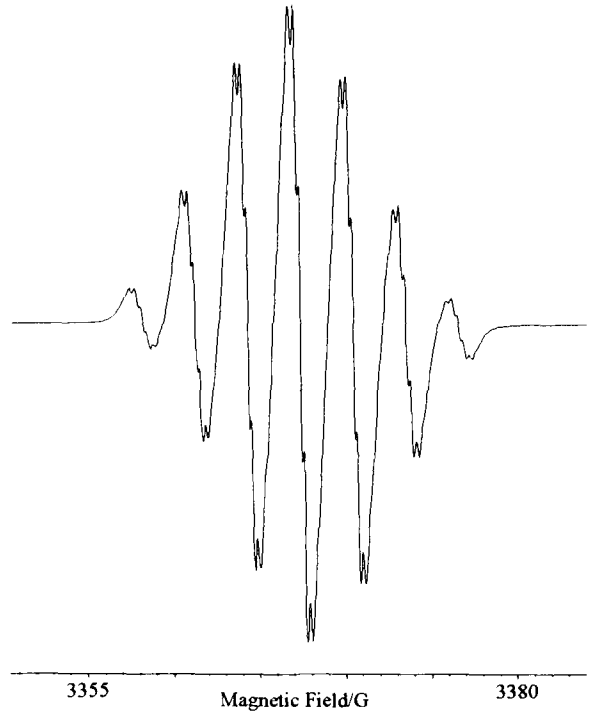

Fig. 3.13(b) 2nd derivative simulated EPR spectrum of **$2a^{1-}$** using parameters given in table 3.5

Parameter	**$2a^{-1}$**
a(H×10)	0.34
a(H×2)	3.067
a(N×2)	3.067
Δ	0.38
g	2.0044

Table 3.5 EPR coupling constants for **$2a^{1-}$** in 0.1 M $TBABF_4$/DMF at 233 K. All hyperfine coupling constants given in G. Δ = linewidth

This result is important with regards to the area of DSSC. EPR evidence of some electron density being located on the ester groups is significant since it is through these

groups that binding of the dye to the TiO_2 occurs and through which charge is subsequently transferred. The amount of electron density located on the ester groups may affect the rates of injection and recombination of the dye since strong coupling of the dye to the TiO_2 manifold is known to enhance both the forward and back reactions. No previous experimental study has shown the exact location of electron density in the linker ligands used in DSSC dyes.

The solution EPR of $\mathbf{2b^{1-}}$ at 233K in solution of 0.1 M $TBABF_4$ in DMF shows hyperfine coupling of the reduction electron to the ^{195}Pt nucleus (natural abundance of 34% I = $^1/_2$) (a(Pt) = 59.5 G, g = 1.98815). The EPR shows a broad line with two ^{195}Pt satellites and any superhyperfine coupling to the ligand for this species remains unresolved at a range of temperatures. This is analogous to the *in-situ* EPR spectroelectrochemistry results for the related complex $\mathbf{2c^{1-}}$ (a(Pt) = 56.0 G, g = 1.99397, fig 3.14). As was the case for $\mathbf{1b^{2-}}$ and $\mathbf{1c^{2-}}$, on introduction of another electron to form both $\mathbf{2b^{2-}}$ and $\mathbf{2c^{2-}}$ the signals collapse as the second electron enters the same orbital as the first and they spin pair thus forming a diamagnetic species.

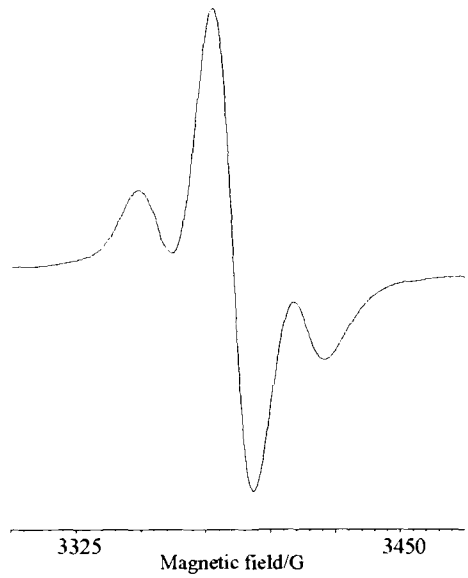

Fig. 3.14 EPR spectrum of $\mathbf{2c^{1-}}$ in solution of 0.1 M $TBABF_4$ in DMF at 293 K. E_{gen} = -1.15 V

The *in-situ* EPR of **3a**, **3b** and **3c** has been reported previously[19] and therefore will not be discussed in detail here. The *in-situ* EPR spectrum of the $\{5,5'(CO_2Et)_2\text{-bpy}\}^{1-}$ ligand ($\mathbf{3a^{1-}}$) shows coupling of the reduction electron to the two ring nitrogen atoms, the 6 equivalent ring hydrogen atoms, 6 equivalent hydrogen atoms on the Me substituent of the ester and also 4 equivalent hydrogen atoms on the CH_2 groups of the ester (table 3.6). As is the case for **2a**, the reduction electron locates itself primarily on the bpy motif with significant electron density found on the ethyl ester substituent.

Parameter	$\mathbf{3a^{-1}}$
a(H×6)	1.18
a(H×6)	0.36
a(N×2)	0.95
a(H×4)	0.135
Δ	0.27
g	2.01445

Table 3.6 EPR coupling constants for $3\mathbf{a}^{1-}$ in 0.1 M $TBABF_4$/DMF at 233 K. All hyperfine coupling constants given in G. Δ = linewidth[19]

The solution EPR of $\mathbf{3b}^{1-}$ at 273 K in solution of 0.1 M $TBABF_4$ in DMF shows hyperfine coupling of the reduction electron to the ^{195}Pt nucleus. The EPR shows a broad line with two ^{195}Pt satellites. Any superhyperfine coupling to the ligand nuclei for this species remains unresolved at a range of temperatures similar to the results found for $\mathbf{2b}^{1-}$. Again in this case the EPR spectrum of $\mathbf{3b}^{1-}$ is analogous to the *in-situ* EPR spectrum for the related mnt complex $\mathbf{3c}^{1-}$ and the magnitude of the coupling of the reduction electron to the Pt nucleus was similar in both species. The poor solubility of **3c** in solution meant that it was difficult to obtain a direduced species therefore no conclusions about the spin pairing nature of the complex could be drawn.

In each case of this EPR study, the results reiterate the findings of the UV/Vis/NIR spectroelectrochemical study. This suggests that on reduction of these molecules of general formula [Pt{X,X'$(CO_2Et)_2$-bpy}(mnt)] the reduction electron locates itself on the derivatised bpy motif, i.e. confirming that there is a bpy based LUMO.

3.1.6 Sensitisation of nanocrystalline TiO_2 films

Immersion of nanocrystalline TiO_2 in 1.7 mM solutions of dyes **1d** (in 1:1 MeCN/DMSO), **2d** (in DMSO) and **3d** (in DMSO) resulted in a strong colouration of the films. UV/visible absorption spectra for the resulting dye sensitised films are shown in figure 3.15, and in all cases exhibit similar 540 - 550 nm absorption maxima to those observed for the solution spectra of **1c, 2c** and **3c** (fig. 3.6).

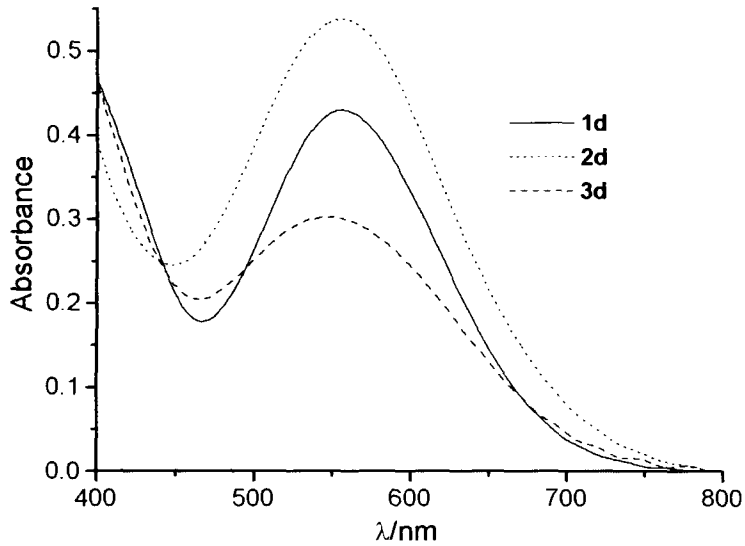

Fig. 3.15 UV/visible spectrum of nanoporous TiO_2 sensitised by dyes **1d, 2d** and **3d**

Dye loadings were determined from these film spectra assuming the molar extinction coefficients determined in solution. These are summarised in table 3.7. It is apparent that approximately monolayer dye coverage is achieved for all three dyes, with differences in film optical density primarily arising from the differences in dye molar extinction coefficient.

	Optical density on TiO_2 films [a]	**Dye coverage ratio** [b]	**Half-lives for recombination decay [s]** [c]	**I_{sc} [mA/cm^2]** [d]	**V_{oc} [mV]** [d]	**Cell efficiency [%]** [d]
1d	0.43	1.05	3.2×10^{-4}	1.94	540	0.64
2d	0.54	0.98	6.5×10^{-6}	2.49	490	0.63
3d	0.30	1.01	-	0.68	420	0.14

Table 3.7 Summary of results obtained for sensitisation of nanocrystalline TiO_2 films with **1d, 2d** and **3d**. [a] Optical densities were obtained at maximum intensity of absorption. [b] Dye coverage ratio was the ratio of dye coverage per TiO_2 (geometric) surface area. Dye coverage was estimated from UV/visible absorption spectra and the ratio was calculated using 7.73×10^{-15} cm^2 as a dye surface area. [c] The data were estimated from figure 3.17. The data for **3a** were less reliable because of small signals. [d] See also figure 3.18

Transient absorption data (after 1 μs) for the resulting dye sensitised films covered in organic solvent were obtained following pulsed laser excitation at 550 nm and are shown in figures 3.16 and 3.17. In all cases, a broad absorption increase was observed between 700 and 1000 nm, assigned to induced absorption of the dye cation/$TiO_2(e^-)$ states generated by electron injection from the dye excited state (fig. 3.16). For **1d**, an absorption maximum was observed at 700 nm and is assigned as dye cation absorption. In contrast for **2d** and **3d**, the transient spectrum increases steadily towards longer wavelengths, indicating that for these dyes the transient signal is dominated by TiO_2 electron absorption, with cation absorption for these dyes being relatively weak over this spectral region. The relatively low signal amplitude for dye **3d** is consistent with the low film optical density due to the low dye molar extinction coefficient.

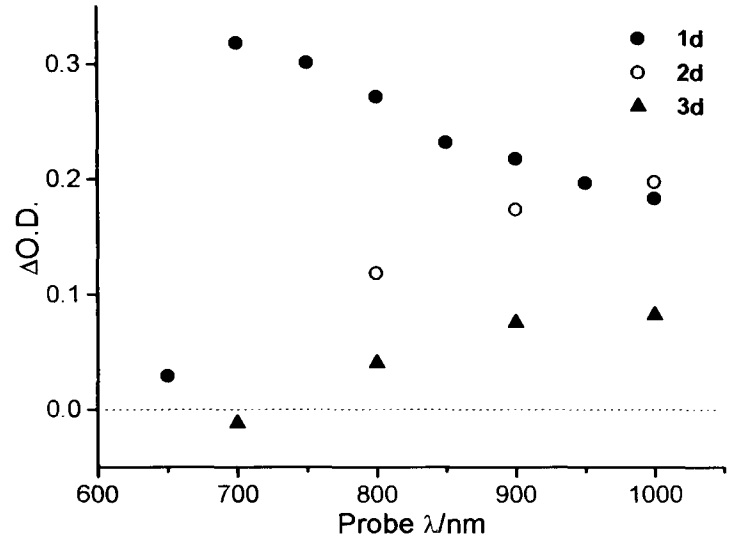

Figure 3.16. Comparison of the difference absorption spectra of **1d, 2d** and **3d** on nanocrystalline TiO_2 film. The spectra were recorded with 550 nm excitation pulse at 10^{-6} s.

Decay dynamics of the transient signal, assigned to the recombination of the TiO_2 electrons with dye cations, are shown in figure 3.17. Half lives for these decay dynamics are summarised in table 3.6. These dynamics are typical of charge recombination dynamics for such dye sensitised TiO_2 films, with dye **2d** showing faster, more dispersive recombination dynamics relative to dye **1d**.

Interfacial recombination reactions (where conduction band electrons recombine with oxidised dye molecules) are one of the primary loss mechanisms which limit device function in dye-sensitised solar cells. There are two steps involved in these reactions (a) electron transport within the TiO_2 and (b) interfacial electron transfer.[31] These control the recombination dynamics within the cell. The kinetics of electron transport within the TiO_2 is shown by stretched exponential recombination dynamics as demonstrated by **2d**. Here the kinetics are limited by electron transport within the TiO_2 which contains an inhomogeneous distribution of 'trap depths' (different energy wells into which conduction band electrons randomly walk). This leads to a broad distribution of

recombination times. Interfacial electron transfer (i.e. electron transfer from TiO_2 to the oxidised dye molecule) is shown by monoexponential recombination kinetics as shown by **1d**. Here, the electrons have sufficient time to equilibrate thermally between available 'trap sites' within the TiO_2 prior to recombination which results in a homogeneous monexponential decay.

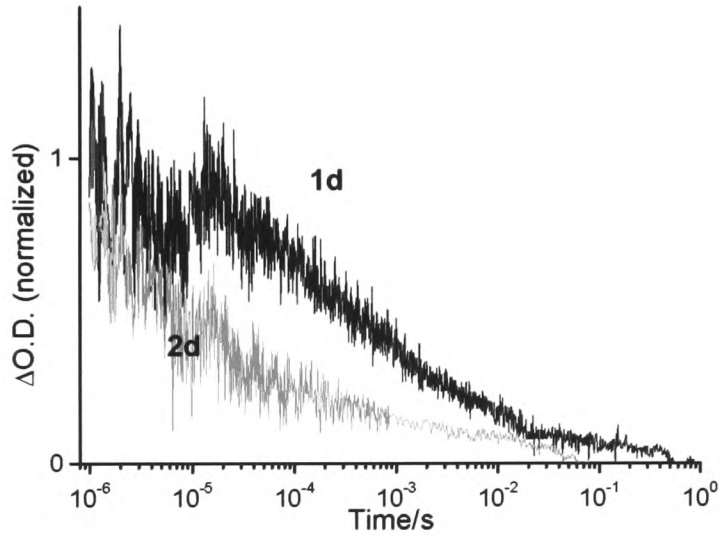

Fig. 3.17. Transient absorption data monitoring the charge recombination kinetics for 4 μm TiO_2 films sensitised with dyes **1d** (black) and **2d** (grey). Experiments employed 550 nm excitation and all data were collected at 900 nm probe wavelength. The half-life values for dyes **1d** and **2d** are 3.2×10^{-4} s and 6.5×10^{-6} s respectively. The data for **3d** were less reliable because of small signals.

Typical current/voltage (I-V) characteristics for photoelectrochemical cells sensitised with dyes **1d, 2d** and **3d** are shown in figure 3.18, with the corresponding device efficiencies given in table 3.6. It is apparent that there is a good correlation between the UV/visible absorbance data, the transient aborption data and the device I-V characteristics. **2d**, which has the highest optical density also has the highest short circuit

current (I_{sc}), whilst **1d** exhibits the slowest recombination dynamics and the highest open circuit voltage (V_{oc}).

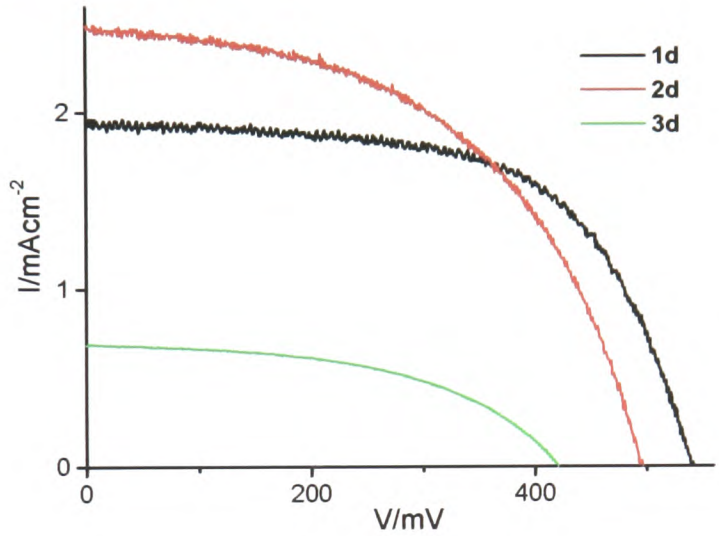

Fig. 3.18 IV characterisation for the liquid DSSC with dyes **1d, 2d** and **3d** under 1 sun illumination. The areas of all samples were 1.0 cm^2. I_{sc}, V_{oc}, *ff* (fill factor) and η_{cell}, (cell efficiency) values are shown in table 3.6.

From the data detailed above, it is apparent that **1d** exhibits the highest photovoltaic device performance of the dye series studied. This is in direct contrast with previous work done on Ru complexes where substitution at the 3,3′ positions of the bpy ring resulted in a significantly inferior dye performance with respect to the analogous 4,4′-disubstituted dye, N719. Although **1d** has the highest photovoltaic performance, its device efficiency remains relatively low compared to the more established sensitiser dye, the di-tetrabutylammonium salt of [Ru{4,4′(CO$_2$H)$_2$-bpy}$_2$(NCS)$_2$], commonly called N719. This lower device efficiency can be primarily attributed to the relatively low optical absorbance of **1d** compared to N719 (with peak molar extinction coefficients in the visible of 5615 M^{-1}cm^{-1} and 14000 M^{-1}cm^{-1} respectively). As the devices presented here employed 4 μm, non-scattering TiO_2 films, this lower optical absorbance

can be expected to have a strong effect on device performance. A significant improvement in device performance for **1d** can be expected by the use of thicker TiO_2 films with the addition of light scattering layers.

3.1.6.1 Device optimisation and comparison with Ruthenium complex (N719)

A more detailed characterisation of the photovoltaic performance and transient kinetics of devices employing **1d** was undertaken to elucidate whether differences in device performance between **1d** and N719 can be attributed to dye optical absorbance alone, or whether other parameters also limit device performance. Figure 3.19 shows current/voltage data for **1d**/TiO_2 solar cells employing both the standard electrolyte **A** (containing the additive t-butyl pyridine, t-BP), as employed in figure 3.17, and an alternative electrolyte **B** in which the t-BP was omitted from the electrolyte. Control data employing the N719 dye are also shown for comparison, with the dye loading of **N719** being selected to give the same peak optical density as that of **1d** (OD = 0.5 at 535 nm).

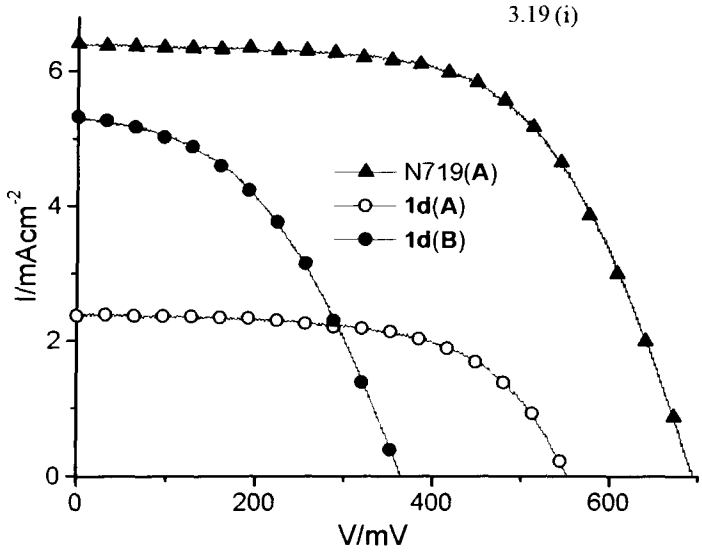

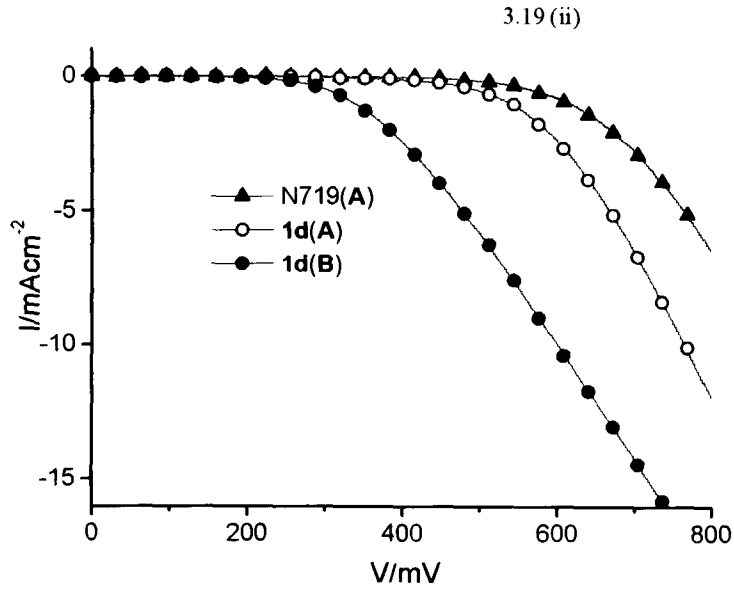

Fig. 3.19. Comparison in terms of cell performance between the cell using electrolyte **A** (containing t-BP) and electrolyte **B** (without t-BP). Graph 3.19 (i) represents the I-V curve of all three cells under 1 sun illumination. The cell performance, I_{sc}, V_{oc}, *ff* and η_{cell} values are shown in table 3.8. Graph 3.19 (ii) shows the data collected under dark conditions.

	I_{sc} [mA/cm^2]	V_{oc} [mV]	*ff* [%]	η_{cell} [%]
1d(A)	2.37	550	61.5	0.8
1d(B)	5.33	370	43.6	0.84
N719(A)	6.41	700	60.4	2.69

Table 3.8 Summary of results obtained for comparison of cell performance between **1d(A)**, **1d(B)** and **N719(A)**

Figure 3.20 shows the corresponding transient absorption signals, with the excitation wavelength of 540 nm corresponding to that at which the optical density of the **N719** and **1d** sensitised devices are identical. Note that these transient data were collected for complete devices rather than for dye sensitised films alone as employed in figure 3.16,

with the probe wavelength of 1000 nm being selected to correspond primarily to absorption of electrons injected into the TiO_2 by the optical laser pulse.

It is apparent that for **1d** the omission of t-BP from the electrolyte results in a significantly higher current density, but at the expense of a lower cell voltage. This effect is attributed to the established influence of t-BP on the TiO_2 conduction band energetics – the absence of t-BP lowers the TiO_2 conduction band, favoring electron injection and resulting in both the larger transient signal and higher short circuit current. The absence of efficient electron injection for dye **1d** in the presence of t-BP is attributed to its lower lying LUMO relative to that of N719. Strikingly, in the absence of t-BP both the short circuit current density and transient signal amplitude obtained with **1d** are of similar magnitude to those observed for the control data for N719. These data are therefore indicative that in the absence of t-BP, the quantum efficiencies of both electron injection and dye regeneration for the **1d**/TiO_2 system are near unity.

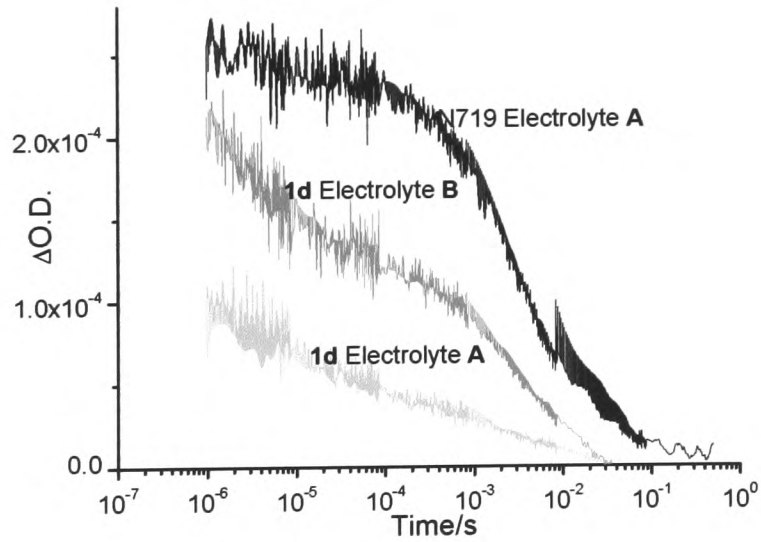

Fig. 3.20 Transient absorption data monitoring charge recombination dynamics for **1d(A)**, **1d(B)** and N719**(A)** following optical excitation at 540 nm. White light was used as a probe light and all signals were detected at 1000 nm.

The lower device voltage obtained with sensitiser **1d** relative to N719 is correlated with the higher dark current associated with this dye. This effect may be associated with the influence of the sensitiser dye on the TiO_2 conduction band energetics. Alternatively this effect may result from an acceleration of the rate constant for electron recombination with the redox electrolyte. Experiments to further address this point will be undertaken as future work.

3.2 Conclusions

This work described in this chapter contains the first detailed electrochemical and spectroelectrochemical study on a family of [Pt(II)(diimine)(dithiolate)] dyes with application in the area of solar cell dyes. It has provided us with valuable structural and electronic information for a number of important complexes. The large torsion angle of **1b** seen in the crystal structure is reflected in the electrochemistry of the complex, thus showing the influence of steric interaction between the pyridiyl rings on the reduction potential of the complexes. The OTTLE study of the final mnt dyes shows trends between the 3,3′, 4,4′ and 5,5′ which indicate that the location of the reduction electron is similar within the three motifs. The EPR study allowed us the opportunity to explore the true electronic nature of the linker groups on the bpy moiety and highlighted that there is significant electron density on the ester substituents of the 4,4′-disubstituted bpy ligand.

This is the first report of a Pt based dye sensitiser where the bpy has been substituted in the 3,3′ positions. Interestingly it shows the best performance of the three sensitisers tested. This result is significant when compared to previous work done in the field, being in sharp contrast with the only report of a Ru sensitiser with a 3,3′-disubstituted bpy which showed an inferior performance to that of its 4,4′ analogue. The work reported in this chapter demonstrates the worth of looking at other anchor ligands in the rational design of solar cell dyes and broadens the scope for further investigations into potential dyes for use in DSSC.

3.3 Experimental

3.3.1 Synthesis

1,10-phenanthroline, {4,4'$(Me)_2$-bpy} and {5,5'-$(Me)_2$-bpy}, purchased from Sigma-Aldrich and K_2PtCl_4 purchased from Johnson Matthey, were used as received. Na_2(mnt) was supplied by Mr. Donald Robertson and prepared as previously reported.[32] {3,3'$(CO_2H)_2$-bpy},[20] {4,4'$(CO_2H)_2$-bpy},[18] {5,5'$(CO_2H)_2$-bpy},[18] [Pt{4,4'$(CO_2H)_2$-bpy}Cl_2],[11] **2a**,[18] **3a**,[18] **3b**[19] and **3c**[19] were synthesised as described in the literature.

{3,3'$(CO_2H)_2$-bpy}

Yield 56.4%. Anal. Calcd for $C_{12}H_8N_2O_4$: C, 59.0; H, 3.3; N, 11.5. Found: C, 58.5; H, 3.3; N, 11.3.

{3,3'$(CO_2Et)_2$-bpy} (1a)

1a was synthesised by an analogous method to that described for the methyl ester previously reported.[20] The product did not separate out in aqueous solution but was extracted into DCM and dried with $MgSO_4$ and the solvent removed. Yield 72.9 %. Anal. Calcd for $C_{16}H_{16}N_2O_4$: C, 64.0; H, 5.4; N, 9.3. Found: C, 62.2; H, 5.3; N, 9.0.

{4,4'$(CO_2H)_2$-bpy}

Yield 36.2 %. Anal. Calcd for $C_{12}H_8N_2O_4.H_2O$: C, 55.0; H, 3.8; N, 10.7. Found: C, 54.8; H, 3.4; N, 10.8.

{4,4'$(CO_2Et)_2$-bpy} (2a)

Yield 38.6 %. Anal. Calcd for $C_{16}H_{16}N_2O_4$: C, 64.0; H, 5.4; N, 9.3. Found: C, 62.6; H, 5.0; N, 9.0.

{5,5'$(CO_2H)_2$-bpy}

Yield 63.2 %. Anal. Calcd for $C_{12}H_8N_2O_4.H_2O$: C, 55.0; H, 3.8; N, 10.7. Found: C, 54.7; H, 3.4; N, 10.6.

{5,5'$(CO_2Et)_2$-bpy} (3a)

Yield 46.6 %. Anal. Calcd for $C_{16}H_{16}N_2O_4$: C, 64.0; H, 5.4; N, 9.3. Found: C, 63.2; H, 5.3; N, 9.3.

[Pt{3,3'$(CO_2H)_2$-bpy}Cl_2]

{3,3'$(CO_2H)_2$-bpy} (0.4 g, 1.60 mmol) and K_2PtCl_4 (0.57 g, 1.36 mmol) were refluxed in 100 mL of water for 18 h. A bright yellow powder precipitated on cooling. Yield 94.8 %. Anal. Calcd for $C_{12}H_8N_2O_4PtCl_2$: C, 28.3; H, 1.6; N, 5.5. Found: C, 29.5; H, 1.8; N, 5.6.

[Pt{3,3'$(CO_2Et)_2$-bpy}Cl_2] (1b)

A suspension of {3,3'$(CO_2Et)_2$-bpy} (0.115 g, 0.38 mmol) and K_2PtCl_4 (0.13 g, 0.32 mmol) were refluxed in 40 mL water for 18 h. A bright yellow powder precipitated on cooling. Yield 70.3 %. Anal. Calcd for $C_{16}H_{16}N_2O_4PtCl_2$: C, 33.9; H, 2.8; N, 4.9. Found: C, 34.4; H, 3.2 ; N 4.7,

[Pt{4,4'$(CO_2H)_2$-bpy}Cl_2]

Yield 87.9 %. Anal. Calcd for $C_{12}H_8N_2O_4PtCl_2$: C, 28.3; H, 1.6; N, 5.5. Found: C, 28.5; H, 2.0; N, 5.7.

[Pt{4,4'$(CO_2Et)_2$-bpy}Cl_2] (2b)

2b was synthesised in the same manner as **1b**. Yield 76.1 %. Anal. Calcd for $C_{16}H_{16}N_2O_4PtCl_2$: C, 33.9; H, 2.8; N, 4.9. Found: C, 32.9; H, 2.4 ; N, 4.9,

[Pt{5,5'$(CO_2H)_2$-bpy}Cl_2]

[Pt{5,5'$(CO_2H)_2$-bpy}Cl_2] was synthesised in the same manner as [Pt{4,4'$(CO_2H)_2$-bpy}Cl_2][11]. Yield 71.8 %. Anal. Calcd for $C_{12}H_8N_2O_4PtCl_2$: C, 28.3; H, 1.6; N, 5.5. Found: C, 28.8; H, 1.7; N, 5.5.

[Pt{5,5'$(CO_2Et)_2$-bpy}Cl_2] (3b)

Yield 76.2 %. Anal. Calcd for $C_{16}H_{16}N_2O_4PtCl_2$: C, 33.9; H, 2.8; N, 4.9. Found: C, 33.0; H, 2.7 ; N, 4.8.

[Pt{3,3'$(CO_2Et)_2$-bpy}(mnt)] (1c)

[Pt{3,3'$(CO_2Et)_2$-bpy}Cl_2] (0.47 g, 0.83 mmol) was dissolved in dry acentonitrile under nitrogen and a solution of Na_2(mnt) (0.23 g, 1.24 mmol) in dry methanol (5 mL) was added. The reaction was allowed to stir at room temperature under N_2 for 4 h. The solvent was removed and the product was washed with methanol before recrystallisation from acetonitrile. Yield 22.1 %. MS (FABMS) *m/z*: 636 (M^+). IR (KBr, cm^{-1}): 1729 (s) (C=O stretch), 2204 (s) (C≡N stretch). Anal. Calcd for $C_{20}H_{16}N_4O_4PtS_2$: C, 37.8; H, 2.5; N, 8.8. Found: C, 37.3; H, 2.5; N, 8.6.

[Pt{3,3'$(CO_2H)_2$-bpy}(mnt)] (1d)

[Pt{3,3'$(CO_2H)_2$-bpy}Cl_2] (0.80 g, 1.57 mmol) was dissolved in 2 equivalents of 1M aqueous solution of potassium hydroxide under nitrogen and a solution of Na_2(mnt) (0.44 g, 2.36 mmol) in dry methanol (5 mL) was added. The reaction was allowed to stir at room temperature under N_2 for 48 h. The product was precipitated using two equivalents of concentrated HCl and filtered. It was subsequently purified by column chromatography using Sephadex-LH20 as a separating medium by a method previously described.[11] Yield 20.0 %. MS (FABMS) *m/z*: 580 (M^+). Anal. Calcd for $C_{16}H_8N_4O_4PtS_2$: C, 33.2; H, 1.4; N, 9.7. Found: C, 32.4; H, 1.9; N, 9.0.

[Pt{4,4'$(CO_2Et)_2$-bpy}(mnt)] (2c)

[Pt{4,4'$(CO_2Et)_2$-bpy}Cl_2] (0.14 g, 0.25 mmol) was dissolved in DMF (15 mL) and heated under nitrogen to just below boiling point (140 °C). A solution of Na_2(mnt) (0.07 g, 0.37 mmol) in dry methanol (5 mL) was added and the reaction mixture was refluxed with stirring under N_2 for 1 hour and then allowed to stir under N_2 at room temperature overnight. The solvent was removed and the product was washed with water and methanol before recrystallisation from a hot saturated solution of DMF. Yield 72.0 %.

MS (FABMS) *m/z*: 636 (M^+). IR (KBr, cm^{-1}): 1730 (s) (C=O stretch), 2207 (s) (C≡N stretch). Anal. Calcd for $C_{20}H_{16}N_4O_4PtS_2$: C, 37.8; H, 2.5; N, 8.8. Found: C, 38.0; H, 3.1; N, 8.6.

[Pt{4,4'$(CO_2H)_2$-bpy}(mnt)] (2d)

2d was synthesised in the same manner as **1d**. Yield 28.5 %. MS (FABMS) *m/z*: 580 (M^+). Anal. Calcd for $C_{16}H_8N_4O_4PtS_2$: C, 33.2; H, 1.4; N, 9.7. Found: C, 32.2; H, 2.1; N 9.0.

[Pt{5,5'$(CO_2Et)_2$-bpy}(mnt)] (3c)

Yield 60.0 %. MS (FABMS) *m/z*: 636 (M^+). IR (KBr, cm^{-1}): 1725 (s) (C=O stretch), 2208 (s) (C≡N stretch). Anal. Calcd for $C_{20}H_{16}N_4O_4PtS_2$: C, 37.8; H, 2.5; N, 8.8. Found: C, 35.6; H, 2.6; N 7.7.

[Pt{5,5'$(CO_2H)_2$-bpy}(mnt)] (3d)

3d was synthesised in the same manner as **1d**. Yield 18.0 %. MS (FABMS) *m/z*: 580 (M^+). Anal. Calcd for $C_{16}H_8N_4O_4PtS_2$: C, 33.2; H, 1.4; N, 9.7. Found: C, 32.1; H, 2.1; N 8.0.

3.3.2 X-Ray Crystallography

Purple needle crystals of [Pt{3,3'$(CO_2Et)_2$bpy}(mnt)] (**1c**), (dimensions 1.00 × 0.08 × 0.06 mm^3) were grown by recrystallisation from a hot saturated solution of **1c** in acetonitrile. Crystal, data collection, and refinement parameters are summarised in table 3.8. The crystal structure was solved by Dr. Iain Oswald and Dr. Simon Parsons.

Single crystal X-ray structure determination was carried out using a Smart APEX CCD diffractometer equipped with an Oxford Cryosystems low-temperature device with Mo-Kα radiation for data collection. An absorption correction was applied using the multi-scan procedure SADABS. The structure was solved by direct methods and refined by

full-matrix least squares against $|F|$ using data ($I > 2\sigma(I)$). Hydrogen atoms were placed in calculated positions. The platinum and sulfur atoms were refined with anisotropic displacement parameters (adps). Other light atoms (C, N, O) were refined isotropically; adps for these atoms were rather distorted when refined, while not significantly contributing to better data-fitting.

Chemical Formula	$C_{22}H_{19}N_5O_4PtS_2$
Fw	676.65
T, K	150
Lattice type	Monoclinic
Space group	$P2_1/c$
a, Å	14.7735(15)
b, Å	21.632(2)
c, Å	7.5450(7)
β, deg	100.815(4)
V, Å^3	2368.4(4)
No. reflections for cell	4515
$2\theta_{max}(°)$	50
Z	4
D_c, Mg m^{-3}	1.898
μ, mm^{-1}	6.140
Reflections collected	21845
Unique [R_{int}]	5694 [0.07]
No. $I > 2\sigma$	3856
T_{min}/T_{max}	0.217/1.000
Parameters	153
R_1 [$F>4\sigma(F)$]	0.0665
wR	0.0751

S	1.0402
$\Delta\rho_{max}$ / eÅ^{-3}	6.91
$\Delta\rho_{min}$ / eÅ^{-3}	-4.03

Table 3.8 Crystallographic data for **1c**.

3.4 References

1 S. Ferrere, *Chem. Mater.*, 2000, **12**, 1083.

2 S. Ferrere, *Inorg. Chim. Acta*, 2002, **329**, 79.

3 S. Ferrere and B. A. Gregg, *J. Am. Chem. Soc.*, 1998, **120**, 843.

4 G. Sauve, M. E. Cass, S. J. Doig, I. Lauermann, K. Pomykal, and N. S. Lewis, *J. Phys. Chem. B*, 2000, **104**, 3488.

5 Y. Wang, J. B. Asbury, and T. Lian, *J. Phys. Chem. A*, 2000, **104**, 4291.

6 J. B. Asbury, E. Hao, Y. Wang, and T. Lian, *J. Phys. Chem. B*, 2000, **104**, 11957.

7 S. D. Cummings and R. Eisenberg, *J. Am. Chem. Soc.*, 1996, **118**, 1949.

8 W. Paw, S. D. Cummings, M. A. Mansour, W. B. Connick, D. K. Geiger, and R. Eisenberg, *Coord. Chem. Rev.*, 1998, **171**, 125.

9 M. Hissler, J. E. McGarrah, W. B. Connick, D. K. Geiger, S. D. Cummings, and R. Eisenberg, *Coord. Chem. Rev.*, 2000, **208**, 115.

10 A. Islam, H. Sugihara, K. Hara, L. Pratap Singh, R. Katoh, M. Yanagida, Y. Takahashi, S. Murata, and H. Arakawa, *New J. Chem.*, 2000, **24**, 343.

11 A. Islam, H. Sugihara, K. Hara, L. P. Singh, R. Katoh, M. Yanagida, Y. Takahashi, S. Murata, H. Arakawa, and G. Fujihashi, *Inorg. Chem.*, 2001, **40**, 5371.

12 E. J. L. McInnes, R. D. Farley, S. A. Macgregor, K. J. Taylor, L. J. Yellowlees, and C. C. Rowlands, *Faraday Trans.*, 1998, **94**, 2985.

13 J. A. Zuleta, M. S. Burberry, and R. Eisenberg, *Coord. Chem. Rev.*, 1990, **97**, 47.

14 J. A. Zuleta, J. M. Bevilacqua, and R. Eisenberg, *Coord. Chem. Rev.*, 1991, **111**, 237.

15 J. Yoo, J.-H. Kim, Y. S. Sohn, and Y. Do, *Inorg. Chim. Acta*, 1997, **263**, 53.

16 P.-H. Xie, Y.-J. Hou, T.-X. Wei, B.-W. Zhang, Y. Cao, and C.-H. Huang, *Inorg. Chim. Acta*, 2000, **308**, 73.

17 B. Z. Shan, Q. Zhao, N. Goswami, D. M. Eichhorn, and D. P. Rillema, *Coord. Chem. Rev.*, 2001, **211**, 117.

18 F. H. Case, *J. Am. Chem. Soc.*, 1946, **68**, 2574.

[19] L. Jack, Ph.D. Thesis, University of Edinburgh, 2003.

[20] S. Dholakia, R. D. Gillard, and F. L. Wimmer, *Polyhedron*, 1985, **4**, 791.

[21] C. S. Database, *Chem. Design Autom. News*, 1993, **8**, 31.

[22] B. W. Smucker, J. M. Hudson, M. A. Omary, and K. R. Dunbar, *Inorg. Chem.*, 2003, **42**, 4714.

[23] K. Kubo, M. Nakano, H. Tamura, and G.-E. Matsubayashi, *Inorg. Chim. Acta*, 2002, **336**, 120.

[24] A. Gund, Keppler, Bernhard K., *Angew. Chem. Int. Ed.*, 1994, **33**, 186.

[25] J. M. Bevilacqua and R. Eisenberg, *Inorg. Chem.*, 1994, **33**, 2913.

[26] Y.-X. Weng, L. Li, Y. Liu, L. Wang, and G.-Z. Yang, *J. Phys. Chem. B*, 2003, **107**, 4356.

[27] P. R. Murray, *University of Edinburgh, unpublished work*, 2005.

[28] E. Koenig and S. Kremer, *Chem. Phys. Lett.*, 1970, **5**, 87.

[29] V. T. Coombe, G. A. Heath, A. J. MacKenzie, and L. J. Yellowlees, *Inorg. Chem.*, 1984, **23**, 3423.

[30] G. A. Heath, L. J. Yellowlees, and P. S. Braterman, *Chem. Commun.*, 1981, 287.

[31] J. N. Clifford, G. Yahioglu, L. R. Milgrom, and J. R. Durrant, *Chem. Commun.*, 2002, 1260.

[32] G. Markl and R. Vybiral, *Tet. Lett.*, 1989, **30**, 2903.

Chapter 4

[Ni(II)(dithione)(dithiolate)] complexes for bulk-heterojunction solar cells

4. Introduction

4.1 Introduction to metal dithiolenes

Metal dithiolenes have been intensely studied since the 1960's for their novel properties which lead to many applications in the fields of conducting and magnetic materials, dyes, non-linear optics and catalysis. The fundamental properties of metal dithiolenes which include geometry, redox activity and intermolecular interactions are important to the overall function of the molecule and give rise to superconducting and ferromagnetic materials.[1, 2] Metal dithiolene complexes are useful in electronic materials since they may exist in several clearly defined oxidation states which are interchangeable *via* fully reversible redox steps. A neutral metal dithiolene complex can be described using a number of resonance forms (fig 4.1).

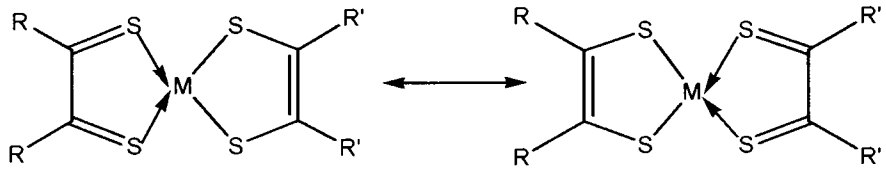

Fig. 4.1 Two resonance forms of a metal dithiolene complex. Changing the properties of the R, R′ substituents changes the electronic distribution across the molecule. Ligands with a C=S motif are dithione ligands and are formally neutral donors and ligands with a C-S motif are dithiolate ligands and are formally dianionic donors.

Metal dithiolene complexes are highly delocalised with frontier orbitals that may be distributed across the entire molecule through to the R groups. This delocalisation leads to a number of effects including the complex having

1. Redox activity with one or more reversible redox processes (depending on the metal).
2. Low energy absorption in the visible/NIR region due to the small HOMO-LUMO gap.

3. Mediation of intermolecular interactions due to the S atoms in the delocalised core.

4.1.1 Dmit and metal complexes of dmit

Dmit (1,3-dithiole-2-thione-4,5-dithiolate) stems from "dimercaptoisotrithione" and was first accurately reported by Steimecke and co-workers in the 1970's (fig. 4.2).[3] Dmit and its related ligands have been used in many applications, mainly in the field of conducting and magnetic materials and the first molecular superconductor containing a transition metal complex was [TTF][Ni(dmit)$_2$]$_2$. The ligand is a sulphur-rich fully conjugated planar ligand which coordinates metals in a square-planar fashion and this fully-planar structure allows extensive stacking of the ligands. The large S atomic orbitals create a significant intermolecular overlap resulting in a delocalised system which enables conduction throughout the material.

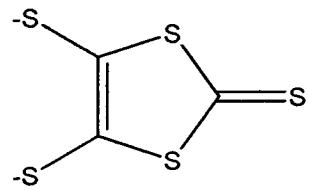

Fig. 4.2 Structure of 1,3-dithiole-2-thione-4,5-dithiolate, dmit

Complexes based on [Ni(dmit)$_2$] are the most widely studied of dmit complexes and [Ni(dmit)$_2$] is a well known electron acceptor in the field of molecular conductors. In these [Ni(dmit)$_2$] complexes the conduction process is essentially ligand centred. The [Ni(dmit)$_2$] molecules form stacks by overlapping of the π-electrons between adjacent molecules and electronic conduction is thus observed. [Ni(dmit)$_2$] stacks form 2D sheet structures through side-by-side interactions in the crystal and these side-by-side, interactions lead to the formation of 2D band structures which can result in metals and superconductors.[4]

4.1.2 Links with organic semiconductors

Interest in $[M(dmit)_2]$ complexes and other dithiolenes also stems from its structural similarity with the organic donor molecule BEDT-TTF (Bis(ethylenedithio)tetrathiafulvalene), where the M is replaced by a C=C (fig. 4.3)

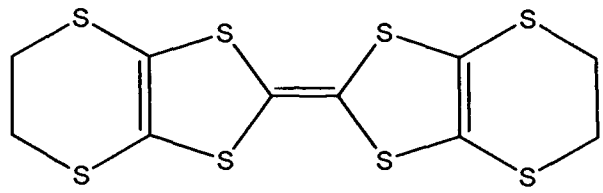

Fig. 4.3 Structure of BEDT-TTF

BEDT-TTF has been shown to form molecular metals and molecular superconductors and has led to the largest number of superconducting organic salts and those with the highest critical temperatures (excluding superconductors based on C_{60}).[5] All organic superconductors are based on molecules related to TTF. Materials based on BEDT-TTF are known as "organic metals" where the metallic properties arise from the overlap of the π-molecular orbitals (which are partly delocalised). In designing dithiolate coordinating ligands, attempts are made to include structural features of "organic metals" into them and this helps to increase the interaction of the molecules *via* the ligands since large sulphur atomic orbitals help to promote effective intermolecular interactions.

4.1.3 Tuning of Ni dithiolene complexes

The electronic and photophysical properties of Ni dithiolene complexes can be tuned by variation of the attached ligand set. Donor substituents on the dithiolene raise the energy of the HOMO more than that of the LUMO. On raising the HOMO, the molecule becomes easier to oxidise and on raising the LUMO, the reduction of the molecule becomes more difficult. Electron withdrawing substituents on the dithiolene lower the HOMO, and the complex becomes more difficult to oxidise and lowering of the LUMO by electron withdrawing groups makes reduction of the complex easier.[6]

4.1.4 Unsymmetrical [Ni(II)(dithione)(dithiolate)], "Push-Pull" Complexes

Unsymmetrical [Ni(II)(dithione)(dithiolate)] complexes, where the dithione is formally a neutral donor ligand and the dithiolate is formally a dianionic species, are of interest due to the current research into using them as NIR dyes. As previously mentioned, molecular superconductors that have been derived from $[Ni(dmit)_2]$ systems exist, a number of which have TTF as a donor molecule. Not many examples of unsymmetrical metal complexes which are part of molecular conducting systems exist. Some do exist though and are usually found in co-existance with TTF.[7]

Unsymmetrical [Ni(II)(dithione)(dithiolate)] complexes (fig 4.4) have previously been reported by Deplano *et al.* and have been assigned as "push-pull" complexes where the "push" is due to an electron donating dithione ligand and the "pull" is due to an electron withdrawing dithiolate ligand.[8] The HOMO in these complexes has previously been assigned to be based partly on the dithiolate ligand and the LUMO based partly on the dithione, though it is widely accepted that both the HOMO and LUMO are spread over the entire molecule. This results in a highly delocalised structure with a small HOMO-LUMO gap and therefore these molecules show an intense NIR band in their absorption spectrum.

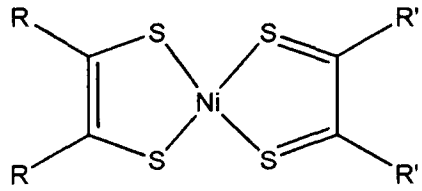

Fig. 4.4 Structure of a [Ni(II)(dithione)(dithiolate)] complex

Changing the characteristics of the R groups changes the electronic characteristics of a "push-pull" complex which results in a redistribution of the electron density and greater emphasis being placed on one of the resonance forms. The C_2S_2 orbitals (with C-C_π and C-S_{π^*} character) are stabilised and destabilised by mixing with metal valence orbitals.[8] For a stable, uncharged, diamagnetic compound, only the lower MO is filled and the

HOMO-LUMO gap is large. The general electronic characteristics show that C_2S_2 π-donors ("push"-ligands) in symmetric complexes raise both the HOMO and LUMO so the HOMO is preferentially depopulated leading to a dicationic complex (e.g.$[Ni(Me_2pipdt)_2]^{2+}$). Π-acceptor ligands ("pull"-ligands) lower the energy of both the HOMO and the LUMO leading to dianionic complexes (e.g. $[Ni(dmit)_2]^{2-}$).

4.1.5 Aims

The current interest in solid-state solar cells which include polymer-blend solar cells has been discussed in section 1.9 of this thesis. One drawback of this type of cell is that the main polymer components are usually short-wavelength absorbing molecules and hence do not absorb in much of the visible region of the solar spectrum. Therefore, replacing one or both of the component polymers with a coloured molecule which has appropriate electronic properties is desirable. Metal bis-dithiolenes (for M = Ni, Pd, Pt) are well known to form metallic and semiconducting materials which absorb at long wavelengths (in the red region of the visible spectrum and the NIR). Small molecules like $[Ni(dmit)_2]$ are highly coloured and have strong intermolecular interactions, however they are also very insoluble and therefore difficult to use in the formation of devices. In contrast to this, unsymmetrical metal dithiolene complexes retain good intermolecular interactions and a strong absorption in the NIR but are more soluble than their symmetric counterparts. Therefore, the aim of the work reported in this chapter is to synthesise and characterise [Ni(II)(dithione)(dithiolate)] complexes and measure the conductivity properties of such a complex in the form of a solution cast film. The ultimate aim of this work is to use a [Ni(II)(dithione)(dithiolate)] complex as a coloured component in a solid-state solar cell. Some of the synthetic work reported in this chapter was done by the author at the Università di Cagliari in collaboration with the group of Prof. Paola Deplano where the chemistry of Nickel dithiolenes has been extensively studied and in many cases standard synthetic procedures to many complex molecules already exist.

4.2 Results and discussion

4.2.1 Synthesis and structure

A numbering scheme for the compounds described in this chapter is seen in table 4.1 and fig. 4.6. 1,4-dibenzylpiperazine-2,3-dithione (Bz_2pipdt, **4a**) was synthesised by a previously reported method which involved the reaction of N,N′-dibenzylethylenediamine and dimethyloxalate to give the dibenzyl substituted piperazine ligand.[9] The diketone group was converted to a dithione using Lawesson's reagent. MeBzpipdt, **5a** and Pr^i_2pipdt, **6a** were used as supplied by Marco Salidu.

The dicationic symmetric Ni dithione molecules, $[Ni(R_1R_2pipdt)_2][BF_4]_2$ were synthesised by a route analogous to that of the previously reported $[Ni(Me_2pipdt)_2][BF_4]_2$ (fig. 4.5).[10] In each case, $NiCl_2$ was dissolved in EtOH and added to a solution of two equivalents of the ligand in DCM. After stirring at room temperature for several minutes the solvent was removed and the crude product redissolved in EtOH and filtered. This process removed unreacted ligand (if any). NaBF4 was added as a solid and the solution stirred until the solid product $[Ni(R_1R_2pipdt)_2][BF_4]_2$ crashed out of solution. $[Ni(R_1R_2pipdt)_2][BF_4]_2$ was recrystallised from hot MeCN with slow dropwise addition of ether. $[TBA]_2[Ni(dmit)_2]$ was synthesised by a previously published method.[3] The unsymmetric dithiolenes were made by an analogous method to $[Ni(Pr^i_2pipdt)(dmit)]$ which has previously been reported (fig. 4.6).[8, 10] Though a mixture of complexes may intuitively be expected with this reaction, it was found not to be the case and a microcrystalline product crashed out of solution in each case. Recrystallisation led to an increase in the crystal size in some cases and hence a structure was refined for crystals of **4c**.

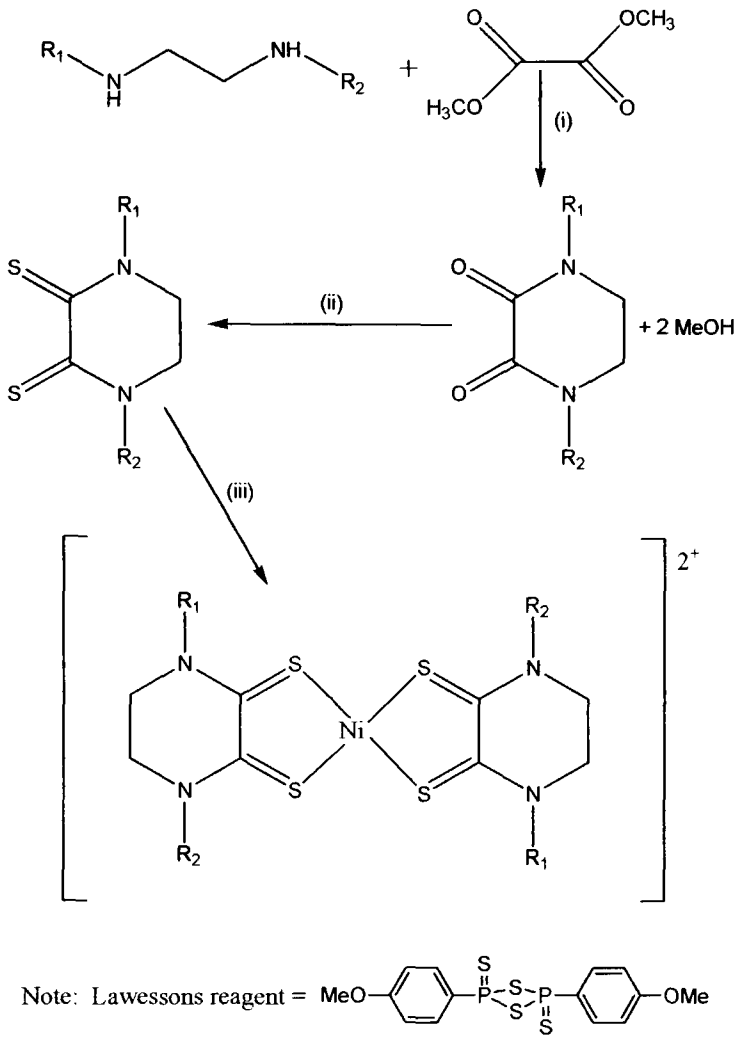

Fig. 4.5 Synthetic scheme for preparation of symmetrical Ni dithione complexes. (i) Reflux in toluene for 6 hours (ii) 1.2 equivalents of Lawesson's reagent, reflux in toluene 15 minutes (iii) 0.5 equivalents of $NiCl_2.6H_20$ in EtOH for 15 minutes at RT

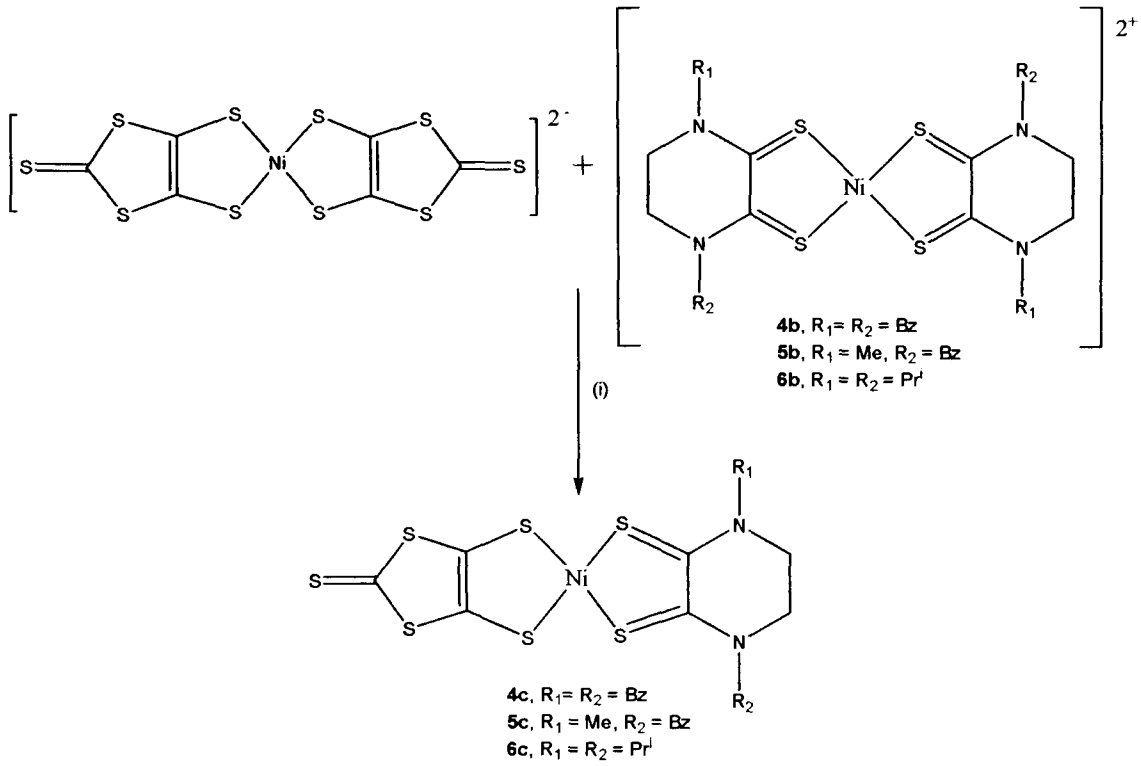

Fig. 4.6 Synthetic scheme for preparation of unsymmetrical Ni dithiolene complexes. (i) Stir in MeCN at RT for 15 minutes.

X-Ray Crystallography

Crystals of **4c** were grown by slow diffusion of diethyl ether into a saturated solution of **4c** in DMF. Attempts at crystallising **5c** were unsuccessful and the crystal structure for **6c** has previously been reported.[8] For **4c** the central Ni atom is coordinated by four S atoms in a square planar environment with Ni-S bonds ranging from 2.1477(5)-2.1628(4) Å. Selected bond lengths and angles are shown in figure 4.7. The crystal lattice shows the complex stacks (fig 4.8) and the interplanar distance is 3.651 Å, which is typical of π-stacked metal dithiolene complexes. The molecule is essentially planar except for the Bz substituents at the pipdt N and the torsion angle of only 5.88° around S12, C22, N32, C62 suggests that the Np_{π}-lone pair is almost parallel to the C_2S_2 π-system as previously reported for **6c**. The Ni-S bond lengths are similar in value to

those previously published for other "push-pull" coordination complexes[8] (and references therein) which suggests that the Ni-S σ bonds are more or less equivalent irrespective of the nature of the ligand and that the Ni-S π interactions have only minor importance or none at all as previously proposed for **6c**.[8] The C-S bond lengths are shorter (*ca.* 0.04 Å) in the pipdt ligands than in dmit (since they have π donors adjacent to the C_2S_2 core). This is consistent with the C-S π^* and C-C π nature of the ligands frontier orbitals. The C-C bond is significantly longer in the pipdt (1.477 Å) than the dmit (1.349 Å) corresponding to the electron poor nature of the pipdt ("push") and electron rich ("pull") dmit ligand.

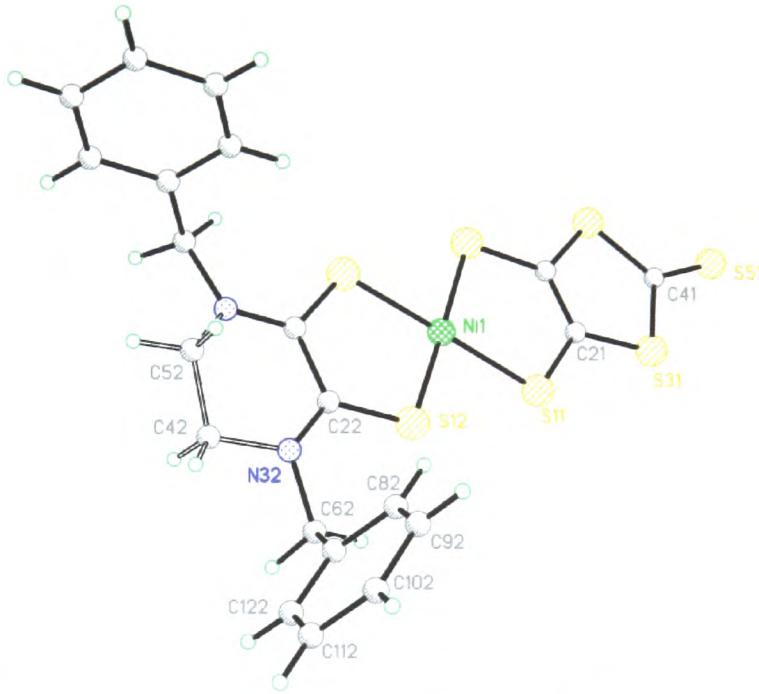

Fig 4.7 X-Ray crystal structure of **4c** showing the atom labeling scheme. Selected bond lengths (Å) and angles (°): Ni-S(12) 2.1477(5), Ni-S(11) 2.1627(4), S(11)-C(21) 1.7306(16), S(12)-C(22) 1.6908(16), C(22)-C(22′) 1.477(3), C(21)-C(21′) 1.349(3), S(12)-Ni-S(11) 87.544(16), S(11)-Ni-S(11′) 94.07(2), S(11′)-Ni-S(12′) 87.541(16), S(12′)-Ni-S(12) 90.84(3).

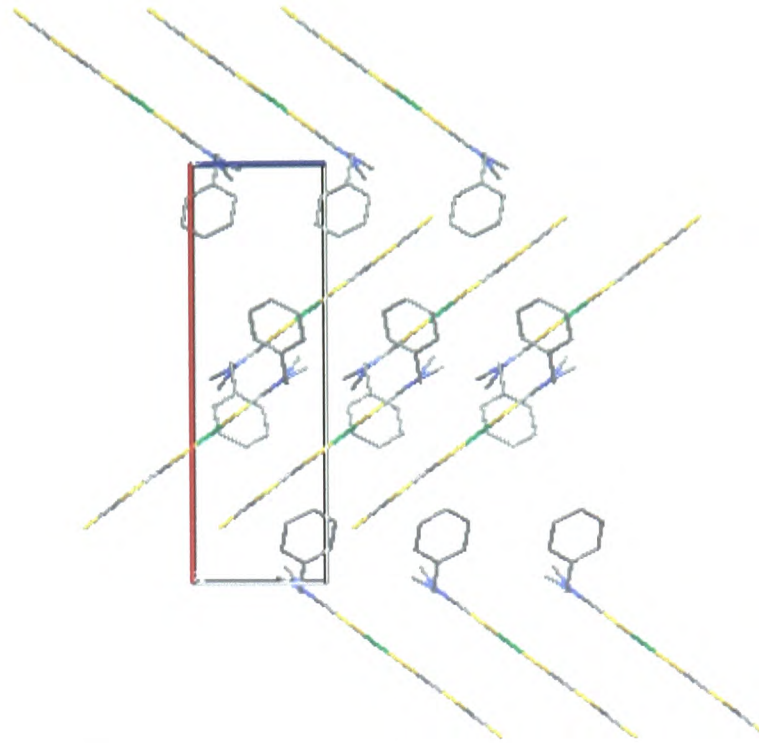

Fig. 4.8 View down the b-axis showing packing motif of **4c**

4.2.2 Electrochemistry

The electrochemistry of **4a**, **4c**, **5a**, **5c**, **6a** and **6c** was studied by performing cyclic voltammetry on the species in solution of 0.1 M $TBABF_4$ in DMF at 293 K. Redox potentials for the processes are listed in table 4.1.

complex number	Name	E_1/V	E_2/V	E_3/V
4a	Bz_2pipdt	--------	-1.24	1.13*
4b	$[Ni(Bz_2pipdt)_2][BF_4]_2$	-----	-----	-----
4c	[Ni(Bz_2pipdt)(dmit)]	-0.91	-0.41	0.69*
5a	MeBzpipdt	-----	-1.30	1.15*
5b	$[Ni(MeBzpipdt)_2][BF_4]_2$	----	-----	----
5c	[Ni(MeBzpipdt)(dmit)]	-0.94	-0.46	0.67*
6a	Pr^i_2pipdt	---	-1.40§	1.01*
6b	$[Ni(Pr^i_2pipdt)_2][BF_4]_2$	-----	------	----
6c	[Ni(Pr^i_2pipdt)(dmit)]	-1.04	-0.49	0.65*

Table 4.1 Redox potentials, $E_{1/2}$, of the free (R_1R_2pipdt) ligands and [Ni(R_1R_2pipdt)(dmit)] complexes. All processes are chemically reversible unless otherwise stated. *irreversible, §quasi reversible processes, E_p.

Each of the free pipdt ligands, **4a**, **5a** and **6a** shows one reduction process within the solvent window (fig. 4.9). This process is chemically reversible for **4a** and **5a** and quasireversible for **6a**. The ease of reduction of the ligands follows the order **4a** > **5a** > **6a**, where **4a** is the easiest to reduce. Therefore the type of substituent on the N of the pipdt ligand influences the reduction potential of the ligand. Changes to the substituent on the pipdt ligand are also seen to affect the spin density located on the reduced form of the ligand which is reported later in this chapter (section 4.2.6).

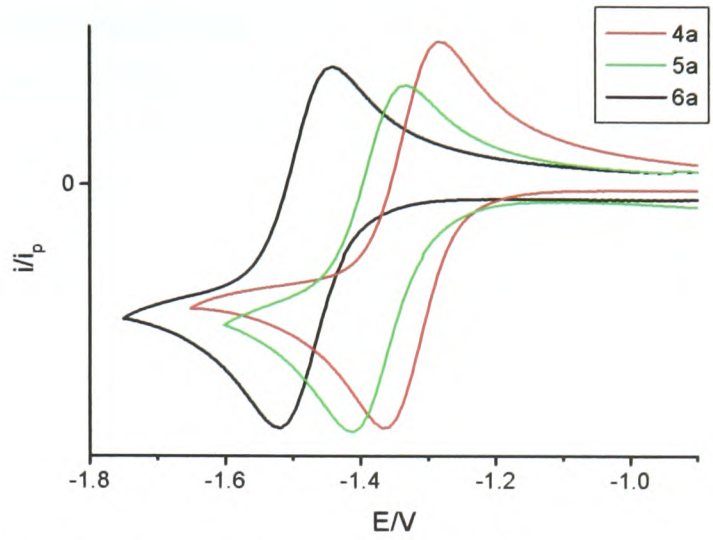

Fig. 4.9 Cyclic voltammogram of the reduction of **4a**, **5a** and **6a** in solution of 0.1 M $TBABF_4$ in DMF at 293 K

Each ligand shows one chemically irreversible oxidation within the solvent window and the ease of oxidation is approximately converse to that of the ease of reduction of the ligands and follows the order **6a**<**4a**≈**5a** (fig. 4.10).

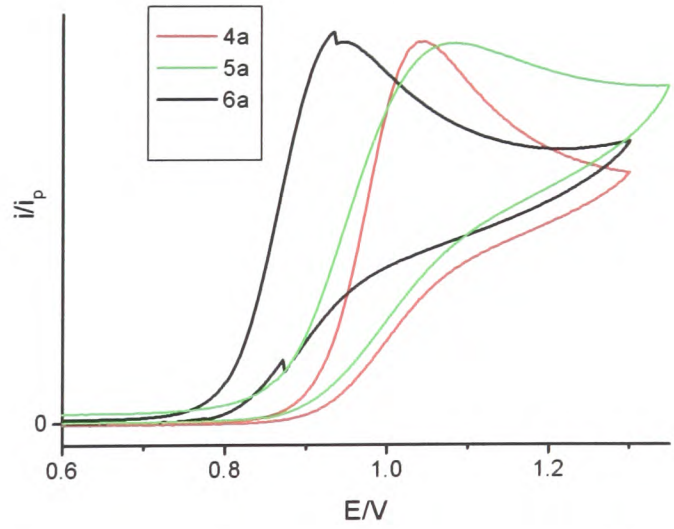

Fig. 4.10 Cyclic voltammogram of the oxidation of **4a**, **5a** and **6a** in solution of 0.1 M $TBABF_4$ in DMF at 293 K

On coordination of a metal centre to the free ligand the reduction potentials of the resulting complexes is shifted to a less negative potential (fig. 4.11). Each complex **4c**, **5c** and **6c** shows two fully chemically reversible reductions within the solvent window. The electrochemistry of **6c** in acetonitrile has previously been published and our results are very similar to those reported.[8] The ease of reduction for the complexes follows the order **4c**<**5c**<**6c** and therefore the reduction potentials of the [Ni(R_1R_2pipdt)(dmit)] complexes are dependant on the R substituent on the pipdt ligand. This can be seen more clearly in the second reduction of the complexes, where the second reduction potential of **6c** is significantly more negative than that of both **4c** and **5c** since these species have one R substituent in common (Bz) and **6c** is different. The results for the reduction of the complexes are consistent with those shown for the free pipdt ligands. A preliminary study into [Ni(R_1R_2pipdt)(dithiolate)] complexes has shown using DFT calculations, electrochemistry and spectroscopic techniques that the LUMO is at least partly located on the R_1R_2pipdt ligand[8] and the results reported here appear consistent with this assignment.

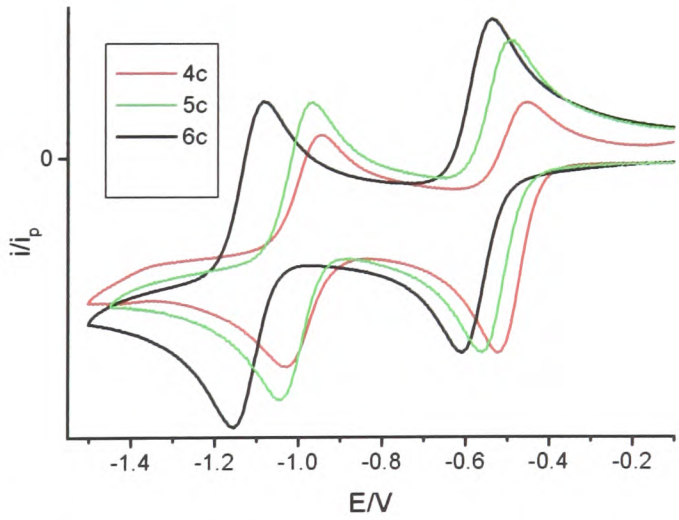

Fig. 4.11 Cyclic voltammogram of the reductions of **4c**, **5c** and **6c** in solution of 0.1 M $TBABF_4$ in DMF at 293 K

Each of the three complexes **4c**, **5c**, and **6c** shows one chemically irreversible oxidation process. The ease of oxidation for the complexes follows the order **6c**<**5c**<**4c**, with **6c** being the easiest to oxidise (fig. 4.12). It has been proposed that in [Ni(R_1R_2pipdt)(dithiolate)] complexes the HOMO is at least partly located on the dithiolate ligand.[8] Since the dithiolate ligand is the same in each case for **4c**, **5c** and **6c** (dmit), a similar oxidation potential for **4c**, **5c** and **6c** might be expected. However it has previously been stated that the valence orbitals in metal dithiolene complexes are spread over the entire molecule. This explanation may be more consistent with the results of the cyclic voltammetry since the oxidation potential of each complex is also affected by changes to the R group on the pipdt ligand.

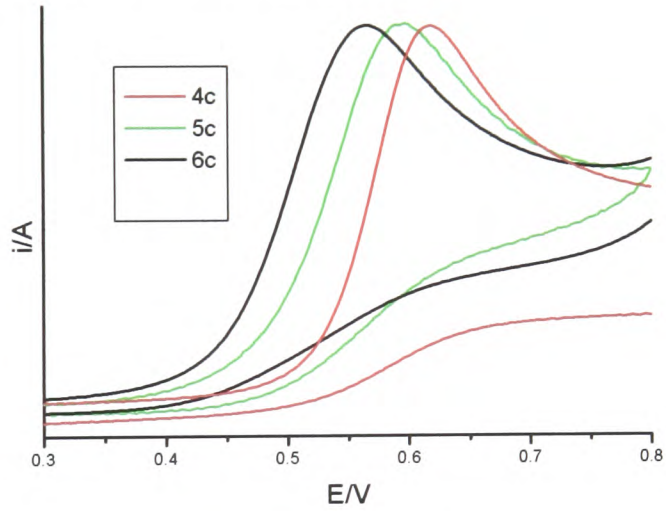

Fig. 4.12 Cyclic voltammogram of the oxidation of **4c**, **5c** and **6c** in solution of 0.1 M $TBABF_4$ in DMF at 293 K

4.2.3 Raman spectroscopy

Raman spectra have previously been collected to provide information on the electron distribution in related dithiolene complexes. These have been used to relate the charge of the complexes in the $[M(dmit)_2]^{n-}$ (n=0, 0.29, 0.5, 1 or 2; M=Ni or Pd) series to the C=C stretching mode A_g, and a linear correlation of this vibration *versus* the charge has been found.[8] In these complexes the C=C stretch shows a shift to higher frequencies as

the negative charge on the complex increases: This peak is found at 1435 cm^{-1} in $[Ni(dmit)_2]^{2-}$ and at 1390 cm^{-1} in $[Ni(dmit)_2]^{1-}$. [Ni(Bz_2pipdt)(dmit)] shows a peak at 1430 cm^{-1}, suggesting that the dmit ligand bears a -2 formal charge as already observed in **5c** and **6c**.[11] These results are indicative of "pull" character (dithiolate) for the dmit ligand and hence "push" character (dithione) for the Bz_2pipdt ligand, with significant separation of charges in the resulting complex.[6] DFT calculations support the spectroscopic results.[8]

4.2.4 UV/visible Spectroscopy

The UV/visible spectra of compounds **4c**, **5c** and **6c** (fig. 4.13) each show an intense peak in the uv, a visible peak and a NIR absorption. Table 4.2 shows the λ_{max} values and a selection of molar extinction coefficients.

Complex	λ_{max}(uv)/nm ($M^{-1}cm^{-1}$)	λ_{max}(visible)/nm ($M^{-1}cm^{-1}$)	λ_{max} (NIR)/nm ($M^{-1}cm^{-1}$)
4c	326.5	487 (9,700)	858 (10,600)
5c	322	486.5 (8,900)	842 (9,300)
6c	319	490.5 (9,000)	829 (8,200)

Table 4.2 Peaks observed in the UV/visible spectra for complexes **4c**, **5c** and **6c** in DMF, ε ($M^{-1}cm^{-1}$) are given in brackets

The UV and visible transitions seen in the spectra for **4c**, **5c** and **6c** occur at similar wavelengths for each species. The low energy NIR band has previously been assigned as LLCT (dithiolate to dithione) for this class of complex.[6] For the NIR transition (which is attributed to the HOMO-LUMO charge transfer due to the small energy difference between the HOMO and LUMO) the λ_{max} follows the order **4c**>**5c**>**6c**. This is consistent with the results of the electrochemistry which showed that E_3-E_2 is smallest for **4c** (table 4.1), i.e. the HOMO-LUMO gap is smallest for **4c** and therefore the λ_{max} for the NIR transition is therefore largest for **4c**.

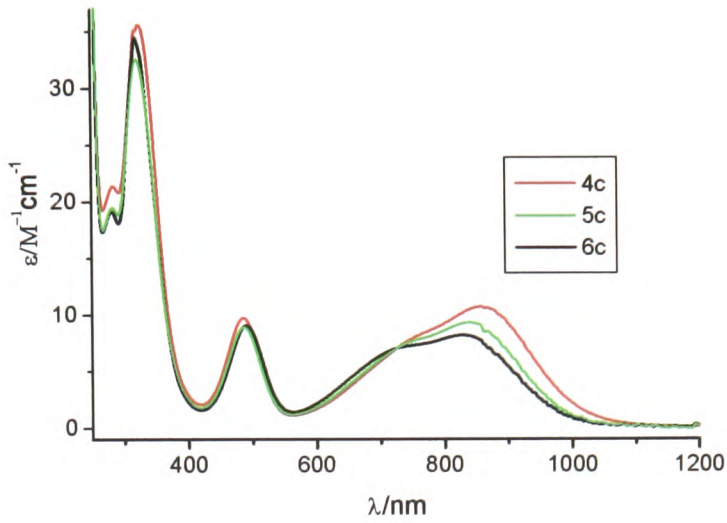

Fig. 4.13 UV/Vis/NIR spectra of **4c**, **5c** and **6c** in solution of DMF at 293 K

4.2.5 UV/Vis/NIR Spectroelectrochemistry

UV/Vis/NIR spectroelectrochemistry was performed on **4a**, **5a** and **6a** to attempt to electronically characterise the ligands further. Each ligand was reduced *in-situ* at 213 K and the UV/Vis/NIR spectra were taken. Each ligand spectrum shows similar features with an intense peak at *ca.* 31,000 cm^{-1} and a smaller peak at *ca.* 23,000 cm^{-1}. On reduction of the species **4a**, **5a** and **6a** to $\mathbf{4a}^{1-}$, $\mathbf{5a}^{1-}$ and $\mathbf{6a}^{1-}$ the peak at *ca.* 31,000 cm^{-1} decreases in intensity and the peak at *ca.* 23,000 cm^{-1} increases in intensity.

Complex	**0**, ν/cm^{-1} ($M^{-1}cm^{-1}$)	**-1**, ν/cm^{-1} ($M^{-1}cm^{-1}$)
4a	30,900 (14,900) 24,100 (2,800)	31,500 (9,400) 23,200 (6,000)
5a	31,200 (12,600) 24,000 (1,100)	31,200 (10,200) 23,600 (1,700)
6a	31,800 (15,200) 24,300 (1,500)	33,800 (6,500) 22,800 (11,300)

Table 4.2 Peaks observed in the UV/visible spectra for ligands **4a**, **5a** and **6a** in their neutral (**0**) and monoreduced (**-1**) states. ε ($M^{-1}cm^{-1}$) are given in brackets.

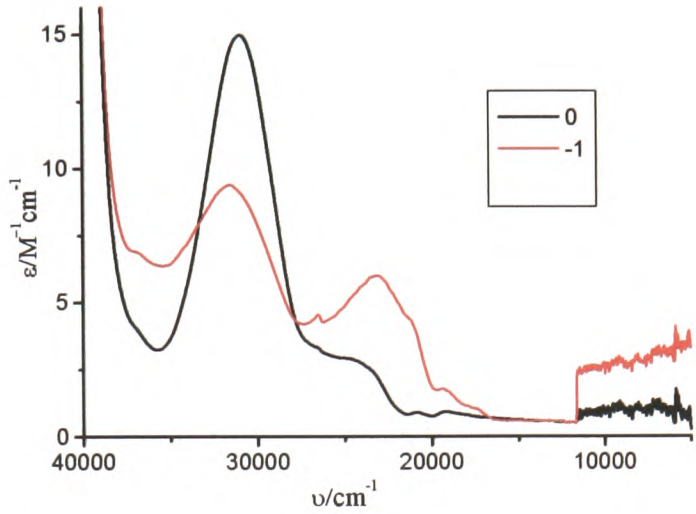

Fig. 4.14 UV/visible spectra of $\mathbf{4a}^{0/1-}$ in 0.1 M $TBABF_4$/DMF at 213 K. E_{gen}= 0.00 V(0), -1.70 V(-1)

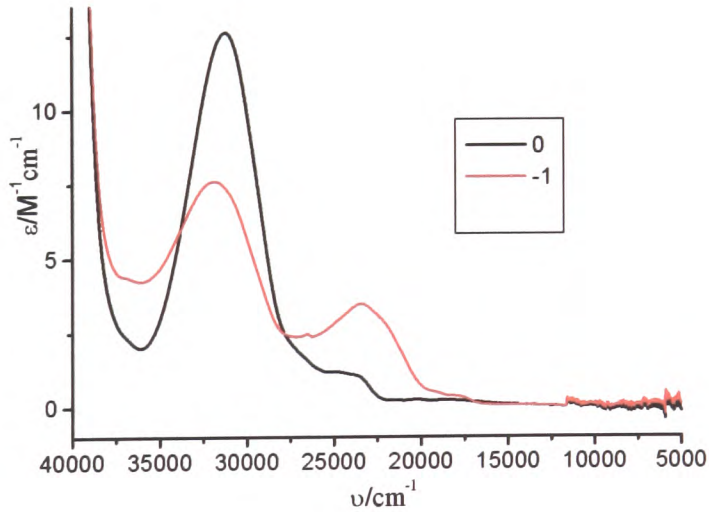

Fig. 4.15 UV/visible spectra of $\mathbf{5a}^{0/1-}$ in 0.1 M $TBABF_4$/DMF at 213 K. E_{gen}= 0.00 V(0), -1.70 V(-1)

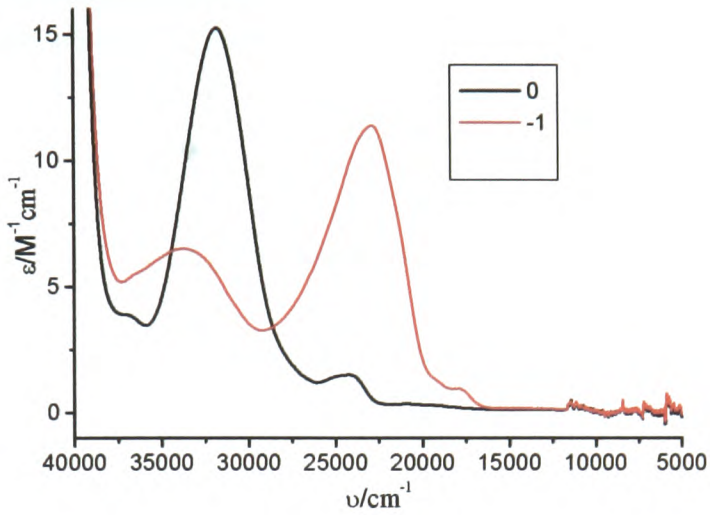

Fig. 4.16 UV/visible spectra of $\mathbf{6a}^{0/1-}$ in 0.1 M $TBABF_4$/DMF at 213 K. E_{gen}= 0.00 V(0), -1.70 V(-1)

For each ligand in every case after recording the final spectrum the potential was adjusted so that the neutral starting material was regenerated and each absorption spectrum was observed to return exactly to that of the starting species, thus the monoreduced species $\mathbf{4a}^{1-}$, $\mathbf{5a}^{1-}$ and $\mathbf{6a}^{1-}$ are all stable at 213 K. It was attempted to study the UV/Vis/NIR spectroelectrochemistry of $\mathbf{4c}^{1-}$ and $\mathbf{6c}^{1-}$, however at low temperatures (213 K) these species precipitate out of a solution of DMF and at less extreme temperatures (233 K) investigations into **4c** showed that the absorption spectrum could not be returned to that of the starting spectrum. This implies that $\mathbf{4c}^{1-}$ is not stable at 233 K therefore no further comparisons may be made. Unfortunately it is impossible to assign any of the transitions which occur in the the free ligands **4a**, **5a** and **6a** and their monoreduced species $\mathbf{4a}^{1-}$, $\mathbf{5a}^{1-}$ and $\mathbf{6a}^{1-}$ since no comparison may be made between their UV/visible spectra and those of their [Ni(R_1R_2pipdt)(dmit)] counterparts.

4.2.6 *In-Situ* EPR Spectroelectrochemistry

In-situ EPR spectroelectrochemistry was performed on **4a**, **4c**, **5a**, **5c**, **6a** and **6c**. The location of the electron introduced was studied by analysing the couplings observed. The purpose of the EPR study was to compare the location of the first reduction electron in **4c**, **5c** and **6c** to its location on the corresponding uncoordinated ligand, **4a**, **5a** and **6a**. Each species was reduced in a solution of 0.1 M $TBABF_4$ in DMF at 233 K.

$\mathbf{4a}^{1-}$ was generated *in-situ* at 233 K to give an EPR active solution (fig. 4.17(a)) and at a higher temperature (293 K) the spectrum is more resolved. The EPR coupling values of $\mathbf{4a}^{1-}$ are listed in table 4.3. The simulation shows that significant electron density is located on the two ring N atoms and two sets of four equivalent H atoms, which are the four ring H atoms and four benzylic H atoms of the Bz substituent. This confirms that reduction of this ligand results in some of the charge being localised on to the R group on the N atom.

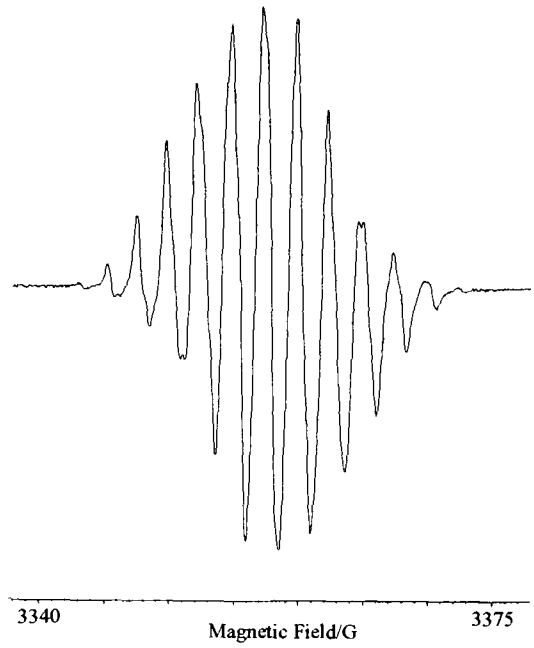

Fig. 4.17(a) EPR spectrum of $\mathbf{4a}^{-1}$ in solution of 0.1 M $TBABF_4$ in DMF at 293 K. E_{gen} = -1.70 V

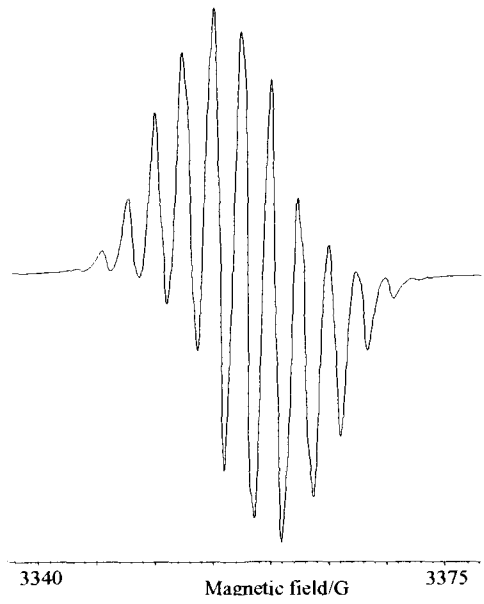

Fig. 4.17(b) Simulated EPR spectrum of $\mathbf{4a}^{-1}$ using the parameters given in table 4.3

Parameter	$\mathbf{4a}^{-1}$
a(H×4)	2.211
a(H×4)	2.211
a(N×2)	2.82
Δ	0.8
g	2.01005

Table 4.3 EPR coupling constants for $\mathbf{4a}^{1-}$ in 0.1 M $TBABF_4$/DMF at 293 K. All hyperfine coupling constants given in G. Δ = linewidth

The *in-situ* EPR spectroelectrochemistry of the corresponding [Ni(R_1R_2pipdt)(dmit)] complex, ($\mathbf{4c}^{1-}$) was also studied and this spectrum is again more resolved at 293 K (fig. 4.18(a) and table 4.4). $\mathbf{4c}^{1-}$ shows coupling to both ring N atoms, the four ring H atoms and a smaller coupling associated with two of the benzyl H atoms. In both cases, on introduction of another electron to the complex and formation of $\mathbf{4a}^{2-}$ and $\mathbf{4c}^{2-}$ respectively, the signal collapses as the second electron enters the same orbital as the first and they spin pair thus becoming diamagnetic.

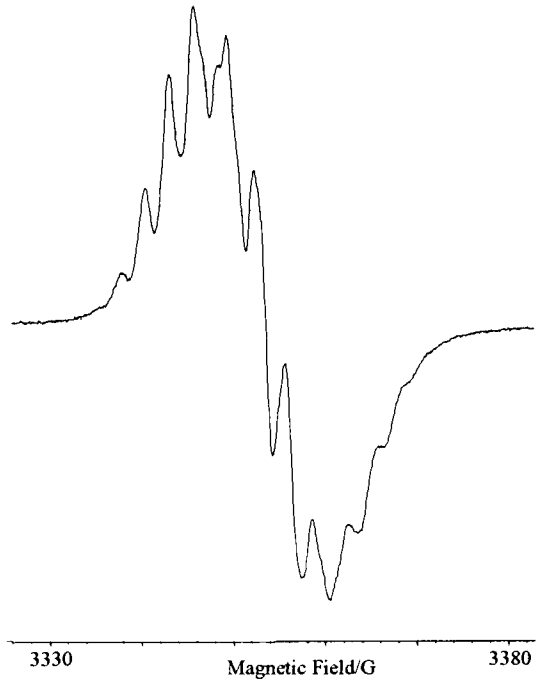

Fig. 4.18(a) EPR spectrum of $\mathbf{4c}^{-1}$ in solution of 0.1 M $TBABF_4$ in DMF at 293 K. E_{gen} = -1.50 V

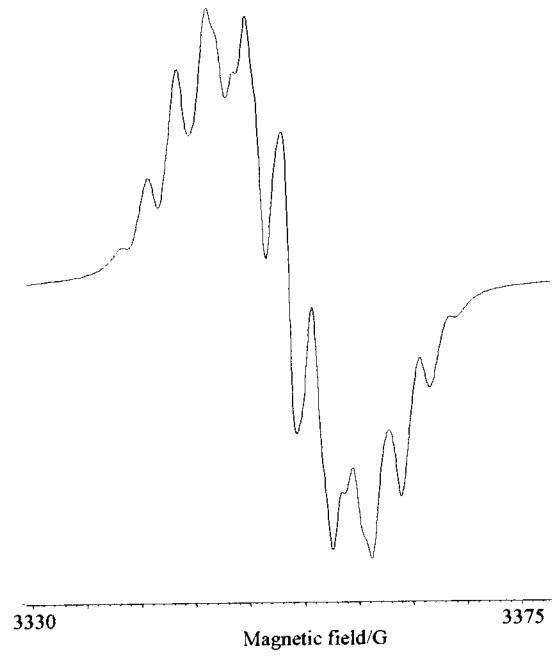

Fig. 4.18(b) Simulated EPR spectrum of $\mathbf{4c}^{-1}$ using the parameters given in table 4.4

Parameter	$\mathbf{4c}^{-1}$
a(N×2)	3.68
a(H×2)	2.211
a(H×4)	2.722
Δ	1.4
g	2.01265

Table 4.4 EPR coupling constants for $\mathbf{4c}^{1-}$ in 0.1 M $TBABF_4$/DMF at 293 K. All hyperfine coupling constants given in G. Δ = linewidth

$\mathbf{5a}^{1-}$ was generated *in-situ* at 233 K to give an EPR active solution (fig 4.19(a)).

Fig. 4.19(a) EPR spectrum of $\mathbf{5a}^{-1}$ in solution of 0.1 M $TBABF_4$ in DMF at 233 K. E_{gen} = -1.75 V

The *in-situ* EPR spectroelectrochemistry of the corresponding [Ni(R_1R_2pipdt)(dmit)] complex, ($\mathbf{5c^{1-}}$) was also studied at 233 K (fig 4.20(a)).

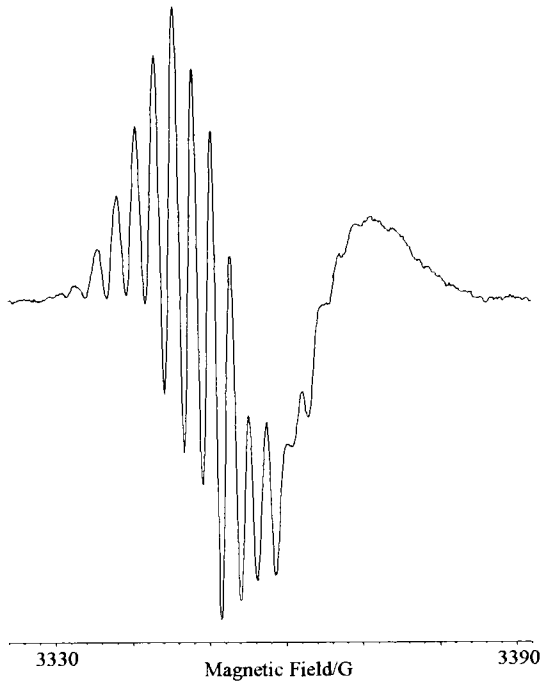

Fig. 4.20(a) EPR spectrum of $\mathbf{5c^{-1}}$ in solution of 0.1 M $TBABF_4$ in DMF at 233 K. E_{gen} = -0.85 V

In both cases, on introduction of another electron to the complex and formation of $\mathbf{5a^{2-}}$ and $\mathbf{5c^{2-}}$ respectively, the signal collapses as the second electron enters the same orbital as the first and they spin pair thus becoming diamagnetic. At the time of writing, attempts to simulate the spectra of $\mathbf{5a^{-1}}$ and $\mathbf{5c^{-1}}$ have been unsuccessful due to the additional complexity introduced by the inequivalence of the R groups in these molecules; however these simulations will be completed in the near future with the help of Prof. L. J. Yellowlees.

$\mathbf{6a^{1-}}$ was generated *in-situ* at 233 K to give an EPR active solution and the spectrum is more resolved at a higher temperature (293 K) (fig. 4.21 (a)). The EPR coupling values of $\mathbf{6a^{1-}}$ are listed in table 4.5. The simulation shows that significant electron density is

located on the two ring N atoms, four equivalent ring H atoms, and a smaller amount of spin density is also located on the the two unique H atoms on the isopropyl substituents.

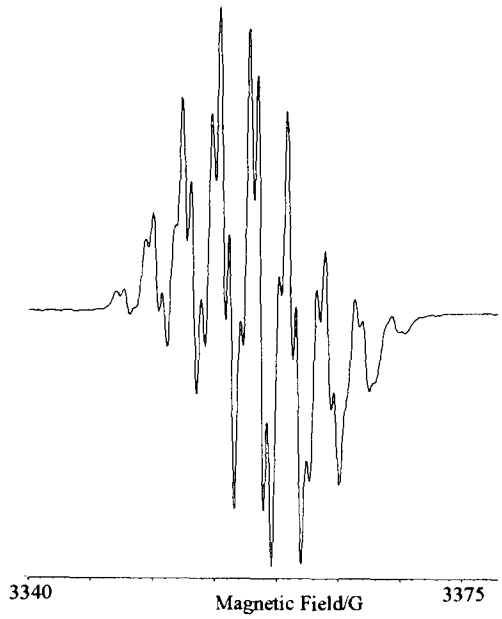

Fig. 4.21(a) EPR spectrum of $\mathbf{6a}^{-1}$ in solution of 0.1 M $TBABF_4$ in DMF at 293 K. E_{gen} = -1.70 V

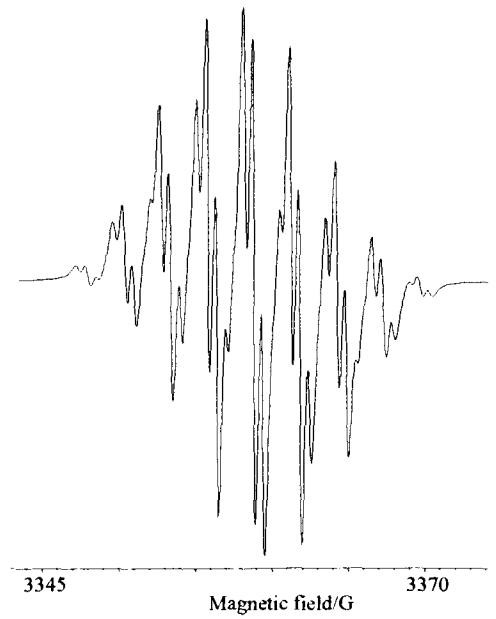

Fig. 4.21(b) Simulated EPR spectrum of $\mathbf{6a}^{-1}$ using the parameters given in table 4.5

Parameter	$\mathbf{6a}^{-1}$
a(H×2)	0.619
a(H×4)	2.392
a(N×2)	3.05
Δ	0.5
g	2.00955

Table 4.5 EPR coupling constants for $\mathbf{6a}^{1-}$ in 0.1 M $TBABF_4$/DMF at 293 K. All hyperfine coupling constants given in G. Δ = linewidth

The *in-situ* EPR spectroelectrochemistry of the corresponding [Ni(R_1R_2pipdt)(dmit)] complex, ($\mathbf{6c}^{1-}$) was studied at 233 K (fig. 4.22(a)) and this spectrum shows coupling to both the ring N atoms, four H atoms on the piperazine ring and a smaller coupling to two H atoms assigned as the unique H substituents on the Pr^i groups (table 4.6). In both cases, on introduction of another electron to the complex and formation of $\mathbf{6a}^{2-}$ and $\mathbf{6c}^{2-}$ respectively, the signal collapses as the second electron enters the same orbital as the first and they spin pair thus becoming diamagnetic.

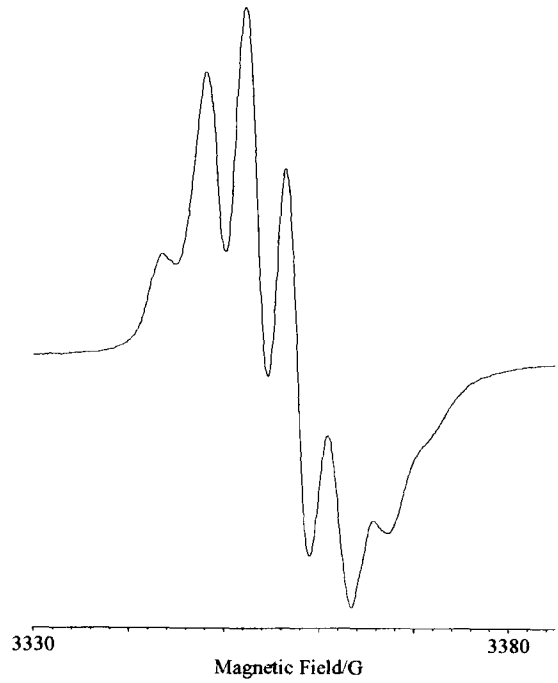

Fig. 4.22(a) EPR spectrum of $\mathbf{6c}^{-1}$ in solution of 0.1 M $TBABF_4$ in DMF at 233 K. E_{gen} = -1.00 V

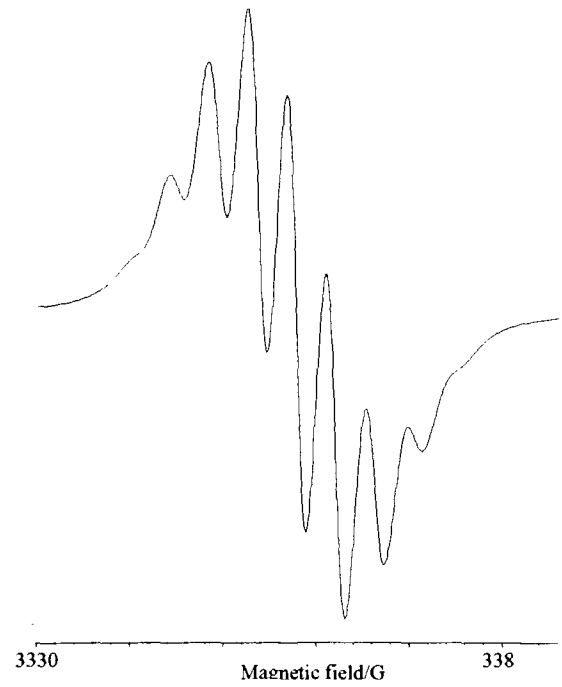

Fig. 4.22(b) Simulated EPR spectrum of $\mathbf{6c}^{-1}$ using the parameters given in table 4.6

Parameter	$\mathbf{6c^{-1}}$
a(H×2)	0.619
a(N×2)	4.206
a(H×4)	4.206
Δ	3.0
g	2.01015

Table 4.6 EPR coupling constants for $\mathbf{6c^{1-}}$ in 0.1 M $TBABF_4$/DMF at 233 K. All hyperfine coupling constants given in G. Δ = linewidth

In each case for a ligand, (**a**) and its corresponding [Ni(R_1R_2pipdt)(dmit)] complex, (**c**) it can be seen that the reduction electron couples to the ring N atoms, ring H atoms and the H atoms on the N-substituent. This suggests that for the [Ni(R_1R_2pipdt)(dmit)] complexes (**4c** and **6c**) the reduction electron locates itself primarily on the dithione ligand. In recent times studies undertaken on locating the position of the frontier orbitals in [Ni(dithione)(dithiolate)] complexes have been based on calculations which suggest that the LUMO is partly based on the dithione ligand. The results of this EPR study show that the first experimental measurements taken are consistent with the findings of these previous theoretical studies.[8, 10]

4.2.7 Thin film studies

Attempts were made to measure the conductive and photoconductive properties of films of **4c**, **5c** and **6c** with the intention to use these molecules as components in bulk-heterojunction solar cells. The work was carried out at Cambridge University by Dr. Neil Robertson and Dr. Neil Greenham.[12] The [Ni(R_1R_2pipdt)(dmit)] complexes were spin coated as a single component solution and in conjunction with a substituted poly(*p*-phenylenvinylene) derivative OC_1C_{10}-PPV, which has previously been used as a component of a bulk-heterojunction solar cell.[13] The [Ni(R_1R_2pipdt)(dmit)] and substituted PPV molecules have complementary electronic and optical properties which

make them suitable for use in a bulk-heterojunction solar cell. However the poor solubility of the [Ni(R_1R_2pipdt)(dmit)] complexes and low viscosity of the solutions makes them difficult to process for spin-coating purposes and films of poor quality prevented any significant results being obtained. It is the author's intent to continue work on these complexes to improve their solubility by attempting to synthesise a [Ni(R_1R_2pipdt)(dmit)] complex which is attached *via* the R substituent to a polymer backbone. It is hoped that this will make the [Ni(R_1R_2pipdt)(dmit)] complexes more suitable for the purpose of spin-coating processing.

4.3 Conclusions

The work reported in this chapter has broadened the experimentally derived knowledge currently available about the ligands and complexes of the family of [Ni(R_1R_2pipdt)(dmit)]. In the past, much of the analysis which has been performed on these complexes has been theoretical in nature and the EPR study in this chapter lends a new dimension to this work. The experimental evidence comfirms previous theoretical suggestions that the LUMO in such complexes, resides at least in part, on the pipdt ligand. The ultimate aim of this work was to use a [Ni(II)(dithione)(dithiolate)] complex in a solid state Donor-Acceptor cell. Although at the time of writing this aim has not been realised, there is evidence to suggest that pursuit of the synthesis of a more complex [Ni(R_1R_2pipdt)(dmit)] dye which would incorporate a potentially polymerisable R group would be an interesting step for future work. This may assist in the possibililty of spin coating the Ni complex and make it easier to process. Although it has not been possible to assess the properties of these [Ni(R_1R_2pipdt)(dmit)] dyes in a Donor-Acceptor cell, they still retain many desirable characteristics (large ε, NIR absorbance, good redox potentials) which make them suitable for use in these cells if they become easier to process in the future .

4.4 Experimental

4.4.1 Raman spectroscopy

Raman spectra were carried out at the Università di Cagliari by Prof. M. L. Mercuri. Spectra were taken at room temperature on a single crystal by using a Raman microscope (BX 40, Olimpus) spectrometer (ISA xy 800) equipped with an Ar^+ laser (λ=514.15 nm). A 180° reflective geometry was adopted. The samples were mounted on a glass microscope slide and the scattering peaks were calibrated against a Si standard (λ=520 cm^{-1}). A typical spectrum was collected with a 300 s time constant at a 1 cm^{-1} resolution and was averaged over 2 scans. No sample decomposition was observed during the experiments.

4.4.2 Synthesis

All chemicals were used as supplied by Sigma-Aldrich. **5a** and **6a** were used as supplied by Marco Salidu at the Università di Cagliari. $[TBA]_2[Ni(dmit)_2]$ was synthesised by a previously published method.[3]

Bz_2pipdt (1,4-dibenzyl-piperazine-2,3-dithione) (4a)

Bz_2pipdt was synthesised as previously reported.[9] The synthesis departed from that of the original synthesis for the conversion of the diketone product to the dithione. Lawessons reagent was used for this conversion as previously described for a related ligand.[14] Yield 51.0 %. MS (FABMS) *m/z*: 327 (M^+). Anal calcd for $C_{18}H_{18}N_2S_2$: C, 66.2; H, 5.6; N, 8.6. Found C, 66.7; H, 6.1; N, 9.3.

$[Ni(Bz_2pipdt)_2][BF_4]_2$ (4b)

$[Ni(Bz_2pipdt)_2][BF_4]_2$ was synthesised by a similar method to that previously reported for Pt analogues of the complex.[15] $NiCl_2.6(H_2O)$ (0.2 g, 0.84 mmol) was dissolved in *ca.* 50 mL EtOH and **4a** (0.55 g, 1.68 mmol) was dissolved in 50 mL DCM and the two solutions were added together and stirred at RT for 30 mins. The solvent was removed and the crude product was dissolved in EtOH before filtering to remove excess ligand.

$NaBF_4$ (0.184 g, 1.68 mmol) was added as a solid to the solution and the mixture was stirred at RT until a solid product fell out. The product, **4b**, was recrystallised by dropwise addition of diethyl ether to a hot solution of **4b** in MeCN. Yield 57.4 % MS (FABMS) *m/z*: 797 ($[\{Ni(Bz_2pipdt)_2\}(BF_4)]^+$). Anal calcd for $C_{36}H_{36}N_4S_4B_2F_8Ni$: C, 48.8; H, 4.1; N, 6.3. Found C, 48.6; H, 4.1; N, 6.2.

[Ni(Bz$_2$pipdt)(dmit)] (4c)

[Ni(Bz$_2$pipdt)(dmit)], **(4c)** was synthesised using a previously reported method.[10] Yield 92.0 % MS (FABMS) *m/z*: 581 (M^+). Anal calcd for $C_{21}H_{18}N_2S_7Ni$: C, 43.4; H, 3.1; N, 4.8. Found C, 43.6; H, 1.6; N, 4.7.

[Ni(MeBzpipdt)$_2$][BF$_4$]$_2$ (5b)

5b was synthesised in the same manner as **4b**. Yield 54.6 %. MS (FABMS) *m/z*: 645 ($[\{Ni(MeBzpipdt)_2\}(BF_4)]^+$). Anal calcd for $C_{24}H_{28}N_4S_4B_2F_8Ni$: C, 39.3; H, 3.85; N, 7.6. Found C, 34.8; H, 3.4; N, 6.4.

[Ni(MeBzpipdt)(dmit)] (5c)

5c was synthesised in the same manner as **4c**. Yield 55.1 %. MS (FABMS) *m/z*: 504 (M^+). Anal calcd for $C_{15}H_{14}N_2S_7Ni$: C, 35.65; H, 2.8; N, 5.5. Found C, 35.8; H, 2.9; N, 5.5.

[Ni(Pr^{i}pipdt)$_2$][BF$_4$]$_2$ (6b)

6b was synthesised in the same manner as **4b**. MS (FABMS) *m/z*: 259 ($[Ni(Pr^ipipdt)_2]^{2+}$), 605 ($[\{Ni(Pr^ipipdt)_2\}(BF_4)]^+$). Yield 66.0 %. Anal calcd for $C_{20}H_{36}N_4S_4B_2F_8Ni$: C, 34.7; H, 5.2; N, 8.1. Found C, 34.5; H, 5.2; N, 7.7.

[Ni(Pr^{i}pipdt)(dmit)] (6c)

6c was synthesised in the same manner as **4c**. Yield 71.4 %. MS (FABMS) *m/z*: 484 (M^+).Anal calcd for $C_{13}H_{18}N_2S_7Ni$: C, 32.2; H, 3.7; N, 5.8. Found C, 32.3; H, 3.65; N, 5.3.

4.4.3 X-Ray Crystallography

Green lath-like needles of **4c** (dimensions 0.58 × 0.19 × 0.07 mm^3) were grown by slow diffusion of diethyl ether into a saturated solution of **4c** in DMF. Single crystal X-ray diffraction data were collected using Mo-Kα radiation on a Smart APEX CCD diffractometer equipped with an Oxford Cryosystems low-temperature device operating at 150 K. An absorption correction was applied using the multi-scan procedure SADABS. The structure was solved by Patterson methods (DIRDIF) and refined by full-matrix least squares against $|F|^2$ using all data (SHELXL-97). The molecule lies with its long axis in a crystallographic mirror plane. C42/C52 are disordered about the mirror, with occupancies both equal to 0.5. N-C and C-C were lightly restrained to 1.45 and 1.52 Å. The part-weight atoms were refined with isotropic displacement parameters, all other non-H atoms were refined with anisotropic displacement parameters. H-atoms were placed in idealized positions. Crystal, data collection and refinement parameters are summarised in Table 4.7. The crystal structure was solved by Stephen Moggach and Dr. Simon Parsons.

Chemical Formula	$C_{21}H_{18}N_2S_7Ni$
Fw	581.5
T, K	150
Lattice type	Orthorhombic
Space group	*P n m a*
a, Å	19.1586(6)
b, Å	19.5819(5)
c, Å	6.1048(2)
V, $Å^3$	2290.29(12)
No. reflections for cell	7912
$\theta_{max}(°)$	28.75
Z	4
D_c, Mg m^{-3}	1.686

μ, mm^{-1}	1.500
Reflections collected	25384
Unique [R_{int}]	2941 [0.0376]
No. $I > 2\sigma$	2487
T_{min}/T_{max}	0.684/0.900
Parameters	144
R_1 [$F>4\sigma(F)$]	0.0298
wR	0.0758
S	1.046
$\Delta\rho_{max}$ / $eÅ^{-3}$	0.50
$\Delta\rho_{min}$ / $eÅ^{-3}$	-0.55

Table 4.7 Crystallographic data for **4c**

4.4.4 Thin film studies

Spin-coating experiments were carried out on a glass substrate using solutions of **4c**, **5c** and **6c** in DMF or DMSO (concentration of 10 mg/mL), however no continuous films could be prepared. In another experiment, solutions of **4c**, **5c** and **6c** in DMF (10 mg/mL), were mixed with OC_1C_{10}-PPV (5 mg/mL) in chlorobenzene in a 1:1 and 1:2 (v:v) ratio and spin coating was then attempted. Non-continuous films of poor quality were achieved and there was evidence of some aggregation of the Ni complexes.

4.5 References

1 U. T. Mueller-Westerhoff and B. Vance, *Comp. Coord. Chem.*, 1987, 595.

2 N. Robertson and L. Cronin, *Coord. Chem. Rev.*, 2002, **227**, 93.

3 G. Steimecke, H. J. Sieler, R. Kirmse, and E. Hoyer, *Phosphorus, Sulfur Relat. Elem.*, 1979, 7, 49.

4 T. Akutagawa and T. Nakamura, *Coord. Chem. Rev.*, 2000, **198**, 297.

5 P. Cassoux, L. Valade, H. Kobayashi, A. Kobayashi, R. A. Clark, and A. E. Underhill, *Coord. Chem. Rev.*, 1991, **110**, 115.

6 F. Bigoli, C.-T. Chen, W.-C. Wu, P. Deplano, M. L. Mercuri, M. A. Pellinghelli, L. Pilia, G. Pintus, A. Serpe, and E. F. Trogu, *Chem. Commun.*, 2001, 2246.

7 F. Bigoli, P. Cassoux, P. Deplano, M. L. Mercuri, M. A. Pellinghelli, G. Pintus, A. Serpe, and E. F. Trogu, *Dalton Trans.*, 2000, 4639.

8 S. Curreli, P. Deplano, C. Faulmann, A. Ienco, C. Mealli, M. L. Mercuri, L. Pilia, G. Pintus, A. Serpe, and E. F. Trogu, *Inorg. Chem.*, 2004, **43**, 5069.

9 R. Isaksson, T. Liljefors, and J. Sandstroem, *J. Chem. Res., Synop.*, 1981, 43.

10 F. Bigoli, C. T. Chen, W. C. Wu, P. Deplano, M. L. Mercuri, M. A. Pellinghelli, L. Pilia, G. Pintus, A. Serpe, and E. F. Trogu, *Chem. Commun.*, 2001, 2246.

11 P. Deplano, *Unpublished work*, 2005.

12 N. Robertson and N. Greenham, *Cambridge University, unpublished work*, 2005.

13 B. Sun, H. J. Snaith, A. S. Dhoot, S. Westenhoff, and N. C. Greenham, *J. Appl. Phys.*, 2005, **97**, 014914/1.

14 M. A. Pellinghelli, J. M. Williams, E. F. Trogu, F. Bigoli, P. Deplano, F. A. Devillanova, J. R. Ferraro, V. Lippolis, P. J. Lukes, and M. L. Mercuri, *Inorg. Chem.*, 1997, **36**, 1218.

15 F. Bigoli, P. Deplano, M. L. Mercuri, M. A. Pellinghelli, L. Pilia, G. Pintus, A. Serpe, and E. F. Trogu, *Inorg. Chem.*, 2002, **41**, 5241.

Chapter 5

Complexes of 1,10-phenanthroline-5,6-dione

5. Introduction

Over the past two decades, there has been much investigation into the synthesis of multicomponent molecular systems that may have uses in several fields such as catalysis, molecular based devices, anti-cancer drugs[1] and light-to-chemical energy conversion systems[2, 3]. The metals involved in such systems (Pt/Pd/Ru) are of interest due to their photophysical and electrochemical properties, while the ligands involved show rich electrochemical activity[2, 4] and are crucial to the molecular architecture. An inherently important ligand investigated in this extensive work is 1,10-phenanthroline-5,6-dione, known as phendione.[5]

5.1 Phendione

Phendione (fig 5.1) has been investivated for many uses due to the numerous binding modes it can achieve. It has been known for many years[6, 7] and may bind as a diimine or catecholate and as previously mentioned has been used as a linker ligand linking two metal centres together.[2] Many mononuclear complexes of phendione have been studied where the ligand may bind through either the diimine or catecholate groups leaving the other side of the ligand unbound. The electrochemistry of complexes such as these with one metal centre has been studied by a number of groups and general trends in the electrochemistry include the shift of the reduction potential of the complex to more positive values on coordination of phendione to a metal centre.[8]

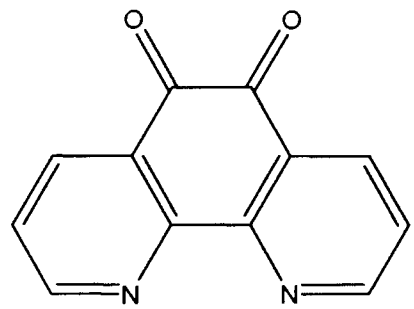

Fig. 5.1 Phendione

5.1.1 Bimetallic complexes of Phendione

In 1975, Balch reported the bichelating ability of phendione as both a diimine and a catelcholate[9] and in 1991, Pierpont reported the synthesis of a number of bimetallic complexes, using reduced phendione as a linker ligand to join both Pt/Ru centres and Pt/Pd centres.[10] The first and second oxidations of these bimetallic structures were shown to be based on the phendione ligand, stressing the significance of the linker ligand. Doherty and Eisenberg have more recently used phendione to create linear chain structures of two or more metal centres (reference [2] and references therein). Phendione bridged complexes can be synthesised by substitution of labile ligands on a metal centre with the diimine moiety of phendione followed by reaction with the dipyridocatecholate (reduced form of the quinone). Alternatively they can be formed by oxidative addition of the dipyriodcatecholate to a low valent metal centre followed by reaction of the diimine with a metal centre attached to two labile ligands.[9, 10] Eisenberg *et al.* have extensively studied these [Pt(II)(phendione)] complexes due to the structural similarity of the metal-catecholate unit to metal-dithiolates used in light-to-chemical energy conversion systems.[2]

5.1.2 Use of Phendione as an anchor ligand for DSSC dyes

A variety of anchor ligands used in DSSC have already been discussed in section 1.6. In this chapter studies performed on dyes with the phendione anchor group are described. It was decided to look at phendione as an alternative linker ligand in DSSC, in an effort to move away from traditional bpy or terpy linkers. There is only one previous literature report of a Ru DSSC dye which uses the phendione anchor ligand. Li *et al.* reported changes in both the IR and UV/visible spectra for phendione based Ru dyes on TiO_2 which supported binding of the dye to TiO_2 *via* the carbonyl groups. Evidence of dye binding *via* a monodentate carbonyl attachment to the TiO_2 was supported by a red shift in the MLCT band of the UV/visible spectrum and the C=O stretch shifting to shorter wavenumber in the IR spectrum.[11, 12] Binding of natural dyes through the C=O functionality is also known. Anthocyanines found in strongly coloured fruits and berries have been shown to bind to the surface of TiO_2 through the C=O group.[13] This chapter

describes preliminary studies made on the potential use of monometallic Pt and Pd complexes of phendione as sensitisers for DSSC. This is the first study of a Pt or Pd compound with the phendione anchor ligand for use in a DSSC.

5.2 Results and Discussion

5.2.1 Synthesis

[Pt(phendione)(mnt)], (7) was synthesised by Dr. Luca Pilia in a number of steps and each intermediate was isolated and analysed. Phendione was synthesised by a previously published method and reaction of this ligand with potassium tetrachloroplatinate gave [Pt(phendione)Cl_2].[14] This was subsequently reacted with the disodium salt of mnt and recrystallised to give the desired product [Pt(phendione)(mnt)], (7) (fig 5.2).

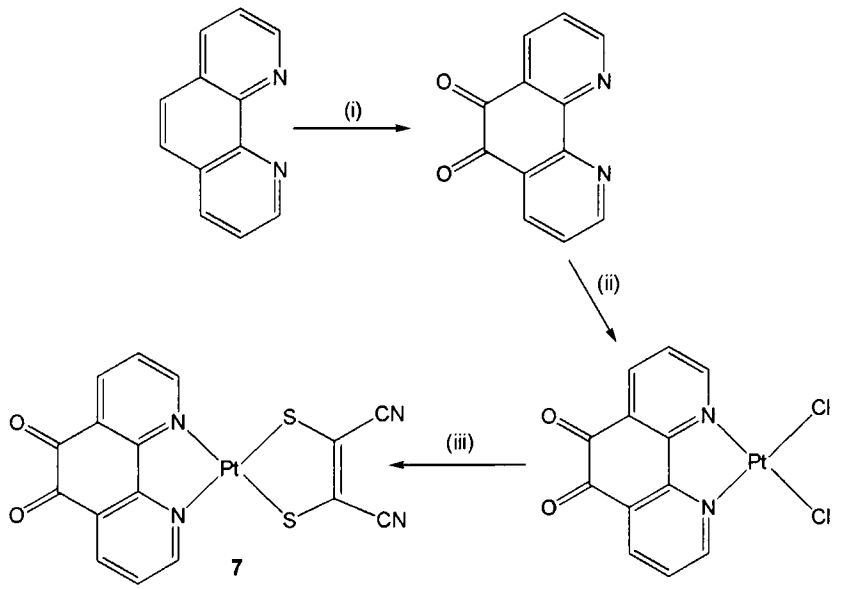

Fig. 5.2 Synthetic scheme for formation of [Pt(phendione)(mnt)], (7). (i) HNO_3, KBr (ii) K_2PtCl_4, H_2O reflux for 4 hours (iii) Na_2(mnt) in DMF

[Pd(phendione)(mnt)], (**8**) was also synthesised in a number of steps and each intermediate was isolated and analysed. [Pd(PhCN)$_2$Cl$_2$] was synthesised by a

previously published method[15] and following this, displacement of the labile coordinating solvent molecules by phendione resulted in the formation of [Pd(phendione)Cl_2].[9] Subsequent reaction of this product with the disodium salt of mnt led to the desired product [Pd(phendione)(mnt)], (**8**) (fig. 5.3). **8** is insoluble in all organic solvents except for DMSO where it is sparingly soluble.

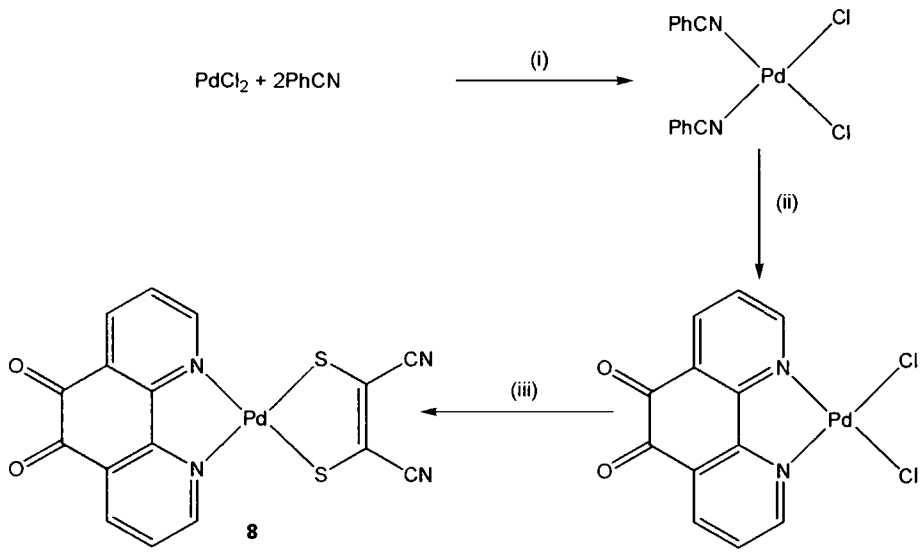

Fig. 5.3 Synthetic scheme for formation of [Pd(phendione)(mnt)], (**8**). (i) 100°C for 20 mins (ii) 1eq. Phendione ligand/DCM (iii) Na_2(mnt) in DMSO

5.2.2 Electrochemistry

The electrochemistry of the phendione ligand, [Pt(phendione)Cl_2] and [Pd(phendione)Cl_2] have previously been studied by Dr. Ken McNamara and will briefly be discussed here.[16] The free phendione ligand shows two reversible reductions which occur at -0.35 V and -1.24 V when measured in a solution of 0.1M $TBABF_4$ in DMF (fig. 5.4).

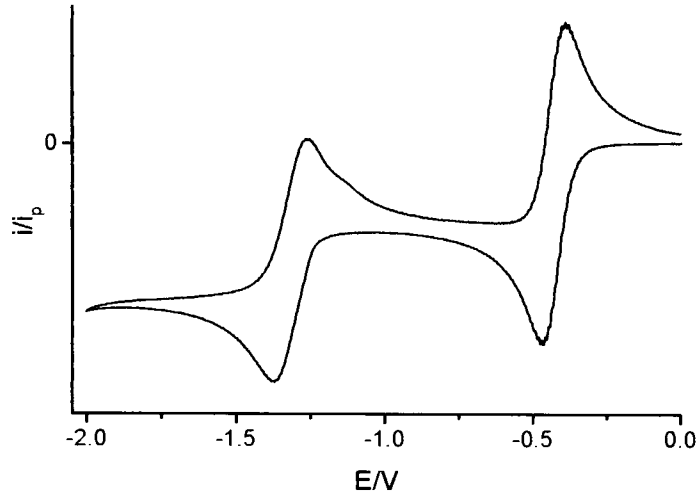

Fig. 5.4 Cyclic voltammogram of the phendione ligand in 0.1 M $TBABF_4$ in DMF at 293K. Scan rate 0.1 Vs^{-1}

The occurrence of two, one electron reductions has previously been confirmed by coulometry.[16] The addition of these two electrons results in the formation of the semiquinone and catecholate forms of phendione (fig. 5.5).

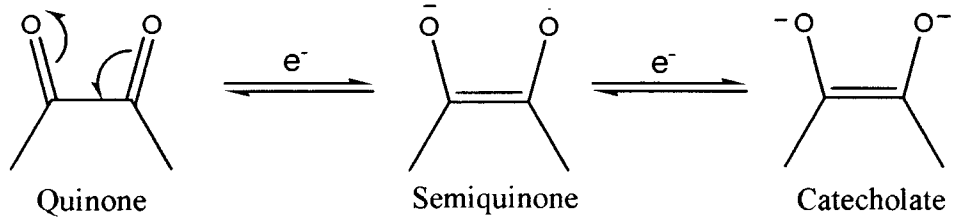

Fig. 5.5 The reduced forms of the quinone in phendione

On coordination of a metal centre to phendione, the reduction potential values seen in the free ligand are shifted to more positive potentials as previously observed.[8] [Pt(phendione)Cl_2] has two reversible reductions at -0.045 V and -0.79 V (fig 5.6).

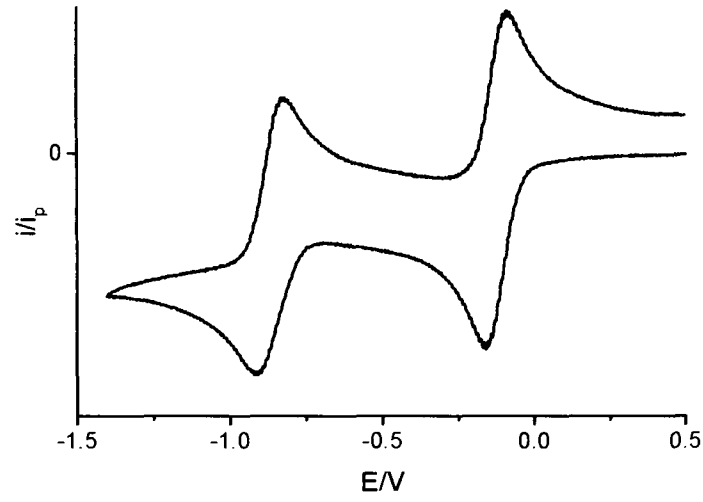

Fig. 5.6 Cyclic voltammogram of [Pt(phendione)Cl_2] in 0.1 M $TBABF_4$ in DMF at 293K. Scan rate 0.1 Vs^{-1}

The first reduction of [Pd(phendione)Cl_2] measured as -0.043 V in a solution of 0.1 M $TBABF_4$ in DMSO is fully reversible and the second reduction which occurs at -0.67 V is quasi reversible (fig. 5.7). At more negative potentials peaks probably associated with daughter products are observed, indicating that electron transfer is followed by rapid chemical reaction. The nature of the daughter products were not investigated further. The reductions are based largely on the ligand as confirmed by the EPR studies which are discussed later in this chapter. Previous studies performed at Edinburgh have shown that separation of the reduction processes in phendione complexes by approximately 0.7 V in indicates that the second reduction electron enters the same orbital as the first reduction electron.[16] This results in a spin paired, diamagnetic, doubly reduced, catecholate species. The results shown here suggest that this may also be the case for [Pt(phendione)Cl_2] and [Pd(phendione)Cl_2].

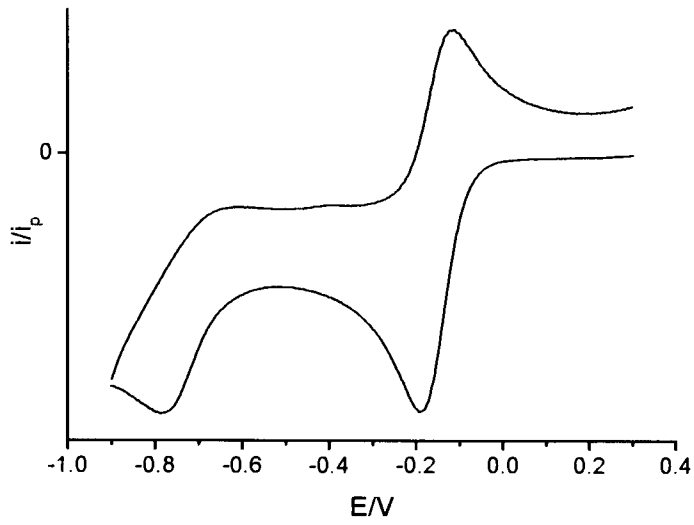

Fig. 5.7 Cyclic voltammogram of [Pd(phendione)Cl_2] in 0.1 M $TBABF_4$ in DMSO at 293K. Scan rate 0.1 Vs^{-1}

The electrochemistry of both **7** and **8** shows one reversible reduction, one quasi reversible reduction which are both associated with the phendione ligand and an irreversible oxidation associated with the mnt moiety. The reduction potentials of **7** and **8** are very similar to those of their respective precursors [Pt(phendione)Cl_2] and [Pd(phendione)Cl_2]. The electrochemistry of **7** in a solution of 0.1 M $TBABF_4$ in DMF shows a reversible reduction at -0.043 V and a quasireversible reduction at -0.79 V (fig. 5.8). An irreversible oxidation associated with mnt is observed at 1.39 V and this is similar to the oxidation potential seen for this ligand in the [Pt(II)(bpy)(mnt)] complexes reported in chapter 3 of this thesis.

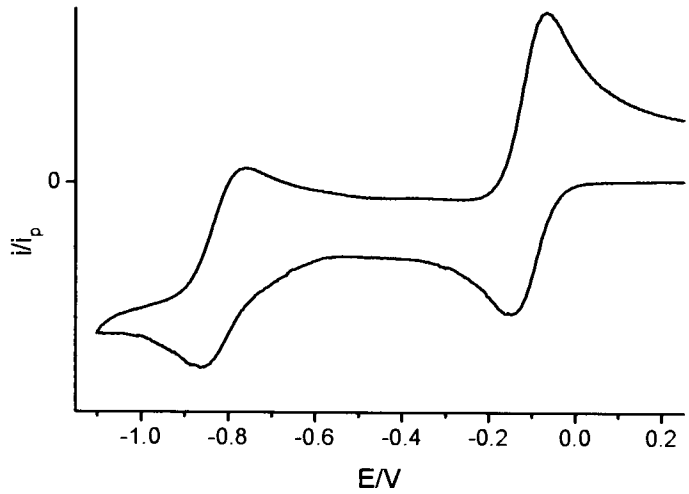

Fig. 5.8 Cyclic voltammogram of [Pt(phendione)(mnt)] (7), in 0.1 M $TBABF_4$ in DMF at 293K. Scan rate 0.1 Vs^{-1}

The electrochemistry of **8** in a solution of 0.1 M $TBABF_4$ in DMSO shows a reversible reduction at -0.035 V, a quasireversible reduction at -0.73 V (fig. 5.9) and an irreversible oxidation associated with mnt at 1.47 V.

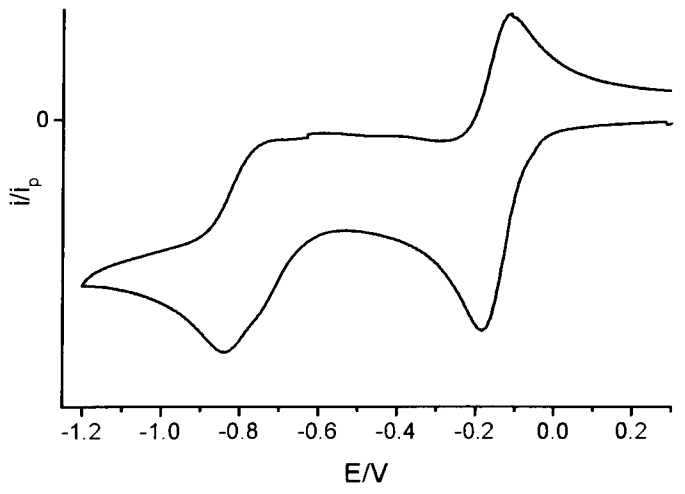

Fig. 5.9 Cyclic voltammogram of [Pd(phendione)(mnt)] (**8**), in 0.1 M $TBABF_4$ in DMSO at 293K. Scan rate 0.1 Vs^{-1}

As the oxidation of both the Pt and Pd complexes occur at very similar potentials, the HOMO may be tentatively assigned to be located at least in part on the mnt motif. [Pt(phendione)(mnt)] and [Pd(phendione)(mnt)] are similar in structure to the [Pt(II)(bpy)(mnt)] complexes described in chapter 3 of this thesis. In this type of [Pt(II)(diimine)(dithiolate)] complex the HOMO has previously been shown to be located on the dithiolate and using this analogy, the HOMO may also be tentatively assigned as dithiolate based in **7** and **8**. In the case of [Pt(bpy)(mnt)], substitution of the chloride ligands by mnt has little if any effect on the LUMO, hence the reduction potentials stay the same. This is analogous to the situation with **7** and **8** where replacing the chloride ligands of the precursor molecules with mnt has little effect on the reduction potentials, therefore the LUMO may be assigned as being located primarily on the derivatised phendione ligand.

Compound	E_1/V	E_2/V	E_3/V
phendione	-1.24	-0.35	-
[Pt(phendione)Cl_2]	-0.79	-0.045	-
[Pt(phendione)(mnt)] (7)	-0.79[§]	-0.043	1.39[*]
[Pd(phendione)Cl_2]	-0.67[§]	-0.043	-
[Pd(phendione)(mnt)] (**8**)	-0.73[§]	-0.035	1.47[*]

Table 5.1 Redox potentials, $E_{1/2}$, of phendione complexes. [§]Quasi reversible and [*]irreversible processes, E_p.

5.2.3 UV/visible Spectroscopy and UV/Vis/NIR Spectroelectrochemistry

The UV/visible spectrum of **7** shows an intense transition at 313 nm which is assigned as the π-π^* intraligand transition of the phendione ligand. The absorption at 392 nm is assigned as an mnt based intraligand transition since this peak appears in the spectrum of the disodium salt of mnt in DMF. The visible band with an absorption maximum at 476 nm has a molar extinction coefficient of 4060 M^{-1} cm^{-1} and is tentatively assigned as a Mixed Metal-Ligand-to-Ligand (MMLL') charge transfer band from the Pt/mnt to phendione (fig. 5.10).

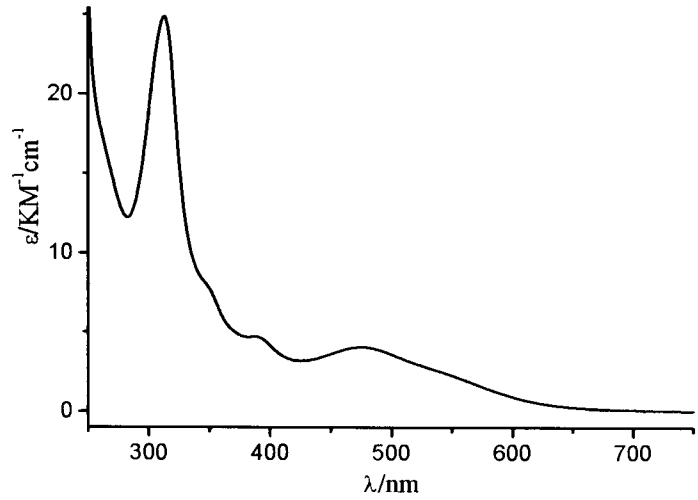

Fig. 5.10 UV/visible spectrum of [Pt(phendione)(mnt)] (7), in DMSO

The UV/visible spectrum of **8,** (fig. 5.11) shows an intense transition at 295 nm which is assigned as the π-π^* intraligand transition of the phendione ligand. The absorption at 390 nm is assigned as an mnt based intraligand transition as previously discussed for 7. A weak shoulder from *ca.* 420 nm to 460 nm is tentatively assigned as a MMLL′ charge transfer band from the Pd/mnt to phendione.

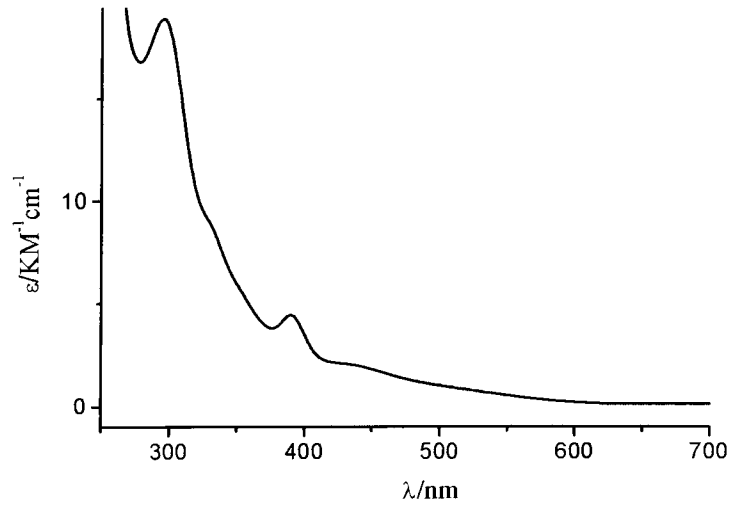

Fig. 5.11 UV/visible spectrum of [Pd(phendione)(mnt)] (**8**), in DMSO

The UV/Vis/NIR spectroelectrochemistry of **7** and **8** was attempted in order to follow the generation of redox active species *via* UV/visible spectroscopy. Unfortunately it was not possible to generate and monitor the redox active species since application of a potential to the solution did not result in any changes in the UV/visible spectra. This is not what was expected since earlier studies on [Pt(phendione)Cl_2] and [Pd(phendione)Cl_2] in their neutral, monoreduced and direduced states showed different spectra. It is likely that the redox products formed were unstable at 293 K.

5.2.4 *In-Situ* EPR Spectroelectrochemistry

The *in-situ* EPR spectra of $\mathbf{7}^{-1}$ and $\mathbf{8}^{-1}$ were recorded in a solution of 0.2 M $TBABF_4$ in DMSO at 293 K. A numbering scheme for the hydrogen atoms on the phendione ligand is shown in figure 5.12. The hydrogen atom positions (and their corresponding coupling constant values) in **7** and **8** were assigned relative to their corresponding precursor molecules [Pt(phendione)Cl_2] and [Pd(phendione)Cl_2] and the free phendione ligand which have previously been studied. These assignments were originally made on the basis of *ab-initio* calculations.[16]

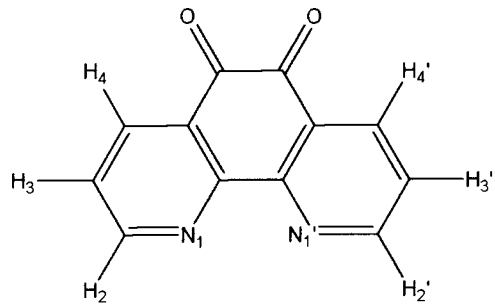

Fig. 5.12 The numbering scheme on the phendione ligand

The EPR spectrum of $\mathbf{7}^{-1}$ (fig. 5.13) shows coupling of the unpaired electron to three pairs of equivalent hydrogens (H_2H_2', H_3H_3', H_4H_4'), the two equivalent nitrogens and the platinum nuclei. EHMO calculations suggest that coupling to H_2 and H_4 is significantly greater than coupling to H_3[16] and are so assigned in table 5.2. The g value for this compound is close to that of a free electron since most of the electron density resides on

the ligand. The coupling constants for each of the nuclei are small when compared with those found for the [Pt(II)(bpy)(mnt)] complexes described in chapter 3. This may be because, in 7^{-1} and 8^{-1} the electron density is mainly localised on the EPR silent oxygen and carbon nuclei of the carbonyl moieties. Previous work on *ab-initio* calculations of the phendione ligand suggested that the reduction electron enters an orbital primarily based (*ca.* 70 %) on the C=O fragments of the phendione.[16] Therefore it may be expected that the reduced species 7^{-1} will show a minimal interaction between the reduction electron and the metal centre. This confirms that the site of reduction of these complexes is primarily based on the phendione ligand and mainly on the carbonyl substituents.

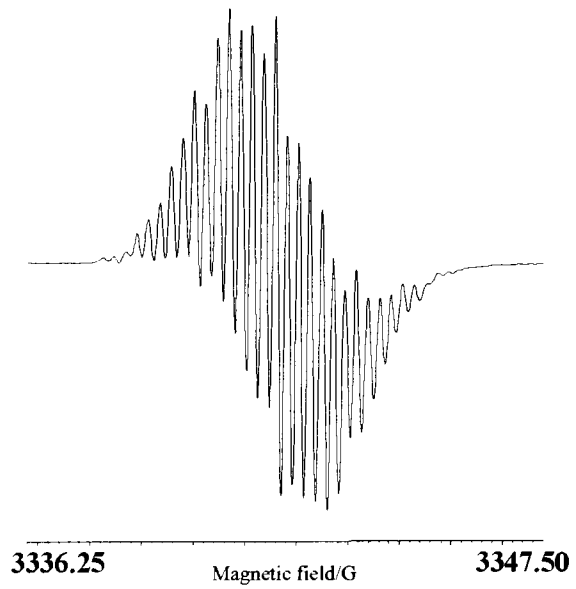

Fig. 5.13 EPR spectrum of 7^{-1} in solution of 0.2 M $TBABF_4$ in DMSO at 293 K. E_{gen} = -0.50 V

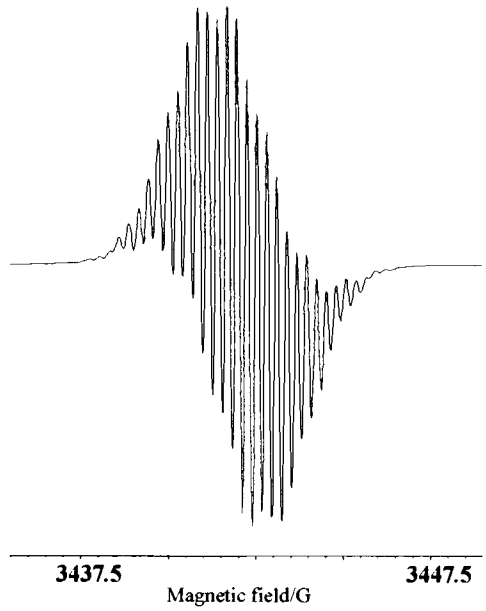

Fig. 5.14 Simulated EPR spectrum of 7^{-1} using parameters given in table 5.2

Parameter	$[phendione]^{-1}$ *	$[Pt(phendione)Cl_2]^{-1}$ *	$[Pt(phendione)(mnt)]^{-1}$
$a(H_2\times2)$	1.124	0.747	0.835
$a(H_3\times2)$	0.165	0.233	0.278
$a(H_4\times2)$	1.526	1.100	1.126
$a(N_1\times2)$	0.567	0.520	0.563
a(Pt)	-	1.700	1.683
Δ	0.14	0.15	0.20
g	2.0039	2.0053	2.0042

Table 5.2 EPR data for reduced phendione and its Pt complexes in solution of 0.2 M $TBABF_4$ in DMSO at 293 K. All hyperfine coupling constants given in G. Δ = linewidth. *Results as reported in reference 14

For $\mathbf{8}^{-1}$, it can be seen from table 5.3 that coupling to H_2 and H_4 is significantly greater than coupling to H_3 and this reflects a similar coupling in the analogous Pt compound. The EPR spectrum of $\mathbf{8}^{-1}$ (fig. 5.15) shows coupling to the three pairs of equivalent hydrogens (*c.f.* 7) and the ring nitrogens, however in this case the spectrum may be simulated with no coupling of the reduction electron to the Pd centre. The g value for this compound is close to that of a free electron since most of the electron density resides on the ligand as was the case for 7^{-1}. Again here it may be postulated that in the reduced state the electron density is mainly localised on the EPR silent carbonyl motifs.

Parameter	$[phendione]^{-1}$ *	$[Pd(phendione)Cl_2]^{-1}$ *	$[Pd(phendione)(mnt)]^{-1}$
$a(H_2\times2)$	1.124	0.751	0.798
$a(H_3\times2)$	0.165	0.242	0.223
$a(H_4\times2)$	1.526	1.109	1.151
$a(N_1\times2)$	0.567	0.551	0.569
a(Pd)	-	0.2	0
Δ	0.14	0.18	0.22
g	2.0039	2.0060	2.004302

Table 5.3 EPR data for reduced phendione and its Pd complexes in solution of 0.2 M $TBABF_4$ in DMSO at 293 K. All hyperfine coupling constants given in G. Δ = linewidth. *Results as reported in reference 14

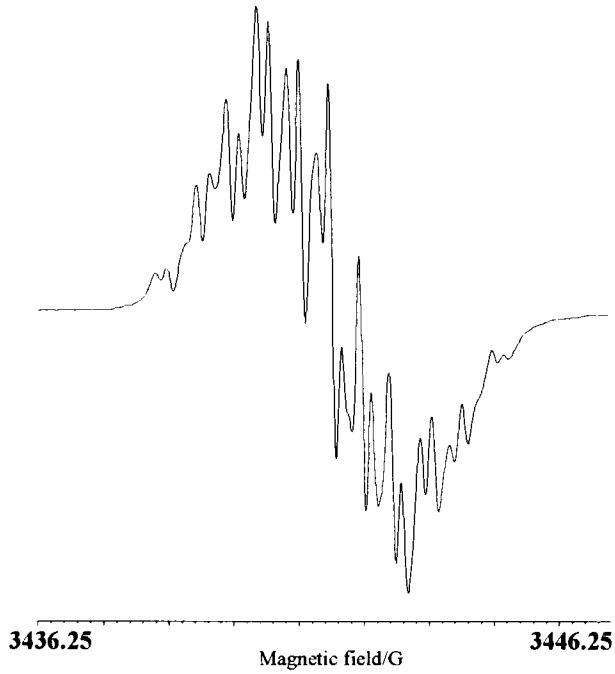

Fig. 5.15 EPR spectrum of $\mathbf{8}^{-1}$ in solution of 0.2 M $TBABF_4$ in DMSO at 293 K. E_{gen} = -0.50 V

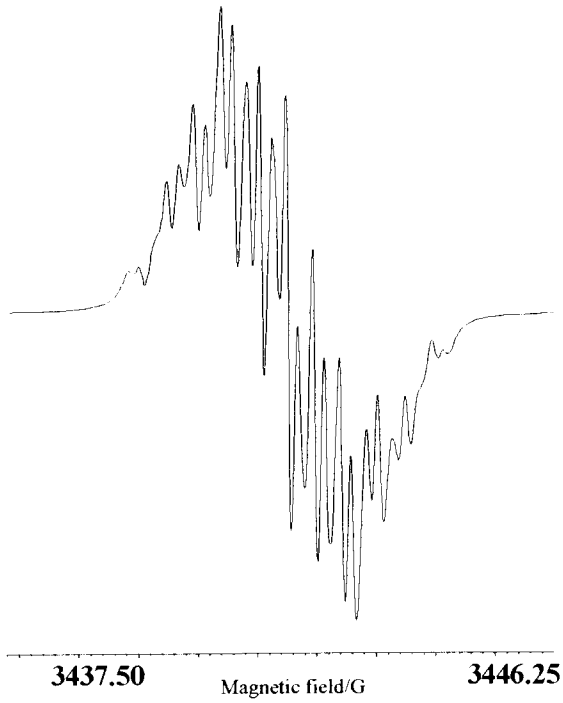

Fig. 5.16 Simulated EPR spectrum of $\mathbf{8}^{-1}$ using parameters given in table 5.3

On comparison of 7^{-1} and 8^{-1} and $[M(phendione)Cl_2]^{-1}$ (M = Pt or Pd) and $(phendione)^{-1}$, which have previously been studied,[16] the spectra show some significant similarities between the related species. The EPR spectra of both 7^{-1} (fig. 5.13) and 8^{-1} (fig. 5.15) are almost identical to the spectra of their respective precursors $[Pt(phendione)Cl_2]^{-1}$ and $[Pd(phendione)Cl_2]^{-1}$. The spectra of these complexes in turn share many common features with that of $(phendione)^{-1}$. Coupling constants for these precursors are shown in tables 5.2 and 5.3. These imply that in the reduced state for 7^{-1} and 8^{-1} the reduction electron resides in the phendione ligand and mainly on the carbonyl groups. This again confirms the LUMO of these complexes to be phendione based as seen for the electrochemistry.

The g values for the monoreduced metal mnt complexes are both greater than that of uncoordinated phendione. This shows that a small but significant spin density is located on the metal centre. However the g values are not dissimilar to those of their respective dichloro analogues. This is also expected since the substitution of chloride ligands by mnt has a negligible effect on the site of reduction i.e. the phendione ligand, as previously discussed for the electrochemistry.

5.2.5 Use as sensitisers for DSSC

It can be seen from the electrochemistry of 7 and **8** that in theory the first reduction potential in both compounds is too positive for them to be used in the current DSSC setup. In general, complexes with a reduction potential less negative than *ca.* -0.6 V are unlikely to be high enough in potential above the conduction band of TiO_2 to efficiently inject electrons into the conduction band. However, binding of phendione complexes to TiO_2 is expected to occur through the quinone oxygens, thereby perhaps inducing changes to the electronic nature of the complexes and indirectly influencing the reduction potential of the complexes when attached to a solid support. It was therefore decided to attempt to attach 7 to the surface of TiO_2 and the TiO_2 was sensitised as described in section 3.2.6 in a saturated solution of the dye in DMSO (5 mg/5 mL). After 22 hours a significant colour change was observed in the TiO_2 as the dye adsorbed

on to the surface. Analysis of the UV/visible spectrum for this 7 on TiO_2 slide showed no significant shift in the position of the λ_{max} of the dye attached to the solid support compared to λ_{max} in solution. In addition to this, solid state electrochemical studies of a film of dye coated TiO_2 showed the first reduction potential of the bound 7 to be identical to its value in solution. In light of these results, it was decided not to carry on with testing these dye molecules as solar cell sensitisers.

5.3 Conclusions

The work done in this chapter builds on previous knowledge from within the field. Electrochemical studies show that substitution of the two chloride ligands in [Pt(phendione)Cl_2] and [Pd(phendione)Cl_2] with mnt does not have any significant effect on the reduction potentials of the compounds, thus confirming the LUMO to be phendione based. This result is further confirmed by the EPR studies which demonstrate 7^{-1} and $\mathbf{8}^{-1}$ to have a very similar spectrum to both $[M(phendione)Cl_2]^{-1}$ and $(phendione)^{\cdot -1}$. Unfortunately we were unable to use 7 as a solar cell sensitiser since it appears that the first reduction potential of the dye is not negative enough to inject electrons into the conduction band of TiO_2. Attempts to study the differences in photophysical and electrochemical properties of the dyes in the solid state showed there to be no significant difference between the molecules in solution or on the solid TiO_2 matrix.

5.4 Experimental

5.4.1 Synthesis

1,10-phenanthroline-5,6-dithione

1,10-phenanthroline-5,6-dione was synthesised by Dr. Luca Pilia of the Università di Cagliari by a previously published method.[14]

[Pt(phendione)Cl_2]

[Pt(phendione)Cl_2] was synthesised by Dr. Luca Pilia of the Università di Cagliari by a previously published method.[14]

[Pt(phendione)(mnt)] (7)

7 was synthesised by Dr. Luca Pilia of the Università di Cagliari by the following method. [Pt(phendione)Cl_2] (0.1 g, 0.21 mmol) was dissolved in warm DMF (30 ml) and Na_2(mnt) (0.047 g, 0.25 mmol) in methanol (10 ml) was added to it. The reaction was allowed to stir for 30 minutes after which the solvent was removed and the crude product was recrystallised from warm DMF. Yield 35.3 %. MS (FABMS) *m/z*: 546 (M^+). IR (KBr, cm^{-1}): 1696 (s) (C=O stretch), 2207 (s) (C≡N stretch). Anal. calcd for $C_{16}H_6N_4O_2PtS_2$: C, 35.2; H, 1.1; N, 10.3. Found C, 35.2; H, 1.6; N, 10.0

[Pd(phendione)Cl_2]

[Pd(phendione)Cl_2] was synthesised by a previously published method.[9] Yield 79.2 %. Anal calcd for $C_{12}H_6N_2O_2PdCl_2$: C, 37.2; H, 1.6; N, 7.2. Found C, 36.7; H, 1.6; N, 6.8

[Pd(phendione)(mnt)] (8)

[Pd(phendione)Cl_2], (0.1 g, 0.26 mmol) was dissolved in DMSO (200 ml) at room temperature and Na_2(mnt) (0.058 g, 0.31 mmol) in a solution of MeOH was added to this. The reaction was stirred for 90 mins at room temperature. The solvent was subsequently removed and the crude product was washed with MeOH and ether. Yield

29.9%. MS (Negative electrospray) *m/z*: 456.6 (M^+). IR (KBr, cm^{-1}): 1699 (s) (C=O stretch), 2205 (s) (C≡N stretch). Anal calcd for $C_{16}H_6N_4O_4PdS_2$: C, 42.1; H, 1.3; N, 12.3. Found C, 40.0; H, 1.75; N, 11.5

[Ni(phendione)Cl_2]

Attempts to synthesise this compound in a similar manner to that of [Pt(phendione)Cl_2] proved unsuccessful. A green insoluble material formed on each occasion.

5.4.2 Studies of 7 on TiO_2

Immersion of nanocrystalline TiO_2 in a solution of 7, (5 mg/5 mL) in DMSO for 22 h at RT resulted in a significant colouration of the film. UV/visible spectra were taken using an uncoloured TiO_2 slide as a blank reference. Solid state electrochemistry was performed by first coating the surface of the working electrode in TiO_2. The working electrode was dipped in a suspension of TiO_2 particles in aqueous solution and then dried with a heat gun. This process was repeated four times to ensure the working electrode was uniformly coated. The working electrode was suspended in a solution of the dye (5 mg/5 mL) in DMSO for 22 h at RT and was rinsed in DMSO before carrying out the cyclic voltammetry. Electrochemical studies were carried out as normal using 0.1 M TBABF4 in DMF as the electrolyte and a scan rate of 20 mVs^{-1} was used.

5.5 Refererences

1 J.-Z. Wu, H. Li, J.-G. Zhang, and J.-H. Xu, *Inorg. Chem. Commun.*, 2002, **5**, 71.

2 W. Paw and R. Eisenberg, *Inorg. Chem.*, 1997, **36**, 2287.

3 W. Paw, S. D. Cummings, M. A. Mansour, W. B. Connick, D. K. Geiger, and R. Eisenberg, *Coord. Chem. Rev.*, 1998, **171**, 125.

4 C. A. Goss and H. D. Abruna, *Inorg. Chem.*, 1985, **24**, 4263.

5 A. D. Shukla and A. Das, *Polyhedron*, 2000, **19**, 2605.

6 G. F. Smith and F. W. Cagle, Jr., *J. Org. Chem.*, 1947, **12**, 781.

7 J. E. Dickeson and L. A. Summers, *Aust. J. Chem.*, 1970, **23**, 1023.

8 M. Shi and F. C. Anson, *Anal. Chem.*, 1998, **70**, 1489.

9 A. Y. Girgis, Y. S. Sohn, and A. L. Balch, *Inorg. Chem.*, 1975, **14**, 2327.

10 G. A. Fox, S. Bhattacharya, and C. G. Pierpont, *Inorg. Chem.*, 1991, **30**, 2895.

11 Z. Xiao, M. Li, M. Xu, and Z. Lu, *J. Phys. Chem. Solids*, 1998, **59**, 911.

12 M. Li, Z. Xiao, Z. Huan, and Z. Lu, *Appl. Surf. Sci.*, 1998, **125**, 217.

13 A. S. Polo, M. K. Itokazu, and N. Y. Murakami Iha, *Coord. Chem. Rev.*, 2004, **248**, 1343.

14 R. C. Conrad and J. V. Rund, *Inorg. Chem.*, 1972, **11**, 129.

15 J. R. Doyle, P. E. Slade, and H. B. Jonassen, *Inorg. Synth.*, 1960, **6**, 216.

16 K. McNamara, *University of Edinburgh, Unpublished Work*, 2003.

Chapter 6

[Pt{5,5′-$(CO_2H)_2$bpy}(tdt)] – Study of a long λ dye

6. Introduction

The aim of this chapter is to assess the properties of two 5,5'-disubstituted Pt complexes as solar cell dyes. These molecules are [Pt{5,5'-$(CO_2H)_2$bpy}(tdt)] (**9**), where tdt = 3,4-toluenedithiolate and its related salt $[TBA]_2$[Pt{5,5'-$(CO_2)_2$bpy}(tdt)] (**10**). The performance of these two molecules as solar cell dyes is assessed relative to a similar dye, [Pt{4,4'-$(CO_2H)_2$bpy}(tdt)], which has been reported previously. 5,5'-disubstituted bipyridines have previously been investigated in Ru systems for use as sensitisers in solar cells and [Ru{5,5'-$(CO_2H)_2$bpy}$_2$ $(X)_2$], (where $X=Cl^-$, CN^- and SCN^-) have been synthesised and used in solar cells and compared with the previously synthesised 4,4'-analogues.[1] The 5,5'-disubstituted compounds showed an enhanced spectral response at lower photon energies, however they were less efficient as solar cell sensitisers than the 4,4' analogues. Prior to the work reported in this thesis, studies on [Pt(II)(diimine)(dithiolate)] solar cell sensitisers were limited to complexes with {4,4'-$(CO_2H)_2$bpy}.[2,3]

By placing electron withdrawing groups at the 5,5' positions of the bpy group, the aim was to lower the LUMO energy (as previously described in section 3.1) and investigate the resulting effect on the optical and electrochemical properties of a Pt dye. 3,4-toluenedithiolate was chosen as the dithiolate since in the previous study of Pt 4,4'-disubstituted dyes, a selection of dithiolates were studied in order to tune the dye properties. Tdt had the least positive oxidation potential (corresponding to the highest HOMO energy) of the dithiolates studied, which in turn led to the longest absorption wavelength.[3] In this chapter, the performances of **9** and **10** as used in a DSSC will be assessed. As discussed in chapter one of this thesis, the majority of dyes currently in use are short wavelength dyes, hence the synthesis of a Pt dye which absorbs at longer wavelengths is desirable.

6.1 Results and Discussion

6.1.1 Synthesis and Structure

[Pt{5,5'-$(CO_2H)_2$bpy}(tdt)], (**9**) was synthesised by a route analogous to [Pt{4,4'-$(CO_2H)_2$bpy}(tdt)], which was previously reported.[3] {5,5'-$(CO_2H)_2$bpy} was synthesised by oxidation of the 5,5'-dimethyl-substituted bpy starting material.[4] Reaction of {5,5'-$(CO_2H)_2$bpy} with potassium tetrachloroplatinate gave the platinum dichloro derivative which was further reacted with toluene-3,4-dithiol to give the desired product **9**. **9** was purified using a size exclusion chromatography gel, Sephadex LH-20. When loading the column it was necessary to dissolve **9** in the minimum amount of KOH in order to load a tight band on the column. This ensured that on eluting the resulting fractions, the pure purple band had a significantly different retention time from other fractions coming off the column. The tetrabutylammonium salt, $[TBA]_2$[Pt{5,5'-$(CO_2)_2$bpy}(tdt)] (**10**), was made by reaction of a basic solution of the purified **9** with an aqueous solution of tetrabutylammoniumbromide (fig.6.1). **10** was synthesised to facilitate dissolution of the compound, since it is soluble in a range of organic solvents including methanol, ethanol, dichloromethane, acetonitrile and DMF. The neutral compound, **9** was found to be soluble only in DMSO.

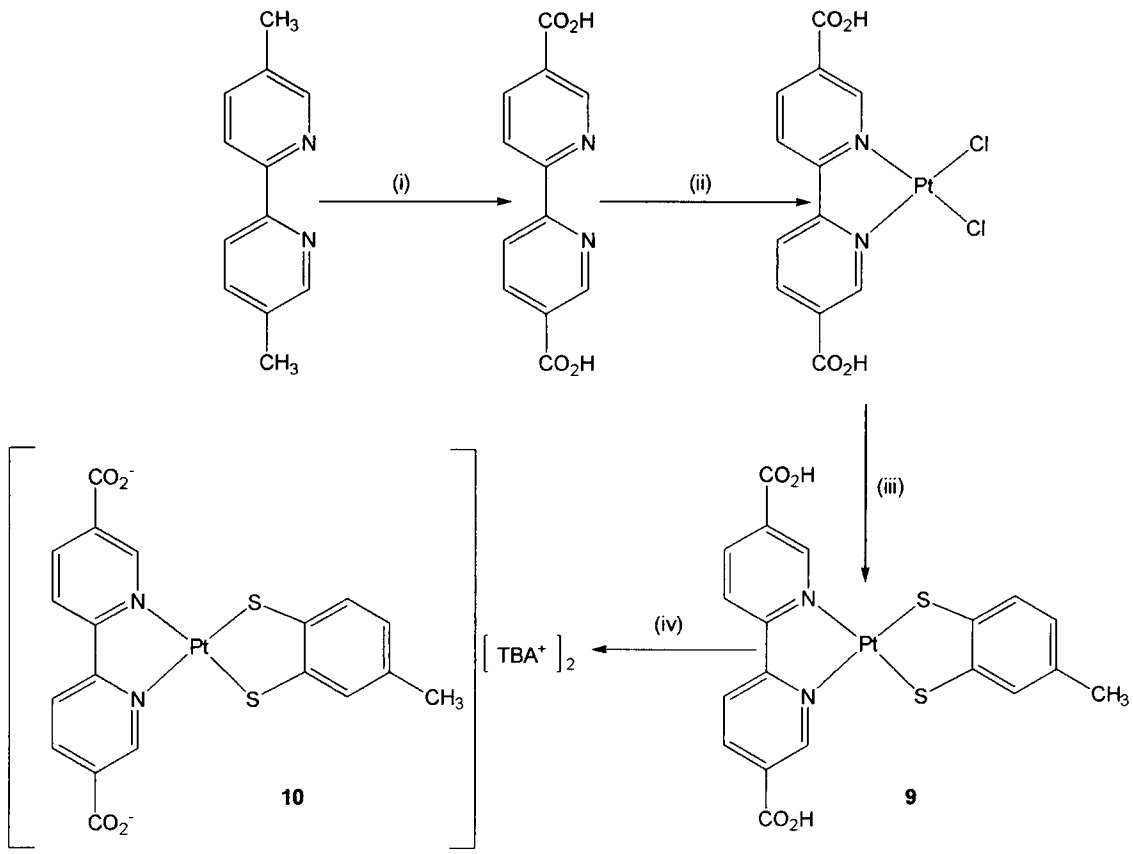

Fig. 6.1 Synthesis of **9** and **10**. (i) $KMnO_{4(aq)}$, 120°C/HCl (ii) K_2PtCl_4, 120 °C (iii) toluene-3,4-dithiol/KOH (iv) KOH/TBA$Br_{(aq)}$

Single crystals of **10**, (fig. 6.2 (a)) were grown by slow diffusion of ethyl acetate into a solution of **10** in ethanol. As mentioned in section 3.1.1, only thirteen crystal structures of the general formula [Pt(II)(bpy)(1,2-dithiolate)] have previously been reported.[5] Seven of these structures are 4,4'-disubstituted and five structures are 5,5'-disubstituted. Only three other crystal structures with 5,5'-dicarboxylic acid substituents on the bpy ring have been previously reported none of which is bonded to Pt. This clearly reflects the much greater amount of study that has been carried out on 4,4'-disubstituted bpy in comparison with the 5,5'-bpy systems, presumably arising from the earlier erroneous view that the 4,4'-positions were electronically more coupled to the bpy. It may also have been influenced by the practical use of the compounds since the 5,5'-bpy systems

seem to be less soluble than the 4,4′-species.[1] Bond lengths and angles are similar to those [Pt(II)(diimine)(dithiolate)] systems previously reported.[6-9]

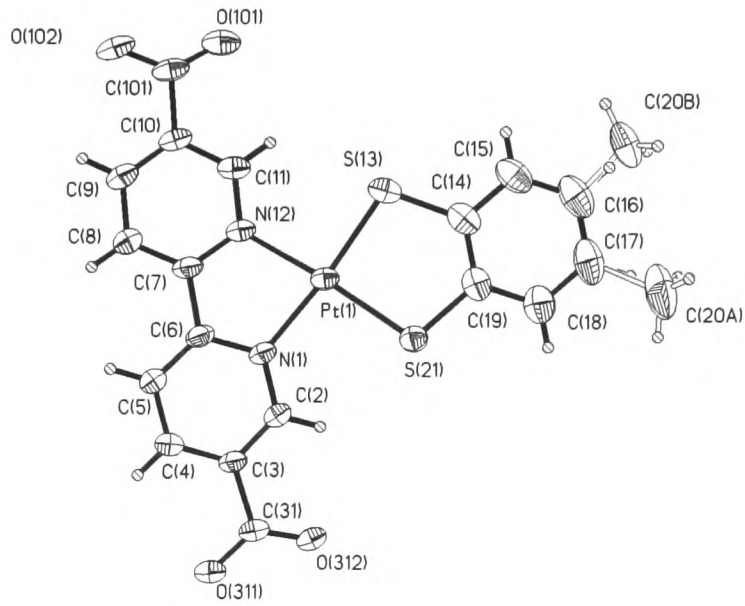

Fig. 6.2 (a) X-Ray Crystal structure of **10**. Selected bond lengths (Å) and angles (°): Pt-S(13) 2.2489(7), Pt-S(21) 2.2528(7), Pt-N(1) 2.052(2), Pt-N(12) 2.047(2), C(14)-C(15) 1.393(4), C(15)-C(16) 1.374(5), C(16)-C(17) 1.393(6), C(17)-C(18) 1.379(5), C(18)-C(19) 1.391(4), C(14)-C(19) 1.396(4), NPtN 79.8(8), SPtS 89.48(3).

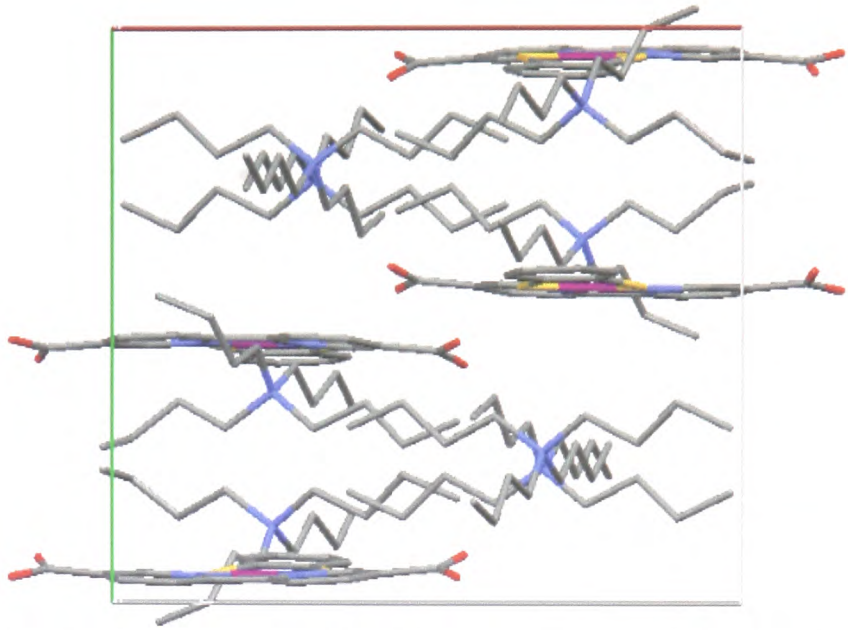

Fig. 6.2 (b) Packing diagram of **10** with a view down the a-axis. Hydrogen atoms and solvent molecules have been omitted for clarity.

The methyl substituent on the dithiolate is disordered over two positions with a relative occupancy of 50 %. The whole molecule is essentially planar with the exception of the carboxylate groups. The bpy functionality shows a 0.0437 Å deviation from the plane and the [Pt(II)(diimine)(dithiolate)] unit shows a 0.0573 Å deviation from planarity. This planarity in the molecule gives rise to the packing in layers of Pt anions separated by layers of TBA counterions (fig. 6.2 (b)). It also results in large electronic delocalisation within the molecule essential for use as a solar-cell dye.

6.1.2 Electrochemistry

9 and **10** were studied by cyclic voltammetry and the redox potentials for the processes are shown in table 6.1. The cyclic voltammogram of **9** in a solution of DMSO shows two reduction peaks (fig. 6.3) and one oxidation peak, all of which are quasi reversible. The cyclic voltammogram of **10** in DMSO shows one reduction and three oxidations, all of which are electrochemically irreversible. Coulometric studies were performed on both

the oxidation and reduction processes of **9** in an attempt to confirm the number of electrons involved in the redox process however the current passed showed a non-integral value for electron transfer and the original complex could not be regenerated on re-reduction. This implies that during the timescale of coulometry, both the oxidation and reduction of **9** are chemically irreversible.

Compound	Reduction (V)		Oxidation (V)		
9	-1.09†	-0.66†	0.55†		
10		-1.27*	0.65*	0.87*	1.1*

Table 6.1 Oxidation and reduction potentials for **9** and **10** vs Ag/AgCl. †quasi reversible and *irreversible, E_p.

As was described in chapter 3, it has been stated that the dithiolate ligand influences the oxidation potentials and the diimine ligand influences the reduction potentials of [Pt(II)(diimine)(dithiolate)] species, since the HOMO is known to be largely dithiolate based and the LUMO is diimine based.[10] The only oxidation in **9** and the first oxidation in **10** occur at similar potentials and this is assigned as the oxidation of the HOMO based on the dithiolate moiety in the molecule. The dithiolate group is identical in both **9** and **10**, hence it is expected that the oxidation potentials for both will be similar. Two further oxidations are seen in **10** at more positive values. These oxidations may represent loss of electrons from the diimine functionality due to the carboxylate anions and therefore lie at more positive potential. Bpy complexes generally show two reductions and both **9** and **10** show reduction processes; however the first reduction in **10** occurs at a much more negative reduction potential than either of the two reductions in **9**, reflecting the two negative charges on the carboxylate anions of **10** which makes the complex more difficult to reduce than the neutral species. No second reduction can be seen for **10** in this solvent window

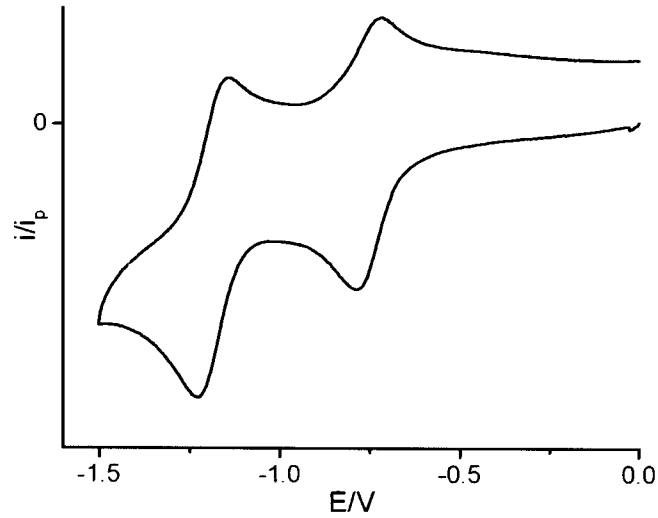

Fig.6.3 Cyclic voltammogram of **9** showing two bpy based quasireversible reductions, scan rate 0.8 V/s, in 0.1MTBABF_4/DMSO at 293 K

6.1.3 UV/Visible spectroscopy

Both **9** and **10** have an intense UV band at approximately 320 nm and this band is assigned to the intraligand π-π^* transition of the {5,5'-$(CO_2H)_2$bpy} ligand. **9** shows an absorbance at 651 nm (ε = 4,900 $M^{-1}cm^{-1}$) and **10** shows an absorbance at 558 nm (ε = 3,000 $M^{-1}cm^{-1}$), both in DMSO (fig. 6.4). These charge transfer transitions in [Pt(II)(diimine)(dithiolate)] complexes have previously been assigned by Eisenberg and co-workers.[11] Charge transfer occurs from a HOMO consisting of a mixture of Pt(d) and dithiolate orbital character to a LUMO which is a low-energy π^* orbital of the {5,5'-$(CO_2H)_2$bpy}. The absorbance maxima of the low energy band for **10** can be tuned between 547 nm (MeCN) and 582 nm (EtOH) in a range of organic solvents, however this change in λ_{max} values showed no obvious solvatochromic trend with respect to solvent polarity. It may be that other factors such as hydrogen bonding with the solvent also play a role in determining the energy of the band. A key requirement of any photosensitiser is that it maximises the overlap of its absorption spectrum with that of the solar emission spectrum. The UV/visible absorption spectrum of **9** in DMSO shows a broad absorbance over much of the low-energy region of the spectrum, with a

maximum at 651 nm. A comparison between the UV/visible absorption spectrum of **9** and that of [[Pt{4,4'-$(CO_2H)_2$bpy}(tdt)] is made later in this chapter in section 6.2.

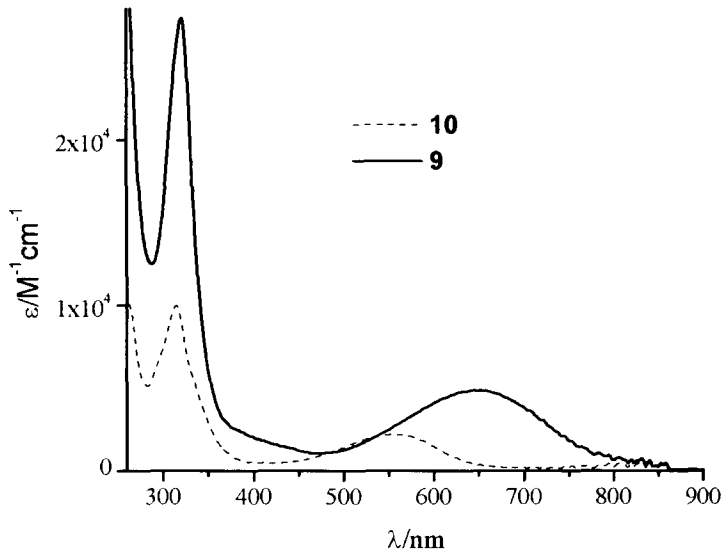

Fig. 6.4 UV/visible spectra of **9** and **10** in DMSO at 293 K

6.1.3.1 UV/Vis/NIR spectroelectrochemistry

Attempts were made to follow the redox processes occurring in both **9** and **10** by UV/Vis/NIR spectroelectrochemistry. There were difficulties however with interpreting these results due to the formation of unstable redox products. Changes in the UV/visible spectra were observed for both **9** and **10** when the first reduction process was investigated. No isosbestic points were found for either of the compounds investigated and the original compounds could not be regenerated. The oxidation of **9** was also investigated but again no isosbestic points were found and the original compound could not be regenerated. All of these results proved consistent with the coulometry results previously discussed in section 6.1.2.

6.1.4 Emission spectroscopy

We were unable to observe emission from a solution of **9** in DMSO dispersed in EtOH at room temperature. In a frozen solution at 77K emission was observed (fig. 6.5). Excitation of the complex at 600 nm gives an emission spectrum with a peak at 700 nm. The corresponding excitation spectrum shows a broad band between 500-600 nm, consistent with the position of the absorption band of **9**. Compounds of the general formula [Pt(II)(diimine)(dithiolate)] are typically emissive in frozen glasses and in more recent years have been found in certain cases to emit in room temperature solutions.[12] It has been stated that emission in [Pt(II)(diimine)(dithiolate)] species is formally a spin forbidden process where the spin character of the emissive state is different to that of the ground state.[13]

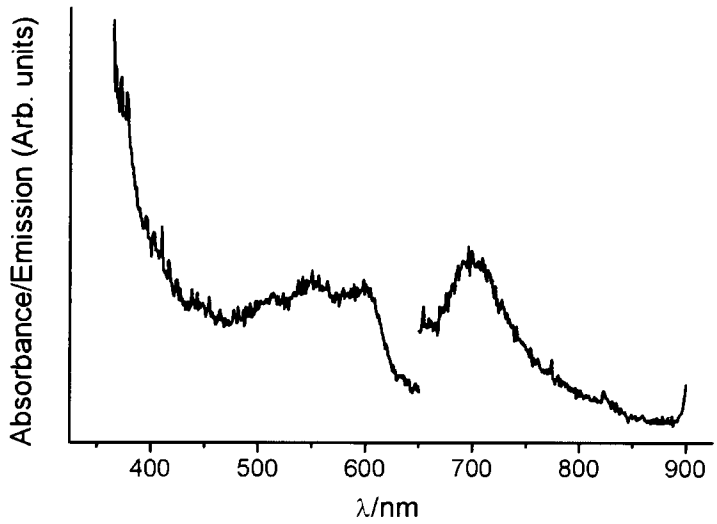

Fig. 6.5 Emission and corresponding excitation spectrum of a frozen solution of **9** in DMSO dispersed in EtOH

6.1.5 Evaluation of the dye as a Photosensitiser

Photoelectrochemical measurements were taken in order to assess the dye as a photosensitiser. Dye binding was achieved by immersion of nanocrystalline TiO_2 films in a saturated solution of both dyes **9** and **10**. Optimisation of the solvent system used for sensitisation of the films resulted in increased UV/Visible absorbance values. The

optimum solution tested was a 1:3.2 DMSO:MeCN solution of Pt complex at a concentration of 1 mg/1 mL. These solutions were used to sensitise 8 μm TiO_2 films for 22 hours at room temperature. The UV/Visible absorption spectrum of **9** on TiO_2 exhibits a broad absorption band between 600-650 nm (fig. 6.6) similar to that of the solution absorbance (651 nm) with a slight broadening and blue shift. The absorption spectrum for **10** on TiO_2 shows a relatively weak absorption band, red shifted (peak 590 nm) with respect to that of the solution absorbance (peak 558 nm). This red shift may be due to donation of electron density from the carboxylate anions to the TiO_2 on binding, thus making it a better electron acceptor and hence closing the HOMO-LUMO gap.

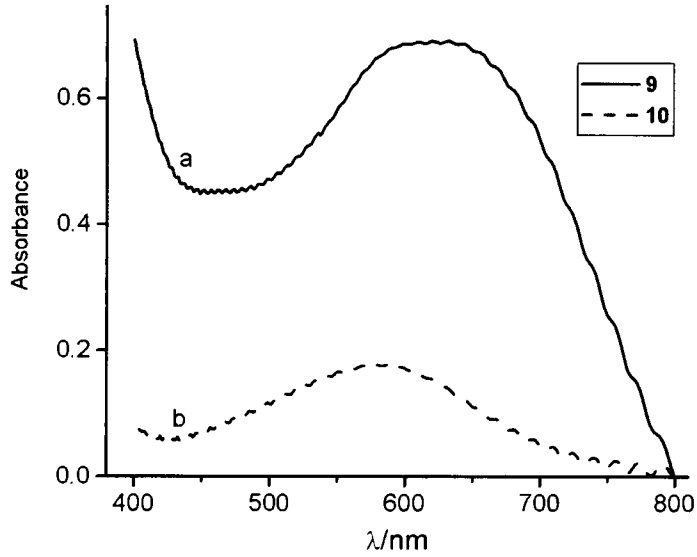

Fig. 6.6 UV/visible absorption spectra of platinum dyes on TiO_2. (a) **9** (b) **10**. Both datasets were collected after dipping the 8 μm TiO_2 film in 1 mg/1 mL solution of the dye in DMSO (**9**) and 1:3.2 DMSO:MeCN (**10**) for 22 h at RT

Dye loadings on the films were estimated employing the dye peak extinction coefficients determined in solution above, and are detailed in table 6.2. In both cases, high dye loadings were achieved, consistent with the high surface area of the TiO_2 films with the acid form of the dye exhibiting the stronger binding.

Dye	Dye coverage [10^{-7}mol/cm^2][a]	Relative injection Yield[b]	Recomb. half-life [s][c]	J_{sc} [A cm^{-2}][d]	V_{oc} [V][d]
9	1.4	1	1.7×10^{-5}	9.8×10^{-6}	8.8×10^{-3}
10	0.6	0.83	0.33	2.0×10^{-5}	0.19

Table 6.2 Summary of results obtained for sensitisation of nanocrystalline TiO_2 films. [a]Dye loadings estimated per cm^2 film estimated from UV/Visible absorption spectra. [b]Relative yield of injected electrons per absorbed photon determined from the initial amplitude of the transient absorption signal in figure 6.7 [c]Recombination half-lives determined from the transient absorption data shown in figure 6.7. [d]Current/voltage characteristics of dye sensitised photoelectrochemical cells under AM 1.5 simulated solar illumination.

The electron transfer function of the sensitiser dyes was evaluated by transient absorption data in the absence of redox electrolyte. Typical data are shown in figure 6.7, monitoring the photoinduced absorption of electrons injected into the TiO_2 following excitation of the sensitiser dyes. For both dyes, an instrument response limited rise was observed, assigned to rapid electron injection. The transient signal subsequently decays due to charge recombination between the injected electrons and the oxidised dye. The initial transient signal was larger with **9**, attributed to the higher optical density obtained for the sensitised films with this dye, although in both cases the small magnitude of the transient signal was indicative of a low yield of electron injection (< 10 %). After normalising for differences in sample optical density, the initial signal magnitudes for the two dyes were similar, indicating similar injection yields for both dyes, as detailed in table 6.2. In contrast, the charge recombination dynamics for the two sensitised films were very different, with the **9** and **10** sensitised films exhibiting recombination half times of 1.7×10^{-5} s and 0.33 s respectively. It is furthermore apparent that the shapes of the transient decays are distinct for the two dyes, with the slower dynamics being less dispersive (near monoexponential), consistent with previous observations.[14]

The slower recombination dynamics for **10** are indicative of weaker electronic coupling between the dye and the TiO_2 surface, consistent with the lower dye coverage obtained with this dye. This is presumably related to the mode of binding of the sensitiser to the TiO_2 surface. We do not know exactly how **9** binds to TiO_2, however previous studies using IR spectroscopy have shown that the average mode of binding of {5,5'-$(CO_2H)_2$bpy} ligands in Ru complexes to TiO_2 to be identical to that of {4,4'-$(CO_2H)_2$bpy}.[1]

The kinetics of electron transport within the TiO_2 is shown by stretched exponential recombination dynamics as seen in fig. 6.7a. Interfacial electron transfer (i.e. electron transfer from TiO_2 to the oxidised dye molecule) is shown by monoexponential recombination kinetics (fig. 6.7 b). These kinetic models have been discussed in more detail in section 3.1.6 of this thesis.[14]

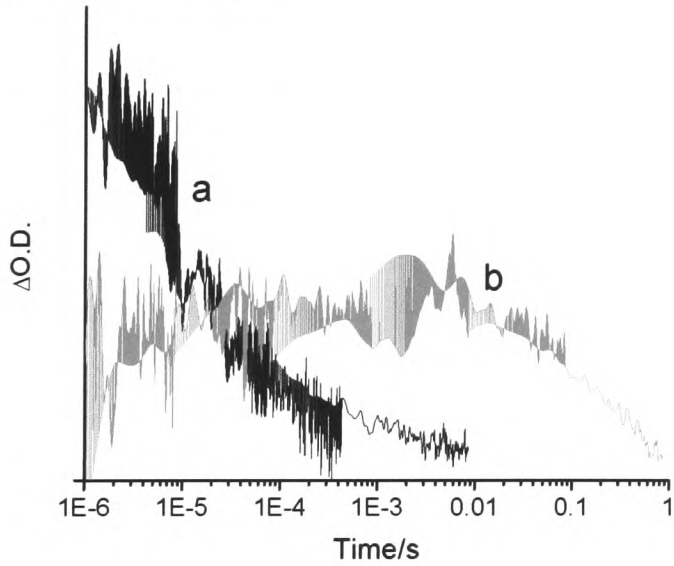

Fig. 6.7 Transient absorption data monitoring the photoinduced absorption of electrons injected into the TiO_2 (λ_{probe} = 1000 nm) following excitation of the sensitiser dyes at 610 nm. Data obtained for for TiO_2 films sensitised with (a) **9** and (b) **10**.

Dye characterisation was further extended to characterisation of the photocurrent-voltage data for the dye sensitised TiO_2 in two electrode 'sandwich type' photoelectrochemical cells. Typical short circuit currents and open circuit voltages are given in table 6.2. It is apparent that the best photovoltaic performance of the dyes in this study was obtained with **10**, despite the lower dye loading and film optical density obtained with this dye, although for both dyes the performance is poor relative to that of [Pt{4,4'-$(CO_2H)_2$bpy}(tdt)].

6.2 Comparison of 9 and 10 with [Pt{4,4'-$(CO_2H)_2$bpy}(tdt)[

The electrochemistry and UV/Visible spectroscopy performed on **9** and **10** allowed the analysis of the HOMO-LUMO energy gaps of the dyes. In our study, tuning the HOMO-LUMO gap was achieved by a variation made to the diimine functionality thus lowering the LUMO. In their study of [Pt(II)(diimine)(dithiolate)] complexes, Arakawa and co-workers varied the dithiolate functionality of the molecule and hence altered the energy of the HOMO and the two studies show complimentary results. The HOMO-LUMO energy gap, as determined from the UV/visible spectrum of both **9** and **10** showed $\Delta E_{HOMO\text{-}LUMO}$ = 1.9 eV for **9** and $\Delta E_{HOMO\text{-}LUMO}$ = 2.22 eV for **10**. Arakawa and co-workers showed $\Delta E_{HOMO\text{-}LUMO}$ = 2.14 eV for [Pt{4,4'-$(CO_2H)_2$bpy}(tdt)] in basic 4:1 ethanol/methanol solution. This value is comparable with our results for **10**. However since the extent of deprotonation in [Pt{4,4'-$(CO_2H)_2$bpy}(tdt)] in basic 4:1 ethanol/methanol solution is unknown it is difficult to make a direct comparison of the HOMO-LUMO energy gaps of [Pt{4,4'-$(CO_2H)_2$bpy}(tdt)] and **9** from UV/visible spectroscopic results. From the electrochemistry it can be seen that the first reduction in **9** is much more facile than the first reduction in [Pt{4,4'-$(CO_2H)_2$bpy}(tdt)]. This implies that placing carboxylic acid substituents at the 5,5' positions of the bpy ring enhances the electron accepting ability of **9** compared to that of [Pt{4,4'-$(CO_2H)_2$bpy}(tdt)].

The oxidation potentials for [Pt{4,4'-$(CO_2H)_2$bpy}(tdt)] and **9** are comparable due to the similar nature of their dithiolate functionalities and hence their HOMOs. Thus the electrochemical data suggest we have tuned the LUMO energy to give a smaller HOMO-LUMO gap in comparison with the 4,4'-analogue. Both the present study and that of Arakawa found that dyes with longer absorption wavelengths are less efficient as solar cell sensitisers. There are a number of reasons why this may be the case.

The rate of electron injection into the conduction band of the TiO_2 is dependent on the height of the electronic state of the excited dye (LUMO) above the conduction band, therefore lowering the LUMO leads to less efficient electron injection to the TiO_2. Also, the low value of the oxidation potentials of these dyes compared to analogous complexes containing other dithiolates e.g. quinoxalinedithiolate (qdt) which have more positive oxidation potentials mean that regeneration of the reduced dye by the redox couple becomes more difficult due to the smaller energy gap between the reduced form of the redox couple (I^-) and the oxidised dye compared with complexes of qdt. This results in more recombination of photoinjected electrons with the oxidised dye and is seen in both the Pt species investigated here and in tdt complexes in general.[3] The rapid charge recombination dynamics seen for **9**, is also consistent with its poorer performance relative to **10**. Furthermore, non-radiative decay of excited electrons may also have an influence on the dye efficiency. This is governed by the energy gap law for MLCT excited states which states that the rate of non-radiative decay of a CT complex increases exponentially with the corresponding decrease in HOMO-LUMO energy gap. Finally complexes with the tdt moiety have consistently lower extinction coefficients (ε), when compared to other [Pt(II)(diimine)(dithiolate)] species. A lower ε value means that the dye has a lower light harvesting efficiency which is a factor in the overall IPCE value for the cell.

6.3 Conclusions

This work illustrated the difficulty with long wavelength dye molecules. There is a general difficulty with low energy absorbing dyes since in lowering the energy of the LUMO, there is a decrease in electron injection from the dye to the conduction band of the semiconductor. It may not be possible to have both the LUMO at high enough energy to provide the driving force required for electron injection and the HOMO at low enough energy to allow efficient dye reduction by the electrolyte and still retain a long wavelength absorbance. Arakawa and co-workers experienced similar difficulties in their investigation of [Pt(II)(diimine)(dithiolate)] dyes. On going to longer wavelengths the performance of the dyes as photosensitisers decreased dramatically. Short wavelength dyes with higher energy LUMOs perform better as photosensitising devices and the performances of our dyes are consistent with those previously reported. Moving to longer wavelength dyes may eventually be achieved in conjunction with a new cell design where it is hoped that a combination of a solid state cell design and a longer wavelength dye may improve the overall function of the cell.

6.4 Experimental

6.4.1 Synthesis

5,5′-$(Me)_2$-2,2′-bpy, 3,4-toluenedithiolate (tdt), purchased from Sigma-Aldrich and K_2PtCl_4 purchased from Johnson Matthey, were used as received. The synthesis of {5,5′-$(CO_2H)_2$bpy} and [Pt{5,5′-$(CO_2H)_2$bpy}Cl_2] has been described already in section 3.1.1.

[Pt{5,5′-$(CO_2H)_2$bpy}(tdt)]

[Pt{5,5′-$(CO_2H)_2$bpy}Cl_2] (0.25 g, 0.49 mmol) was dissolved in a minimum amount of 0.1 M KOH (10 mL). To this mixture, tdt (0.11 g, 0.68 mmol) and 10 mL MeOH were added. A dark purple solution formed immediately and was allowed to stir for an additional two hours. The product [Pt{5,5′-$(CO_2H)_2$bpy}(tdt)], was precipitated using 0.1 M HCl. The black precipitate was collected by filtration and washed with water. The crude product was redissolved in the minimum amount of 1 M KOH and purified by column chromatography using a Sephadex-LH 20 column, with water as the eluent. The main purple band was collected and precipitated as the neutral complex by addition of 0.1 M HCl. [Pt{5,5′-$(CO_2H)_2$bpy}(tdt)] was isolated by filtration, washed with water and dried under vacuum. Yield 40.7 %. Anal. Calcd for $C_{19}H_{14}N_2O_4PtS_2$: C, 38.5; H, 2.4; N, 4.7. Found: C, 36.1; H, 2.6; N, 4.2. MS (FABMS) *m/z*: 593 (M^+). IR (KBr, cm^{-1}): 1609 (m) ($\nu_{asym}CO_2$).

[TBA]$_2$[Pt{5,5′-$(CO_2)_2$bpy}(tdt)]

[Pt{5,5′-$(CO_2H)_2$bpy}(tdt)] (0.05 g, 0.084 mmol) was dissolved in the minimum amount of 0.1M KOH and 2 ml 0.1M tetrabutylammoniumbromide (TBABr) was added. The product was extracted using DCM. The DCM was evaporated and ether was added to the purple solid. Trituration of the solid and repeated washing with diethyl ether resulted in a magenta powder of [TBA]$_2$[Pt{5,5′-$(CO_2)_2$bpy}(tdt)]. Yield 50.5 %. Anal. Calcd for $C_{51}H_{84}N_4O_4PtS_2$: C, 56.9; H, 7.9; N, 5.2. Found: C, 56.6; H, 8.9; N, 4.6. MS (FABMS) *m/z*: 1077 (M^+). IR (KBr, cm^{-1}): 1627 (s) ($\nu_{asym}CO_2$).

6.4.2 X-Ray Crystallography

Purple block crystals of **10**.EtOH.EtOAc (dimensions 0.57 x 0.55 x 0.45 mm^3), were grown by slow diffusion of ethyl acetate into an ethanolic solution of **10**. Crystal, data collection, and refinement parameters are summarised in table 6.3. Diffraction data were collected with Mo-Kα radiation on a Smart APEX CCD diffractometer equipped with an Oxford Cryosystems low-temperature device. An absorption correction was applied using the multi-scan procedure SADABS.[15] The structure was solved by direct methods and refined by full-matrix least squares against $|F|^2$ using all data (θ_{max} = 28.95 Å) (SHEXTL);[16] hydrogen atoms were placed in idealised positions. The methyl group of the dithiolate ligand was disordered over two positions; refinement of the relative weight of the components converged to 0.5:0.5, and this occupancy ratio was subsequently applied as a constraint. Difference electron density maps implied the presence of a disordered solvent region, and this (comprising 192 e per cell) was treated in the manner described by van der Sluis and Spek.[17] The crystal structure was solved by Dr. Alice Dawson and Dr. Simon Parsons.

Chemical Formula	$C_{57}H_{98}N_4O_7PtS_2$
Fw	1210.61
T, K	150
Lattice type	Monoclinic
Space group	$P2_1/c$
a, Å	16.4091(7)
b, Å	14.4709(6)
c, Å	27.5157(12)
β, °	105.5480(10)
V, $Å^3$	6294.6(5)
No. reflections for cell	6294
$2\theta_{max}$(°)	57.9
Z	4

D_c, Mg m^{-3}	1.277
μ, mm^{-1}	2.344
Reflections collected	56147
Unique [R_{int}]	15448 [0.0277]
No. $I > 2\sigma$	13231
T_{min}/T_{max}	0.823/1.00
Parameters	604
R_1 [$F>4\sigma(F)$]	0.0301
w$R(F^2)$	0.0802
S	1.084
$\Delta\rho_{max}$ / e$Å^{-3}$	1.72
$\Delta\rho_{min}$ / e$Å^{-3}$	0.63

Table 6.3 Crystallographic data for **10**.EtOH.EtOAc

6.5 References

1 R. Argazzi, C. A. Bignozzi, T. A. Heimer, F. N. Castellano, and G. J. Meyer, *Inorg. Chem.*, 1994, **33**, 5741.

2 A. Islam, H. Sugihara, K. Hara, L. Pratap Singh, R. Katoh, M. Yanagida, Y. Takahashi, S. Murata, and H. Arakawa, *New J. Chem.*, 2000, **24**, 343.

3 A. Islam, H. Sugihara, K. Hara, L. P. Singh, R. Katoh, M. Yanagida, Y. Takahashi, S. Murata, H. Arakawa, and G. Fujihashi, *Inorg. Chem.*, 2001, **40**, 5371.

4 F. H. Case, *J. Am. Chem. Soc.*, 1946, **68**, 2574.

5 C. S. Database, *Chem. Design Autom. News*, 1993, **8**, 31.

6 J. M. Bevilacqua and R. Eisenberg, *Inorg. Chem.*, 1994, **33**, 2913.

7 C. E. Keefer, R. D. Bereman, S. T. Purrington, B. W. Knight, and P. D. Boyle, *Inorg. Chem.*, 1999, **38**, 2294.

8 C. J. Adams, *Dalton Trans.*, 2002, 1545.

9 W. B. Connick and H. B. Gray, *J. Am. Chem. Soc.*, 1997, **119**, 11620.

10 W. Paw, S. D. Cummings, M. A. Mansour, W. B. Connick, D. K. Geiger, and R. Eisenberg, *Coord. Chem. Rev.*, 1998, **171**, 125.

11 M. Hissler, J. E. McGarrah, W. B. Connick, D. K. Geiger, S. D. Cummings, and R. Eisenberg, *Coord. Chem. Rev.*, 2000, **208**, 115.

12 F. Barigelletti, D. Sandrini, M. Maestri, V. Balzani, A. Von Zelewsky, L. Chassot, P. Jolliet, and U. Maeder, *Inorg. Chem.*, 1988, 27, 3644.

13 J. A. Zuleta, J. M. Bevilacqua, J. M. Rehm, and R. Eisenberg, *Inorg. Chem.*, 1992, 31, 1332.

14 J. N. Clifford, G. Yahioglu, L. R. Milgrom, and J. R. Durrant, *Chem. Commun.*, 2002, 1260.

15 G. M. Sheldrick, SADABS, University of Gottingen, Germany, 2002.

16 G. M. Sheldrick, SHELXTL, University of Gottingen, Germany, 1997.

17 P. Van der Sluis and A. L. Spek, *Acta Crystallogr., Sect. A:*, 1990, A46, 194.

Publications

FULL PAPER

Dalton
www.rsc.org/dalton

Synthesis, structure and properties of [Pt(2,2′-bipyridyl-5,5′-dicarboxylic acid)(3,4-toluenedithiolate)]: tuning molecular properties for application in dye-sensitised solar cells

Elaine A. M. Geary,[a] Narukuni Hirata,[b] John Clifford,[b] James R. Durrant,[b] Simon Parsons,[a] Alice Dawson,[a] Lesley J. Yellowlees[a] and Neil Robertson*[a]

[a] *School of Chemistry, Joseph Black Building, Kings Buildings, West Mains Road, Edinburgh, UK EH9 3JJ. E-mail: neil.robertson@ed.ac.uk; Fax: +441316504743; Tel: +441316504755*

[b] *Centre for Electronic Materials and Devices, Department of Chemistry, Imperial College, London, UK SW7 2AZ*

Received 3rd June 2003, Accepted 15th August 2003
First published as an Advance Article on the web 27th August 2003

The platinum diimine dithiolate complex, [Pt(2,2′-bipyridyl-5,5′-dicarboxylicacid)(3,4-toluenedithiolate)] ([Pt(5,5′-dcbpy)(tdt)]) and its tetrabutylammonium salt $[TBA]_2[Pt(5,5'\text{-dcbpy})(tdt)]$ have been prepared, spectroscopically and electrochemically characterised and attached on to TiO_2 substrate to be used as solar cell sensitisers. A single-crystal X-ray structure was obtained for $[TBA]_2[Pt(5,5'\text{-dcbpy})(tdt)]\cdot EtOH\cdot EtOAc$. The effect of the position of the two carboxylic acid substituents on the electrochemistry of the 5,5′-disubstituted complexes is discussed in comparison with the previously reported [Pt(4,4′-dcbpy)(tdt)]. Electrochemical studies show no major change in the HOMO after movement of the carboxylic acid groups, consistent with assignment of the HOMO as largely dithiolate based. Movement of the carboxylic acid groups makes the diimine electronic character and hence the LUMO of the complexes different. Electrochemical studies show a change to lower energy of the LUMO represented by changes in reduction potential of the compound on moving the carboxylic acid substituents from the 4,4′ to the 5,5′ positions. Both [Pt(5,5′-dcbpy)(tdt)] and $[TBA]_2[Pt(5,5'\text{-dcbpy})(tdt)]$ have been used as solar cell sensitisers, with the di-TBA salt giving lower dye loading but superior photovoltaic performance. The consequences of tuning the complex through the position of the carboxylic acid groups are discussed.

Introduction

Over the past decade the charge transfer excited state of a series of square-planar compounds of the general formula Pt(II)-(diimine)(dithiolate) has been investigated.[1–3] These complexes have shown room-temperature solution luminescence and a highly solvatochromic charge transfer (CT) absorption. Recent investigations have stated that the transition is a "Mixed Metal-Ligand-to-Ligand Charge-Transfer" (MMLL′CT) involving a HOMO which is a mixture of Pt(d) and dithiolate orbitals and a LUMO which is primarily a π^* diimine orbital.[1,2] Subsituents on the diimine affect the electronic and photophysical properties of the LUMO while substituents on the dithiolate affect the HOMO properties. Tuning of these Pt(II)(diimine)(dithiolate) complexes, by ligand variation[3–8] has also shown that the excited state energies can be tuned by up to 1 eV.[1]

Tuning the electrochemical and photophysical properties of dyes is particularly relevant to the area of photovoltaic cells. In dye-sensitised solar cells, the dye molecule absorbs visible light and, after excitation injects electrons into the conduction band of a semiconductor (TiO_2). The oxidised dye molecule is subsequently reduced by electron donation from a redox system such as the iodide/triiodide couple. The function of these cells is crucially dependent on the optical and electrochemical properties of dyes.[1,2] The majority of dyes currently in use are short wavelength dyes and hence absorb at high energy. Longer wavelength dyes are desirable to allow absorption of light over a greater region of the solar spectrum and hence harvest more solar energy. All dyes previously investigated for solar cells contain some functional group present to attach the dye molecule to the TiO_2 surface. Most commonly 2,2′-bipyridyl-4,4′-dicarboxylic acid (4,4′-dcbpy) has been used, where the carboxylic acid groups anchor the dye molecule to TiO_2.[9]

In a study of bipyridinecarbonitirile complexes of Mo and W, however, Baxter and Connor concluded that the nitriles in the 5,5′ positions exert a greater electron withdrawing effect upon the metal than nitriles in the 4,4′ positions of the bpy ligand.[10] Furthermore, recent DFT calculations, electrochemical, spectroelectrochemical and EPR studies on $[Pt(5,5'\text{-}(X)_2\text{-bpy})Cl_2]$ complexes (X = H, Me, CO_2Me, CO_2Et, NH_2) showed that electron density at the 5,5′ positions is significantly greater than at the 4,4′ positions.[11,12] It is therefore expected that substituents at the 5,5′ positions would have a greater effect on the electronic character of the bpy than substituents at the 4,4′ positions.

5,5′-Disubstituted bipyridines have previously been investigated in Ru systems for use as sensitisers in solar cells.[13] $Ru(5,5'\text{-dcbpy})_2(X)_2$, (where $X = Cl^-$, CN^- and SCN^-) have been synthesised and used in solar cells and compared with the previously synthesised 4,4′-analogues. The (5,5′-dcbpy) compounds showed an enhanced spectral response at lower photon energies, however they were less efficient as solar cell sensitisers than the 4,4′ analogues. Pt(II)(diimine)(dithiolate) complexes have been recently investigated for their possible use as sensitisers in photovoltaic cells,[14,15] however studies were limited to complexes with 4,4′-dcbpy.

In this context we have studied [Pt(2,2′-bipyridyl-5,5′-dicarboxylicacid)(3,4-toluenedithiolate)] ([Pt(5,5′-dcbpy)(tdt)]) and its tetrabutylammonium salt ($[TBA]_2[Pt(5,5'\text{-dcbpy})(tdt)]$). The related complex ([Pt(4,4′-dcbpy)(tdt)]) was previously investigated by Arakawa and co-workers.[15] By placing electron withdrawing groups at the 5,5′ positions of the bipyridyl group, we aim to lower the LUMO energy and investigate the effect on the optical and electrochemical properties and the performance in a dye-sensitised solar cell of a Pt-based dye molecule.

Experimental

5,5′-Dimethyl-2,2′-bipyridine, 3,4-toluenedithiolate (tdt), purchased from Sigma-Aldrich and K_2PtCl_4 purchased from Johnson Matthey, were used as received.

DOI: 10.1039/b306241d

Synthesis of 5,5′-dcbpy

5,5′-dcbpy was synthesised by a previously reported method.[16] Yield 95.1%. Found: C, 51.6; H, 3.1; N, 10.3. Calc. for $C_{12}H_8N_2O_4$: C, 52.0; H,3.3; N,11.5%. IR ν/cm^{-1}: 1593s (ν_{asym}CO), 1685s. *m/z*: 245 (M^+).

Synthesis of [Pt(5,5′-dcbpy)Cl$_2$]

[Pt(5,5′-dcbpy)Cl$_2$] was synthesised by an analogous method to the 4,4′ analogue.[15] Yield 76.21%. Found: C, 28.8; H, 1.7; N, 5.5. $C_{12}H_8N_2O_4PtCl_2$ requires C, 28.3; H, 1.6; N, 5.5%. IR ν/cm^{-1}: 1616s (ν_{asym}CO). *m/z*: 510 (M^+).

Synthesis of [Pt(5,5′-dcbpy)(tdt)]

[Pt(5,5′-dcbpy)Cl$_2$] (0.25 g, 0.49 mmol) was dissolved in a minimum amount of 0.1 M KOH (10 ml). To this mixture, tdt (0.11 g, 0.68 mmol) and 10 ml MeOH were added. A dark purple solution formed immediately and was allowed to stir for an additional 2 h. The product, [Pt(5,5′-dcbpy)(tdt)], was precipitated using 0.1 M HCl. The black precipitate was collected by filtration and washed with water. The crude product was redissolved in the minimum amount of 1 M KOH and purified by column chromatography using a Sephadex-LH 20 column, with water as the eluent. The main purple band was collected and precipitated as the neutral complex by addition of 0.1 M HCl. [Pt(5,5′-dcbpy)(tdt)] was isolated by filtration, washed with water and dried under vacuum. Yield 40.7%. Found: C, 36.1; H, 2.6; N, 4.2. $C_{19}H_{14}N_2O_4S_2Pt\cdot 2H_2O$ requires C, 36.2; H, 2.9; N, 4.5%. IR ν/cm^{-1}: 1609m (ν_{asym}CO). *m/z* 593 (M^+).

Synthesis of [TBA]$_2$[Pt(5,5′-dcbpy)(tdt)]

[Pt(5,5′-dcbpy)(tdt)] (0.05 g, 0.084 mmol) was dissolved in the minimum amount of 0.1 M KOH and 2 ml 0.1 M tetrabutylammoniumbromide (TBABr) was added. The product was extracted using dichloromethane (DCM). The DCM was evaporated and ether was added to the purple solid. Trituration of the solid and repeated washing with diethyl ether resulted in a magenta powder of [TBA]$_2$[Pt(5,5′-dcbpy)(tdt)]. Yield 50.5%. Calc. for $C_{51}H_{84}N_4O_4S_2Pt$: C, 56.9; H, 7.9; N, 5.2. Found: C, 56.6; H, 8.9; N, 4.6%. IR ν/cm^{-1}: 1627s. *m/z* 1077 (M^+).

X-Ray crystallography

Crystal data for [TBA]$_2$[Pt(5,5′-dcbpy)(tdt)]·EtOH·EtOAc, $C_{57}H_{98}N_4O_7PtS_2$, M = 1210.61. A purple block of dimensions 0.57 × 0.55 × 0.45 mm was used for data collection. The crystal structure was monoclinic, space group $P2_1/c$, a = 16.4091(7), b = 14.4709(6), c = 27.5157(12) Å, β = 105.5480(10)°, V = 6294.6(5) Å^3 at T = 150 K. Z = 4, D_c = 1.277 Mg m^{-3}, μ = 2.344 mm^{-1}. Diffraction data were collected with Mo-Kα radiation on a Smart APEX CCD diffractometer equipped with an Oxford Cryosystems low-temperature device. An absorption correction was applied using the multi-scan procedure SADABS (range of transmission: 0.823–1.000).[17] The structure was solved by direct methods and refined by full-matrix least squares against $|F|^2$ using all data (θ_{max} = 28.95°) (SHEXTL);[18] hydrogen atoms were placed in idealised positions. The methyl group of the thiolate ligand was disordered over two positions; refinement of the relative weight of the components converged to 0.5 : 0.5, and this occupancy ratio was subsequently applied as a constraint. Difference electron density maps implied the presence of a disordered solvent region, and this (comprising 192 e per cell) was treated in the manner described by van der Sluis and Spek.[19] Calculation of the formula, M, $F(000)$ *etc.* have assumed that this region corresponds to one molecule of ethyl acetate per formula unit. The refinement converged to $R1$ = 0.0301 [based on $|F|$ and 13231 data with $|F| > 4\sigma(|F|)$]; $wR2$ = 0.0802 (based on $|F|^2$ and all 15448 data) for 604 parameters. The final difference map extremes were +1.72 and −0.63 e Å^{-3}.

CCDC reference number 211901.

See http://www.rsc.org/suppdata/dt/b3/b306241d/ for crystallographic data in CIF or other electronic format.

Other experimental

All UV-vis spectra were recorded on a Perkin-Elmer Lambda 9 spectrophotometer controlled by a Datalink PC, running UV/Winlab software.

Electrochemical studies were carried out using a DELL GX110 PC with General Purpose Electrochemical System (GPES), version 4.8, software connected to an autolab system containing a PGSTAT 20 potentiostat. The techniques used a three-electrode configuration, with a 0.5 mm diameter Pt disc working electrode, a Pt rod counter electrode and an Ag/AgCl (saturated KCl) reference electrode against which the ferrocenium/ferrocene couple was measured to be +0.55 V. The supporting electrolyte was 0.1 M tetrabutylammonium tetrafluoroborate (TBABF$_4$).

OTTLE (Optically Transparent Thin Layer Electrode) measurements were taken using a quartz cell of 0.5 mm, a Pt/Rh gauze working electrode, an Ag/AgCl reference electrode and a Pt wire counter electrode.[20] UV-vis spectra were recorded on a Perkin-Elmer Lambda 9 spectrophotometer, controlled by a Datalink PC, running UV/Winlab software. Spectroelectrochemical measurements were carried out on both [Pt(5,5′-dcbpy)(tdt)] and [TBA]$_2$[Pt(5,5′-dcbpy)(tdt)]. Ottle measurements on [Pt(5,5′-dcbpy)(tdt)] were carried out at 298 K in DMSO and at 233 K in a 1 : 3 solution of DMSO–MeCN. Ottle measurements on [TBA]$_2$[Pt(5,5′-dcbpy)(tdt)] were carried out at 233 K in DMF. 0.1 M TBABF$_4$ was used as the supporting electrolyte in all cases.

Electronic emission spectra were recorded on a Jobin Yvon Spex Fluoromax spectrofluorimeter, connected to a DSC Datalink PC running Instruments S.A. Datamax software. All emission spectra were recorded with [Pt(5,5′-dcbpy)(tdt)] dissolved in DMSO and dispersed in EtOH. All spectra were recorded in standard Wilmad 5 mm quartz NMR tubes contained in a liquid nitrogen filled fused silica Dewar.

Nanoporous TiO_2 thin films (8 μm thick) on conductive glasses were prepared as previously reported.[21] The size of the samples was 1 cm^2. The thin films were sensitised at room temperate for 22 h in 1.7 mM DMSO solution ([Pt(5,5′-dcbpy)(tdt)]) or 0.93 mM solution of ([TBA]$_2$[Pt(5,5′-dcbpy)(tdt)]) in 1 : 3.2 DMSO–MeCN. Transient absorption studies were carried out employing 610 nm excitation of the sensitiser dye, monitoring the photoinduced absorption of the TiO_2 electron at 1000 nm.[21] Photoelectrochemical measurements were performed as previously described employing 'sandwich type' photovoltaic cells with platinised counter electrode.[22] The electrolyte used contained 0.1 M LiI, 0.8 M TBAI, 0.1 M I_2, 0.5 M ^{t}BuPy in acetonitrile. The working electrode had an illuminated surface area of 1.0 cm^2. Experiments were conducted under AM 1.5 simulated sunlight.

Results and discussion

[Pt(5,5′-dcbpy)(tdt)] was synthesised by a route analogous to [Pt(4,4′-dcbpy)(tdt)] which was previously reported.[15] 5,5′-dcbpy was synthesised by oxidation of the dimethylbipyridine starting material. Reaction of 5,5′-dcbpy with potassium tetrachloroplatinate and potassium chloride gave the platinum dichloro derivative which was further reacted with toluene-3,4-dithiol to give the desired product [Pt(5,5′-dcbpy)(tdt)]. The tetrabutylammonium salt was made by reaction of a basic solution of [Pt(5,5′-dcbpy)(tdt)] with an aqueous solution of tetrabutylammonium bromide (Fig. 1).

[TBA]$_2$[Pt(5,5′-dcbpy)(tdt)] was synthesised to facilitate dissolution of the compound, since it is soluble in a range of organic solvents including methanol, ethanol, dichloro-

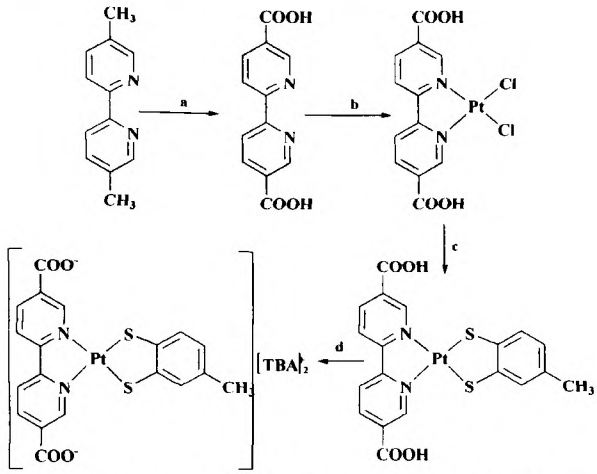

Fig. 1 Synthesis of [Pt(5,5′-dcbpy)(tdt)] and $[TBA]_2$[Pt(5,5′-dcbpy)(tdt)]. (a) $KMnO_{4(aq)}$, 120 °C/HCl. (b) K_2PtCl_4, 120 °C. (c) Toluene-3,4-dithiol/KOH. (d) KOH/$TBABr_{(aq)}$.

methane, dimethylformamide and acetonitrile. The neutral [Pt(5,5′-dcbpy)(tdt)] was found to be soluble only in DMSO.

Single crystals of $[TBA]_2$[Pt(5,5′-dcbpy)(tdt)] were grown by slow diffusion of ethyl acetate into ethanol solution (Fig. 2). Only five crystal structures of Pt(diimine)(1,2-dithiolate) systems have been previously reported.[23] Four of the five feature a 4,4′-disubstituted bpy and the remaining one features an unsubstituted bpy. There are no previous reports of crystals with a 5,5′-disubstituted bpy in a Pt(diimine)(dithiolate) complex and only two other crystal structures with the 5,5′-dicarboxybpy functionality have been previously reported. Neither of these is bonded to Pt. This clearly reflects the much greater amount of study that has been carried out on 4,4′-disubstituted bpy in comparison with the 5,5′-bpy systems, presumably arising from the earlier view that the 4,4′-positions were electronically more coupled to the bpy. It may also have been influenced by the practical use of the compounds since the 5,5′-bpy systems seem to be less soluble than the 4,4′-species.[13] Bond lengths and angles are similar to those for Pt(diimine)-(dithiolate) systems previously reported.[7,24–26]

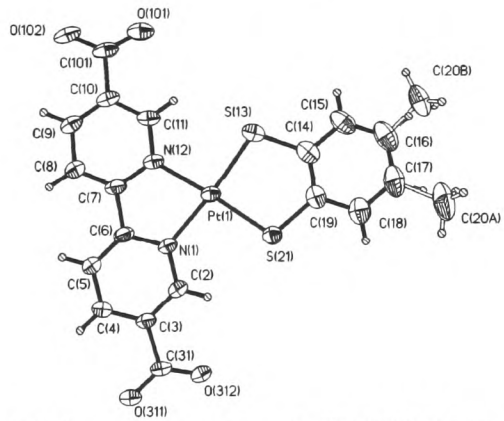

Fig. 2 X-Ray crystal structure of $[TBA]_2$[Pt(5,5′-dcbpy)(tdt)]. Selected bond lengths (Å) and angles (°): Pt–S(13) 2.2489(7), Pt–S(21) 2.2528(7), Pt–N(1) 2.052(2), Pt–N(12) 2.047(2), C(14)–C(15) 1.393(4), C(15)–C(16) 1.374(5), C(16)–C(17) 1.393(6), C(17)–C(18) 1.379(5), C(18)–C(19) 1.391(4), C(14)–C(19) 1.396(4); N–Pt–N 79.8(8), S–Pt–S 89.48(3).

The methyl substituent on the dithiolate is disordered over two positions with a relative occupancy of 50%. The molecule is essentially planar over the whole molecule with the exception of the carboxylate groups. The bpy functionality shows a 0.0437 Å deviation from the plane and the Pt(diimine)(dithiolate) unit shows a 0.0573 Å deviation from planarity. This planarity in the molecule gives rise to the packing in layers of Pt anions separated by layers of TBA counterions. It also results in large electronic delocalisation within the molecule essential for use as a solar-cell dye.

Both [Pt(5,5′-dcbpy)(tdt)] and $[TBA]_2$[Pt(5,5′-dcbpy)(tdt)] have an intense UV band at approximately 320 nm and this band is assigned to the intraligand π–π^* transition of the 5,5′-dcbpy.[27] [Pt(5,5′-dcbpy)(tdt)] shows an absorbance at 651 nm (ε = 4884 M^{-1} cm^{-1}) and $[TBA]_2$[Pt(5,5′-dcbpy)(tdt)] shows an absorbance at 558 nm (ε = 3022 M^{-1} cm^{-1}), both in DMSO (Fig. 3). These charge transfer transitions in Pt(diimine)(dithiolate) complexes have previously been assigned by Eisenberg and co-workers.[3] Charge transfer occurs from a HOMO consisting of a mixture of Pt(d) and dithiolate orbital character to a LUMO which is a low-energy π^* orbital of the 5,5′-dcbpy. The absorbance maxima of the low energy band for $[TBA]_2$-[Pt(5,5′-dcbpy)(tdt)] can be tuned between 547 nm (MeCN) and 582 nm (EtOH) in a range of organic solvents, however this change in λ_{max} values showed no obvious solvatochromic trend with respect to solvent polarity. It may be that other factors such as hydrogen bonding with the solvent also play a role in determining the energy of the band.

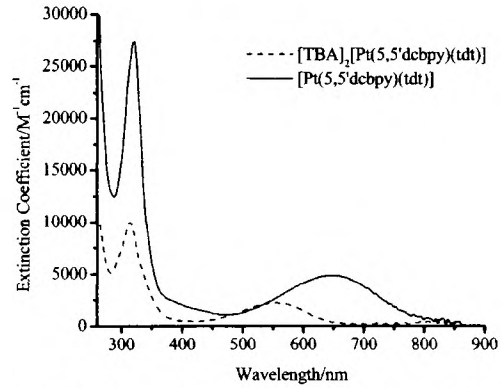

Fig. 3 UV-vis spectra of [Pt(5,5′-dcbpy)(tdt)] and $[TBA]_2$[Pt(5,5′-dcbpy)(tdt)] in DMSO.

[Pt(5,5′-dcbpy)(tdt)] and $[TBA]_2$[Pt(5,5′-dcbpy)(tdt)] were studied by cyclic voltammetry. The cyclic voltammogram of [Pt(5,5′-dcbpy)(tdt)] in a solution of DMSO shows two reduction peaks (Fig. 4) and one oxidation peak, all of which are electrochemically reversible and showed straight line plots of i_{max} *vs.* (scan rate)$^{1/2}$. The cyclic voltammogram of $[Pt(5,5'\text{-}dcbpy)(tdt)]^{2-}$ in DMSO shows one reduction and three

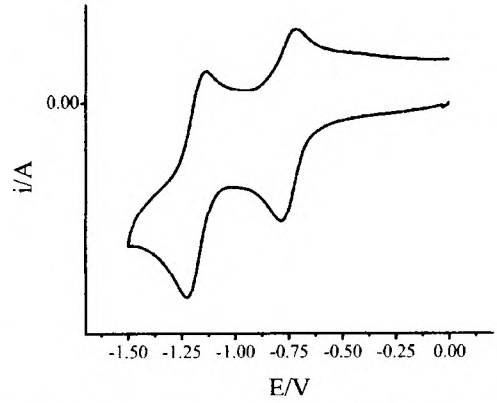

Fig. 4 Cyclic voltammogram of [Pt(5,5′-dcpby)(tdt)] showing two bpy based electrochemically reversible reductions, scan rate 0.8 V s^{-1}, in 0.1 M $TBABF_4$/DMSO at 293 K.

Table 1 Oxidation and reduction potentials for [Pt(5,5′-dcbpy)(tdt)] and $[TBA]_2$[Pt(5,5′-dcbpy)(tdt)] *vs.* Ag/AgCl

Compound	Reduction/V		Oxidation/V		
[Pt(5,5′-dcbpy)(tdt)]	−1.09[a]	−0.66[a]	0.55[a]		
$[TBA]_2$[Pt(5,5′-dcbpy)(tdt)]		−1.27[b]	0.65[b]	0.87[b]	1.1[b]

[a] Peaks are electrochemically reversible and values shown represent $E_{1/2}$. [b] Peaks are electrochemically irreversible and values shown represent peak potential.

oxidations, all of which are electrochemically irreversible. The results are shown in Table 1. Coulometric studies were performed on the oxidation of [Pt(5,5′-dcbpy)(tdt)] in an attempt to confirm the number of electrons involved in the redox process. The current passed however showed a non-integral value for electron transfer and the original complex could not be regenerated on re-reduction. This implies that during the timescale of coulometry, oxidation of [Pt(5,5′-dcbpy)(tdt)] is chemically irreversible.

It has been previously stated that the dithiolate ligand influences the oxidation potentials and the diimine ligand influences the reduction potentials of Pt(II)(diimine)(dithiolate) species, since the HOMO is partly dithiolate based and the LUMO is diimine based. The dithiolate group is identical in both [Pt(5,5′-dcbpy)(tdt)] and $[Pt(5,5'\text{-dcbpy})(tdt)]^{2-}$, hence it is expected that the oxidation potentials for both be similar. The only oxidation in [Pt(5,5′-dcbpy)(tdt)] and the first oxidation in $[Pt(5,5'\text{-dcbpy})(tdt)]^{2-}$ occur at similar potentials and this is assigned as the oxidation of the HOMO based on the dithiolate moiety in the molecule.[15] Two further oxidations are seen in $[TBA]_2$[Pt(5,5′-dcbpy)(tdt)] at higher oxidation potentials. These oxidations may represent loss of electrons from the diimine functionality due to the carboxylate anions and lie at more positive potential. Bpy complexes generally show two reductions. Both [Pt(5,5′-dcbpy)(tdt)] and $[Pt(5,5'\text{-dcbpy})(tdt)]^{2-}$ show reduction processes, however the first reduction in $[Pt(5,5'\text{-dcbpy})(tdt)]^{2-}$ occurs at a much lower reduction potential than either of the two reductions in [Pt(5,5′-dcbpy)(tdt)], reflecting the two negative charges on the carboxylate groups of $[Pt(5,5'\text{-dcbpy})(tdt)]^{2-}$ which is more difficult to reduce than the neutral species. No second reduction can be seen for $[Pt(5,5'\text{-dcbpy})(tdt)]^{2-}$ in this solvent window.

Attempts were made to follow the redox processes occurring in both [Pt(5,5′-dcbpy)(tdt)] and $[TBA]_2$[Pt(5,5′-dcbpy)(tdt)] by spectroelectrochemistry. There were difficulties, however, with interpreting these results due to the formation of unstable redox products. Changes in the UV-Vis spectra were observed for both [Pt(5,5′-dcbpy)(tdt)] and $[Pt(5,5'\text{-dcbpy})(tdt)]^{2-}$ when the first reduction process was investigated. No isosbestic points were found for either of the compounds investigated and the original compounds could not be regenerated. The oxidation of [Pt(5,5′-dcbpy)(tdt)] was also investigated but again no isosbestic points were found and the original compound could not be regenerated. All of these results proved consistent with the coulometry results previously discussed.

We were unable to observe emission from a solution of [Pt(5,5′-dcbpy)(tdt)] in DMSO dispersed in EtOH at room temperature. In a frozen solution at 77 K emission was observed (Fig. 5). Excitation of the complex at 600 nm gives an emission spectrum with a peak at 700 nm. The corresponding excitation spectrum shows a broad band between 500 and 600 nm, consistent with the position of the absorption band of [Pt(5,5′-dcbpy)(tdt)]. Compounds of the general formula Pt(NN)(SS) are typically emissive in frozen solutions and in more recent years have been found in certain cases to emit in room-temperature solutions.[28,29] It has been stated that emission in Pt(II)(diimine)(dithiolate) species is formally a spin-forbidden process where the spin character of the emissive state is different to that of the ground state.[4] Our data appear consistent with this assignment.

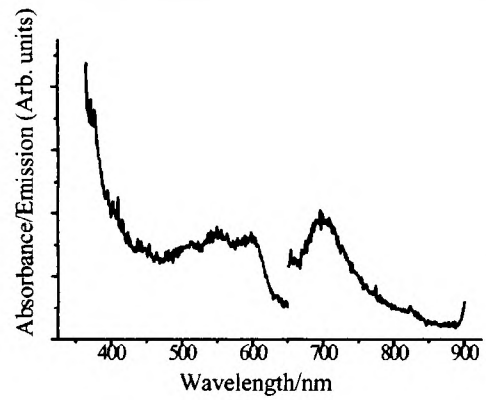

Fig. 5 Emission and corresponding excitation spectrum of a frozen solution of [Pt(5,5′-dcbpy)(tdt)] in DMSO dispersed in EtOH.

Evaluation of the dye as a photosensitiser

Photoelectrochemical measurements were taken in order to assess the dye as a photosensitiser. Dye binding was achieved by immersion of nanocrystalline TiO_2 films in a solution of the dye. Optimisation of the solvent system used for sensitisation of the films resulted in increased UV-Vis absorbance values. The optimum solution tested was a 1 : 3.2 DMSO–MeCN solution of Pt complex at a concentration of 1 mg ml^{-1}. These solutions were used to sensitise 8 μm TiO_2 films for 22 h at room temperature. The UV-Vis absorption spectrum of [Pt(5,5′-dcbpy)(tdt)] on TiO_2 exhibits a broad absorption band between 600 and 650 nm (Fig. 6) similar to that of the solution absorbance (651 nm) with a slight broadening and blue shift. The absorption spectrum for $[TBA]_2$[Pt(5,5′-dcbpy)(tdt)] on TiO_2 shows a relatively weak absorption band, red shifted (590 nm) with respect to that of the solution absorbance (558 nm). This red shift may be due to donation of electron density from the carboxylate anions to the TiO_2 on binding, thus making it a better electron acceptor and hence reducing the HOMO–LUMO gap. Dye loadings on

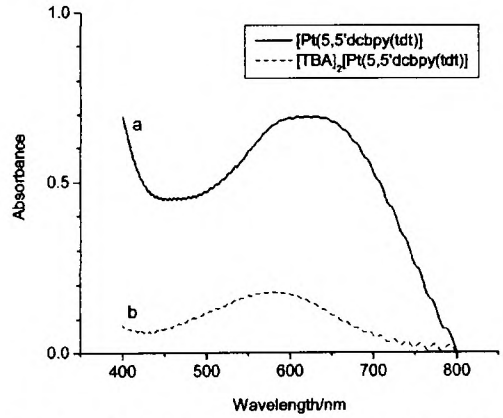

Fig. 6 UV-vis absorption spectra of platinum dyes on TiO_2: (a) [Pt(5,5′-dcbpy)(tdt)], (b) $[TBA]_2$[Pt(5,5′-dcbpy)(tdt)]. Both data were collected after dipping the 8 μm TiO_2 film in 1 mg ml^{-1} solution of the dye in DMSO ([Pt(5,5′-dcbpy)(tdt)]) and 1 : 3.2 DMSO–MeCN ($[TBA]_2$[Pt(5,5′-dcbpy)(tdt)]) for 22 h at room temperature.

Table 2 Summary of results obtained for sensitisation of nanocrystalline TiO_2 films

	Dye coverage[a]/10^{-7} mol cm^{-2}	Relative injection yield[b]	Recomb. half-time[c]/s	J_{sc}[d]/A cm^{-2}	V_{oc}[d]/V
1	1.4	1	1.7×10^{-5}	9.8×10^{-6}	8.8×10^{-3}
2	0.6	0.83	0.15	2.0×10^{-5}	0.19

[a] Dye loadings per cm^2 film estimated from UV-vis absorption spectra. [b] Relative yield of injected electrons per absorbed photon determined from the initial amplitude of the transient absorption signal in Fig. 7. [c] Recombination half-times determined from the transient absorption data shown in Fig. 7. [d] Current–voltage characteristics of dye sensitised photoelectrochemical cells under AM 1.5 simulated solar illumination. **1** = [Pt(5,5′-dcpby)(tdt)]. **2** = $[TBA]_2$[Pt(5,5′-dcpby)(tdt)].

the films were estimated employing the dye peak extinction coefficients determined in solution above, and are detailed in Table 2. In both cases, high dye loadings were achieved, consistent with the high surface area of the TiO_2 films (roughness factor ~800), with the acid form of the dye exhibiting the stronger binding.

The electron transfer function of the sensitiser dyes were evaluated by transient absorption data in the absence of redox electrolyte. Typical data are shown in Fig. 7, monitoring the photoinduced absorption of electrons injected into the TiO_2 following excitation of the sensitiser dyes. For both dyes, an instrument response limited rise was observed, assigned to rapid electron injection. The transient signal subsequently decays due to charge recombination between the injected electrons and the oxidised dye. The initial transient signal was largest with the [Pt(5,5′-dcbpy)(tdt)] sensitiser dye, attributed to the higher optical density obtained for the sensitised films with this dye, although in both cases the small magnitude of the transient signal was indicative of a low yield of electron injection (<10%). After normalising for differences in sample optical density, the initial signal magnitudes for the two dyes were similar, indicating similar injection yields for both dyes, as detailed in Table 2. In contrast, the charge recombination dynamics for the two sensitised films were very different, with the [Pt(5,5′-dcbpy)(tdt)] and $[TBA]_2$[Pt(5,5′-dcbpy)(tdt)] sensitised films exhibiting recombination half times of 1.7×10^{-5} and 0.33 s, respectively. It is furthermore apparent that the shape of the transient decay are distinct for the two dyes, with the slower dynamics being less dispersive (near monoexponential), consistent with our previous observations.[30] The slower recombination dynamics for the $[TBA]_2$[Pt(5,5′-dcbpy)(tdt)] dye are indicative of weaker electronic coupling between the dye and the TiO_2 surface, consistent with the lower dye coverage obtained with this dye. This is presumably related to the mode of binding of the sensitiser to the TiO_2 surface. We do not know exactly how [Pt(5,5′-dcbpy)(tdt)] binds to TiO_2, however previous studies using IR spectroscopy have shown that the average mode of binding of 5,5′-dcbpy ligands in Ru complexes to TiO_2 to be identical to that of 4,4′-dcbpy.[13]

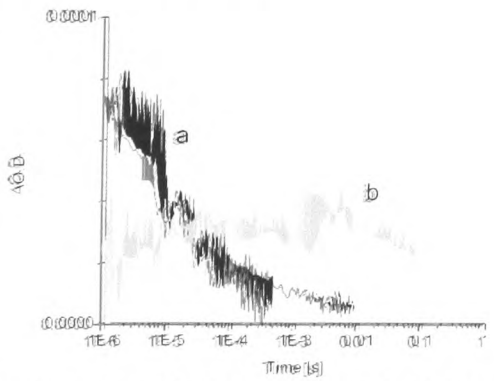

Fig. 7 Transient absorption data monitoring the photoinduced absorption of electrons injected into the TiO_2 (λ_{probe} = 1000 nm) following excitation of the sensitiser dyes at 610 nm. Data obtained for TiO_2 films sensitised with (a) [Pt(5,5′-dcbpy)(tdt)] and (b) $[TBA]_2$[Pt(5,5′-dcbpy)(tdt)].

Dye characterisation was further extended to characterisation of the photocurrent–voltage data for the dye sensitised TiO_2 in two electrode 'sandwich type' photoelectrochemical cells. Typical short circuit currents and open circuit voltages are given in Table 2. It is apparent that the better photovoltaic performance of the dyes in our study was obtained with $[TBA]_2$[Pt(5,5′-dcbpy)(tdt)], despite the lower dye loading and film optical density obtained with this dye, although for both dyes the performance is poor relative to that of [Pt(4,4′-dcbpy)(tdt)].

The electrochemistry and UV-vis spectroscopy performed on [Pt(5,5′-dcbpy)(tdt)] and $[TBA]_2$[Pt(5,5′-dcbpy)(tdt)] were consistent with related complexes[2] and allowed the analysis of the HOMO–LUMO energy gaps of the dyes. In our study, tuning the HOMO–LUMO gap was achieved by a variation made to the diimine functionality thus lowering the LUMO. In their study of Pt(diimine)(dithiolate) complexes, Arakawa and co-workers varied the dithiolate functionality of the molecule and hence altered the energy of the HOMO and the two studies show complementary results. The HOMO–LUMO energy gap as determined from the UV/Vis spectrum of both [Pt(5,5′-dcbpy)(tdt)] and $[TBA]_2$[Pt(5,5′-dcbpy)(tdt)] showed $\Delta E_{HOMO\text{-}LUMO}$ = 1.9 eV for [Pt(5,5′-dcbpy)(tdt)] and $\Delta E_{HOMO\text{-}LUMO}$ = 2.22 eV for $[TBA]_2$[Pt(5,5′-dcbpy)(tdt)]. Arakawa and co-workers showed $\Delta E_{HOMO\text{-}LUMO}$ = 2.14 eV for [Pt(4,4′dcbpy)(tdt)] in basic 4 : 1 ethanol–methanol solution. This value is comparable with our results for $[TBA]_2$[Pt(5,5′-dcbpy)(tdt)]. However, since the extent of deprotonation in [Pt(4,4′dcbpy)(tdt)] in basic 4 : 1 ethanol–methanol solution is unknown it is difficult to make a direct comparison of the HOMO–LUMO energy gaps of [Pt(4,4′-dcbpy)(tdt)] and [Pt(5,5′-dcbpy)(tdt)] from UV-Vis spectroscopic results. From the electrochemistry it can be seen that the first reduction in [Pt(5,5′-dcbpy)(tdt)] is much more facile than the first reduction in [Pt(4,4′-dcbpy)(tdt)]. This implies that placing carboxylate substituents at the 5,5′ positions of the bpy ring enhances the electron accepting ability of the complex compared to that of the 4,4′-dicarboxylate bipyridyl.

The oxidation potentials for [Pt(4,4′-dcbpy)(tdt)] and [Pt(5,5′-dcbpy)(tdt)] are comparable due to the similar nature of their dithiolate functionalities and hence their HOMOs. Thus the electrochemical data suggest we have tuned the LUMO energy to give a smaller HOMO–LUMO gap in comparison with the 4,4′-analogue. Both the present study and that of Arakawa found that dyes with longer absorption wavelengths are less efficient as solar cell sensitisers. There are a number of reasons why this may be the case.

The rate of electron injection into the conduction band of the TiO_2 is dependent on the height of the electronic state of the excited dye (LUMO) above the conduction band, therefore lowering the LUMO leads to less efficient electron injection to the TiO_2. Also, the low value of the oxidation potentials of these dyes compared to analogous dithiolate-containing complexes such as quinoxalinedithiolate (qdt) mean that regeneration of the reduced dye by the redox couple becomes more difficult due to the decrease in the energy gap between the reduced form of the redox couple (I^-) and the oxidised dye.[15] This results in more recombination of excited dye electrons with the oxidised dye. This is seen in both Pt species investigated here and in tdt

complexes in general. Rapid charge recombination dynamics for the [Pt(5,5′-dcbpy)(tdt)] dye, is also consistent with its poorer performance relative to its di-TBA salt. Furthermore, non-radiative decay of excited electrons may also have an influence on the dye efficiency. This is governed by the energy gap law for MLCT excited states which states that the rate of non-radiative decay of a CT complex increases exponentially with the corresponding decrease in HOMO–LUMO energy gap. Complexes with the tdt moiety have consistently lower extinction coefficients when compared to other Pt(diimine)-(dithiolate) species. A lower ε value means that the dye has a lower light harvesting efficiency. This is a factor in the overall IPCE (Incident-Photon-to-Current Efficiency) of the cell.

Conclusions

This work illustrated the difficulty with long-wavelength dye molecules. There is a general difficulty with low energy absorbing dyes since in lowering the energy of the LUMO, there is a decrease in electron injection from the dye to the conduction band of the semiconductor. It may not be possible to have both the LUMO at high enough energy to overcome the driving force required for electron injection and the HOMO at low enough energy to allow efficient dye reduction by the electrolyte and still retain a long wavelength absorbance. Arakawa and co-workers experienced similar difficulties in their investigation of Pt(II)(diimine)(dithiolate) dyes. On going to longer wavelengths the performance of the dyes as photosensitisers decreased dramatically. Short-wavelength dyes with higher energy LUMOs perform better as photosensitising devices and the performance of our dye is consistent with those previously reported.

References

1 S. D. Cummings and R. Eisenberg, *J. Am. Chem. Soc.*, 1996, **118**, 1949.
2 W. Paw, S. D. Cummings, M. A. Mansour, W. B. Connick, D. K. Geiger and R. Eisenberg, *Coord. Chem. Rev.*, 1998, **171**, 125.
3 M. Hissler, J. E. McGarrah, W. B. Connick, D. K. Geiger, S. D. Cummings and R. Eisenberg, *Coord. Chem. Rev.*, 2000, **208**, 115.
4 J. A. Zuleta, J. M. Bevilacqua, J. M. Rehm and R. Eisenberg, *Inorg. Chem.*, 1992, **31**, 1332.
5 J. A. Zuleta, J. M. Bevilacqua, D. M. Proserpio, P. D. Harvey and R. Eisenberg, *Inorg. Chem.*, 1992, **31**, 2396.
6 J. M. Bevilacqua and R. Eisenberg, *Inorg. Chem.*, 1994, **33**, 1886.
7 J. M. Bevilacqua and R. Eisenberg, *Inorg. Chem.*, 1994, **33**, 2913.
8 S. D. Cummings and R. Eisenberg, *Inorg. Chem.*, 1995, **34**, 3396.
9 M. K. Nazeeruddin, A. Kay, I. Rodicio, R. Humphry-Baker, E. Müller, P. Liksa, N. Vlachopoulos and M. Grätzel, *J. Am. Chem. Soc.*, 1993, **115**, 6382.
10 P. N. W. Baxter and J. A. Connor, *J. Organomet. Chem.*, 1988, **355**, 193.
11 L. Jack, PhD Thesis, University of Edinburgh, 2003.
12 E. J. L. McInnes, R. D. Farley, S. A. Macgregor, K. J. Taylor, L. J. Yellowlees and C. C. Rowlands, *J. Chem. Soc., Faraday Trans.*, 1998, **94**, 2985.
13 R. Argazzi, C. A. Bignozzi, T. A. Heimer, F. N. Castellano and G. J. Meyer, *Inorg. Chem.*, 1994, **33**, 5741.
14 A. Islam, H. Sugihara, K. Hara, L. P. Singh, R. Katoh, M. Yanagida, Y. Takahashi, S. Murata and H. Arakawa, *New J. Chem.*, 2000, **24**, 343.
15 A. Islam, H. Sugihara, K. Hara, L. P. Singh, R. Katoh, M. Yanagida, Y. Takahashi, S. Murata, H. Arakawa and G. Fujihashi, *Inorg. Chem.*, 2001, **40**, 5371.
16 F. H. Case, *J. Am. Chem. Soc.*, 1946, **68**, 2574.
17 G. M. Sheldrick, SADABS University of Göttingen, Germany, 2002.
18 G. M. Sheldrick, SHELXTL, University of Göttingen, Germany, 1997.
19 P. v. d. Sluis and A. L. Spek, *Acta Crystallogr., Sect. A*, 1990, **46**, 194.
20 S. A. McGregor, E. J. L. McInnes, R. J. Sorbie and L. J. Yellowlees, in: *Molecular Electrochemistry of Inorganic, Bioinorganic and Organometallic Compounds*, ed. A. J. L. Pombeiro and J. A. McCleverty, Kluwer, Dordrecht, 1993, p. 503.
21 R. L. Willis, C. Olson, B. O'Regan, T. Lutz, J. Nelson and J. R. Durrant, *J. Phys. Chem. B*, 2002, **106**, 7605.
22 E. Palomares, J. Clifford, S. Haque, T. Lutz and J. Durrant, *J. Am. Chem. Soc.*, 2003, **125**, 475.
23 Cambridge Structural Database F. H. Allen and O. Kennard, *Chem. Des. Autom. News*, 1993, **8**, 31.
24 C. E. Keefer, R. D. Bereman, S. T. Purrington, B. W. Knight and P. D. Boyle, *Inorg. Chem.*, 1999, **38**, 2294.
25 C. J. Adams, *J. Chem Soc., Dalton Trans.*, 2002, 1545.
26 W. B. Connick and H. B. Gray, *J. Am. Chem. Soc.*, 1997, **119**, 11620.
27 S. D. Cummings and R. Eisenberg, *Inorg. Chem.*, 1995, **34**, 2007.
28 D. L. Webb and L. A. Rossiello, *Inorg. Chem.*, 1971, **10**, 2213.
29 F. Barigelletti, D. Sandrini, M. Maestri, V. Balzani, A. Von Zelewsky, L. Chassot, P. Jolliet and U. Maeder, *Inorg. Chem.*, 1988, **27**, 3644.
30 J. N. Clifford, G. Yahioglu, L. R. Milgrom and J. R. Durrant, *Chem. Commun.*, 2002, 1260.

Inorg. Chem. 2005, 44, 242–250

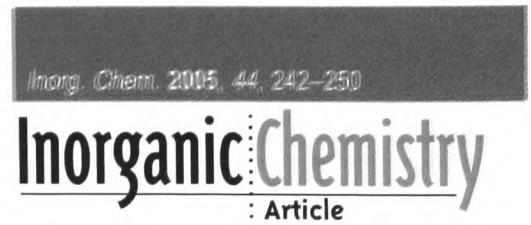

Synthesis, Structure, and Properties of [Pt(II)(diimine)(dithiolate)] Dyes with 3,3′-, 4,4′-, and 5,5′-Disubstituted Bipyridyl: Applications in Dye-Sensitized Solar Cells

Elaine A. M. Geary,[†] Lesley J. Yellowlees,[†] Lorna A. Jack,[†] Iain D. H. Oswald,[†] Simon Parsons,[†] Narukuni Hirata,[‡] James R. Durrant,[‡] and Neil Robertson*[,†]

School of Chemistry, University of Edinburgh, Joseph Black Building, Kings Buildings, West Mains Road, Edinburgh, U.K., EH9 3JJ, and Centre for Electronic Materials and Devices, Department of Chemistry, Imperial College London, U.K., SW7 2AZ

Received August 30, 2004

A family of [Pt(II)(diimine)(dithiolate)] complexes of general formula [Pt{*X*,*X*′(CO$_2$R)$_2$-2,2′-bipyridyl}(maleonitriledithiolate)] (where *X* = 3, 4, or 5 and R = H or Et) have been synthesized, spectroscopically and electrochemically characterized, and attached to a TiO_2 substrate to be tested as solar cell sensitizers. A single-crystal X-ray structure showing a large torsion angle between the bipyridyl rings was determined for [Pt{3,3′(CO$_2$Et)$_2$-2,2′-bipyridyl}(maleonitriledithiolate)]·MeCN. The effect of changing the position of the bipyridyl substituents from 3,3′ to 4,4′ and 5,5′ is discussed with reference to structural and electronic changes seen within the different members of the family of molecules. The first UV/vis/NIR spectroelectrochemical study of complexes of this general formula is discussed. All three complexes (where R = H) were tested as solar cell sensitizers, with the 3,3′-disubstituted bipyridyl complex giving an intermediate dye loading value but superior photovoltaic performance to those of the other two. The performance of this sensitizer is then compared with that of a well-known Ru polypyridyl sensitizer, the ditetrabutylammonium salt of [RuL$_2$(NCS)$_2$] (L = 2,2′-bipyridyl-4,4′-dicarboxylato), commonly called N719.

Introduction

In the early 1990s a new avenue of solar cell technology was discovered with the advent of the dye-sensitized solar cell (DSSC).[1] In recent times the synthesis of transition-metal dye molecules for use as solar cell sensitizers has received much interest. Dye molecules anchored to the surface of nanocrystalline TiO_2 absorb visible light and in their excited state they inject an electron into the conduction band of the TiO_2. Ruthenium polypyridyl dyes have received much attention due to their outstanding performance as sensitizers in DSSC, reaching efficiencies of up to 11%.[2−4] Other metal-centered dyes have also been used, including complexes of Fe,[5−7] Os,[8] and Re.[9,10] In the past few years, [Pt(II)(diimine)(dithiolate)] compounds have been investigated for their use in solar cells[11−13] as they possess a number of key features that make them of interest as sensitizers. These include an absorption band in the visible region with a relatively large molar extinction coefficient and in some cases, luminescent properties in fluid solution.

The charge-transfer transition in [Pt(II)(diimine)(dithiolate)] dyes has been assigned as a "mixed metal−ligand

* Corresponding author. Fax: +441316504743. Tel: +441316504755. E-mail: neil.robertson@ed.ac.uk

† University of Edinburgh.

‡ Imperial College London.

(1) O'Regan, B.; Graetzel, M. *Nature* **1991**, *353*, 737.
(2) Nazeeruddin, M. K.; Kay, A.; Rodicio, I.; Humphry-Baker, R.; Mueller, E.; Liska, P.; Vlachopoulos, N.; Graetzel, M. *J. Am. Chem. Soc.* **1993**, *115*, 6382.
(3) Bignozzi, C. A.; Argazzi, R.; Kleverlaan, C. J. *Chem. Soc. Rev.* **2000**, *29*, 87.
(4) Nazeeruddin, M. K.; Graetzel, M. *Comp. Coord. Chem. II* **2004**, *9*, 719.
(5) Ferrere, S. *Chem. Mater.* **2000**, *12*, 1083.
(6) Ferrere, S. *Inorg. Chim. Acta* **2002**, *329*, 79.
(7) Ferrere, S.; Gregg, B. A. *J. Am. Chem. Soc.* **1998**, *120*, 843.
(8) Sauve, G.; Cass, M. E.; Doig, S. J.; Lauermann, I.; Pomykal, K.; Lewis, N. S. *J. Phys. Chem. B* **2000**, *104*, 3488.
(9) Asbury, J. B.; Hao, E.; Wang, Y.; Lian, T. *J. Phys. Chem. B* **2000**, *104*, 11957.
(10) Wang, Y.; Asbury, J. B.; Lian, T. *J. Phys. Chem. A* **2000**, *104*, 4291.
(11) Hissler, M.; McGarrah, J. E.; Connick, W. B.; Geiger, D. K.; Cummings, S. D.; Eisenberg, R. *Coord. Chem. Rev.* **2000**, *208*, 115.
(12) Islam, A.; Sugihara, H.; Hara, K.; Singh, L. P.; Katoh, R.; Yanagida, M.; Takahashi, Y.; Murata, S.; Arakawa, H.; Fujihashi, G. *Inorg. Chem.* **2001**, *40*, 5371.
(13) Geary, E. A. M.; Hirata, N.; Clifford, J.; Durrant, J. R.; Parsons, S.; Dawson, A.; Yellowlees, L. J.; Robertson, N. *Dalton Trans.* **2003**, 3757.

10.1021/ic048799t CCC: $30.25
Published on Web 12/24/2004

to ligand" charge transfer (MMLL'CT) involving a HOMO that is a mixture of Pt(d) and dithiolate S(p) and a LUMO that involves a π^* bpy orbital.[11,14] Substituents on the diimine ligand affect the LUMO energy while substituents on the dithiolate ligand affect the HOMO energy and, therefore, the photophysical and electrochemical properties of the molecule. Tuning of these Pt dye compounds by manipulation of both the HOMO and the LUMO energy levels has been shown by several groups.[12,15] This tuning is relevant in these systems, since the electrochemical and photophysical properties of the dye greatly affect the overall performance of the solar cell.

All dyes investigated for DSSC contain a functionality that anchors the dye to the TiO_2 surface. For the majority of dyes this anchor is {4,4'$(CO_2H)_2$-bpy}, where bpy is 2,2'-bipyridyl. We are interested in what effect the position of the carboxylic acid functionality on the bpy has on the photophysical and electrochemical properties of the dye. Previous publications have shown that the LUMO energy can be altered by changing the position of the carboxylic acid on the bpy ring.[13,15] DFT calculations, electrochemistry, spectroelectrochemistry, and EPR on a family of compounds of general formula [Pt{5,5'$(X)_2$-bpy}Cl_2] (X = H, Me, CO_2Me, CO_2Et, NH_2) have shown that the electron density at the 5,5'-positions is significantly greater than the 4,4'-positions.[16] Therefore, it is expected that substituents at the 5,5'-position have more influence on the electronic characteristics of the bpy than substituents at the 4,4'- or 3,3'-positions. We have shown that by moving the COOH groups from the 4,4'- to the 5,5'-positions on the bpy ring, the HOMO−LUMO energy gap of a [Pt(II)(diimine)(dithiolate)] dye is reduced and this results in shifting the absorbance of the dye to longer wavelength.[13] Most currently available solar cell dyes absorb at shorter wavelengths, and longer wavelength dyes are therefore desirable, since they allow us to harness more of the available solar energy.

Maleonitriledithiolate (mnt) was chosen in our study as the common dithiolate for several reasons. Pt(II) compounds containing mnt have been shown to be emissive in fluid solution as well as frozen glass. The oxidation potential of these complexes is much more positive than the minimum +0.2 V required for this liquid electrolyte solar cell. Finally, previous [Pt(II)(diimine)(mnt)] complexes that have been studied have shown a strong absorption in the visible region.[17,18]

Pt coordination complexes containing a 3,3'-disubstituted bpy ligand have previously been reported in other fields, and [Pt{3,3'$(CO_2H)_2$-bpy}$(Cl)_2$] has been investigated as an anticancer agent.[19] However, no study has been reported of a [Pt(II)(diimine)(dithiolate)] complex with a 3,3'-disubstituted bpy ligand, and initial studies on solar cell dyes containing the {3,3'$(CO_2H)_2$-bpy} anchor have been limited to Ru dyes.[20] In this publication we report the synthesis, characterization, and properties of a family of [Pt(II)-(diimine)(dithiolate)] dyes where the variation lies in the position of the COOH group on the bpy ring. We include the first report of a Pt dye containing the {3,3'$(CO_2H)_2$-bpy} anchor and the first crystal structure of a 3,3'-disubstituted bpy in a [Pt(bpy)(1,2-dithiolate)] complex. Our aim is to compare the electrochemical and optical properties of dyes with carboxylic acid substituents at the 3,3'-, 4,4'-,and 5,5'-positions and assess their performances in a DSSC.

Experimental Section

1,10-Phenanthroline, {4,4'$(Me)_2$-bpy}, and {5,5'-$(Me)_2$-bpy}, purchased from Sigma-Aldrich and K_2PtCl_4, purchased from Johnson Matthey, were used as received. Na_2(*mnt*) was prepared as previously reported.[21]

Synthesis of {3,3'$(CO_2H)_2$-bpy}. {3,3'$(CO_2H)_2$-bpy} was synthesized by a previously reported method.[22] The white solid was recrystallized from water. Yield: 56.4%. Anal. Calcd for $C_{12}H_8N_2O_4$: C, 59.0; H, 3.3; N, 11.5. Found: C, 58.5; H, 3.3; N, 11.3.

Synthesis of {3,3'$(CO_2Et)_2$-bpy}. {3,3'$(CO_2Et)_2$-bpy} was synthesized by a previously reported method.[22] The product did not separate out in aqueous solution but was extracted into DCM and dried with $MgSO_4$ and the solvent removed. Yield: 72.9%. Anal. Calcd for $C_{16}H_{16}N_2O_4$: C, 64.0; H, 5.4; N, 9.3. Found: C, 62.2; H, 5.3; N, 9.0.

Synthesis of {4,4'$(CO_2H)_2$-bpy}. {4,4'$(CO_2H)_2$-bpy} was synthesized by a previously reported method.[23] Yield: 36.2%. Anal. Calcd for $C_{12}H_8N_2O_4 \cdot H_2O$: C, 55.0; H, 3.8; N, 10.7. Found: C, 54.8; H, 3.4; N, 10.8.

Synthesis of {4,4'$(CO_2Et)_2$-bpy}. {4,4'$(CO_2Et)_2$-bpy} was synthesized by a previously reported method.[23] Yield: 38.6%. Anal. Calcd for $C_{16}H_{16}N_2O_4$: C, 64.0; H, 5.4; N, 9.3. Found: C, 62.6; H, 5.0; N, 9.0.

Synthesis of {5,5'$(CO_2H)_2$-bpy}. {5,5'$(CO_2H)_2$-bpy} was synthesized by a previously reported method.[23] Yield: 63.2%. Anal. Calcd for $C_{12}H_8N_2O_4 \cdot H_2O$: C, 55.0; H, 3.8; N, 10.7. Found: C, 54.7; H, 3.4; N, 10.6.

Synthesis of {5,5'$(CO_2Et)_2$-bpy}. {5,5'$(CO_2Et)_2$-bpy} was synthesized by a previously reported method.[23] Yield: 46.6%. Anal. Calcd for $C_{16}H_{16}N_2O_4$: C, 64.0; H, 5.4; N, 9.3. Found: C, 63.2; H, 5.3; N, 9.3.

Synthesis of [Pt{3,3'$(CO_2H)_2$-bpy}Cl_2]. {3,3'$(CO_2H)_2$-bpy} (0.40 g, 1.60 mmol) and K_2PtCl_4 (0.57 g, 1.36 mmol) were refluxed in 100 mL of water for 18 h. A bright yellow powder precipitated on cooling. Yield: 94.8%. Anal. Calcd for $C_{12}H_8N_2O_4PtCl_2$: C, 28.3; H, 1.6; N, 5.5. Found: C, 29.5; H, 1.8; N, 5.6.

Synthesis of [Pt{3,3'$(CO_2Et)_2$-bpy}Cl_2]. A suspension of {3,3'$(CO_2Et)_2$-bpy} (0.115 g, 0.38 mmol) and K_2PtCl_4 (0.13 g, 0.32 mmol) was refluxed in 40 mL of water for 18 h.[22] A bright yellow powder precipitated on cooling. Yield: 70.3%. Anal. Calcd for $C_{16}H_{16}N_2O_4PtCl_2$: C, 33.9; H, 2.8; N, 4.9. Found: C, 34.4; H, 3.2; N 4.7.

(14) Cummings, S. D.; Eisenberg, R. *J. Am. Chem. Soc.* **1996**, *118*, 1949.
(15) Paw, W.; Cummings, S. D.; Mansour, M. A.; Connick, W. B.; Geiger, D. K.; Eisenberg, R. *Coord. Chem. Rev.* **1998**, *171*, 125.
(16) McInnes, E. J. L.; Farley, R. D.; Macgregor, S. A.; Taylor, K. J.; Yellowlees, L. J.; Rowlands, C. C. *J. Chem. Soc., Faraday Trans.* **1998**, *94*, 2985.
(17) Zuleta, J. A.; Burberry, M. S.; Eisenberg, R. *Coord. Chem. Rev.* **1990**, *97*, 47.
(18) Zuleta, J. A.; Bevilacqua, J. M.; Eisenberg, R. *Coord. Chem. Rev.* **1991**, *111*, 237.
(19) Yoo, J.; Kim, J.-H.; Sohn, Y. S.; Do, Y. *Inorg. Chim. Acta* **1997**, *263*, 53.
(20) Xie, P.-H.; Hou, Y.-J.; Wei, T.-X.; Zhang, B.-W.; Cao, Y.; Huang, C.-H. *Inorg. Chim. Acta* **2000**, *308*, 73.
(21) Markl, G.; Vybiral, R. *Tetrahedron Lett.* **1989**, *30*, 2903.
(22) Dholakia, S.; Gillard, R. D.; Wimmer, F. L. *Polyhedron* **1985**, *4*, 791.
(23) Case, F. H. *J. Am. Chem. Soc.* **1946**, *68*, 2574.

Synthesis of [Pt{4,4′(CO$_2$H)$_2$-bpy}Cl$_2$]. [Pt{4,4′(CO$_2$H)$_2$-bpy}Cl$_2$] was synthesized by a previously reported method.[12] Yield: 87.9%. Anal. Calcd for $C_{12}H_8N_2O_4PtCl_2$: C, 28.3; H, 1.6; N, 5.5. Found: C, 28.5; H, 2.0; N, 5.7.

Synthesis of [Pt{4,4′(CO$_2$Et)$_2$-bpy}Cl$_2$]. [Pt{4,4′(CO$_2$Et)$_2$-bpy}Cl$_2$] was synthesized in the same manner as the 3,3′-analogue. Yield: 76.1%. Anal. Calcd for $C_{16}H_{16}N_2O_4PtCl_2$: C, 33.9; H, 2.8; N, 4.9. Found: C, 32.9; H, 2.4; N, 4.9.

Synthesis of [Pt{5,5′(CO$_2$H)$_2$-bpy}Cl$_2$]. [Pt{5,5′(CO$_2$H)$_2$-bpy}Cl$_2$] was synthesized by a previously reported method.[13] Yield: 71.8%. Anal. Calcd for $C_{12}H_8N_2O_4PtCl_2$: C, 28.3; H, 1.6; N, 5.5. Found: C, 28.8; H, 1.7; N, 5.5.

Synthesis of [Pt{5,5′(CO$_2$Et)$_2$-bpy}Cl$_2$]. [Pt{5,5′(CO$_2$Et)$_2$-bpy}Cl$_2$] was synthesized in the same manner as the 3,3′-analogue. Yield: 76.2%. Anal. Calcd for $C_{16}H_{16}N_2O_4PtCl_2$: C, 33.9; H, 2.8; N, 4.9. Found: C, 33.0; H, 2.7; N, 4.8.

Synthesis of [Pt{3,3′(CO$_2$H)$_2$-bpy}(mnt)] (1a). [Pt{3,3′(CO$_2$H)$_2$-bpy}Cl$_2$] (0.80 g, 1.57 mmol) was dissolved in 2 equiv of 1 M aqueous solution of potassium hydroxide under nitrogen, and a solution of Na$_2$(mnt) (0.44 g, 2.36 mmol) in dry methanol (5 mL) was added. The reaction was allowed to stir at room temperature under N_2 for 48 h. The product was precipitated using 2 equiv of concentrated HCl and filtered. It was subsequently purified by column chromatography using Sephadex-LH20 as a separating medium by a method previously described.[12] Yield: 20.0%. MS (FABMS) *m/z*: 580 (M$^+$). Anal. Calcd for $C_{16}H_8N_4O_4PtS_2$: C, 33.2; H, 1.4; N, 9.7. Found: C, 32.4; H, 1.9; N, 9.0.

Synthesis of [Pt{3,3′(CO$_2$Et)$_2$-bpy}(mnt)] (1b). [Pt{3,3′-(CO$_2$Et)$_2$-bpy}Cl$_2$] (0.47 g, 0.83 mmol) was dissolved in dry acentonitrile under nitrogen and a solution of Na$_2$(mnt) (0.23 g, 1.24 mmol) in dry methanol (5 mL) was added. The reaction was allowed to stir at room temperature under N_2 for 4 h. The solvent was removed and the product was washed with methanol before recrystallization from acentonitrile. Yield: 22.1%. MS (FABMS) *m/z*: 636 (M$^+$). IR (KBr, cm^{-1}): 1729 (s) (C=O stretch), 2204 (s) (C≡N stretch). Anal. Calcd for $C_{20}H_{16}N_4O_4PtS_2$: C, 37.8; H, 2.5; N, 8.8. Found: C, 37.3; H, 2.5; N, 8.6.

Synthesis of [Pt{4,4′(CO$_2$H)$_2$-bpy}(mnt)] (2a). Compound **2a** was synthesized by an analogous method to compound **1a**. Yield: 28.5%. MS (FABMS) *m/z*: 580 (M$^+$). Anal. Calcd for $C_{16}H_8N_4O_4PtS_2$: C, 33.2; H, 1.4; N, 9.7. Found: C, 32.2; H, 2.1; N 9.0.

Synthesis of [Pt{4,4′(CO$_2$Et)$_2$-bpy}(mnt)] (2b). [Pt{4,4′-(CO$_2$Et)$_2$-bpy}Cl$_2$] (0.14 g, 0.25 mmol) was dissolved in DMF (15 mL) and heated under nitrogen to just below the boiling point (140 °C). A solution of Na$_2$(mnt) (0.07 g, 0.37 mmol) in dry methanol (5 mL) was added and the reaction mixture was refluxed with stirring under N_2 for 1 h and then allowed to stir under N_2 at room temperature overnight. The solvent was removed and the product was washed with water and methanol before recrystallization from a hot saturated solution of DMF. Yield: 72.0%. MS (FABMS) *m/z*: 636 (M$^+$). IR (KBr, cm^{-1}): 1730 (s) (C=O stretch), 2207 (s) (C≡N stretch). Anal. Calcd for $C_{20}H_{16}N_4O_4PtS_2$: C, 37.8; H, 2.5; N, 8.8. Found: C, 38.0; H, 3.1; N, 8.6.

Synthesis of [Pt{5,5′(CO$_2$H)$_2$-bpy}(mnt)] (3a). Compound **3a** was synthesized by an analogous method to compound **1a**. Yield: 18.0%. MS (FABMS) *m/z*: 580 (M$^+$). Anal. Calcd for $C_{16}H_8N_4O_4PtS_2$: C, 33.2; H, 1.4; N, 9.7. Found: C, 32.1; H, 2.1; N 8.0.

Synthesis of [Pt{5,5′(CO$_2$Et)$_2$-bpy}(mnt)] (3b). [Pt{5,5′(CO$_2$Et)$_2$-bpy}Cl$_2$] (0.25 g, 0.44 mmol) was suspended in DMSO (15 mL) under nitrogen and a solution of Na$_2$(mnt) (0.12 g, 0.66 mmol) in dry methanol (5 mL) was added. The reaction was allowed to stir at room temperature under N_2 for 48 h. The solvent was removed and the product was recrystallized from a hot saturated solution of DMF. Yield: 60.0%. MS (FABMS) *m/z*: 636 (M$^+$). IR (KBr, cm^{-1}): 1725 (s) (C=O stretch), 2208 (s) (C≡N stretch). Anal. Calcd for $C_{20}H_{16}N_4O_4PtS_2$: C, 37.8; H, 2.5; N, 8.8. Found: C, 35.6; H, 2.6; N 7.7.

Table 1. Crystallographic Data for 1b

chemical formula	$C_{22}H_{19}N_5O_4PtS_2$	D_c, Mg m^{-3}	1.898
fw	676.65	μ, mm^{-1}	6.140
T, K	150	reflcts collected	21845
lattice type	monoclinic	unique (R_{int})	5694 (0.07)
space group	$P2_1/c$	no. $I > 2\sigma$	3856
a, Å	14.7735(15)	T_{min}/T_{max}	0.217/1.000
b, Å	21.632(2)	parameters	153
c, Å	7.5450(7)	R_1 [$F > 4\sigma(F)$]	0.0665
β, deg	100.815(4)	wR	0.0751
V, Å^3	2368.4(4)	S	1.0402
no. reflns for cell	4515	$\Delta\rho_{max}$/e Å^{-3})	6.91
$2\theta_{max}$ (deg)	50	$\Delta\rho_{min}$/e Å^{-3}	−4.03
Z	4		

X-ray Crystallography. Purple needle-shaped crystals of [Pt{3,3′(CO$_2$Et)$_2$bpy}(mnt)] (**1b**) (dimensions 1.00 × 0.08 × 0.06 mm^3) were grown by recrystallization from a hot saturated solution of **1b** in acetonitrile. Crystal, data collection, and refinement parameters are summarized in Table 1.

Single-crystal X-ray structure determination was carried out using a Smart APEX CCD diffractometer equipped with an Oxford Cryosystems low-temperature device with Mo Kα radiation for data collection. An absorption correction was applied using the multiscan procedure SADABS.[24] The structure was solved by direct methods and refined by full-matrix least squares against $|F|$ using data where $I > 2\sigma(I)$.[25] Hydrogen atoms were placed in calculated positions. The platinum and sulfur atoms were refined with anisotropic displacement parameters (adps). Other light atoms (C, N, O) were refined isotropically; adps for these atoms were rather distorted when refined, while not significantly contributing to better data-fitting.

Other Experimental Information. All UV/vis spectra were recorded on a Perkin-Elmer Lambda 9 spectrophotometer controlled by a Datalink PC, running UV/Winlab software.

Electrochemical studies were carried out using a DELL GX110 PC with General Purpose Electrochemical System (GPES), version 4.8, software connected to an autolab system containing a PGSTAT 20 potentiostat. The techniques used a three-electrode configuration, with a 0.5 mm diameter Pt disk working electrode, a Pt rod counter electrode, and an Ag/AgCl (saturated KCl) reference electrode against which the ferrocenium/ferrocene couple was measured to be +0.55 V. The supporting electrolyte was 0.1 M tetrabutylammonium tetrafluoroborate (TBABF$_4$).

OTTLE (optically transparent thin layer electrode) measurements were taken using a quartz cell of 0.5 mm, a Pt/Rh gauze working electrode, an Ag/AgCl reference electrode, and a Pt wire counter electrode.[26] UV/vis spectra were recorded on a Perkin-Elmer Lambda 9 spectrophotometer, controlled by a Datalink PC, running UV/Winlab software. Spectroelectrochemical measurements were carried out on each of compounds **1b**, **2b**, and **3b**. Measurements on all samples were carried out at 213 K in DMF. TBABF$_4$ (0.1 M) was used as the supporting electrolyte in all cases.

Electronic emission spectra were recorded on a Jobin Yvon Spex Fluoromax spectrofluorimeter, connected to a DSC Datalink PC

(24) Sheldrick, G. M. *SADABS. Bruker-AXS* **1997**.
(25) Betteridge, P. W.; Carruthers, J. R.; Cooper, R. I.; Prout, K.; Watkin, D. J. *J. Appl. Crystallogr.* **2003**, *36*, 1487.
(26) McGregor, S. A.; McInnes, E. J. L.; Sorbie, R. J.; Yellowlees, L. J. *Molecular Electrochemistry of Inorganic, Bioinorganic and Organometallic Compounds*; Kluwer: Dordrecht, The Netherlands, 1993; p 503.

Scheme 1. Preparation of Complexes **1a**, **2a**, **3a**, **1b**, **2b**, and **3b**[a]

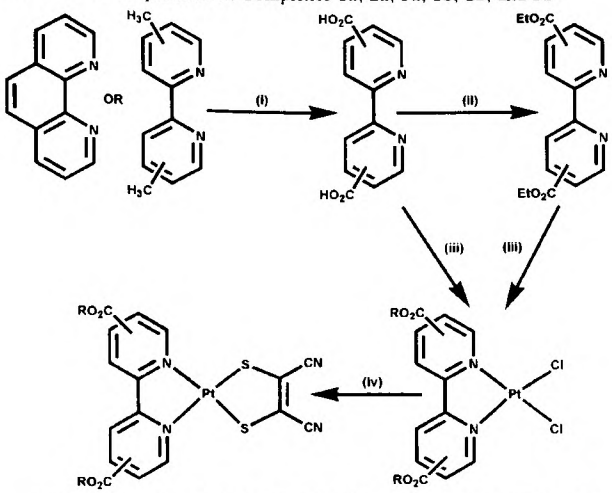

[a] (i) $KMnO_4$(aq), 120 °C/HCl; (ii) $EtOH/H_2SO_4$, 115 °C; (iii) K_2PtCl_4, 125 °C; (iv) Na_2(mnt), rt (140 °C for **2b**).

running Instruments S. A. Datamax software. All emission spectra were recorded with compounds **1b**, **2b**, and **3b** dissolved in DMSO and dispersed in EtOH. All frozen spectra were recorded in standard Wilmad 5 mm quartz NMR tubes contained in a liquid nitrogen filled fused silica dewar.

Nanoporous TiO_2 thin films (4 μm thick) on FTO conductive glass were prepared as previously reported.[27] The size of all samples was 1 cm^2. The thin films were sensitized at room temperature for 21 h in a 1.7 mM solution of **1a** in DMSO:MeCN (1:1) and a 1.7 mM solution of **2a** and **3a** both in DMSO. Device fabrication was completed as previously described by employing "sandwich type" photovoltaic cells with I^-/I_3^- system electrolyte and a transparent platinized FTO counter electrode. [28] The electrolyte used contained 0.1 M LiI, 0.8 M TBAI, 0.1 M I_2, and 0.5 M ^{t}BuPy in acetonitrile. The working electrode had an illuminated surface area of 1.0 cm^2. Transient absorption studies were carried out as reported previously, employing an excitation wavelength of 540 nm.[27] Photoelectrochemical measurements were conducted under AM 1.5 simulated sunlight as detailed previously.[28]

Results and Discussion

Synthesis and Structure. The [Pt{*X*,*X*′(CO_2H)$_2$-bpy}(mnt)] (*X*,*X*′ = 3,3′, 4,4′, or 5,5′) complexes (**1a**, **2a**, and **3a**) were synthesized by a route analogous to those reported previously.[12,13] The dicarboxylic acid substituted-bpy ligand was made by oxidation of 1,10-phenanthroline to give the 3,3′-dicarboxylic acid product and by oxidation of the 4,4′- and 5,5′-dimethyl-substituted bpy to give the 4,4′- and 5,5′-dicarboxylic acid products, respectively. Reaction of {*X*,*X*′(CO_2H)$_2$-bpy} with potassium tetrachloroplatinate gave the dichloro-substituted platinum precursors [Pt{*X*,*X*′(CO_2H)$_2$-bpy}Cl_2]. Further reaction of these molecules with the disodium salt of mnt gave the desired products **1a**, **2a**, and **3a** (Scheme 1).

Compounds **1b**, **2b**, and **3b** were synthesized to facilitate characterization of the dye molecules, since they are soluble

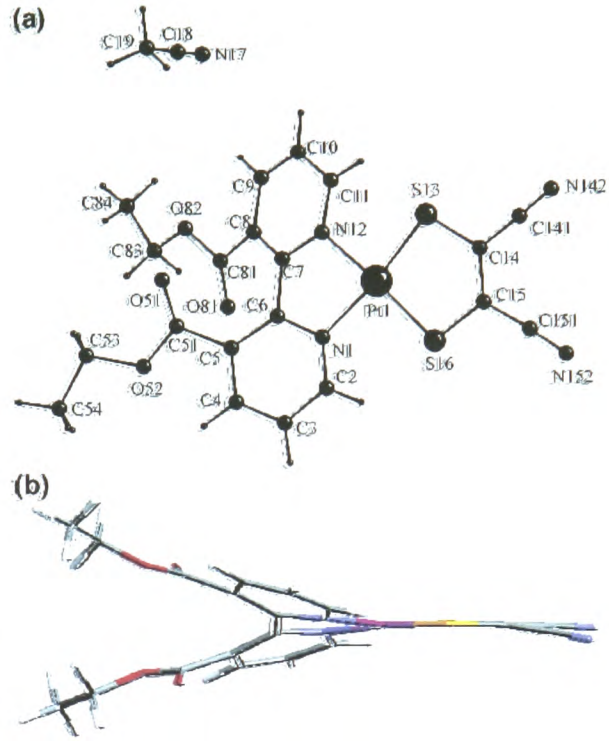

Figure 1. (a) X-ray crystal structure of **1b**. Selected bond lengths (Å) and angles (deg): Pt−S(13), 2.258(2); Pt−S(16), 2.245(3); Pt−N(1), 2.074(10); Pt−N(12), 2.058(8); N(1)−Pt−N(12), 79.4(3); N(12)−Pt−S(13), 96.2(2); S(13)−Pt−S(16), 89.54(9); S(16)−Pt−N(1), 95.3(1). (b) X-ray crystal structure of **1b** with a view down the C=C bond of mnt, showing the large torsion angle induced between the pyridyl rings by the 3,3′CO_2Et substituents. Sulfur atoms are shown in yellow, platinum in pink, carbon in gray, nitrogen in pale blue, oxygen in red, and hydrogen in white.

in a greater number of organic solvents, including DMF and acetonitrile. They were synthesized by a method similar to those of compounds **1a**, **2a**, and **3a**. Esterification of {*X*,*X*′(CO_2H)$_2$-bpy} gave {*X*,*X*′(CO_2Et)$_2$-bpy} and refluxing these ligands with potassium tetrachloroplatinate gave the dichloro-substituted platinum precursors [Pt{*X*,*X*′(CO_2Et)$_2$-bpy}Cl_2]. Further reation of these molecules with the disodium salt of mnt gave the desired products **1b**, **2b**, and **3b** (Scheme 1).

Only 12 crystal structures of [Pt(bpy)(1,2-dithiolate)] systems have previously been reported.[29] Five of the 12 structures have a 4,4′-disubstituted bpy, one is a 5,5′-disubstituted bpy, and the remaining six feature an unsubstituted bpy. Only 10 structures are known of any complex where Pt is attached to a 3,3′-disubstituted bpy. There have, however, been no previous reports of a crystal structure with a 3,3′-disubstituted bpy in a [Pt(bpy)(dithiolate)] complex. The structure of **1b** shows bond lengths and angles to be similar to those for [Pt(bpy)(dithiolate)] complexes previously reported (Figure 1a).[29] The [Pt(bpy)(dithiolate)] unit shows a 0.0768 Å deviation from planarity. In general, bpy ligands have been seen to retain a planar geometry at square planar Pt centers. Only four of the 12 published [Pt(bpy)(1,2-

(27) Willis, R. L.; Olson, C.; O'Regan, B.; Lutz, T.; Nelson, J.; Durrant, J. R. *J. Phys. Chem. B* **2002**, *106*, 7605.
(28) Palomares, E.; Clifford, J. N.; Haque, S. A.; Lutz, T.; Durrant, J. R. *J. Am. Chem. Soc.* **2003**, *125*, (2), 475.
(29) Cambridge Structural Database. *Chem. Des. Autom. News* **1993**, *8*, 31.

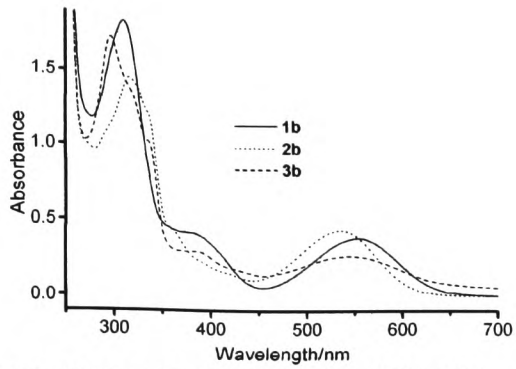

Figure 2. UV/vis spectra of **1b**, **2b**, and **3b** in DMF at 298 K.

Table 2. Absorption Maxima and Molar Extinction Coefficients for Compounds **1b**, **2b**, and **3b** (in Solution of DMF)

compd	λ_{max}/nm (ν/cm^{-1})	ϵ/M^{-1} cm^{-1}
1b	556 (18 000)	4200
2b	537 (18 640)	5600
3b	546 (18 330)	3100

dithiolate)] structures show a bpy torsion angle of greater than 5° and the greatest of these is only 12.7° (in a 4,4′-^{t}Bu$_2$ substituted bpy). Three of these examples occur in 4,4′-^{t}Bu$_2$-substituted bpy ligands and one in an unsubstituted bpy ligand.[30,31] Unsurprisingly, the steric interference between the ethyl chains on the ester substituents of **1b** causes a twist in the pyridine rings with respect to one another. This results in a significant torsion angle of 30.7° between the pyridine rings in the 3,3′-disubstituted bpy moiety, the largest known angle in any [Pt(bpy)(1,2-dithiolate)] complex. This is only slightly smaller than the largest torsion angle of 31.1°, where in a [Pt(bpy)(Cl)$_2$] complex the 3,3′-positions of bpy were substituted with a crown ether.[32] The twisting of the two pyridine rings with respect to each other as seen in the crystal structure may in some part help in the explanation of the interesting electrochemistry of the complex (see Figure 1b). The complex packs in layers with short contacts of 3.488 and 3.810 Å between the sulfur atom on the mnt and the carbonyl oxygen atom from the ester group on the bpy.

UV/Visible Spectroscopy. The UV/vis spectra of compounds **1b**, **2b**, and **3b** in solution show an intense UV band at approximately 300 nm (Figure 2) assigned to the intraligand $\pi-\pi^*$ transition of the diethyl ester-bpy ligand.[14] The charge-transfer band of compounds **1b**, **2b**, and **3b** stretches from 450 to 650 nm with absorbance maxima listed in Table 2. The charge transfer band in [Pt(diimine)(dithiolate)] complexes has previously been assigned by Eisenberg and co-workers. This CT is said to occur from a HOMO consisting of a mixture of Pt(d) and dithiolate(p) orbital character to a low-energy π^* orbital LUMO located on the bpy.[11,14]

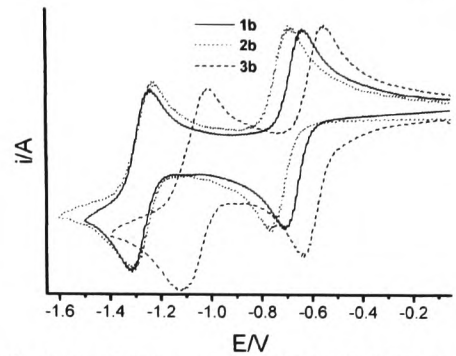

Figure 3. Cyclic voltammogram of **1b**, **2b**, and **3b** showing the two bpy based electrochemically reversible reductions, scan rate 0.1 V s^{-1}, in 0.1 M TBABF$_4$/DMF at 298 K.

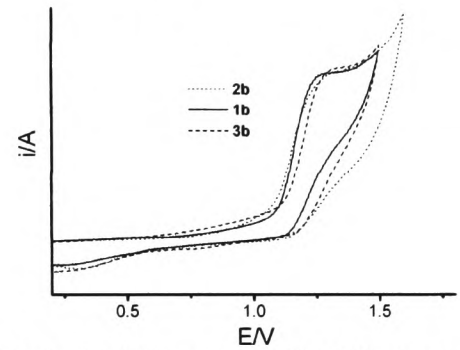

Figure 4. Cyclic voltammogram of **1b**, **2b** and **3b**, showing the partly mnt based irreversible oxidation, scan rate 0.1 V s^{-1}, in 0.1 M TBABF$_4$/DMF at 298 K.

Table 3. Oxidation and Reduction Potentials for Compounds **1a**, **2a**, **3a**, **1b**, **2b**, and **3b** vs Ag/AgCl in Solution of 0.1 M TBABF$_4$/DMF at 298 K

compd	reduction/V		oxidation/V
1a	−1.05[b]	−0.69[b]	+1.27[b]
2a	−1.19[b]	−0.82[b]	+1.27[b]
3a	−1.16[b]	−0.69[b]	+1.27[b]
1b	−1.20[a]	−0.59[a]	+1.35[b]
2b	−1.20[a]	−0.65[a]	+1.39[b]
3b	−0.99[a]	−0.52[a]	+1.41[b]

[a] Peaks are electrochemically reversible and values shown represent $E_{1/2}$. [b] Peaks are electrochemically irreversible and values shown represent peak potential.

Electrochemistry. The electrochemistry of compounds **1b**, **2b**, and **3b** was studied by cyclic voltammetry. All of the scans (in a solution of DMF/0.1 M TBABF$_4$) show two fully reversible reduction peaks (Figure 3), as evidenced by straight line plots of i_{max} vs (scan rate)$^{1/2}$ and one irreversible oxidation peak (Figure 4) (see also Table 3). Previous studies have shown that the diimine ligand influences the reduction potential of the compound and the dithiolate ligand influences the oxidation potential, since the LUMO resides on the bpy and the HOMO is at least partly dithiolate based.[12−14] The oxidation for all three ester dyes occurs at very similar potentials; therefore, this is assigned as the oxidation of the HOMO on the dithiolate moiety. The dithiolate moiety is identical in all three of the complexes; hence, it is expected that these oxidations will occur at similar potentials. Both of the reductions on **3b** occur at the least negative potential

(30) Kubo, K.; Nakano, M.; Tamura, H.; Matsubayashi, G.-E. *Inorg. Chim. Acta* **2002**, *336*, 120.
(31) Smucker, B. W.; Hudson, J. M.; Omary, M. A.; Dunbar, K. R. *Inorg. Chem.* **2003**, *42*, 4714.
(32) Gund, A.; Keppler, B. K. *Angew. Chem., Int. Ed. Engl.* **1994**, *33*, 186.
(33) Heath, G. A.; Yellowlees, L. J.; Braterman, P. S. *Chem. Commun.* **1981**, 287.
(34) Coombe, V. T.; Heath, G. A.; MacKenzie, A. J.; Yellowlees, L. J. *Inorg. Chem.* **1984**, *23*, 3423.

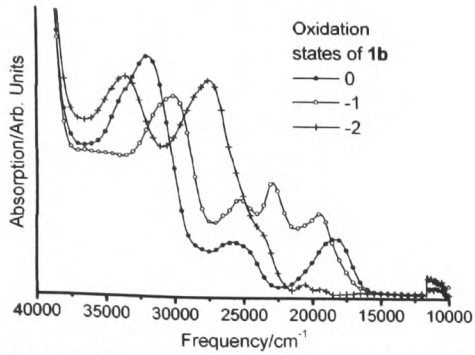

Figure 5. UV/vis/NIR of **1b** in 0, −1, and −2 oxidation states. Spectra were run in 0.1 M $TBABF_4$/DMF at 213 K. E_{gen} = 0 V (0), −1.0 V (−1), −1.6 V (−2).

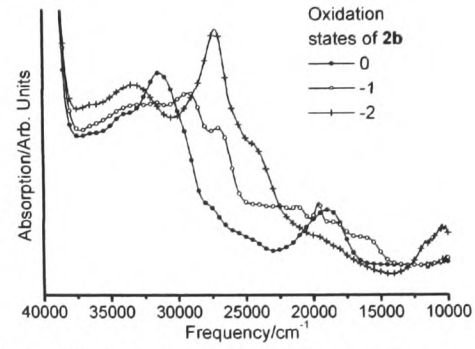

Figure 6. UV/vis/NIR of **2b** in 0, −1, and −2 oxidation states. Spectra were run in 0.1 M $TBABF_4$/DMF at 213 K. E_{gen} = 0 V (0), −1.0 V (−1), −1.6 V (−2).

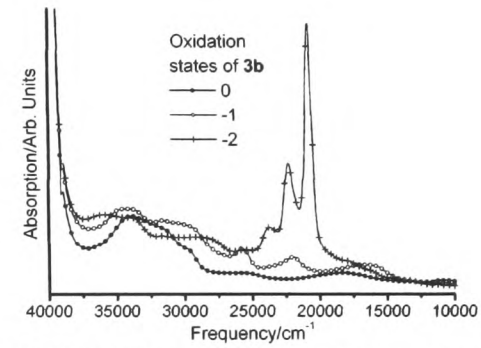

Figure 7. UV/vis/NIR of **3b** in 0, −1, and −2 oxidation states. Spectra were run in 0.1 M $TBABF_4$/DMF at 213 K. E_{gen} = 0 V (0), −0.8 V (−1), −1.3 V (−2).

of the three compounds, consistent with our previous findings.[13] This is due to the more electron withdrawing nature of the 5,5′-position of the bpy ring with respect to its 4,4′- and 3,3′-analogues. The first reduction potential of **1b** occurs at less negative potential than that of **2b**. As the crystal structure of **1b** shows a significant torsion angle (30.7°) between the two pyridine rings of the bpy moiety, this lack of planar character may interfere with the delocalization of charge between the two pyridine rings in the bpy, thus causing it to behave more like two separate pyridine rings than a bpy functionality. Therefore, the electrochemical response of 3,3′-disubstituted bpy is influenced by both electronic and steric effects and this results in its electrochemistry being intermediate between that of the 5,5′- and 4,4′-disubstituted ligands. The cyclic voltammetry of compounds **1a**, **2a**, and **3a** in DMF showed very similar oxidation and reduction potentials to those of **1b**, **2b**, and **3b**. In addition to this, the similarity of the UV/vis spectra of **1b**, **2b**, and **3b** in DMF and those of **1a**, **2a**, and **3a** on TiO_2 enables the data for **1b**, **2b**, and **3b** in solution to be used as models for **1a**, **2a**, and **3a** on TiO_2 (see Table 3).

Spectroelectrochemistry. UV/vis/NIR spectroelectrochemistry was performed to electronically characterize the frontier orbitals of compounds **1b**, **2b**, and **3b**. This involved electrochemical reduction of **1b**, **2b**, and **3b** to $\mathbf{1b}^{1-}$, $\mathbf{2b}^{1-}$, and $\mathbf{3b}^{1-}$ and also to $\mathbf{1b}^{2-}$, $\mathbf{2b}^{2-}$, and $\mathbf{3b}^{2-}$, respectively. The irreversible nature of the one-electron oxidation process precludes spectroelectrochemical study of the oxidized molecules. Each of the neutral complexes shows a similar spectrum with several diagnostic peaks present (Figures 5−7). Peaks at greater than 30 000 cm^{-1} are assigned as $\pi-\pi^*$ intraligand bpy transitions, as previously reported.[14] In **1b**, **3b**, and as a broad shoulder in **2b**, the absorbance at approximately 26 000 cm^{-1} is assigned as a mainly Pt-based d−π^* MLCT. Each of the three neutral compounds shows an absorbance at approximately 19 000 cm^{-1}, which is assigned as MMLL′CT verified by the absence of the peak in each of the corresponding $[Pt\{X,X'(CO_2Et)_2\text{-bpy}\}Cl_2]$ precursors. The three monoreduced species $\mathbf{1b}^{1-}$, $\mathbf{2b}^{1-}$, and $\mathbf{3b}^{1-}$ show similar spectral properties to each other (Figures 5−7). On reduction there is a decrease in the intensity of the $\pi-\pi^*$ absorbance of the bpy ligand above 30 000 cm^{-1}. Furthermore, all three monoreduced species show a multiplet of bands in the visible region. Similar peaks are also observed in the spectra of the related dichloride species $[Pt\{X,X'(CO_2Et)_2\text{-bpy}\}Cl_2]^{1-}$; hence, the reduction electron appears to enter an orbital primarily based on the derivatized bpy ligand, consistent with the results of the electrochemical study. No additional features may be observed that differ between the $[Pt\{X,X'(CO_2Et)_2\text{-bpy}\}Cl_2]^{1-}$ and $[Pt\{X,X'(CO_2Et)_2\text{-bpy}\}(mnt)]^{1-}$ spectra; therefore, the bands in $[Pt\{X,X'(CO_2Et)_2\text{-bpy}\}(mnt)]^{1-}$ complexes may be confidently assigned as intraligand transitions of the monoreduced derivatized bpy ligand.

The spectra of the direduced species $\mathbf{1b}^{2-}$, $\mathbf{2b}^{2-}$, and $\mathbf{3b}^{2-}$ are all very different from the monoreduced species with $\mathbf{1b}^{2-}$ and $\mathbf{2b}^{2-}$ being similar and $\mathbf{3b}^{2-}$ showing a very intense absorption centered at 22 500 cm^{-1}. Once again the spectra are remarkably consistent with those of $[Pt\{X,X'(CO_2Et)_2\text{-bpy}\}Cl_2]^{2-}$, and it can therefore be concluded that the second reduction electron is entering an orbital primarily based on the derivatized bpy ligand. Hence, all bands in the low-energy region of the absorption spectra are assigned to the intraligand transitions of the direduced bpy ligand.

In every case, after recording the final spectra the potential was adjusted so that the neutral starting material was regenerated, and the absorption spectra were observed to return to exactly that of the starting species. Thus, the monoreduced and direduced species are all stable at 213 K.

Luminescence Studies. We observed weak emission from a solution of each of compounds **1b**, **2b**, and **3b** in DMSO

Table 4. Emission and Corresponding Excitation Values for Compounds **1b**, **2b**, and **3b** in Frozen Glass of DMSO Dispersed in EtOH

compd	emission observed (nm) after excitation at 550 nm	excitation peaks (nm) corresponding to emission at tabulated wavelength
1b	655	375, 525, 565
2b	630	345, 420, 555
2b	680	not observed
3b	670	370, 495, 530, 575
3b	735	400−530,[a] 575

[a] Broad band absorbance.

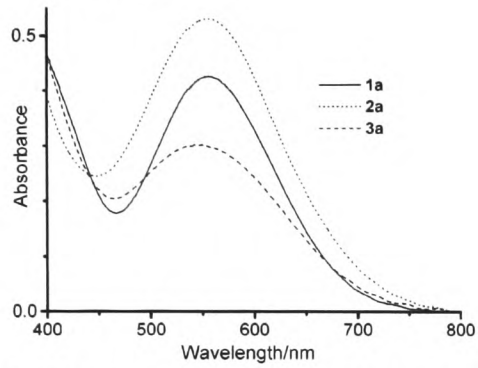

Figure 8. UV/vis measurement for nanoporous TiO_2 sensitized by dyes **1a**, **2a**, and **3a**.

dispersed in EtOH at room temperature. Each of the complexes showed similar emissive properties. Excitation of the complexes at 550 nm gave an emission spectrum with a peak at approximately 700 nm. The corresponding excitation spectra showed a peak at approximately 450 nm. In a frozen solution at 77 K, much stronger emission was observed. The emission and corresponding excitation values for **1b**, **2b**, and **3b** are shown in Table 4. The observed excitation wavelengths correspond largely to those seen in the absorption spectra of **1b**, **2b**, and **3b**, thus confirming **1b**, **2b**, and **3b** to be the emissive species in solution. This observation of emission in fluid solution confirms that the excited-state lifetime of these complexes is long in comparison with the time scale of electron injection into the TiO_2 conduction band. To draw further conclusions from these preliminary results, a more detailed study of the lifetimes of the emitting states involved in the luminescence is currently underway.

Sensitization of Nanocrystalline TiO_2 Films. Immersion of nanocrystalline TiO_2 in 1.7 mM solutions of dyes **1a** (in 1:1 MeCN/DMSO), **2a** (in DMSO), and **3a** (in DMSO) resulted in a strong coloration of the films. UV/visible absorption spectra for the resulting dye sensitized films are shown in Figure 8 and in all cases exhibit similar 540−550 nm absorption maxima to that observed for the solution spectra of **1b**, **2b**, and **3b** (Figure 2).

Dye loadings were determined from these film spectra by assuming the molar extinction coefficients determined in solution. These are summarized in Table 5. It is apparent that approximately monolayer dye coverage is achieved for all three dyes, with differences in film optical density primarily arising from the differences in dye molar extinction coefficient.

Table 5. Summary of Results Obtained for Sensitization of Nanocrystalline TiO_2 Films with **1a**, **2a**, and **3a**

	optical density on TiO_2 films[a]	dye coverage ratio[b]	half-times for recombination decay/s[c]	I_{sc}/mA/cm^2 [d]	V_{oc}/mV[d]	cell efficiency/%[d]
1a	0.43	1.05	3.2×10^{-4}	1.94	540	0.64
2a	0.54	0.98	6.5×10^{-6}	2.49	490	0.63
3a	030	1.01	−	0.68	420	0.14

[a] Optical densities were obtained at a maximum. [b] Dye coverage ratio was the ratio of dye coverage area per TiO_2 surface area. Dye coverage was estimated from UV/vis absorption spectra and the ratio was calculated using 7.73×10^{-15} cm^2 as a dye surface area. [c] The data were estimated from Figure 10. The data for **3a** were less reliable because of small signals. [d] See also Figure 11

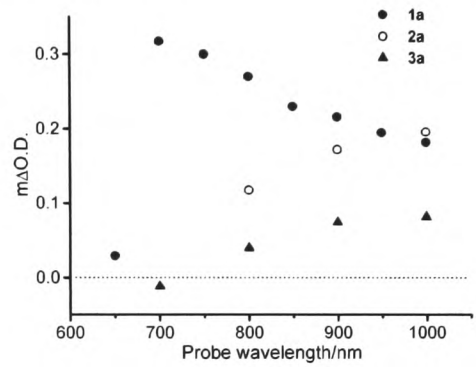

Figure 9. Comparison of the difference absorption spectra of **1a**, **2a**, and **3a** on nanocrystalline TiO_2 film. The spectra were recorded with 550 nm excitation pulse at 10^{-6} s.

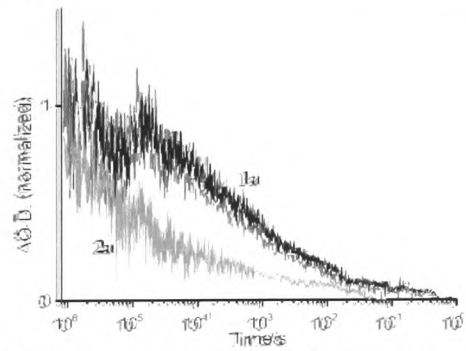

Figure 10. Transient absorption data monitoring the charge recombination kinetics for 4 μm TiO_2 films sensitized with dyes **1a** (black) and **2a** (gray). Experiments employed 550 nm excitation, and all data were collected at 900 nm probe wavelength. The half-life values for dyes **1a** and **2a** are 3.2×10^{-4} and 6.5×10^{-6} s, respectively. The data for **3a** were less reliable because of small signals.

Transient absorption data for the resulting dye-sensitized films covered in organic solvent were obtained following pulsed laser excitation and are shown in Figures 9 and 10. In all cases, a broad absorption increase was observed between 700 and 1000 nm, assigned to induced absorption of the dye cation/$TiO_2(e^-)$ states generated by electron injection from the dye excited state (Figure 9). For **1a**, an absorption maximum was observed at 700 nm and is assigned as dye cation absorption. In contrast, for **2a** and **3a**, the transient spectrum increases steadily toward longer wavelengths, indicating that for these dyes the transient signal is dominated by TiO_2 electron absorption, with cation absorption for these dyes being relatively weak over this spectral

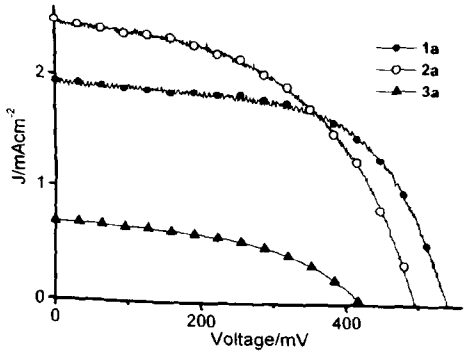

Figure 11. $I-V$ characterization for the liquid DSSC with dyes **1a**, **2a**, and **3a** under 1 sun and AM 1.5 intense illumination. The areas of all samples were 1.0 cm^2. I_{sc}, V_{oc}, ff (fill factor), and efficiency were 1.94 mA, 540 mV, 61.4%, and 0.64% for **1a**; 2.49 mA, 490 mV, 51.3%, and 0.63% for **2a**; 0.68 mA, 420 mV, 50.5%, and 0.14% for **3b**, respectively (see also Table 5).

region. The relatively low signal amplitude for dye **3a** is consistent with the low film optical density due to the low dye molar extinction coefficient.

Decay dynamics of the transient signal, assigned to the recombination of the TiO_2 electrons with dye cations, are shown in Figure 10. Half-times for these decay dynamics are summarized in Table 5. These dynamics are typical of charge recombination dynamics for such dye-sensitized TiO_2 films,[13,30] with dye **2a** showing faster, more dispersive recombination dynamics relative to dye **1a**.

Typical current/voltage characteristics for photoelectrochemical cells sensitized with dyes **1a**, **2a** and **3a** are shown in Figure 11, with the corresponding device efficiencies given in Table 5. It is apparent that there is a good correlation between the UV/visible absorbance data, the transient aborption data, and the device current/voltage characteristics. **2a**, which has the highest optical density, also has the highest short circuit current (I_{sc}), while **1a** exhibits the slowest recombination dynamics and the highest open circuit voltage (V_{oc}).

From the data detailed above, it is apparent that **1a** exhibits the highest photovoltaic device performance of the dye series studied. This device efficiency, however, remains relatively low compared to the more established sensitizer dye, the ditetrabutylammonium salt of $[RuL_2(NCS)_2]$ (L = 2,2′-bipyridyl-4,4′-dicarboxylato), commonly called N719. This lower device efficiency can be primarily attributed to the relatively low optical absorbance of **1a** compared to $[RuL_2(NCS)_2]$ (with peak molar extinction coefficients in the visible of 5615 and 14 000 M^{-1} cm^{-1}, respectively). As the devices presented here employed 4 μm, nonscattering TiO_2 films, this lower optical absorbance can be expected to have a strong effect on device performance. A significant improvement in device performance for **1a** can be expected by the use of thicker TiO_2 films with the addition of light scattering layers. A more detailed characterization of the photovoltaic performance and transient kinetics of devices employing **1a** was undertaken to elucidate whether differences in device performance between **1a** and N719 can be attributed to dye optical absorbance alone or whether other

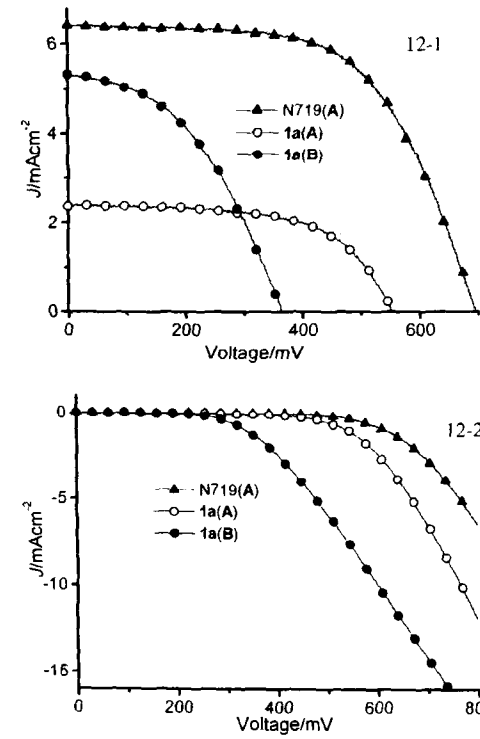

Figure 12. Comparison in terms of cell performance between the cell using electrolyte A (containing *tert*-butyl pyridine (t-BP)) and electrolyte B (without *tert*-butyl pyridine) in the electrolyte. Graph 12-1 represents $I-V$ curve of all three cells under 1 sun illumination. The cell performance, I_{sc}, V_{oc}, ff, and efficiency, were 2.37 mA, 550 mV, 61.5%, and 0.80% for **1a** using electrolyte A; 5.33 mA, 370 mV, 43.6%, and 0.84% for **1a** using electrolyte B; 6.41 mA, 700 mV, 60.4%, and 2.69% for N719 using electrolyte A, respectively. Graph 12-2 shows the data collected under dark conditions.

parameters also limit device performance. Figure 12 shows current/voltage data for **1a**/TiO_2 solar cells employing both the standard electrolyte A (containing the additive *tert*-butyl pyridine (t-BP)), as employed in Figure 9, and an alternative electrolyte B, in which the t-BP was omitted from the electrolyte. Control data employing the N719 dye are also shown for comparison, with the dye loading of N719 being selected to give the same peak optical density as that of **1a** (OD = 0.5 at 535 nm).

Figure 13 shows the corresponding transient absorption signals, with the excitation wavelength of 540 nm corresponding to that at which the optical density of the N719- and **1a**-sensitized devices are identical. Note that these transient data were collected for complete devices rather than for dye-sensitized films alone, as employed in Figure 9, with the probe wavelength of 1000 nm being selected to correspond primarily to absorption of electrons injected into the TiO_2 by the optical laser pulse. It is apparent that for **1a** the omission of t-BP from the electrolyte results in a significantly higher current density, but at the expense of a lower cell voltage. This observation is correlated with a larger transient signal, assigned to long-lived I_2^- product states. This effect is attributed to the established influence of t-BP on the TiO_2 conduction band energetics; the absence of t-BP lowers the TiO_2 conduction band, favoring electron injection and

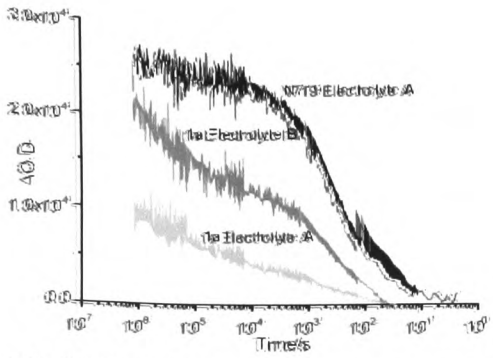

Figure 13. Transient absorption data monitoring charge recombination dynamics following optical excitation at 540 nm. White light was used as a probe light, and all signals were detected at 1000 nm. A comparison in terms of transient absorption decay between the cells with and without t-BP in the electrolyte suggests its effect on the LUMO energy level of the dyes. The N719 cell with t-BP was used as a control cell.

resulting in both the larger transient signal and higher short circuit current. The absence of efficient electron injection for dye **1a** in the presence of t-BP is attributed to the lower dye excited-state oxidation potential relative to N719 (770 mV vs SCE). Strikingly, in the absence of t-BP, both the short circuit current density and transient signal amplitude obtained with **1a** are of similar magnitude to those observed for the control data for N719. These data are therefore indicative that, in the absence of t-BP, the quantum efficiencies of both electron injection and dye regeneration for the **1a**/TiO_2 system are near unity.

The lower device voltage obtained with sensitizer **1a** relative to N719 is correlated with the higher dark current associated with this dye. This effect may be associated with the influence of the sensitizer dye on the TiO_2 conduction band energetics. Alternatively, this effect may result from an acceleration of the rate constant for electron recombination with the redox electrolyte. Experiments to further address this point are in progress.

Conclusions

This work has provided us with valuable structural and electronic information for the family of [Pt{*X*,*X*′(CO_2R)$_2$-bpy}(mnt)] complexes. The large torsion angle of **1b** seen in the crystal structure is reflected in the electrochemistry of the complex, thus showing the influence of twisting the bipyridyl rings on the reduction potential of the complexes. The spectroelectrochemical study shows that for all three complexes the reduction electron must be localized on the derivatized bpy moiety of the molecule. This reconfirms previous reports that the LUMO is mainly localized on the bpy. This is the first report of a Pt-based dye sensitizer where the bpy has been substituted in the 3,3′-positions. Interestingly, it shows the best performance of the three sensitizers tested. This result is significant when compared to previous work done in the field, being in sharp contrast with the only report of a Ru sensitizer with a 3,3′-disubstituted bpy, which showed an inferior performance to that of its 4,4′-analogue. The work reported in this paper demonstrates the worth of looking at other anchor ligands in the rational design of solar cell dyes and broadens the scope for further investigations into potential dyes for use in DSSC.

Acknowledgment. We thank Donald Robertson for providing us with the Na_2(mnt) used in this study. Financial support from the EPSRC is gratefully acknowledged.

Supporting Information Available: Crystallographic data for **1b**. This material is available free of charge via the Internet http://pubs.acs.org.

IC048799T